Università degli studi di Trieste

DEPARTMENT OF MATHEMATICS AND GEOSCIENCES
Ph.D. degree in Earth Science and Fluid Mechanics
XXXI cycle

A multidisciplinary geophysical approach to recognize and quantify the gas occurrence in the Northern Adriatic

Ph.D. student:
Giulia Matilde Ferrante

Thesis Supervisor:
Dr. Angelo Camerlenghi

Thesis co-Supervisors:
Dr. Federica Donda
Dr. Valentina Volpi
Dr. Umberta Tinivella

Thesis submitted in 2018

Contents

List of Figures

List of Tables

Introduction

A good understanding of fluid occurrence in sedimentary basins is needed to properly reconstruct their tectonic and geological evolution. Recognizing accumulation, migration and expulsion of fluids help in modeling plumbing systems and thus potential hydrocarbon plays. Furthermore, depending on the type of fluid and the processed involved, there could be a number of hazards caused by fluids release from the subsurface, including risks to seabed infrastructures and instability in the upper unconsolidated sedimentary layers.

Altough tectonics can produce a predominantly vertical fracture network which may serve as migration path, fluid flows are able to open conduits through hydrofracturing and/or dissolution and produce non-tectonic faulting. Locally, they can deform the sedimentary sequence and trigger remobilization and intrusion (Maestrelli et al., 2017). Expulsion of fluids is responsible for the development of mud-volcanoes, craters, outcrops.

However, such processes are very difficult to study in detail, because of their often inaccessible, episodic, unpredictable and occasionally violent nature (Huuse et al., 2010). Indeed, geophysical characterization of fluid distribution within sediments present several issues that make it not trivial.

Hence, there is a distinct need to integrate observations from all available sources. In this thesis, seismic data and geophysical wireline logs, together with borehole drilling reports and geochemical analysis, were used to characterize and quantify the gas occurrence in the Northern Adriatic.

The study area is characterized by widespread occurrence of gas in the subsurface, testified by the presence of fluid related seabed and sub-seabed features (Donda et al., 2015, and references therein).

In 2009 and 2014 OGS carried out two 2D multichannel seismic surveys to constrain the relationship between gas emissions, migration paths and the regional geological setting. A further aim was to characterize the gas-charged fluids occurring within the sedimentary succession. Two seismic lines from these datasets were analyzed in the framework of this PhD thesis (GEA project, '*G*as *E*missions in the Northern *A*driatic Sea').

The objective of this work is to determine the distribution of gas and estimate its concentration along the two selected perpendicular seismic profiles, through the petrophysical characterization of the sediments with the use of well-log to seismic attributes correlation.

A multidisciplinary approach was applied both in the analysis and in the interpretation of the data, through the integration of geological information with geophysical data. This allowed to investigate the role of tectonics in relation to gas migration and to provide an hypothesis on the gas geological play and plumbing syst.

The proper characterization of the gas occurrence in the study area has a direct climatological implication. Due to the shallow water in the Northern Adriatic, the potential transfer of gas from sediment to the water column and then into the atmosphere could be significant. Therefore, understanding the mechanisms of gas seepage is crucial, since methane, the main component of the gas in the area, plays a major role as a greenhouse gas.

Part I

Study area and state of the art

Chapter 1

Geological and oceanographic setting of the Northern Adriatic Sea

1.1 Geological, structural and stratigraphic setting

The study area lies at the northern boundary of the **Adria Plate**, which at present consists of the relatively stable Adriatic basin including the Po Valley, the Adriatic Sea and the Apulian platform, bordered to the East by the Hellenides and the Dinarides, to the North by the Alps and to the West by the Apennines (Fig.1.2). The relationship between Adria and Africa (or Nubia) Plates still remains controversial. Geomagnetic data would suggest that Adria extends as a promontory of the African Plate into the Adriatic region (Mele, 2001). However, there are also some pieces of evidence that Adria would be an independent micro-plate between Africa and Eurasia (Nocquet and Calais, 2003). Oldow et al. (2002) hypothesize that the Gargano-Dubrovnik fault would divide Adria into two blocks: a north-western part with little motion relative to Europe and a south-eastern part moving together with Nubia. Other studies suggest the Adriatic as an area of distributed deformation (Nocquet et al., 2001). Battaglia et al. (2004) used GPS data to test the proposed models and showed that present-day velocities are best fitted by considering Adria as an independent micro-plate (Fig.1.2). While the origin of the Adria Plate in terms of plate tectonics is out of the scope of the present thesis, it is noteworthy that Adria is experiencing different external stress fields which partly account for the faults identified in the data utilized in the present study.
The **structural setting** of the study area is the result of two different tectonic stages: a Mid-Late Jurassic and Early Cretaceous extensional phase, and a complex Cenozoic compressional regime (Donda et al., 2015, and references therein). From Late Cretaceous, when the beginning of the compressional regime occurred, Adria Plate represented the foredeep and foreland for the adjacent chains, being involved in the southeast-directed Alpine subduction, in the NE-directed Dinaric subduction (Di Stefano et al., 2009) and from late Oligocene to Miocene also in the Apennines westward subduction (Carminati et al., 2003; Cuffaro et al., 2010, Fig.1.3).
As a consequence of the compressional events, several inflection phases took place in the area and produced up to 8000 m-deep foredeep basins filled with clastic sequences (Fantoni and Franciosi, 2010; Ghielmi et al., 2010). A faster subsidence of the Pleistocene sediments along the western side of the northern Adria margin is recorded. This asymmetry has been associated with a retreat of the Apennines subduction hinge, which is still moving toward the north-east (Devoti et al., 2008, Fig.1.3).
The **stratigraphy** of the study area is composed by a Cretaceous-Paleocene carbonate succession, comprising the Maiolica, Marne a Fucoidi, Soccher and Scaglia formations, overlain by the Eocene-Late Miocene turbidite deposits belonging to the Gallare Marls formation (Zecchin et al., 2017, and references

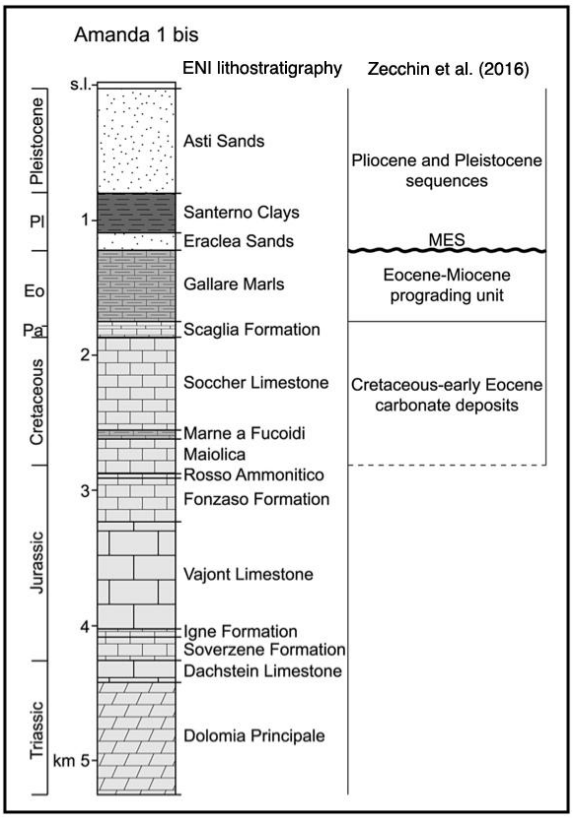

Figure 1.1: Stratigraphic succession of the study area as shown by Amanda 1 bis well. MES - Messinian Erosion Surface. From Zecchin et al. (2017).

therein). The top of it is marked by an erosional unconformity, the Mediterranean-wide *Messinian Unconformity* produced by sea-level draw down during the Messinan salinity crisis (Ghielmi et al., 2010). The Pliocene is represented by a southward prograding unit, whereas the uppermost part of the succession consists of shallow-marine to continental foredeep deposits controlled by late Quaternary glacial-eustatic changes (Fig.1.1).

The structural setting of the northern Apennines plays a key role in the depositional and paleogeographic evolution of the study area (Zecchin et al., 2017). From the Pliocene, the Apennines were the ones that most likely controlled all the deformation processes, subsidence and sediment supply. However, Brancolini et al., (under review) suggest that since the Early Pliocene, subduction below the Apennine chain ceased and that the Adria Plate movements have been only driven by the kinematic of the adjacent plates, particularly the SE-NW Nubia-Europe convergence. As a consequence the Adriatic region has been fragmented in four blocks: i.e. Po Plain, Northern, Central and Southern Adriatic, separated by major tectonic lineaments. In this framework, the Northern Adriatic region may be regarded as a wedge bounded to the west by the Schio-Vicenza Fault system and to the south-east by the Kvarner Fault.

In more recent times (Pleistocene), subsidence affected the coastline favoring the fluvial sedimentation by the Po river. Subsidence interests the entire Po Basin and the whole northern Adriatic sea, and induced the Italian Government to stop any fluid extraction activity in the study area.

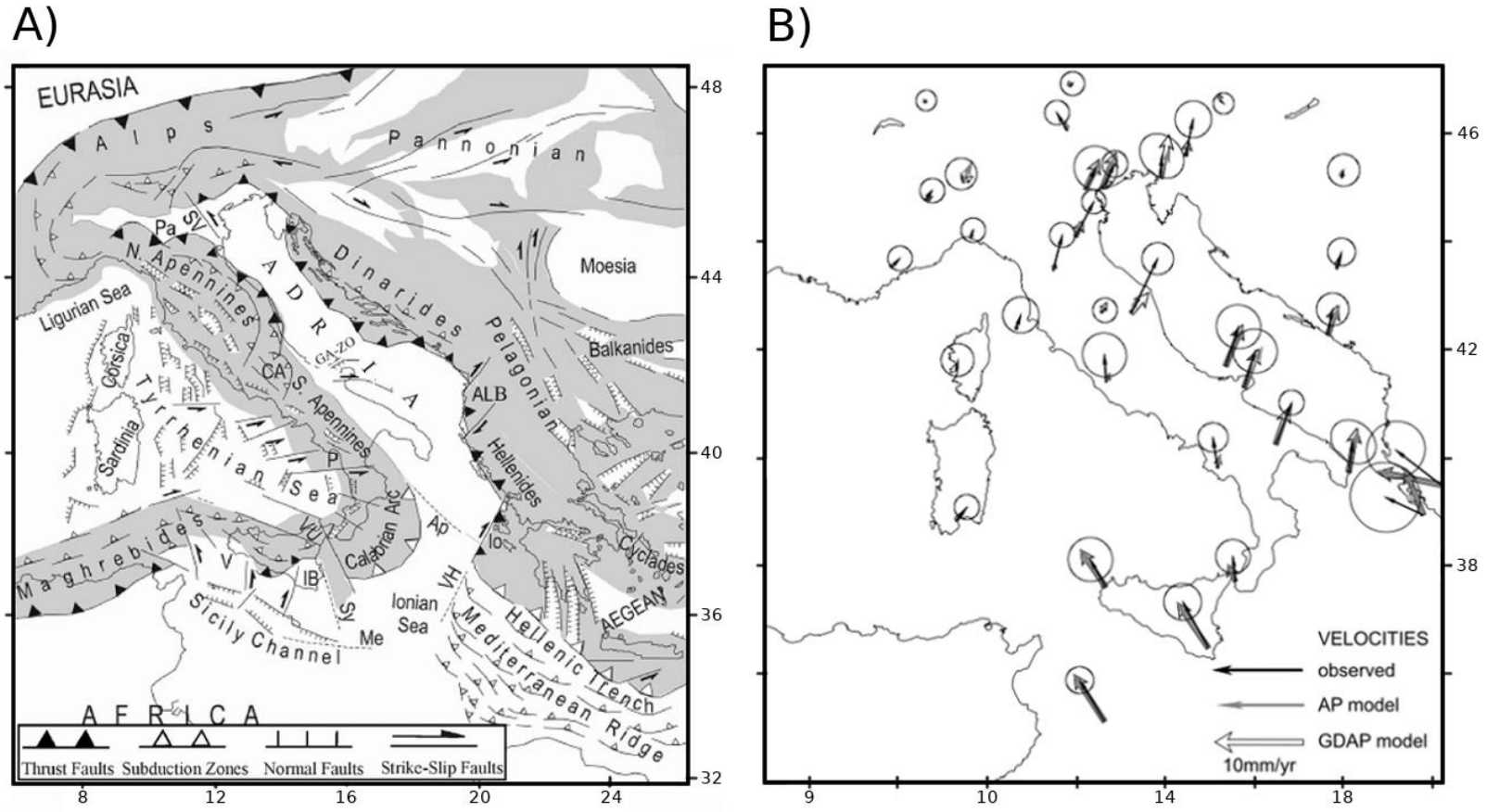

Figure 1.2: A) Tectonic features in the Adriatic region and surroundings. Grey area identify the orogenic belts. Ap=Apulian escarpment; AL=Albania; CA=Central Apennines; GA=Gargano zone; IB=Iblean block; Io=Ionian islands; Me=Medina fault; P=Palinuro fault; Pa=Padanian region; SV=Schio-Vicenza fault system; Sy=Syracuse escarpment; VH=Victor Hensen fault system; V=Ventura block; VU=Vulcano fault. Modified from Mantovani et al. (2006); B) Observed and modeled GPS velocities and their 95% confidence ellipse for the single block (AP) and the two blocks (GDAP) model of Adria. All is referenced to the stable Eurasian frame. Modified from Battaglia et al. (2004).

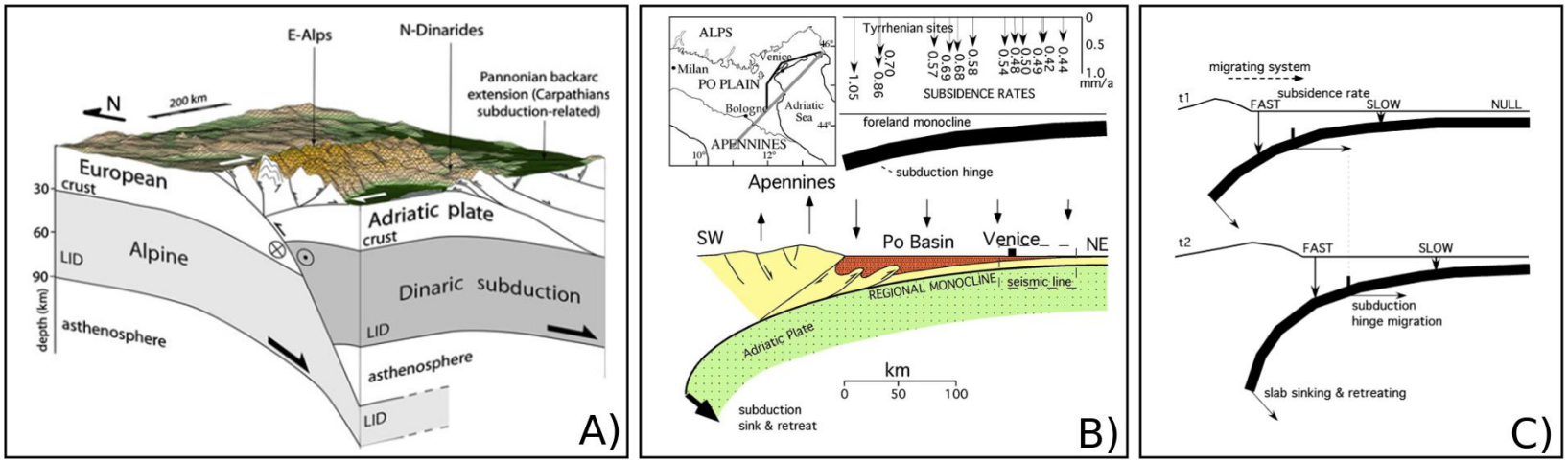

Figure 1.3: A) 3D reconstruction at the interference between the Alpine and Dinaric subductions. The area also suffers from the field subsidence related to the Apennines; B) Subsidence rates. The dip of the regional monocline recorded the faster subsidence to the south-west and it can be explained by the northeastward slab retreat of the Adriatic slab; C) Model of the migration of the subsidence rates which decrease moving toward the foreland of the subduction. As the subduction hinge retreats toward the foreland, the subsidence rate increases. Modified from Cuffaro et al. (2010).

1.2 Oceanographic setting

The Adriatic Sea is divided into three basins. The northern section, which hosts the study area, is characterized by an average depth of about 35 m, average salinity of 37-38‰ and average temperature of 25°. Here, the broad and shallow shelf is exposed to the north-easterly Bora wind, and is a site of dense waters formation. Furthermore, several important rivers flow in this area, such as the Po and the Tagliamento rivers, which are responsible for high fresh-water discharge. The central basin shows an average depth of about 140 m, with the presence of a 270 m-deep depression, the Mid-Adriatic Pit (Van Straaten, 1970). The southern section, characterized by a wide depression more than 1200 m-deep (South-Adriatic Pit), has an average salinity of 38.4-38.9‰ and average temperature of 18° (see Fig.1.4).

There are numerous rivers discharging into the Adriatic basin, plus underground freshwater seeping into the sea along the eastern coast. River discharge affects both the sedimentation and the circulation of the coasts, and its effect is particularly evident in the northern basin with the Po River and in the southern basin with Neretva river and a group of Albanian rivers (Brambati et al., 1983). Most of the river input in the Adriatic Sea comes from the Po river which is the largest Italian river and supplies over the 11% of the total freshwater flow into the Mediterranean, the 28% into the entire Adriatic Sea and 50% into its northern part (Degobbis et al., 2000). Both rivers and submarine springs along the Balkan coasts together contribute another 29% of freshwater flow into the Adriatic basin. This high input not only determines the low salinity but also models the coast and influence the currents system.

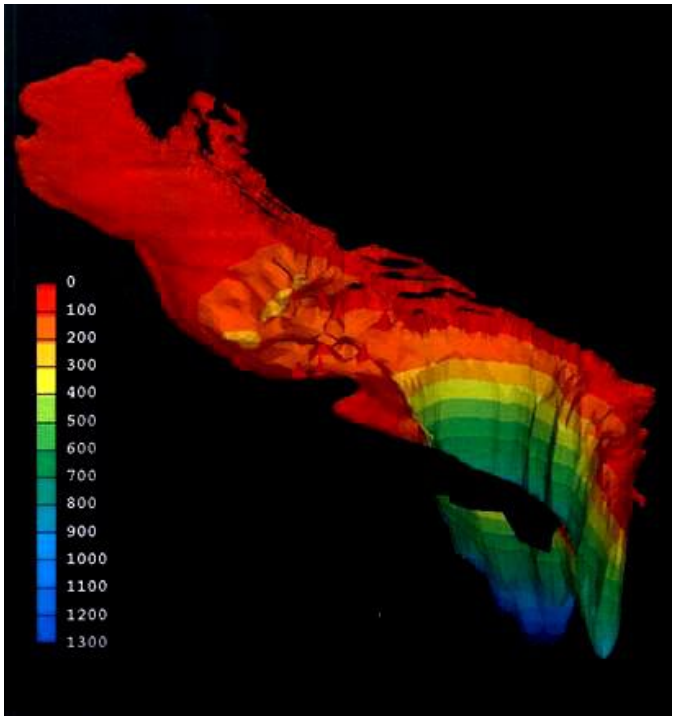

Figure 1.4: Bathymetry of the Adriatic Sea. From http://engineering.dartmouth.edu/adriatic/index.html.

The Adriatic Sea is characterized by a **cyclonic superficial water circulation**: the waters flow northward along the Croatian coast and flow southward along the Italian coast. Cyclonic gyres could be formed in each of the three basins, with different intensity depending to the season and the freshwater inputs (Fig.1.5). There is also some evidence of local anticyclonic cells (Gordini, 2009, and references therein).

Tidal phenomena are more important in the Adriatic than the rest of the Mediterranean basin, reaching amplitudes around 150-200 cm in the northern part. Meteorological factors (as winds and pressure conditions), seiches and the geological-morphological characteristics of the basin have also a strong influence on short term sea level changes. Seasonal and long-term fluctuation oceanographic and biological conditions occur, mainly due to atmospheric forcing, freshwater discharges, variable intrusion of high salinity waters and a very variable and complex circulation (Joksimović et al., 2016).

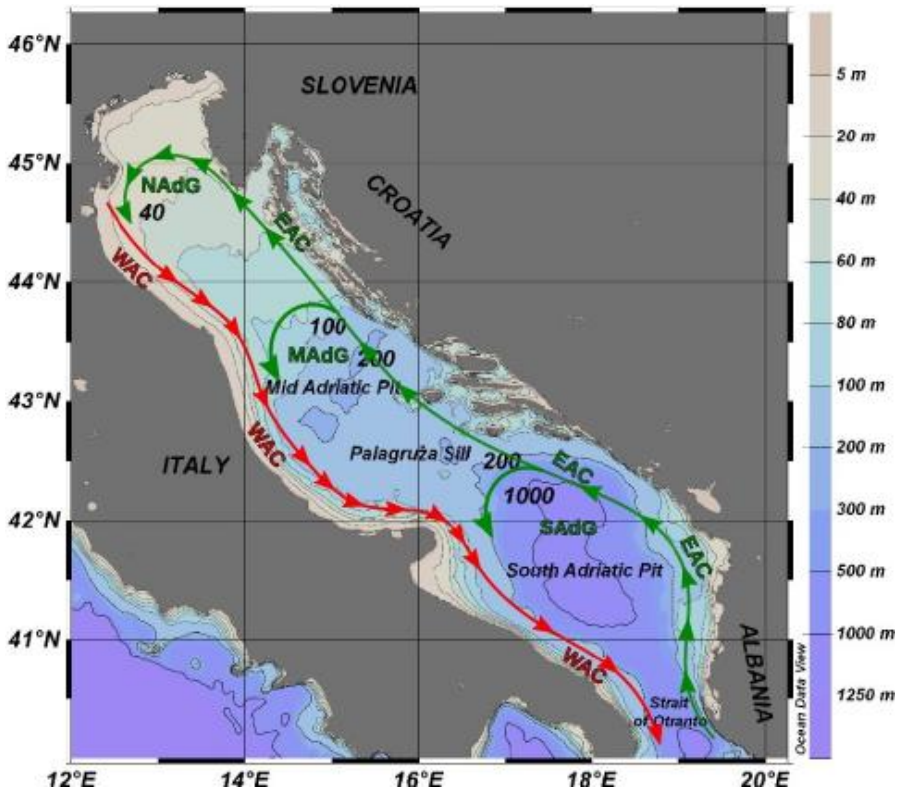

Figure 1.5: Adriatic Sea: bathymetry, morphology and main surface circulation. EAC: Eastern Adriatic Current; WAC: Western Adriatic Current; NAdG: North Adriatic Gyre; MAdG: Middle Adriatic Gyre; SAdG: South Adriatic Gyre. From Lipizer et al. (2014).

The Adriatic Sea is the most productive basin of the entire Mediterranean Sea, and along the western coast the high nutrient load is responsible for high production. Because of its strategic position (it connects northern and western to the eastern European countries), the Adriatic Sea is crucial for several kind of human activities (fishery, industry, tourism...) which caused intense environmental alterations in the last centuries.

Chapter 2

Overview on fluid flow features in hydrocarbon plumbing systems

Fluid flow features represent detectable anomalies generated during past and/or present subsurface flow of fluids (oil, gas, brine, groundwater and magmatic fluids) from source to the seabed or land surface (Cartwright et al., 2007; Løseth et al., 2009).
In seismic data, these features typically consist in signal anomalies related to a wide range of geological structures such as pockmarks, mud volcanoes, gas hydrates, chimneys, pipes, sediment injections, carbonate mounds, seeps and related diagenetic phenomena (Cartwright et al., 2007; Løseth et al., 2009; Huuse et al., 2010). The type of structure generated depends on a variety of parameters as for instance the source of fluid, the flow type, the structural setting and the nature of the hosting sediment for the fluid flow (Van Rensbergen et al., 2003; Cartwright et al., 2007; Huuse et al., 2010).
In any case, fluid fill can be interpreted on seismic data. Therefore, there should be a reasonable confidence in the validity of the amplitudes in the seismic dataset. Processing should try to avoid any steps that cause amplitude artefacts. This is the approach followed in this work. Amplitudes should be everywhere proportional to reflectivity. This is not achievable, but what can be done is to make sure but what that local lateral variation of amplitude on a particular group of reflectors is proportional to reflectivity change. Often, it is reasonable to assume that the average absolute reflectivity over a long time window varies little, so, for example, a long-gate gain operator can be applied to the data.
Calibration of amplitude to reflectivity is possible from a well tie, but it is valid only over a limited interval. Following the amplitude anomaly through the seismic processing sequence from the raw gathers may be helpful; this may reveal an artefact being introduce in a particular processing step. Check for every big change in amplitude spectra is also crucial. Avoiding amplitude distortion algorithm is essential.
Apart from processing artefact, there are a number of factors that can lead to a misunderstanding in amplitude anomalies interpretation. Amongst them, lateral amplitude changes are related to changes in porosity rather than fluid fill. This is particularly true for well-consolidated sands and carbonates (Bacon et al., 2003). Another example of complication for the study of amplitudes is tuning (Bacon et al., 2003). It is a phenomenon of constructive or destructive interference form closely spaced reflectors. At a spacing less than one-quarter of the wavelength, reflections interference produce a single event of high amplitude that could be erroneously interpreted as a seismic anomaly.

In this chapter the diversity of seismically imaged fluid flow features in hydrocarbon plumbing systems is reviewed (sec.2.2 and sec.2.3). Gas hydrates and mud volcanoes, not present in the study area, are not treated. Instead, special attention is given to the case of gas flow. This chapter will be reminded in the discussion and interpretation of final results.

2.1 Hydrocarbon plumbing systems

Hydrocarbon plumbing systems (HPSs) are assemblages of permeable pathways that allow hydrocarbons to ascend from the deeper source area of a basin where they are generated to shallower reservoirs where they can become trapped in sufficient quantities to form accumulations (Andresen, 2012). In a broader sense, they describe the pathways, timing and controls of fluid leakage.
The pathways involved in any given HPS are highly variable, depending on geological context, but they generally involve a combination of stratal (along bedding) and cross-stratal hydrocarbon migration (England et al., 1987). One of the most enigmatic aspects of hydrocarbon migration is the common observation that shallow accumulations often occur directly above the kitchen (source rock), separated by several thousand metres of low permeability sediments (Aplin et al., 1999). Cartwright et al. (2007) suggest that highly focused vertical hydrocarbon migration may occur mainly through a diverse set of geological features that they termed **seal bypass systems**, and which can be subdivided into three main classes: (1) faults, (2) pipes, (3) intrusions. The first two classes are investigated more in sec.2.2.2, while intrusions are neglected.
Andresen (2012) showed how it is possible to group a set of seemingly disparate fluid flow phenomena observed on seismic data (such as a bottom simulating reflection, pipes and pockmarks) and link them together explicitly as part of a single connected flow system. Where hydrocarbons are proven to be part of the flow, then this can in turn be described as an HPS (Foschi and Cartwright, 2016).

2.1.1 Why fluids migrate? Triggering mechanisms

In its simplest sense, fluid migration is driven by pressure differential between the pore fluid pressure within a sub-surface permeable sedimentary rock and a lower pressured (usually shallower) aquifer or the earth's surface/seabed (Huuse et al., 2010).
Overpressure in the water phase will drive water flow. Given the low compressibility of water, the flow resulting from pressure release alone is very limited, except on a local scale along permeable faults and fractures. During burial and at shallow depths, the main flow of pore water is driven by compaction, which is a slow process, even when overpressure is released abruptly with a resulting increase in the net effective stress (Bjørlykke, 1993). However, buoyancy of any hydrocarbons present increases the pressure difference and can result in strong flow of the hydrocarbon phase. Furthermore, fluid viscosity may also play an important part through the viscosity differences amongst brine, low-viscosity gas/air and viscous oil (Jonk, 2010).
Flow can be composed of either water, hydrocarbons or both. If fluid migration is sufficiently vigorous, unconsolidated sediment may be entrained when its fluidization velocity is exceeded. If subsurface pressures are sufficiently high, the rock least principle stress (commonly termed the fracture gradient) can be exceeded and a fracture network is generated (**hydrofracturing**). This can lead to seal breach and the resultant fracture network may become utilized as a path for focused fluid flows and/or for fluidized sediment injection (Huuse et al., 2010).
Except hydrofracturing, as commonly observed in evaporite provinces worldwide (Bertoni et al., 2017), opening of conduits can be associated to **sediment dissolution and deformation**. However, once the fracture is established, the pressure gradient along the fracture will lead to fast fluid flow and possibly to entrainment of sediments (Huuse et al., 2010; Van Rensbergen et al., 2003). Furthermore, the increased buoyancy provided by gas exsolution in the upper few meters of the subsurface may vastly increase the flow velocity (Brown, 1990).
Focused fluid flow, in most of the cases, is thought to be triggered by local fluid overpressure when faults and overlying sediments are impermeable, rather than by the simple increasing effective stress with burial and porosity reduction. Bertoni et al. (2017) suggest that overpressure is needed to create the necessary fluid flow and lead to hydrofracturing and conduit formation. In any case, lateral drainage has to be

somehow inhibited.
Overpressure in sediments is driven by a variety of mechanisms, active over a range of time scales, the most prevalent being unbalanced compaction due to rapid burial relative to pore-fluid drainage (Yardley and Swarbrick, 2000), lateral transfer of pressure due to tectonic stress and differential loading, diagenesis, cementation and hydrocarbon generation (Osborne and Swarbrick, 1997). These relatively slow mechanisms of pressure build up may be collectively considered as "priming" mechanisms pre-conditioning the sedimentary basins for rapid fluid flow and thus for sediment remobilization (Huuse et al., 2010).

Sedimentary basins are often characterized by very complicated plumbing systems that had begun to be unravelled by 3D or 4D (time lapse seismic) seismic only in the past decades (Cartwright et al., 2007).
Understanding of seismically imaged fluid flow features and seal by-pass systems would be vastly improved by a number of factors, including better outcrop analogues and integration with basin and fluid migration modelling approaches (Huuse et al., 2010). Sampling and continuous chemical and physical measurements of active fluid flow systems are also very effective. This is of particular importance giving the fact that exploitable hydrocarbon plays are becoming more and more diverse and they demand an integrated and multidisciplinary approach. For example, deep biogenic gas reservoirs are nowadays under production worldwide and this requires a good understanding of both the deeper and the shallower parts of the plumbing system.
Apart from impacting hydrocarbon plumbing systems, the occurrence of fluid flow features may also have implications for the extraction of groundwater and geothermal energy, storage of CO_2 and nuclear waste, and for the global organic carbon cycle of the Earth (Andresen, 2012).

2.2 Vertically focused fluid flow seismic features

2.2.1 Pockmarks

Because of buoyancy forces, gas generated at both great and shallow depths tries to escape to the surface. If possible, it reaches the surface through pre-existing zones of weakness and can form craters at the seafloor. (Chopra and Marfurt, 2007). These erosional features are called pockmarks (Fig.2.1 for a 3D example) and they play a role in the carbon cycle between the water column and the sediments. It should be noted that pockmarks can not only be formed by gas, but also by groundwater flowing through sediments (Judd and Hovland, 2007). Pockmarks occurrence on the seabed is one of the main indicators of recent fluid flow. They are release pathways for fluids, but not all of them are actively seeping gas. Some can be inactive or activated afterwards. Pockmarks have different morphologies, size (height, width), orientation and shapes. The most common shapes are circular and elliptical. In the areas where there is flat seabed, their orientation is based on the dominant tidal current (Judd and Hovland, 2007). Furthermore, composite pockmarks can occur in places where normal pockmarks fuse in one another into complex shapes. Also, there are the so called buried ("fossil") pockmarks which occur at various levels within the sedimentary succession (Judd and Hovland, 2007). Buried pockmarks are relevant since they represent the time when gas seepage was active and the time when there was a new deposition of sediments over pockmark and when this process stopped (Long, 1992). These buried pockmarks can form when gas escapes and the sediments then collapse, filling the free space. They can also be reactivated when a pockmark overlies a deep succession which is connected with vertical columns of disturbed sediments (Judd and Hovland, 2007).

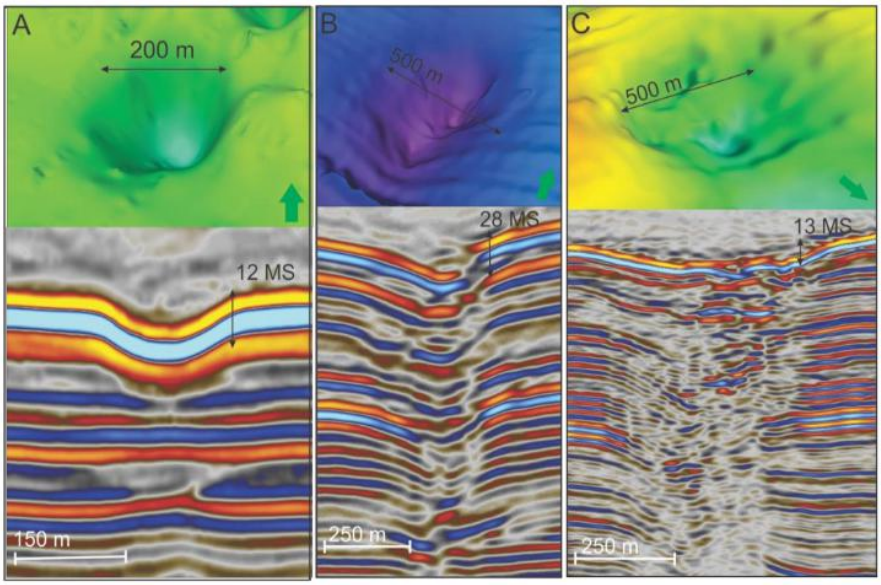

Figure 2.1: Examples of pockmarks in 3D from A) Nyegga region, mid-Norwegian margin; B) and C) Vestnesa ridge, offshore western Svalbard. From Virs (2015).

Pockmarks are found worldwide in a variety of depositional environments, including continental shelves, slopes and ocean basins. They generally form in soft, fine-grained sediments such as clay, mud and silts. The finer the sediments are, the greater the size of the pockmark is. The factors that define the distribution of pockmarks can be thought to be formation mechanism and sediment suitability for pockmark formation (Virs, 2015).
Although pockmarks can be controlled by faults and differential compaction, many of them seems uncorrelated to underlying stratigraphy or geological structures, implying that the fluids responsible for their formation originated at very shallow depths (Chopra and Marfurt, 2007).

2.2.2 Chimney and pipes

Gas chimneys and pipes are vertical features in which the normal sequence of seismic reflections has been disturbed by the upward migration of pore fluids, such as gas (Judd and Hovland, 2007). They are recognized as vertical extensive either low- or high-amplitude anomalies on seismic data (Løseth et al., 2011; Heggland, 2005; Cartwright et al., 2007).
A clear distinction between chimneys and pipes is not given in the literature and the two terms are often used variably from paper to paper. Gas chimneys are normally associated with dimmed and distorted amplitudes, while pipes may consist of vertically stacked either high- or low amplitude anomalies (Andresen, 2012). Seismic chimney can be defined as a vertical zone (kilometers wide) of low-amplitude (blanking) and distorted seismic reflections, while a pipe is narrower zone (hundreds of meters wide). Also, pipe structures represent fluid flow conduits where little or no sediments is entrained (Huuse et al., 2010). Both of them are recognized on seismic data as zones of low-coherence reflection.
Three major conditions cause this poor data quality (Chopra and Marfurt, 2007):

- There may be considerable absorption of compressional-wave energy if gas bubbles are present in the pores;

- Energy is scattered incoherently because of the not homogeneous saturation of the sediments;
- The presence of gas results in a significant drop in compressional wave velocity. In shallow sediments, this velocity may be less than that of the compressional wave velocity in water. Consequently, seismic sections exhibit depressions in time, multiphating and apparent faults.

Real fracturing due to gas overpressure, gas driven dissolution and cementation, sediment mobilization and intrusions may also influence the clarity in chimneys and pipes definitions (Cartwright and Huuse, 2005; Løseth et al., 2009). Shear waves are relatively insensitive to the presence of gas (via the effect on density) and they can be used to accurately image through a gas chimney.
Nevertheless, such features have been explained as zones of distributed connected fractures within otherwise impermeable (for example clay-rich) sediments, and hence represent vertical pathways for fluid flow from the time of their formation (Cartwright and Huuse, 2005). The flow of gas through the chimney fractured network can lead to the formation, at the seafloor, of pockmarks or, if the gas is methane, to the precipitation of authigenic carbonates (Mazzini et al., 2016).

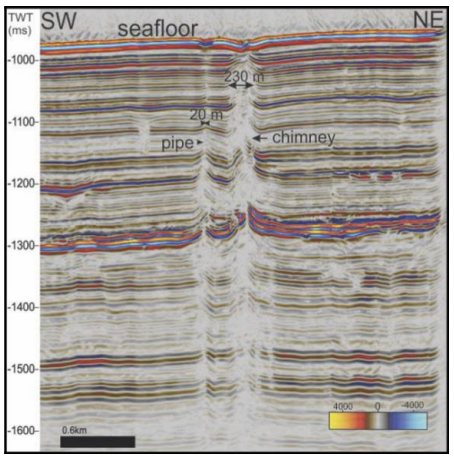

Figure 2.2: Size of pipes and chimneys from offshore Svalbard margin. From Virs (2015).

Gas chimneys have vertical extent of up to or greater than 1000 m (Løseth et al., 2009). Also, at their top, a frequently high amplitude anomaly is observed, possibly related to gas accumulation. Chimneys and pipes show from straight columnar shapes to diffuse structures with poorly defined boundaries. Strong variations within their lateral extent (resulting in strongly irregular shapes) suggest the chimney/pipe probably experienced lateral migration of fluids, possibly feeding local accumulations. In other cases, pipes interacted, resulting in coalescent structures (Maestrelli et al., 2017, Fig.2.3).
Commonly, when looking at the seismic section, at gas chimney outer borders, up-bending reflections or down-bending reflections can be observed. However, according to seismic theory and to well documented seismic pipe architectures (Moss and Cartwright, 2010; Cartwright and Santamarina, 2015), the presence and the passage of hydrocarbons or mixed fluid, due to their lower impedance contrast, should lead to a pull down effect and/or amplification of the horizons rather than an upward deflection.
In general, conduits generated by the upward migration of hydrocarbon through the stratigraphic sequence can lead (if gas is trapped) to a pull down effect (Maestrelli et al., 2017). Upwards deflections, when present, are thought to be the real internal architecture of the conduit, suggesting the importance of dragging and deformation effects induced by the intrusive mechanism during fluid flow processes. It is important to underline that a high velocity material inside the chimney can also cause pull-up reflections. This is the case of gas hydrates, but also small carbonate accumulations emplaced in the conduit (Plaza-Faverola et al., 2011; Plaza-Faverola and Keiding, 2019). Also, interpreters should pay attention to processing artefacts.
Gas chimneys occur throughout the world and they are significant structures as leakage structures. Some of them constitute a rooted link between the reservoir and the shallow subsurface (Cartwright et al., 2007). When the chimney is deeply rooted, it can indicate either a breached or poor hydrocarbon seal, or more favorably, a reservoir that is charged beyond its sealing capacity (Maestrelli et al., 2017).
The upper termination of the leakage zone is set at the uppermost level of vertical migration. On seismic data the top of the leakage zone is the uppermost observed leakage anomaly.

According to Løseth et al. (2009), the top of a leakage zone can be used to:

- Define when the leakage was active;
- Define levels of laterally distributed reservoir rocks or "gathering systems";
- Indicate the hydrocarbon-sourcing points, e.g., the point or area where hydrocarbons from reservoirs migrate vertically through the successions;
- Suggest levels of effective migration seals.

Furthermore, as extensively reported in the literature (e.g. Cathles et al., 2010), chimneys frequently originate on top of shallow gas accumulations.

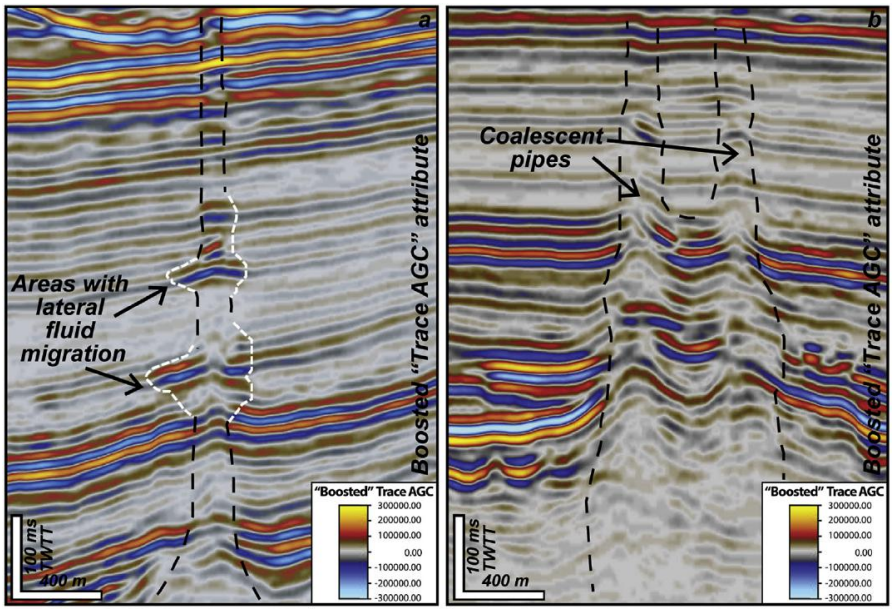

Figure 2.3: (a) Fluid escape pipe showing lateral migration of fluids, exploiting lateral porosity. Brights indicating presence of fluid fade ahead from the conduit at different heights, indicating scattered activation of the leakage structure. After the primary eruption, secondary drainage events were not able to push the fluids up the paleo-seabed (probably due to the lack of sufficient overpressure) and led these to escape laterally. (b) Two pipes showing a coalescent root. From Maestrelli et al. (2017).

The observed spatial coincidence of the chimney/pipe with faulting strongly suggests that the vertical fluid pathways are exploiting paths of structurally enhanced permeability (Bertoni et al., 2017, Fig.2.4). At depth, the circulation of fluids is mostly controlled by fracture networks, commonly a consequence of the tectonic regime affecting the areas under study. The tectonic deformation has a two-fold effect on fluid migration: the creation of overpressured area and the establishment of pathways (Bertoni et al., 2017). Indeed, faults are one of the three main groups of seal by-pass systems documented by Cartwright et al. (2007). They may act as fluid conduits (Nunn, 1996) but equally prevent the migration of fluids and hydrocarbons to the surface (Cartwright et al., 2007). The same structures can behave as barriers or dynamic conduits depending on the timing of the plumbing system and/in the tectonic regime. It is

then very important to re-construct the play between faults/fractures and fluid flow features. For example, if chimneys are correlated with faults, it means that faults are leaking, thereby reducing the risk of overpressure (crucial for reservoir stability).

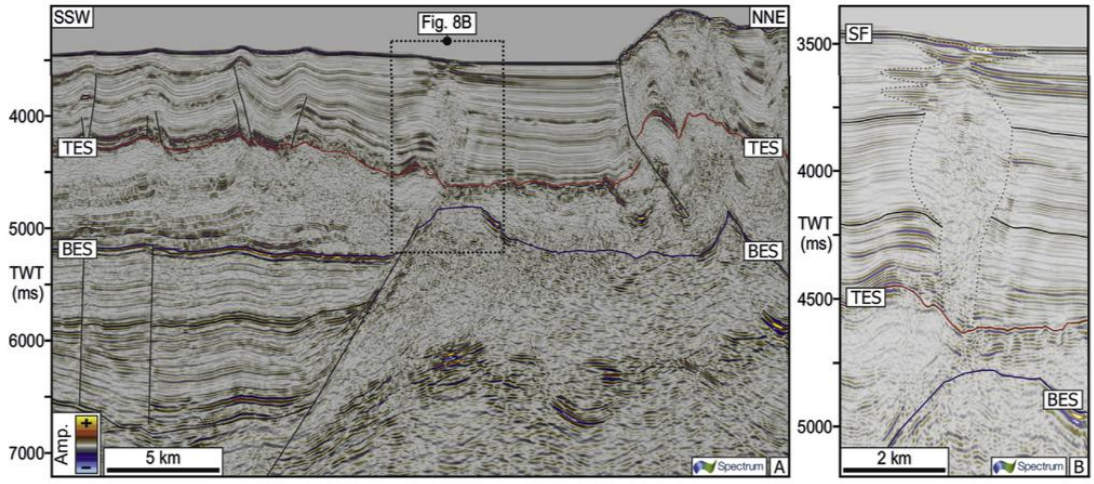

Figure 2.4: A) Seismic section crossing the Herodotus Basin at the edges of the Eratosthenes Block (Eastern Mediterranean); B) Zoom showing the chimney associated with clastic intrusion. The dotted lines enclose the area of sub-vertical disrupted seismic character. SF: Seafloor. TES: Top Erosional Surface (Top Messinian evaporites). BES: Base Erosional surface (Base Messinian evaporites). From Bertoni et al. (2017).

2.2.3 Methane-derived authigenic carbonates

Authigenic carbonate refers to any carbonate mineral precipitated inorganically in situ, whether at the sediment-water interface or within sediment pore waters (Schrag et al., 2013). Most authigenic carbonate is formed in sediments when alkalinity is produced from diagenetic reactions, usually those that reduce sulfate or ferric iron resulting in supersaturation of carbonate minerals, including calcite, dolomite, or siderite. Precipitation of pyrite can also be an important source of alkalinity (Schrag et al., 2013). Because most reduction of iron and sulfate occurs through oxidation of methane (anaerobic methane oxidation) or organic carbon, the DIC (dissolved inorganic carbon) from which authigenic carbonate forms is generally depleted in ^{13}C, although enrichment is possible if carbonate precipitation occurs deeper in the sediment column.

Methane-derived authigenic carbonates include crusts, concretions and mounds and are related to the seepage of methane-rich fluids to the seafloor where anaerobic methane oxidation coupled with bacterial sulfate reduction results in the carbonates precipitation (Boetius et al., 2000; Judd and Hovland, 2007).

Several observations are described typically in provinces characterized by the presence of other focused fluid flow features such as pockmarks (Judd and Hovland, 2007; Andresen, 2012). Indeed very often, methane-derived carbonates are studied to assess the past and/or present presence of gas within the shallower sediments and possibly its migration path.

Furthermore, these rock outcrops are characterized by a rich community of associated flora and fauna and thus represent a unique hotspot of biodiversity. The concretions play a fundamental role as habitat for reproduction and nurseries of demersal and pelagic species (Gordini et al., 2012).

Last but not least, some authors (e.g. Schrag et al., 2013) suggest that authigenic carbonates, including

the methane-derived ones, have played a major role in the carbon isotope mass balance over Earth history, although they represent a minor component of the modern isotope mass balance because of high levels of atmospheric oxygen in the modern world.

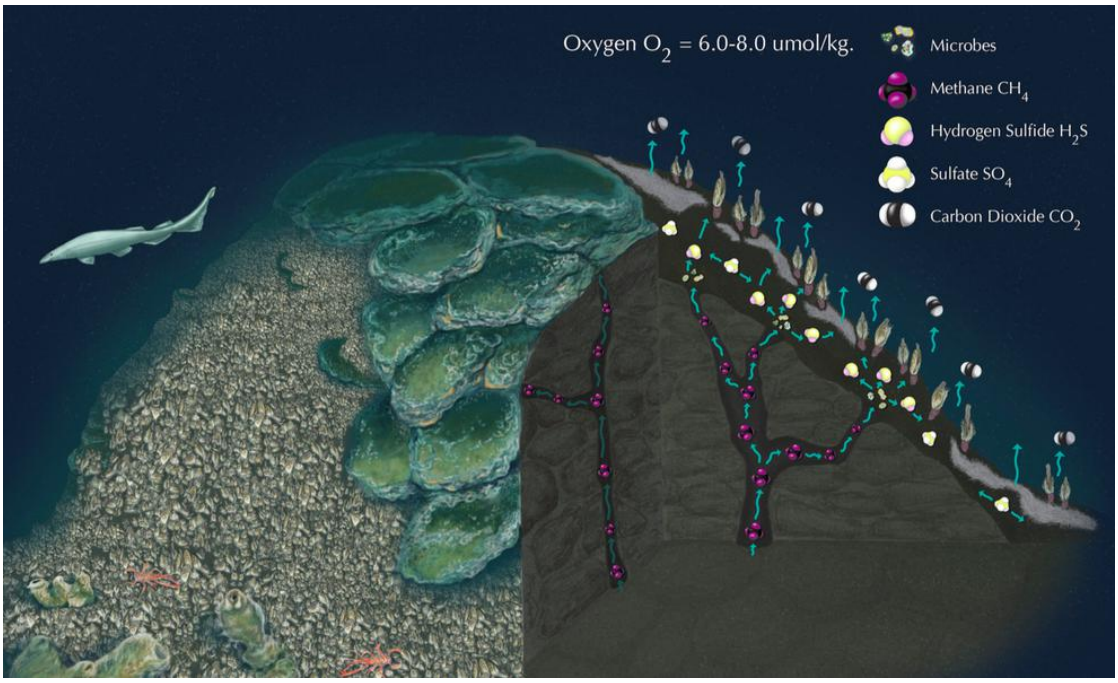

Figure 2.5: Illustration of a mound offshore Santa Monica, characterized by a large quantity of exposed carbonate. The cutaway details how the dissolved methane travels through fractures in the carbonate, the microbes take in the methane and expire hydrogen sulphide, and the chemosynthetic bacteria and clams take in the hydrogen sulphide and the sulfate present in the sediment, then expire carbon dioxide into the water. From https://www.mbari.org/wp-content/uploads/2015/10/Lance.pdf.

2.3 Laterally extensive fluid flow seismic features

Laterally extensive fluid flow features may arise whenever fluid flow is focused in certain stratigraphic levels, as for instance high porosity beds, or at specific subsurface depths. They include structures such as BSR (bottom simulating reflector), free gas zones, hydrocarbon-related diagenetic fronts (Andresen, 2012) and they are often recognized as high amplitude anomalies in the seismic data (e.g. Bünz et al., 2003; Berndt, 2005). Very local hydrocarbon accumulations can also result in bright reflections (for example bright and flat spots) which are considered important DHIs (direct hydrocarbon indicators).
All these features should be considered as part of the more complex specific plumbing system which include the presence of vertical fluid flow.
For the purpose of this thesis, no hydrate- or diagenetic- related features are treated. Instead, enhanced reflections and polygonal faults are investigated.

2.3.1 Enhanced reflections, bright spots and flat spots

The distribution of bright anomalies along specific horizons can testify to the fluid lateral propagation and accumulation. Maestrelli et al. (2017) suggest that fluid migration is a Darcy flow, exploiting paths with favourable effective permeability. Lateral migration can developed from chimney/pipe conduits to the surrounding sediments, producing bright anomalies in the vicinity of such features. It is then very common to find them in shallow sediments and to image them very well in sub-bottom high-resolution seismic profiles.

Bright spot is a high amplitude, negative phase reflection representing the top of a gas-charged sediment, normally accompanied by a strong positive reflection from the underlying gas-water interface (**flat spot**, Judd and Hovland (1992)). Such signature is the result of the impedance contrast between adjacent media, which can not involve any gas presence. For example, interbedding of lignite, coal or gravel in softer sediments can produce similar reflections (Judd and Hovland, 1992). This is why it is common practice to look for various characteristics of gasified sediments, including phase reversal and reduction in VP and to perform AVO analysis (Maestrelli et al., 2017). It should be noted that even a very small percentage of gas can arise in a very bright seismic response, as if gas saturation would be much greater (the effect of oil is more linear over the entire saturation range, with little effect at low oil saturation but an often strong effect at high saturation).

Enhanced reflections are coherent reflections which have an increased amplitude for part of their extent (equivalent to the bright spots, Judd and Hovland (1992)). It is not uncommon for enhanced reflections to extend laterally from zones of acoustic turbidity. Acoustic turbidity (or chaotic reflections) is the result of the scattering of acoustic energy by the presence of gas bubbles in shallow sediments (Schroot and Schuttenhelm, 2003) and can be produced with only 1% by volume of gas (Fannin, 1980; Hosseinyar et al., 2014). It was demonstrated that acoustic characterization of gassy sediments can be used to define bubble size distribution and fractional volume (Wilkens and Richardson, 1998).

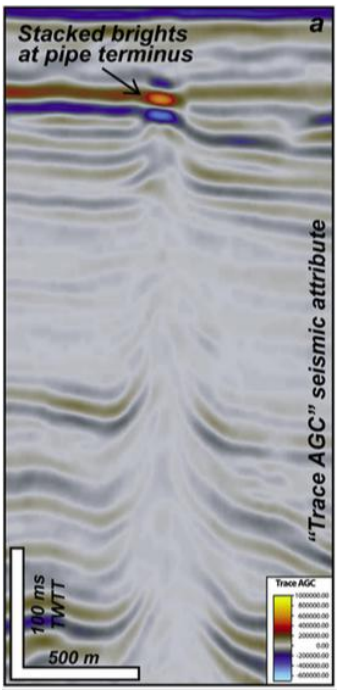

Figure 2.6: (a) Portion of a straight pipe showing high deflection of seismic horizons and stacked bright in correspondence of the pipe terminus, example from Loyal Field (Scotland, UK). From Maestrelli et al. (2017)

However, it is thought that, in very shallow sediments, gas may occur either as accumulations within porous (silt and sand-rich) sediments, or finely disseminated within impermeable (clay-rich) sediments. It would seem that acoustic turbidity characterizes the latter situation, and enhanced reflections the former. Again, it is common for reflections on adjacent sections of a gas-affected profile to exhibit pull-down. As these reflections extend towards the zone of acoustic turbidity they are deflected downwards by the decrease in the acoustic velocity in the gas-bearing zone.

Another seismic effect that can result by the presence of fluid flow is acoustic blanking. It may result from the adsorption of acoustic energy in the overlying gas-charged sediments (Schroot and Schuttenhelm, 2003). However, it can be also caused by the disruption of sediment layering by the migration of pore fluids. The difference between acoustic blanking and turbidity, by some authors, is suspected to be the amount of free gas accumulated in the sediment (Baltzer et al., 2005).

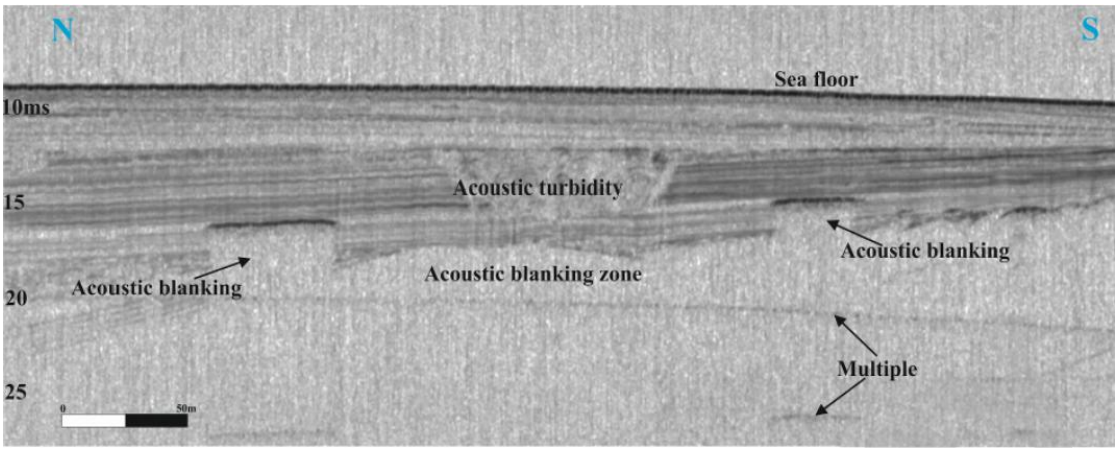

Figure 2.7: Acoustic turbidity and blanking in sub-bottom record from the Persian Gulf. From Hosseinyar et al. (2014).

2.3.2 Polygonal fault systems

Polygonal fault systems are a relatively recently discovered class of non-tectonic faults. They are widely developed in fine-grained sedimentary successions and have been recognized in over 50 basins worldwide (Cartwright and Huuse, 2005). They are normal faults with modest throw values (10-100 m), organized with a characteristic polygonal pattern (Cartwright et al., 2003). They are related to sediment compaction and fluid expulsion (Berndt, 2005). As they deform the subsurface after deposition, they are very important features of fluid flow and hydrocarbon plumbing systems.
Polygonal faulting has been attributed to four genetic mechanism: gravity collapse, density inversion, syneresis and compactional loading (Cartwright et al., 2003).

- Gravity collapse would explain polygonal faults as the result of sliding down a slope, with a basal detachment at the boundary separating the intraformational faults from undeformed, deeper sedimentary units. The downslope gravitational stress provides the necessary conditions for a failure, but this would be expected to produce a strong alignment of fault strikes parallel with the slope contours, which is not the case in several recognized cases around the world.

- In models which consider density inversions as driving mechanism for polygonal faults genesis, conditions for a reversed density gradient are established by sealing of clay units during early burial. This density inversion then leads to folding of the sediments, with consequent fracturing of the folded regions and dewatering of the sediments, eventually leading to a restored equilibrium density gradient. However, many polygonal fault systems are not characterized by a regular arrangement of anticlinal and synclinal density inversion folds that this model requires.

- Syneresis is defined as the "spontaneous contraction of a gel without the evaporation of the solvent" and it a very known process in chemical engineering. Clay-rich sediments have the potential to form ideal gels on deposition because of their micron-scale particle size and the high mass to surface area ration of the particles. The tensile stresses resulting from syneresis could lead to the propagation of fractures at shallow depths and more specifically of shear fracures at greater depths, where the vertical stress is considerable. These shear fractures would radially propagate with the time, as a function of accumulating displacement, and are accompanied by pore fluid expulsion. However,

even if could be in principle be a good genetic explanation for polygonal faults, known example of syneresis are at a comparatively small scale compared with basin-wide polygonal fault systems.

- The gravitation loading model, instead, suggests that normal gravitational loading of certain types of sediments can lead to failure without invoke additional stresses or overpressure, because of exceptionally low friction coefficient. However, there is a lack of constraints of the key parameters (such as shear and Bulk moduli) governing failure.

In summary, there is no agreement about the underlying processes.
These enigmatic structures have considerable implications for the flow of pore water and hydrocarbon in sedimentary basins and for a more general soil mechanical view of clay consolidation (Cartwright et al., 2007). In several examples from the literature (e.g. Chen et al., 2013), deepwater polygonal faults are considered to be important for the focused fluid flow of gas.

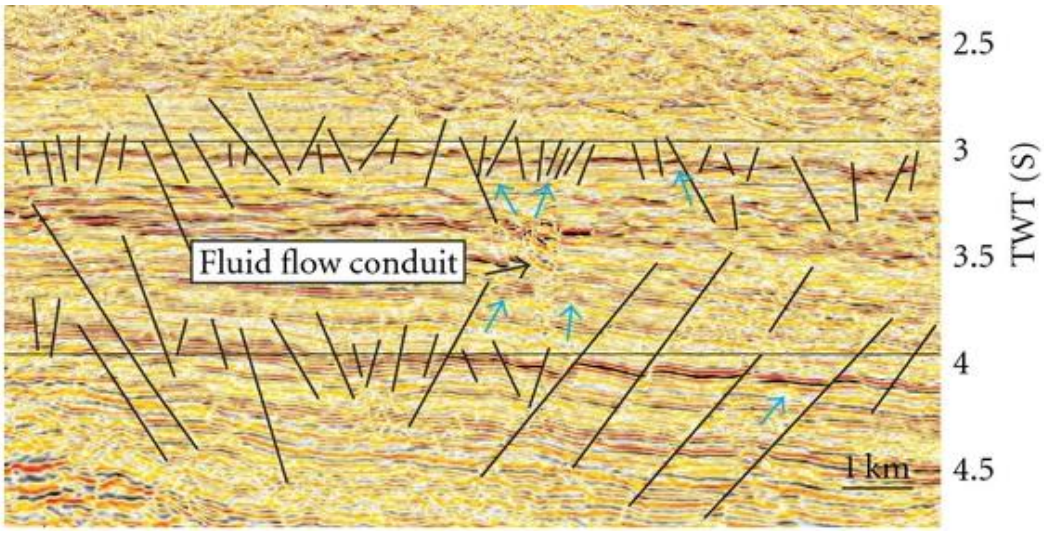

Figure 2.8: Migration of fluid flow through polygonal faults. The dimmed seismic reflectors and fluid flow pipes are visible. From Chen et al. (2013).

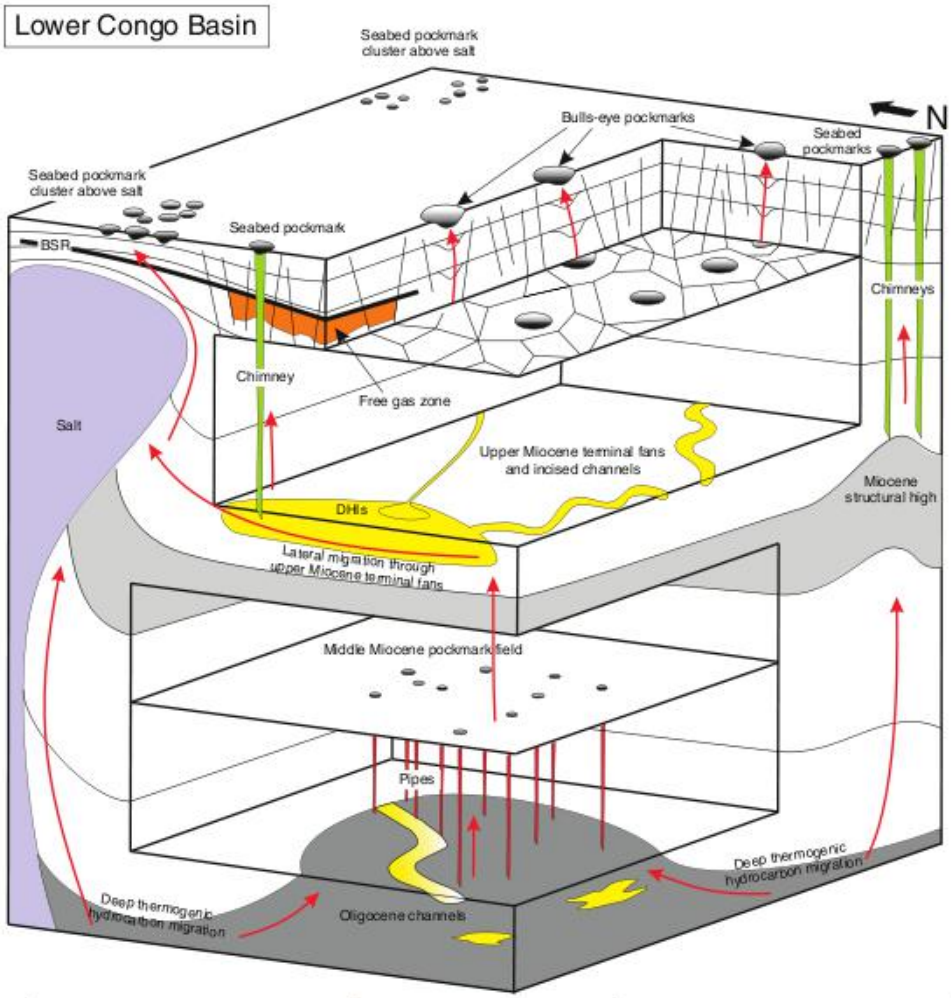

Figure 2.9: Simplified diagram illustrating the fluid plumbing system of the salt mini basins offshore Angola, reported as example of hydrocarbon plumbing system. Red arrows indicate fluid migration pathways. From Andresen (2012).

Chapter 3

Gas occurrence in the Northern Adriatic Sea

3.1 Hydrocarbon exploration

Italy is an important hydrocarbon-producing country in southern Europe (Cazzini et al., 2015) and oil and gas fields are mostly located in the Apennine thrust belt, in the adjacent foredeep basins and in the Adriatic foreland (Bertello et al., 2010). Gas fields (principally biogenic) are concentrated in the Po Plain, in the northern and central Adriatic Basin, oil fields occur in the western Po Plain, in the southern Apennines and in Sicily (Cazzini et al., 2015).

In 1944 the first gas field (Caviaga field, mixed biogenic-thermogenic gas) was discovered in the Po foredeep depression, marking the beginning of the modern upstream industry in Italy. Exploration for biogenic gas progressively moved southeastward leading to the discovery of Ravenna field in 1952. In the 1960's exploration moved offshore. The first offshore discovery was Ravenna Mare, and subsequently industry begun to explore the northern Adriatic and then the southern Adriatic area. In the offshore Adriatic, 127 fields/discoveries are reported until 2012 (representing 22% of the total for the whole of Italy, 582). The majority (110) are gas fields and only 17 are oil fields (Cazzini et al., 2015). At present, 54 out of the 110 gas fields are under production or under development; the remaining 56 are on hold, under appraisal, already abandoned, or they are sub-commercial discoveries. For oil, six out of 17 fields are currently producing (Cazzini et al., 2015).

Most of the Italian biogenic gas fields are located in the Po Plain-Adriatic foredeep, together with producing biogenic gas fields in Croatian waters

Figure 3.1: Italian offshore is divided in 7 zones and the study area lies in Zone A. Modified from http://unmig.sviluppoeconomico.gov.it/videpi/videpi.asp.

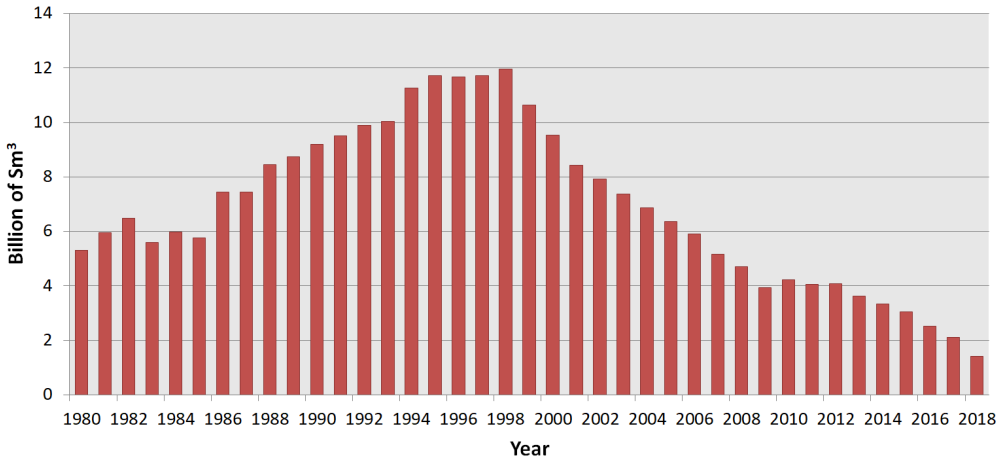

Figure 3.2: Total natural gas production in Zone A. Production is reported per year, in billion of Standard Cubic Meter (Sm^3)[1]. Data from http://unmig.mise.gov.it/unmig/produzione/produzione.asp.

(Cazzini et al., 2015). Here, reservoir rocks are thought to consist of the very thick (several thousands of metres) Plio-Pleistocene siliciclastic successions dominated by deep-marine turbidite deposits (Ghielmi et al., 2010).
In the external part of the Adriatic foreland, traps are related to gentle anticlines resulting from differential compaction of Pliocene-Pleistocene turbidite sandstones over pre-existing Mesozoic structural highs or derived from more recent Pliocene normal faults. The traps are sealed up-dip by Pleistocene shales, known as "Argille del Santerno" (Cazzini et al., 2015). Other types of differential compaction traps are related to paleo-highs in the Oligocene-Miocene substratum eroded during the late Messinian (Ghielmi et al., 2010). These traps occur frequently in the Venetian offshore area, i.e. the study area. Here, microbial gases occur within **Pliocene-to-Pleistocene turbiditic sands**, and they are commonly characterized by multiple pools within thin sand beds at approximately 1200-1500 mbsf (Casero, 2004; Bertello et al., 2008; Casero and Bigi, 2013). Several gas fields have been discovered and exploited off the Venice Lagoon during the 60's, while no hydrocarbon-related activities are currently underway in the study area. The Venice Lagoon is part of the Italian exploration and production Zone A (see Fig.3.1), which still nowadays is an important gas-producing area in Italy (Fig.3.2).

3.2 Evidence of gas-rich fluids in the OGS seismic dataset

In 2009 and 2014 OGS carried out two seismic surveys in the Northern Adriatic Sea, in the frame of the STENAP "Stratigraphic and tectonic evolution of the Northern Adriatic Sea in the Plio-Quaternary" and GANDI "GAs emissions in the Northern ADriatIc Sea" projects (see chapter 4.1).
Multichannel seismic lines revealed that the Plio Quaternary succession is characterized by a package of reflections with **highly variable amplitude, continuity and frequency** and a widespread distribution of **wipe-out zones**, represented by an acoustically opaque facies, where reflections appear strongly dimmed and high frequencies are lost (Donda et al., 2015). They appear to be up to 2–3 *km* wide, with a vertical extent of several hundreds of metres (Donda et al., 2015).

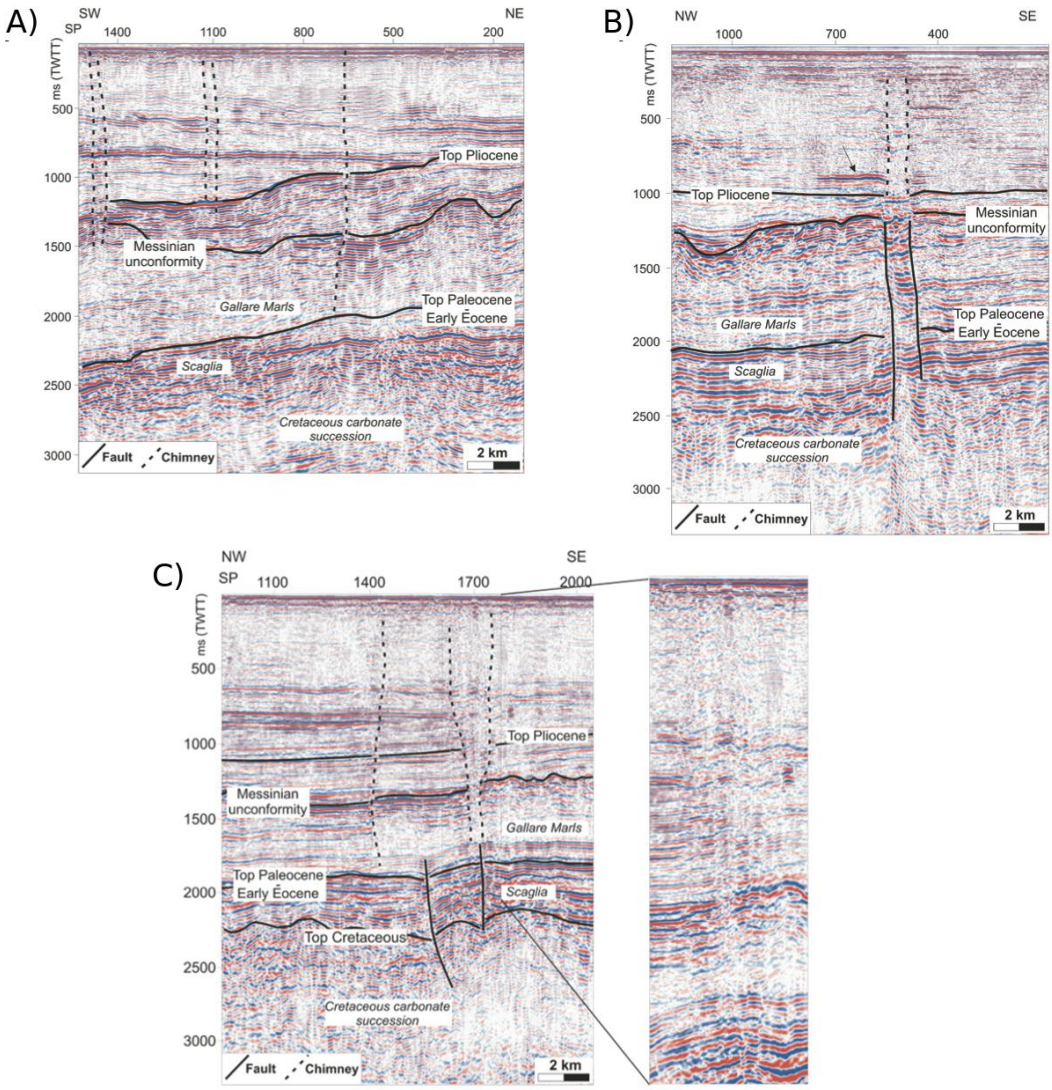

Figure 3.3: Part of STENAP survey multichannel seismic lines: A) STENAP 15; B) STENAP 07 and C) STENAP 05. Chimneys originate and terminate at different stratigraphic levels. They are also recognizable in the Eocene-Miocene succession, extending for up to 2000 m vertically (A) and appearing to be locally associated with deep-seated faults, which root in the Mesozoic carbonate sequences (B). The black arrow in B) indicates a bright spot. In C) the largest identified chimney in the entire study area is shown. Upward-convex reflector configurations within it may indicate sediments mobilization due to upward gas-enriched fluid migration (see zoom). From Donda et al. (2015).

These anomalies were interpreted as **gas chimneys**, i.e. the expression of vertical pathways of gas-charged fluid migration both in deep and shallow sediments (Donda et al., 2013), which cause acoustic low-velocity zones and a decrease of the seismic signal frequency (Vadakkepuliyambatta et al., 2013). Chimneys originate and terminate at different stratigraphic levels. They are capped by high-amplitude

seismic reflections, showing a reversed polarity with respect to the seafloor reflector, indicating local gas accumulation and interpreted as bright spots (Donda et al., 2015, Donda et al., accepted; Fig.3.3). Chimneys are generally observed within Plio-Quaternary sequence, although, in places, they are also recognized in the Eocene-Miocene succession, extending for up to 2000 *m* vertically (Fig.3.3). Wipe-out zones appear to be locally associated with deep-seated faults, which root in the Mesozoic carbonate sequences (Fig.3.3). In the Plio-Quaternary succession it is difficult to discern if chimneys occur along faults and/or fractures. However, some of them appear to be preferentially aligned, suggesting a structural control on the fluid migration paths (Donda et al., 2015). This would indicate that faults may act as open pathways for fluid migration from the deeper stratigraphic successions up to the surface (Fig.3.3). Whether or not these faults are tectonically active is still unclear at this moment.

3.3 Gas seeps and rocky outcrops

In the Adriatic Sea, fluid-related seabed and sub-seabed features have been widely documented. In particular, there are numerous reports since the 1970's of the occurrence of gas seeps in the Northern Adriatic Sea.
On the OGS CHIRP data, gas flares were observed and recorded within the water column with variable heights that range from 4 *m* to 20 *m*. These gas seeps appear to be locally associated with distinct rock outcrops, represented by bio-concretionned carbonate rocks, irregularly distributed on the seafloor. These have been known since the 18th century and their exact locations have been mapped firstly by the local fishermen, because of their fishing value (and danger).

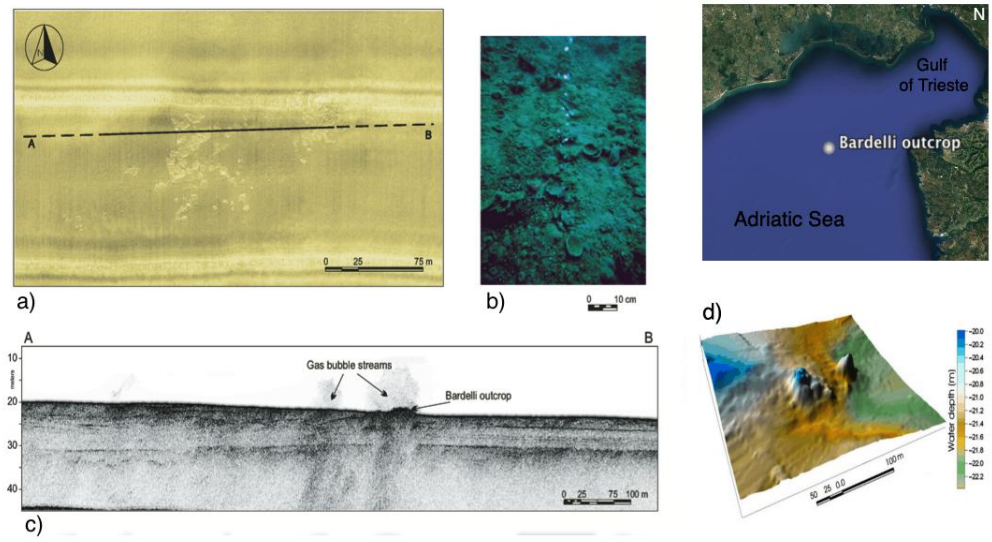

Figure 3.4: Example of a rock outcrop, i.e. the Bardelli site. a) SSS data collected around the rock outcrop; b) underwater picture showing gas bubbling from the seafloor; (c) Sub-bottom profile collected across the rock outcrop; d) Multibeam bathymetry data. Modified from Gordini et al. (2012) and Donda et al. (2015).

They rise up to 3-4 *m* above the seafloor, are patchly distributed and have an important ecological role, e.g. they offer shelter, reproduction and nursery ground to fish and invertebrate species, including some under stress due to severe fishing pressure (Tosi et al., 2017). They are called with various dialectal names: *tegnue*, *trezze*, *pressure*, *lastrure*, *grebeni* and some of them even have proper nouns.
Recent geological and geophysical data support two possible genetic models: the first one has been developed for a group of rocky outcrops named "Tegnue di Chioggia", which are interpreted as coralligenous buildups growing along paleo tidal channels (Tosi et al., 2017); the second model involves the role of the gas seeps, thus leading to interpret such deposits as **methane-derived carbonates** (Gordini, 2009; Gordini et al., 2012; Donda et al., 2013, 2015). In fact, shallow gases permeate the Late Pleistocene and Holocene succession, with gas peaks between 15 *m* and 25 *m* below the seafloor (Curzi et al., 1997, 1998; Calderoni et al., 1998; Donda et al., 2008). The current hypothesis is that gases most likely originate from laterally persistent peat layers, which are widely distributed throughout the Northern Adriatic Sea and formed between 16000 and 24000 years BP in an alluvial plain environment (Gordini, 2009; Correggiari et al., 1996; Zecchin et al., 2011) during phases of climate improvements in the last glacial phase (i.e., the Laugerie Interstadial; Zecchin et al. (2011)). It should be noted that sea level had to be low during this glacial interval so extensive peat deposits could form in a subaerial environment.

3.4 Gas sampling

OGS sampled three seeping sites from three different zones in the study area. Sample location was chosen based on evidence of gas flares in the water column, as recorded in CHIRP data previously acquired. Gas samples were collected during a scuba diving survey in May 2016, and were collected using 250-*ml* vacuum vials from a few centimeters above the seabed. The gas samples were then analyzed at Isotech Laboratories Inc. (Illinois, USA) to determine the proportions of $C_1^- C_6^+$ hydrocarbons, He, H_2, O_2, Ar, CO_2, CO, and N_2. The samples were also outsourced to Beta Analytic (Florida, USA) for the radiocarbon analysis of methane via accelerator mass spectrometry. Table 3.1 presents the results of these geochemical analyses (Donda et al., accepted).
Results show that gases are mainly composed of **methane**. The methane $\delta^{13}C$ values range between -73.7 and -64.7‰VPDB[2], while the δD values range from -264.2 to -223.6‰VSMOW[3]. The $^{14}C_1$ pMC [4] values range from 1.3 to 1.8, which indicates an apparent age of the organic material source for the gas between ca. 32,000 to 34,000 yrs BP (Donda et al., accepted).
The analysis shows several evidences for the **microbial origin** of the methane: 1) the ratios of methane to ethane and propane $(C_1 / (C_2 + C_3)) > 1000$ (Bernard et al., 1976); 2) the $\delta^{13}C_{CH_4}$ values are generally less than approximately -55‰, which is expected for biogenic gases (Whiticar, 1999, Fig.3.5); and 3) the stable carbon and hydrogen isotope compositions of methane plotted in the field of biogenic gas (Whiticar, 1999); see Fig.3.5. These characteristics argue for a microbial origin through CO_2 reduction, which is the main primary methanogenic pathway in marine sediments (Whiticar, 1999).
From the gas composition analysis, hydrocarbons with densities higher than methane are sparse. In addition, the observed stable isotopes and the age of the organic source material collectively support a relatively shallow primary microbial methane source. This source is supposed to be represented by laterally persistent, Late Pleistocene, peat layers, which are widely distributed throughout the Northern Adriatic Sea. (Donda et al., accepted).

[2]For isotopic measurements on carbonates, organic carbon and hydrocarbons the V(Vienna)PDB standard is used. PDB = sample taken from an internal calcite structure from a fossil Belemnitella americana from the Cretaceous Pee Dee Formation in South Carolina.

[3]Vienna Standard Mean Ocean Water (VSMOW) is a water standard defining the isotopic composition of fresh water.

[4]pMC is 'percent modern carbon' calculated against a reference sample of natural ^{14}C activity from year 1950.

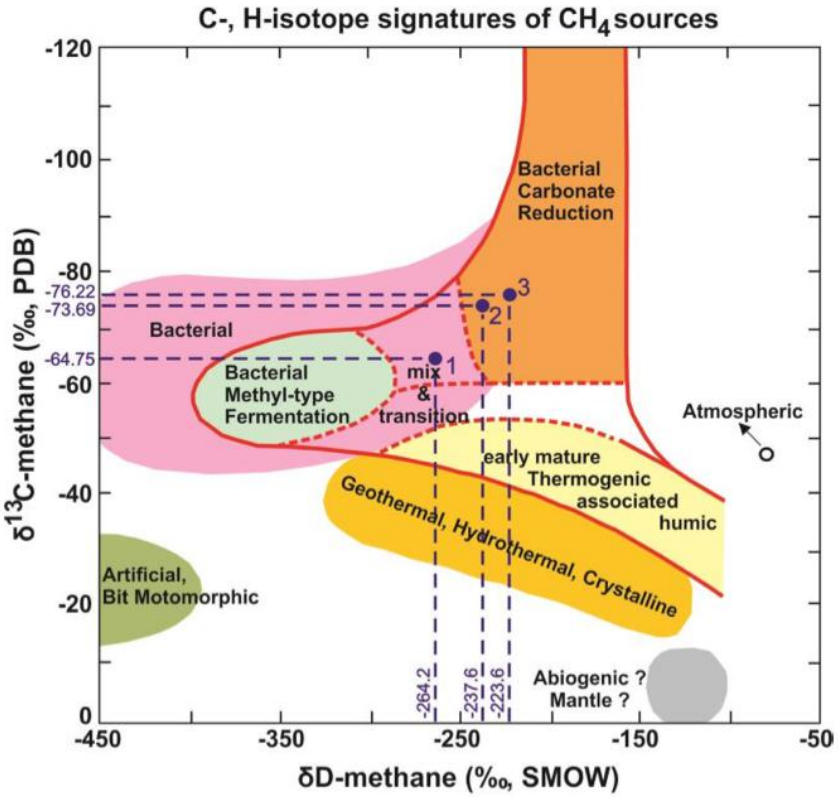

Figure 3.5: $\delta^{13}C_{CH_4}$ vs δD_{CH_4} plot showing the major methane types (modified after Whiticar (1999)). Gases sampled in the northern Adriatic sea reveal the microbial origin of the methane. From Donda et al., accepted.

Table 3.1: Gas analysis results (from Donda et al., accepted).

Sample 1	Chemical mol %	δ^{13} ‰	δD ‰	^{14}C conc. (pMC)	**Sample 2**	Chemical mol %	δ^{13} ‰	δD ‰	^{14}C conc. (pMC)	**Sample 3**	Chemical mol %	δ^{13} ‰	δD ‰	^{14}C conc. (pMC)
Carbon Monoxide	nd				Carbon Monoxide	nd				Carbon Monoxide	nd			
Helium	nd				Helium	nd				Helium	nd			
Hydrogen	nd				Hydrogen	nd				Hydrogen	nd			
Argon	0.431				Argon	0.0970				Argon	0.415			
Oxygen	9.70				Oxygen	0.98				Oxygen	7.67			
Nitrogen	35.92				Nitrogen	8.95				Nitrogen	31.36			
Carbon Dioxide	0.99				Carbon Dioxide	0.40				Carbon Dioxide	0.049			
Methane	52.96	-64.75	-264.2	1.3 ± 0.1	Methane	89.57	-73.69	-237.6	1.8 ± 0.1	Methane	60.50	-76.22	-223.6	1.8 ± 0.1
Ethane	0.0003				Ethane	0.0021				Ethane	0.0011			
Ethylene	nd				Ethylene	nd				Ethylene	nd			
Propane	nd				Propane	nd				Propane	nd			
Propylene	nd				Propylene	nd				Propylene	nd			
Iso-butane	nd				Iso-butane	nd				Iso-butane	nd			
N-butane	nd				N-butane	nd				N-butane	nd			
Iso-pentane	nd				Iso-pentane	nd				Iso-pentane	nd			
N-pentane	nd				N-pentane	nd				N-pentane	nd			
Hexanes+	0.0003				Hexanes+	nd				Hexanes+	nd			

Part II

Data analysis

Chapter 4

GEA data

4.1 Borehole data

All the well log data used in this thesis come from the ViDEPI (Visibility of petroleum exploration data in Italy, http://unmig.sviluppoeconomico.gov.it/videpi/videpi.asp) database, which has been designed to make all the documents concerning Italian oil exploration easily accessible. The public documentation concerns expired mining permits and concessions, filed since 1957 with UNMIG, National Mining Office for hydrocarbon and geothermal energy of the Ministry for Economic Development. This dataset includes well data and multichannel seismic profiles acquired since 1957 by several oil companies for hydrocarbon exploration (mostly by ENI). Well data consist of composite logs charts, which contain information on 1) lithology derived from cuttings; 2) geological formation name and age; 3) depth; 4) lithostratigraphy; 5) fluid occurrence; 6) depositional environment; 7) biostratigraphy; 8) geophysical logs. The available technical reports concerning the exploration permits provide technical information on the drilling parameters, and on the local geological and structural setting around the drilling sites.
In the northernmost Adriatic Sea, several tens of boreholes have been drilled and exploited microbial gases from the Pliocene-to-Pleistocene turbiditic sands; among them, 18 composite logs are currently available, due to the fact that wells resulted sterile. In this study, 5 of them have been selected and analyzed and used to constrain two seismic lines. Table 4.1 summarizes the logs available for the selected boreholes. Fig.4.1 shows the location of the selected boreholes.

Table 4.1: Logs available in the selected boreholes

	Max depth	SP	Gamma-ray	Resistivity	Sonic	FDC-neutron
Amanda Bis	7305 m	x	x	x		x
Arcobaleno	1943 m		x	x	x	
Arlecchino	1658 m	x	x	x	x	
Rachele	1641 m	x		x	x	
Triglia Mare	1845 m	x	x	x		

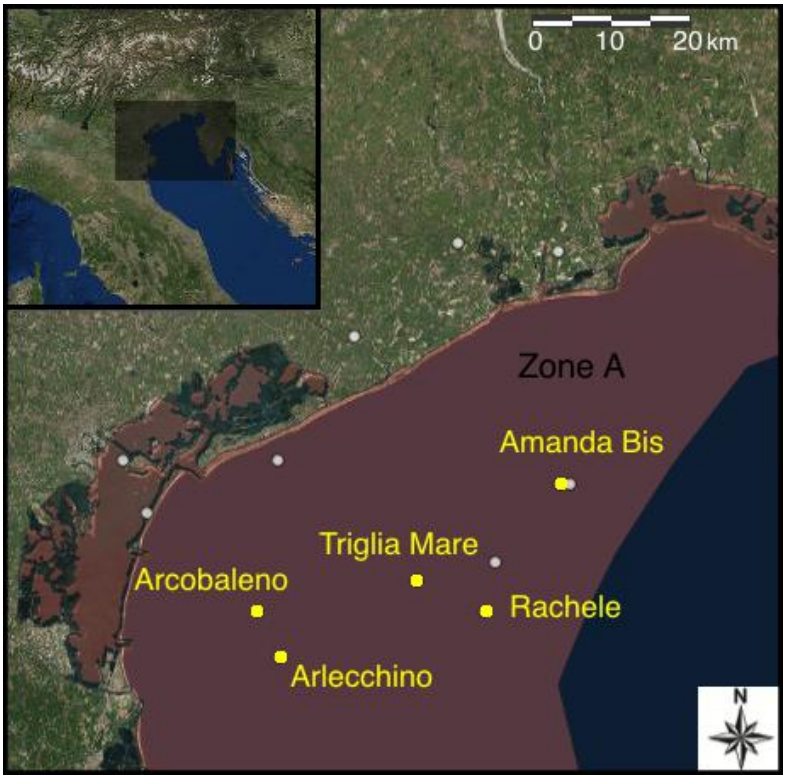

Figure 4.1: Boreholes made available from ViDEPI project in the study area. Boreholes chosen for the analysis are in yellow. Modified from http://unmig.sviluppoeconomico.gov.it/videpi/videpi.asp.

4.2 Multichannel seismic profiles

The seismic data analyzed in this thesis were collected by the R/V OGS Explora in the Northern Adriatic Sea within the framework of two projects: STENAP and GANDI. In 2009, the STENAP (Seismostratigraphic and Tectonic Evolution of the Northern Adriatic Sea in the Plio-Quaternary) cruise acquired ca 820 *km* of multichannel 2D seismic reflection lines, CHIRP sub-bottom profiles and swath morpho-bathymetry data Donda et al. (2015). In 2014, GANDI (GAs emissions in the northern ADriatIc Sea) cruise collected approximately *450 km* of multi-channel seismic lines, sub-bottom CHIRP profiles and morpho-bathymetry data. These data were collected with the main aim to constrain the relationship between the gas emissions and the regional geological setting of the study area and to characterize the gas-charged fluids occurring within the sedimentary succession (Donda et al., accepted).
Seismic acquisition parameters of both cruises are reported in Table 4.2.
Two perpendicular seismic lines, the STENAP 08 and the GANDI 09, had been chosen and re-processed to perform gas quantification. Their locations are reported in Fig.4.2.

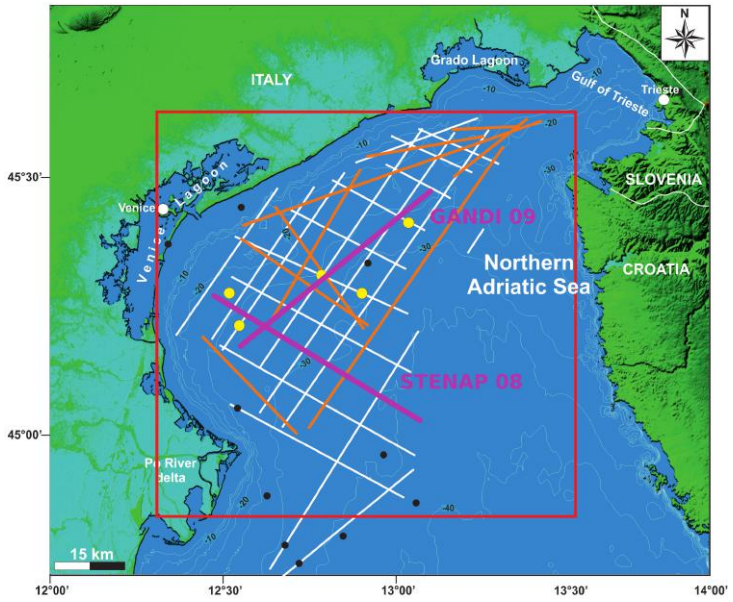

Figure 4.2: Position map of STENAP (white lines) and GANDI (orange lines) multichannel seismic lines. The two analyzed seismic profiles are highlighted in purple. Black dots: wells, yellow dots: wells used in this study. Modified from Donda et al. (2015).

Table 4.2: STENAP and GANDI acquisition parameters

STENAP					
Source		Streamer		Recording	
Model	Sleeve guns	**Model**	Sercel Seal	**Model**	Sercel Seal
Array	1180 cu.in/2360 (TM)	**Length**	600/1200 m	**Sampling rate**	1.0 ms
Shot interval	12.5 m / 25 m (TM)	**Ch. Dist**	12.5 m	**LC filters**	3 Hz
Depth	5 m ± 0.5m	**Depth**	3 m ± 0.5m	**HC filters**	Antialias
Pressure	2000 psi	**Min off.**	9/25 m	**Aux channels**	Ch. 12
		Max off.	609 /1225 m		
		Max fold	24/48		
GANDI					
Source		Streamer		Recording	
Model	GI-GUN Sercel	**Model**	Sercel Seal	**Model**	Sercel Seal
Array	4x210 cu.in (13.5l)	**Length**	1500 m	**Sampling rate**	1.0 ms
Gun Mode	105G+105l Harmonic	**Ch. No**	120	**Record length**	8 s
Shot interval	25 m	**Ch. Dist**	12.5 m	**LC filters**	3 Hz
Depth	3 m ± 0.5m	**Depth**	3 m ± 0.5m	**HC filters**	Antialias
Pressure	140 atm	**Min off.**	25 m	**Aux channels**	Ch. 12
		Max off.	15 25 m		
		Max fold	30		

Chapter 5

Seismic processing

The seismic reflection method is based on the principle that acoustic waves, generated mechanically, propagate into the subsurface. Energy travels through the water and into the rock layers. Part of the seismic energy is reflected back to the surface from different layers, due to the acoustic impedance contrasts produced by the different velocity of the seismic wave and density of the rock layers at lithological boundaries. For marine seismic acquisition the upcoming waves are captured by sensitive instruments called seismic receivers (hydrophones) within a log cable towed behind the vessel. See Fig.5.1 for the acquisition setting.

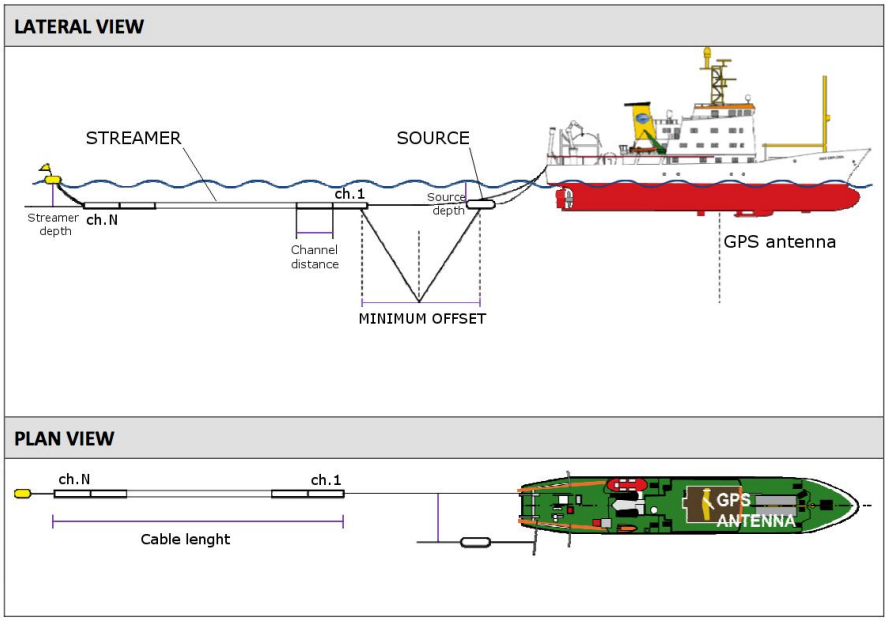

Figure 5.1: Seismic data acquisition scheme.

Receivers record the traveltime and relative amplitude of the upcoming reflected signal. Data processing is required because seismic reflections can be wrongly located when the reflection point is not at the midpoint of the source and receiver. Furthermore, they become weaker as the depth of the path increases. In addition, during propagation, seismic signal is affected by noise, generally not desirable in the image. For example, a *multiple* reflection, which is a seismic event that experiences more than

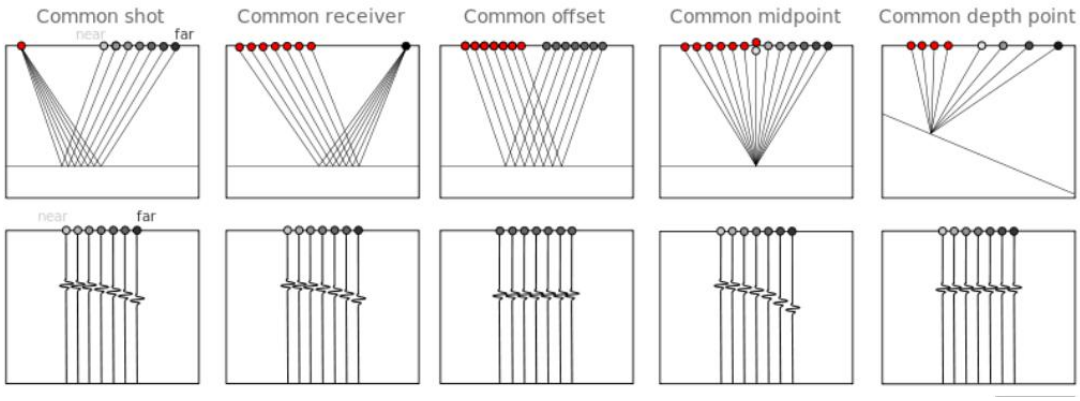

Figure 5.2: Seismic gathers.

one reflection in the subsurface, is a common example of seismic noise. The final result is an optimum seismic section (**stack section**) that represents a 2D section of the investigated subsurface space. The processing flow is then adapted to specific characteristic of the raw data with the main goal of improving the signal to noise ratio. Each step is performed on the data sorted in the appropriate way. A collection of seismic traces which share some common geometric attributes is called a *gather*. Gathers are sorted from field records in order to examine the dependence of amplitude, signal-to-noise ratio (S/N), move-out (the change in arrival time of the same reflection at different source-receiver offsets), frequency content and phase on offset, incidence angle and azimuth. During the processing, traces are commonly re-sorted various times to accomplish the needs of algorithms and improve performances. The two selected seismic profiles (STENAP 08 and GANDI 09, see Fig.4.2 for location) were processed by applying two different flows: a first processing flow has been applied to better image the subsurface, more suitable for the seismic interpretation (sec.5.1); a second flow consisted of specific algorithms to improve S/N and to remove multiple events without affecting the original amplitude information (sec.5.2). The STENAP 08 and the GANDI 09 lines were recorded with two different acquisition systems (Table 4.2). They are both strongly affected by short period multiples (noise generated from seismic energy reverberations in relatively thin layers, with strong impedance contrast) and long period multiples. Several issues arise from the very shallow water bottom, first of all a very small critical distance (Fig.5.3). A critical angle can be defined as the angle at which there is no reflected energy and corresponds to a critical distance. For $x > x_{critical}$ there are not P-wave reflections, all seismic energy is refracted. If v_1 and v_2 are the velocities of layers 1 and 2 (see Fig.5.3), h is the thickness of layer 1 and ϕ the angle of incidence in respect to the normal direction:

$$x_{critical} = \frac{2hv_1}{\sqrt{v_2^2 - v_1^2}} = 2h\,tan(\phi_c) \tag{5.1}$$

Due to the very shallow water column (25 m at maximum) the critical distance is very small, around 90 m. This means that, apart for the first 4-5 channels, refractions are always present and mixed with reflections. Water column refractions are mixed with first reflections making very difficult to separate them from the useful signal. It is possible to distinguish wavelets only in the very near offsets and, in any case, they are distorted both in phase and in amplitude. The GANDI 09 line suffers from poor fold coverage, sometimes with entire shots missing. Furthermore the editing forced the muting of various noisy traces along both lines, especially in the near offset.

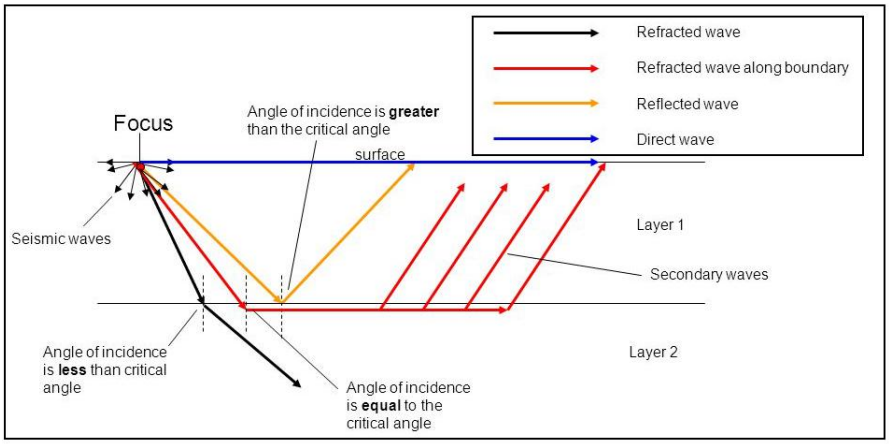

Figure 5.3: Seismic refraction.

The main objective of the signal processing was focused on the noise (random noise, refractions, out-of-plane reflections and reverberations) removal, through the application of specific filters in time-domain or in the $\tau - p$ domain (explain later in subsec.5.1.2), where signal can be more easily be separated from noise and filtered or muted.
Data were strongly affected by multiples, so much of the processing targeted their elimination with the application of deconvolution before and post stack. **Deconvolution** is a process designed to restore a waveshape to the form it had before it underwent a linear filtering action of the rocks encountered during its travel path. In particular, pre-stack spiking deconvolution is aimed at improving temporal resolution by compressing the effective source wavelet contained in the seismic trace, predictive deconvolution is applied to attenuate multiples related to surface or near-surface reflectors.
In the case of the amplitude preserving processing sequence, deconvolution is not appropriate due to the fact that it can affect the amplitude content of the seismic traces. Instead, *SRME* technique (Surface-Related Multiples Elimination) was applied, using primary reflections to predict multiples. Once the predicted multiple model is created, it is adaptively subtracted from the original data.
To have a more accurate image of the subsurface the migration process was applied, by which seismic event are re-located in the location where they actually occurred in the subsurface, particularly important in the presence of geological features such as faults, folds or general discontinuities. Several tests were carried out to investigate the migration parameters. **Migration** was performed pre-stack, on common offset gathers, in time domain. *Kirchhoff summation method* was applied. However, as the used migration algorithm can change relative amplitudes, it was not applied in the amplitude preserving processing.
Unwanted frequencies were excluded after the main steps, with a post-stack time-variant filter at the end of both flows.
In sec.5.1 and sec.5.2, the two applied processing sequences are described and examples of application of the main steps reported. Final results are the stacks of the two lines, in the amplitude preserving and 'imaging' version.
The processing was performed using the Paradigm commercial package and the open source seismic utilities package Seismic Unix (Cohen and Stockwell, 2008).
In the following processing sequences discrimination and removal of refractions is carried out both in $x - t$ and in $\tau - p$ domain.

5.1 Processing sequence

The applied processing flow (Fig.5.4) is described in details in the following paragraphs.

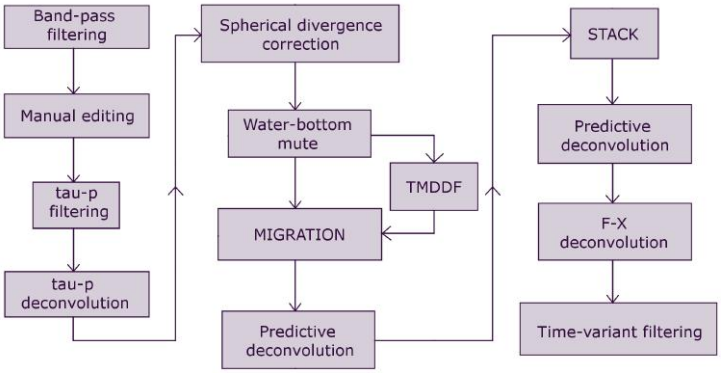

Figure 5.4: Processing flow

5.1.1 Frequency filtering and trace editing

Normally, marine data are contaminated by swell and cable noise. These types of noise carry very low frequency energy, but can be high in amplitudes. They can be recognized by their distinctive linear pattern and vertical streaks (see Fig.5.5 A)). In addition, high-frequency ambient noise is often present.

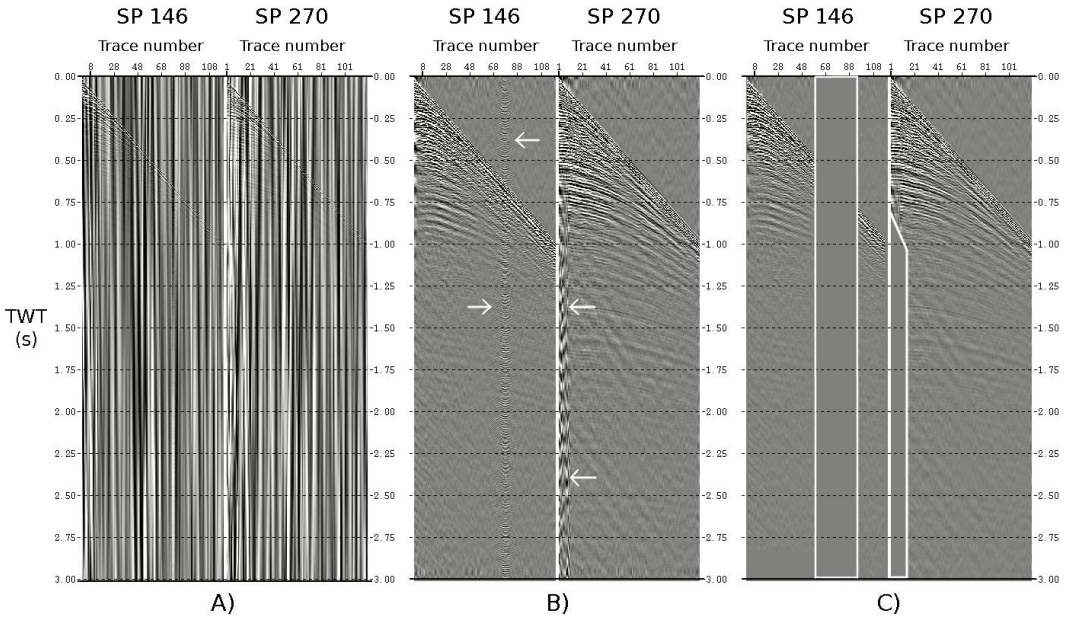

Figure 5.5: GANDI 09 shot point gather 146 and 270. A) Raw shot points; B) After band-pass filter; C) After manual editing.

These noises can be removed from shot records applying a band pass filter. Frequency-domain filtering involves multiplying the amplitude spectrum of the input seismic trace by that of the filter operator. A $5 \div 10 - 120 \div 240$ Hz band-pass filtering, with Hann tapering, was performed at various stages in the applied processing flow (see Fig.5.5 B)).
Noisy traces, traces with transient glitches (spikes) or monofrequency signals were then deleted by manual editing. In the GANDI 09 line this sometimes required deleting some of the near offset traces of problematic shots, losing signal from the shallowest strata but avoiding the presence of unwanted noise in the following stages of the processing (see Fig.5.5 C)). This must be considered if interpreting amplitude anomalies.
Furthermore, inconsistent shots were muted. Refractions, when clearly recognizable and not in interference with reflections, were cut off.

5.1.2 Filtering in $\tau - p$ domain

Both lines (but especially the GANDI 09 line) were affected by the presence of out-of-plane events (reflections from lateral external source, see Fig.5.6 A)), so that a filtering in $\tau - p$ domain was performed. Ray parameter p represents the wave ray slowness $1/v$, where v is velocity of the acoustic wave. A seismic gather can be described in terms of slope $p = dt/dx$ and intercept time τ, the arrival time obtained by projecting the slope back to $x = 0$, where x is the source-receiver distance (Yilmaz, 2001). In $\tau - p$ domain, events can be separated by their ray parameter p. Linear events map to points and hyperbolic events map to elliptical curves (see Fig.5.7 A)), and what is not a reflection event can be filtered out.

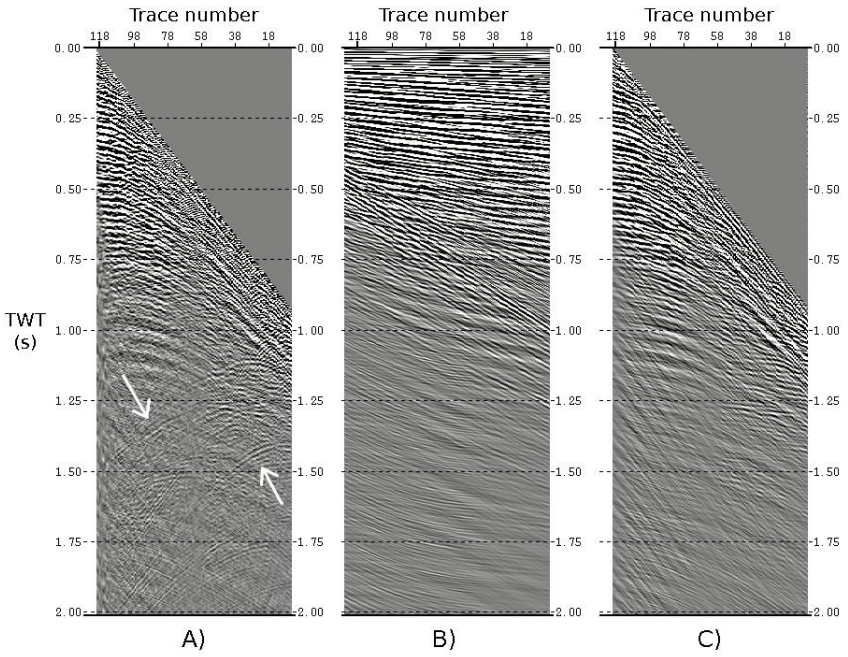

Figure 5.6: GANDI 09 shot point 685. A) Shot point 685 in time domain. It is characterized by the presence of out-of-plane events, highlighted by white arrows; B) Shot point 685 in $\tau - p$ domain after filtering; C) Shot point 685 transformed back in time domain.

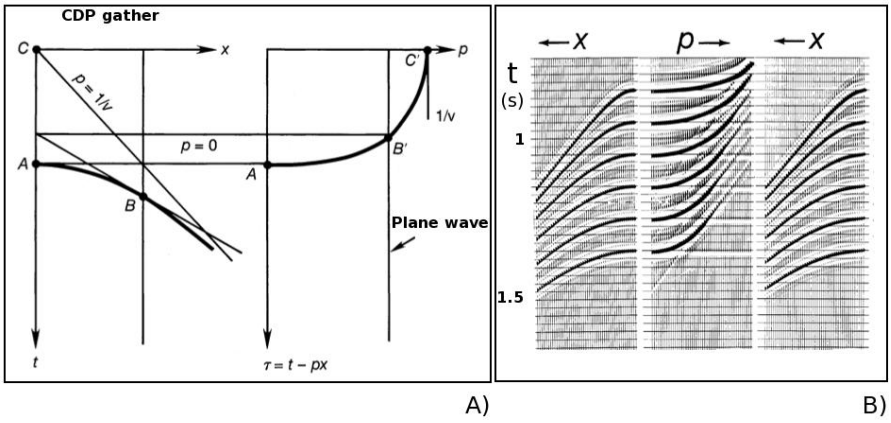

Figure 5.7: $\tau - p$ transformation. A) Theoretical representation; B) Synthetic example from time-domain to $\tau - p$ domain and back to time-domain. Modified from Yilmaz (2001).

The filtered results are then transformed back into a time record (see Fig.5.7 for a synthetic example). $\tau - p$ mapping is used to filter out unwanted signals, to apply deconvolution and for other purposes, including trace interpolation.
In both processing flows, $\tau - p$ transformation was used to filter out out-of-plane reflections, probably due to the presence of big objects in the water column (such as abandoned platforms).
Considering that the minimum value of velocity can be assumed as the gas-bearing sediment velocity v_{gas}:

$$\begin{cases} p = \dfrac{sin\phi}{v} \\ v_{gas} \simeq 1250\, m/s \end{cases} \tag{5.2}$$

the data p range, defined as $-1/v < p < 1/v$, is $p = [-800, 800]\ \mu s/m$.

Out-of-plane events are the ones reflected back with an angle of $[0, \pi]$, i.e. the ones with negative p values (Fig.5.8). They can be filtered out simply keeping p range equals to $[0, 800]$.
Transformation in $\tau - p$ domain was applied also to attenuate water column reverberations. Shot records are transformed in CDP gathers and a normal moveout (NMO) correction (see subsec.5.1.9) is applied, using $v_{NMO} = 1520\, m/s$. This flattens only water reverberations, leaving all the other reflections (characterized by greater velocities) under-corrected. Then, in $\tau - p$ domain, only events with negative slowness (under-corrected) are kept. CDPs are then transformed back in $x - t$ domain and, eventually, NMO is removed (see Fig.5.10 D)).

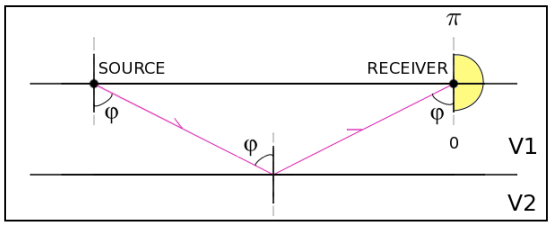

Figure 5.8: Out-of-plane events.

5.1.3 Predictive deconvolution in $\tau - p$ domain

Predictive Deconvolution is an important step of seismic processing, applied to improve temporal resolution of traces, allowing better vertical definition of subsurface geology. It is also used to attenuate multiple reflections that occur when the seismic energy is reflected more than once. In this case, it is called *predictive deconvolution* and the multiple reflections are considered as noise to be eliminated.

Deconvolution is based on the application of a *Wiener filter* $f(t)$ which is designed so that the least-squares error E between the actual ($f(t) * w(t)$) and the desired d output is minimized ($*$ represents the convolution operation)

$$E = \Sigma_i (d_i - (f(t) * w(t))_i)^2 \tag{5.3}$$

where $w(t)$ is a minimum phase wavelet.
This is a typical least squares problem, and the minimum error is obtained by setting the partial derivatives of E to zero:

$$\frac{\partial E}{\partial f_j} = 0, \qquad j = 0...(n-1) \tag{5.4}$$

$$\Downarrow$$

$$\Sigma_{i=0}^{n-1} r_{j-i} f_i = g_j \tag{5.5}$$

where g_j is the j-th term of the crosscorrelation between $d(t)$ and $w(t)$ and r_j is the j-th term of the autocorrelation of $w(t)$ ($\star$ represents the correlation operation):

$$g_j = \Sigma_i d_i w_{i-j} = (d(t) \star w(t))_j \tag{5.6}$$

$$r_j = \Sigma_i w_i w_{i-j} = (w(t) \star w(t))_j \tag{5.7}$$

and the minimum error is:

$$E_{min} = \Sigma_i \delta_i^2 - \Sigma_j f_j g_j \tag{5.8}$$

If $g(t)$ and $r(t)$ are known, Eq.5.5 can be solved uniquely to find the filter $f(t)$. Equations 5.5 are known as the *normal equations*. The associated autocorrelation matrix of R_{ij} is called *Toeplitz matrix* and it can be inverted efficiently using a recursion procedure.
The simplest application of the Eq.5.5 is the design of an inverse optimum filter such that the desired output is a zero-lag spike. This kind of deconvolution, called *spiking deconvolution*, could be seen as special case of the more general predictive deconvolution. The goal of predictive deconvolution is to generalize the normal equations to remove multiple contamination.
To perform deconvolution, autocorrelation of the wavelet $r_w(t)$ and crosscorrelation between the desired output and the wavelet $g(t)$ need to be known. Unfortunately, in most cases, the source wavelet is not known. However, it can be proved that wavelet autocorrelation $r_w(t)$ is a scaled version of trace correlation $r_s(t)$ (see Appendix A), which can be computed:

$$r_s(t) = C\, r_w(t) \tag{5.9}$$

where C is the scaling.
The other function required is the crosscorrelation between $d(t)$ and $w(t)$: $g(t)$. This, again, requires the wavelet to be known. One method to overcome this problem is to replace the crosscorrelation $g(t)$ with the wavelet autocorrelation $r_w(t)$. This can be done requiring the desired output $d(t)$ to be a time-advanced version of the input (see Appendix A). Basically Eq.5.5 are solved for the *prediction filter* $f(t) = p(t)$ that can transform the input signal to the same signal but only advanced a certain number of samples (let's say α samples or lag). Then, a prediction error filter can be designed and applied to the gathers to suppress the multiple field. Prediction error filter is defined as:

$$a(t) = (1, \underbrace{0, 0, ..., 0}, \overbrace{-p_0, -p_1, ..., -p_{n-1}}). \tag{5.10}$$

with $(\alpha - 1)$ zeroes and n filter coefficients.
Seismic trace $s(t) = m(t) + e(t)$ includes a predictable part (multiples m) and a non-predictable part

(primaries e) and a prediction error filter can be designed to remove the predictable part.
The procedure is the following:

- Autocorrelate the traces;
- Construct the predictive normal Eq.5.5 using the trace autocorrelations;
- Set prediction lag α;
- Set operator length n;
- Solve Eq.5.5 to find the prediction filter $p(t)$;
- Construct the prediction error filter $a(t)$;
- Convolve $a(t)$ with the trace $s(t)$ to get the deconvoluted output $e(t)$.

A first predictive deconvolution is applied in $\tau - p$ domain. In fact, multiple suppression in $\tau - p$ domain is very effective, as multiple are exactly periodic in this domain and can be more easily separated. A synthetic example of application of $\tau - p$ deconvolution is shown in Fig.5.9.

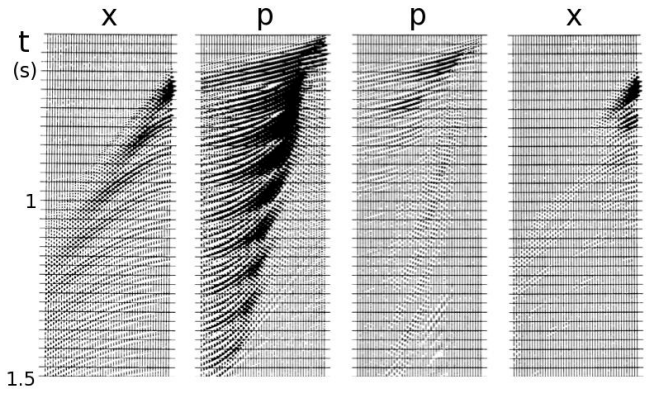

Figure 5.9: Synthetic example of deconvolution in $\tau - p$ domain. A) $x - t$ domain; B) $\tau - p$ domain; C) $\tau - p$ domain after deconvolution; D) $x - t$ domain after deconvolution. Modified from Yilmaz (2001).

Deconvolution parameters were set on the basis of the autocorrelation function. The operator length n should include the first strong energy packet of the autocorrelation; the prediction lag α should allow to bypass the wavelet and possible correlation between primaries and it is often set to the second zero of the autocorrelation. A pre-whitening ϵ is applied to avoid possible divergence of the deconvolution filter. Deconvolution parameters are reported in Table 5.1. Application of the whole procedure on STENAP 08 shot point 759 is reported in Fig.5.10.

Table 5.1: $\tau - p$ deconvolution parameters.

	$n\ (ms)$	$\alpha\ (ms)$	ϵ (%)	Time window (ms)
GANDI 09	60	13	0.1	0-3000
STENAP 08	55	10	0.1	0-3000

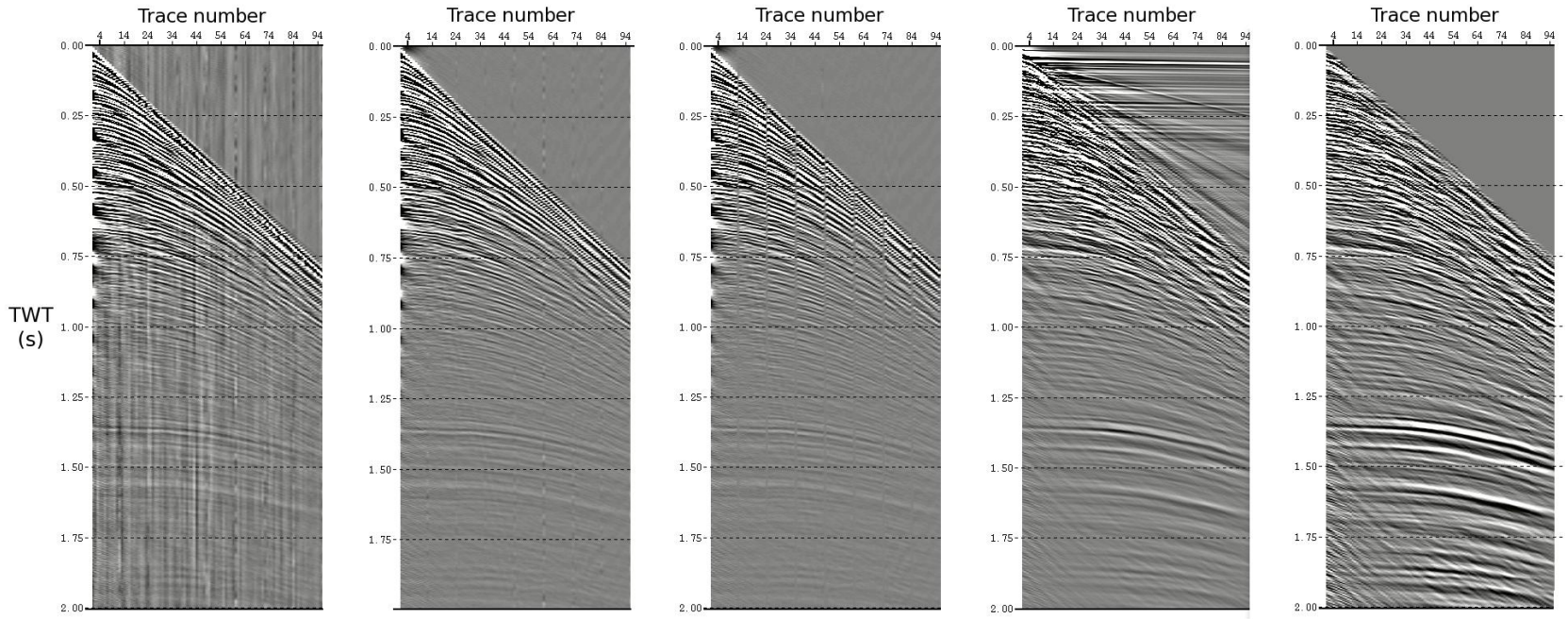

Figure 5.10: STENAP 08 shot point 759: from raw shot, to filter shot, to edited shot, to filter and $\tau - p$ deconvoluted shot.

5.1.4 Velocity analysis

Velocity analysis is required to find the optimum velocity to flatten reflection hyperbola (see subsec.5.1.9). The aim in velocity analysis is to obtain picks that correspond to the best coherency of the signal along an hyperbolic trajectory over the entire spread length of the CDP gather (Yilmaz, 2001). There are different ways to determine the velocity and the one used in these processing flows is the analysis of velocity spectra.
The velocity spectrum is obtained when the stacking results for a range of velocities are plotted in a panel for each velocity, side by side, on a plane of velocity versus two-way travel-time (TWT). This can be plotted as traces or as iso-amplitudes.
Coherency is evaluated in velocity spectrum calculating the semblance, which is the normalized output-to-input energy ratio (Yilmaz, 2001). Velocity functions are picked on the semblance panels following the best coherence. They represent the RMS velocity field of the seismic section which will then used when stacking. The RMS velocity is that of a wave through subsurface layers of different interval velocity along a specific raypath, while the interval velocity is the velocity of the single layer. Accuracy on velocity picking depends on a number of factors, among them: cable length, TW zero-offset time associated with the reflection event, and the velocity itself (Yilmaz, 2001). The higher the velocity, the deeper the reflector and the shorter the cable, the poorer the velocity resolution. The resolution in velocity picking depends also on the signal bandwidth (Yilmaz, 2001): the more compact the wavelet is along the reflection traveltime trajectory in the gather, the more accurate is the velocity pick. This is why pre-stack deconvolution prior to velocity analysis can be useful and has been applied.
In the STENAP 08 and the GANDI 09 lines, semblance analysis did not provide satisfying results. At short TWT, reflections were still not clearly recognizable and at longer TWT they were too weak. At near offsets and short TWT the primaries were strongly contaminates by water column reverberations. For this reason, sonic-log data were incorporated in the velocity estimation. Velocity field of the GANDI 09 was calculated using the sonic-log information for the shallowest 1600 ms, laterally extrapolated along the line, and a semblance analysis for the deepest part. Instead, velocity field of the STENAP 08 was entirely built using sonic-log of Arcobaleno well. Velocities calculated using sonic-logs were properly converted from interval to RMS velocity with the Dix formula.
Both velocity sections are reported in Fig.5.11 and Fig.5.12.

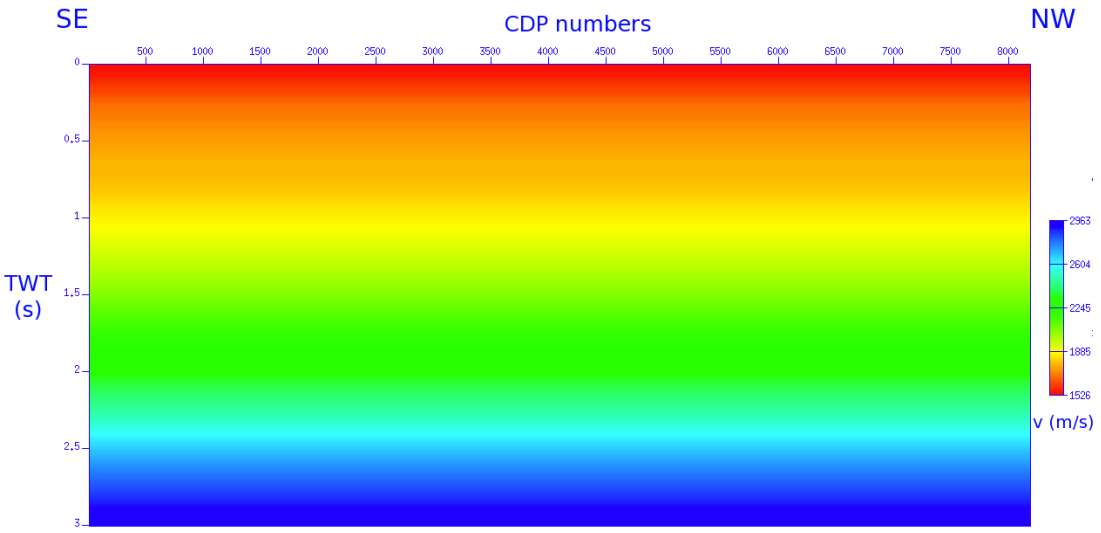

Figure 5.11: STENAP 08 velocity section.

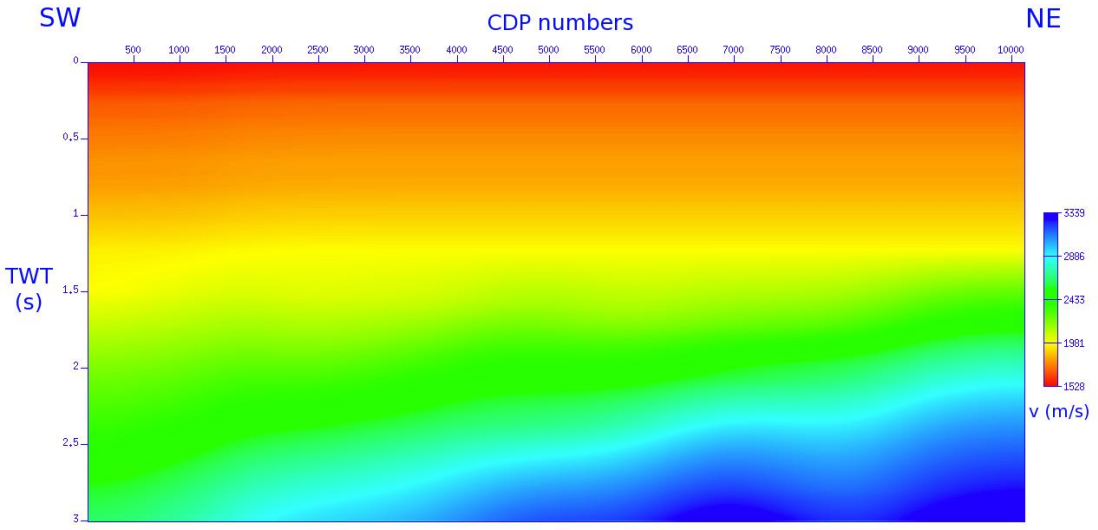

Figure 5.12: GANDI 09 velocity section.

5.1.5 Spherical divergence correction

Conceptually, a single shot is thought as a point source that generates a spherical wavefield (Yilmaz, 2001). The strength of the seismic reflections decreases with the depth of the reflecting surface. There are several reasons for that:

- As the wavefield spreads, it loses energy. The same amount of energy is spread out over a larger surface in three dimensions. This is known as *spherical divergence*;
- As the energy travels, some of it is reflected at each interface and only a proportion continues. This is know as *transmission loss*;
- Depending on the angle of incidence, some of this energy is converted to S-waves, refractions, etc. This is know as loss from *converted waves*;
- As the energy travels it is scattered; the Earth is not homogeneous and when seismic waves encounter variations, wave fronts are distorted and energy is deflected in all possible directions. This is known as *seismic scattering*.

Typically, a time-dependent gain is applied correct for spherical divergence. Very often, a $1/t^n$ function is used, with n ranging between 1 and 2. This correction considers an homogeneous medium, where energy density decays proportionately to $1/r^2$ (r is the radius of the wavefront). However, such gain can distort amplitudes, as it doesn't take into account velocity variations. Wave amplitude is proportional to the square root of energy density[1], so that it decays as $1/r = 1/vt$.
Velocity sections reported in Fig.5.11 and Fig.5.12 are used to correct for geometrical spreading.

5.1.6 Trimmed Mean Dynamic Dip Filter

Prior to migration, a Trimmed Mean Dynamic Dip Filter (TMDDF) is applied to the CDP gathers of both lines. TMDDF processes pre-stack datasets to improve the S/N, the objective is to remove high amplitude

[1]In practice, velocity usually increases with depth, which causes further divergence of the wavefront and a more rapid decay in amplitudes with distance.

noise and locally weak coherent events without eliminating useful trace information. At each sample of each trace it computes a series of trimmed means along rays (dips), using the sample itself and some number of leading and trailing near traces. The output sample is the trimmed mean that yields the highest amplitude. Trimmed mean operation means that a user-determined number of the smallest and largest samples along the dips are removed from the summation to reduce the effects of random noise.

The range of dips tested is defined by parameters p_{min} and p_{max}, the highest and lowest dips to include. Parameter n_{dips} specifies the number of dips to try within the range $p_{min} \div p_{max}$. The result should be relatively insensitive to n_{dips}, but if it is too large, computer time will be waisted, if it is too small, events at certain angles may be degraded. Also, the number of traces in mean computation ($gate$) should be set. In this processing flow, a small p interval is filtered with a considerable improvement of lateral continuity of reflectors. However, TMDDF causes a low-pass filtering effect, leading to a loss in resolution of very thin layers. This is the reason why the whole processing sequence was carried out in two way: excluding or including this filter. Both results are then used for the interpretation. Furthermore, in the process of removing high energy noise, TMDDF can create high frequency artifacts. Then, it is worthwhile to apply a band-pass frequency filter to its output.

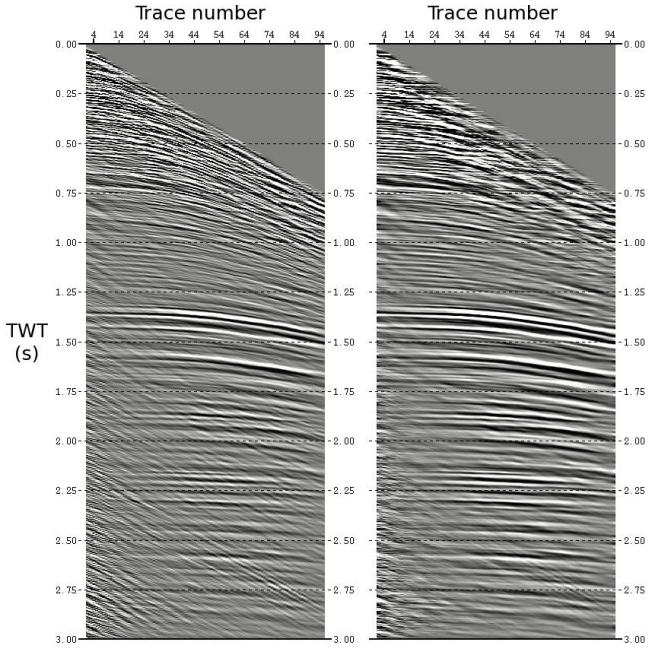

Figure 5.13: SP 759 before and after TMDDF application.

Table 5.2: TMDDF parameters.

	p_{min} $(\mu s/m)$	p_{max} $(\mu s/m)$	n_{dips}	$gate$
GANDI 09	-10	10	9	5
STENAP 08	-10	10	9	5

5.1.7 Migration

Seismic data were organized in common-offset and migrated in time with a pre-stack Kirchhoff migration. A double-square-root (DSR) operator was used and several tests were carried out, changing velocity fields and aperture angles. Migration is a processing step needed to properly locate every reflection.

Ideally, stacked data (see subsec.5.1.9) form a zero-offset section, with the source-target (reflector) raypath coincident to the target-receiver ones. This raypath must be perpendicular to the reflector itself, following the Snell's Law. If reflector interfaces are horizontal, the involved raypath will not be vertical, the apparent position of reflection points will not correspond to the effective ones. This is why they need to be migrated. The main objective of migration is to enhance the **spatial resolution** of a seismic section (Yilmaz, 2001). Migration properly locate reflection energy in time and space, the effect of this is enhanced spatial

resolution, as the Fresnel zone is collapsed [2]. In practice, migration does:

- Move dipping reflectors to their true subsurface positions;
- Collapse diffractions to their apexes.

Migration is also called *seismic imaging* because it produces a clearer image of subsurface.
Reflection elements are placed in their echo positions (on the vertical) only if the they belong to horizontal layers and the main goal of migration is to reallocate in the section elements not parallel to the ground (supposed to be flat).
The second meaning of migration is related to diffracted events. A diffraction occurs every time the reflecting element size is comparable to the signal wavelength: in these conditions the geometrical optics approximation is not valid anymore and the element reflects energy in all directions. There is a need to bring diffracted energy back to the diffractor element. In the Appendix B the theory on which most of the numerical methods are based, the so called *exploding reflectors method*, is described.
Amongst the various migration algorithms that can be used, Kirchhoff summation method was used. It is easy to implement and it can handle dips up to 90°.

The diffraction summation that incorporates the obliquity, spherical spreading and wavelet shaping factors is called the **Kirchhoff summation** and the migration method based on this summation is called the Kirchhoff migration (Yilmaz, 2001). Input data have to be multiplied by the obliquity and spherical spreading factors. Then a special filter ρ is applied and summing is performed. The summation of amplitudes is done along hyperbolic trajectories (defined by Eq.5.11), and the necessary amplitude and phase treatment of the summed amplitudes are given by the integral solution to the scalar wave equation (Yilmaz, 2001). In Kirchhoff migration, diffraction hyperbola are collapsed by summing the amplitudes, then placing them at the apex at time τ.

$$t^2 = r^2 + \frac{4x^2}{v_{RMS}^2} \tag{5.11}$$

The velocity used in Eq.5.11 is the RMS velocity, which can be allowed to vary laterally. However, lateral variation in velocity distorts the hyperbolic nature of the diffraction pattern and somehow must be considered (Yilmaz, 2001). This is why velocity fields needs to be laterally smoothed enough that the hyperbolic approximation still holds.
Berkhout (1980) is an excellent references for the mathematical treatment of the Kirchhoff migration method.
The integral solution of the scalar wave equation yields three terms; the far-field term which is proportional to $1/r$, and two other terms which are proportional to $1/r^2$. It is the far-field term that makes the most contribution to the summation that is used in practical implementation of Kirchhoff migration (Yilmaz, 2001). The output image $P_{out}(x_0, z = v\tau/2, t = 0)$ at a subsurface location (x_0, z) using only the far-field term is computed from the 2-D zero-offset wavefield $P_{in}(x, z = 0, t)$, which is measured at the surface $(z = 0)$, by the following summation over a spatial aperture:

$$P_{out} = \Sigma_\theta \frac{\Delta x}{2\pi} \sigma(x) \left[\frac{cos\theta}{\sqrt{v_{RMS} r}} \rho(t) * P_{in} \right] \tag{5.12}$$

where v_{RMS} is the RMS velocity at the output point (x_0, z) and $r = \sqrt{(x - x_0)^2 + z^2}$, the distance between the input $(x, z = 0)$ and the output (x_0, z) points. The asterisk denotes convolution of the rho filter $\rho(t)$ with the input wavefield P_{in}.

[2]The effect of wave propagation that migration corrects for is the "low pass" filter effect caused by the increasing size of the Fresnel zone with depth. Migration corrects for this by collapsing the Fresnel zone to approximately the dominant wavelength.

The rho filter $\rho(t)$ corresponds to the time derivative of the measured wavefield, which yields the 90° phase shift and adjustment of the amplitude spectrum by the ramp function ω. For 2D migration, the half-derivative of the wavefield is used. This is equivalent to the 45° phase shift and the adjustment of the amplitude spectrum by a function of frequency defined as $\sqrt{\omega}$. Since the ρ filter is independent of the spatial variables, it actually can be applied to the output of the summation in Eq.5.12. Finally, the far-field term in Eq.5.12 is proportional to the cosine of the angle of propagation (the directivity term or the obliquity factor) and is inversely proportional to vr (the spherical spreading term) in 3D. In 2D, the spherical spreading term is $\sqrt{vr}$.
Eq.5.12 can be used to compute the wavefield at any depth z. The output image P_{out} is computed at $(x_0, z = \tau/2, t = 0)$ using the input wavefield P_{in} at $(x, z = 0, t - r/v)$. To obtain the migrated section at an output time τ, Eq.5.12 must be evaluated at $z = v\tau/2$ and the imaging principle must be invoked by mapping amplitudes of the resulting wavefield at $t = 0$ onto the migrated section at output time τ. The complete migrated section is obtained by performing the summation in Eq.5.12 and setting $t = 0$ for each output location. The range of the summation is called the migration aperture. Migration aperture between 10° and 60° were investigated in the seismic data analyzed in this thesis.
To perform migration, a double-square root (DSR) operator was used. **DSR** equation describes downward continuation of both shots and receivers into the earth. It is exact for all dips and offsets. It neglects the velocity gradient dv/dz and so it is also applicable to a stratified earth. The DSR equation can be extended, with some approximation, to treat weak lateral velocity variations.
A comprehensive mathematical treatise of the DSR equation is found in Claerbout (1985).
DSR operator is made of two terms: one associated with downward continuation of shots and the other associated with downward continuation of receivers, that can be treated separately. By alternating between common-receiver and common-shot gathers, the entire dataset can be downward continued. This is, however, computationally very expensive. Most of today's seismic data processing is, in fact, in midpoint offset coordinates, rather than in shot-receiver coordinates.
In such coordinates, DSR equation takes the following form:

$$DSR(Y, H) = \sqrt{1 - (Y + H)^2} + \sqrt{1 - (Y - H)^2} \tag{5.13}$$

where Y and H are the normalized midpoint and offset wavenumbers, respectively (ω is the frequency):

$$Y = \frac{vk_y}{2\omega} \qquad H = \frac{vk_h}{2\omega} \tag{5.14}$$

The vertical wavenumber can be defined in terms of normalized midpoint-offset wavenumbers Y and H:

$$k_z = \frac{\omega}{v} DSR(Y, H). \tag{5.15}$$

and inserted into the extrapolation equation:

$$P(k_y, k_h, z, \omega) = P(k_y, k_h, 0, \omega)\ \exp(-ik_z z), \tag{5.16}$$

where $P(ky, kh, 0, \omega)$ is the Fourier transform of the pre-stack data $P(y, h, z = 0, \tau)$ in midpoint-offset coordinates. This extrapolation equation can be used to downward continue midpoint-offset gathers.
The conventional migration approach is composed of two separable operators, the NMO correction and stack applied in offset space, and the migration applied in midpoint space. However, this means accepting zero-dip and zero-offset assumptions. This is why an approach based on DSR equation was preferred.
Data were gained with an automatic-gain-control (AGC), using a window length of 0.5 *s* prior to migration. Then, they were organized in common-offset gathers and migrated with a Kirchhoff migration. A DSR operator was used. Several tests were carried out. The GANDI 09 line was migrated both with a velocity field built extrapolating Arcobaleno sonic-log ('LOG velocity field') and with an RMS velocity field

calculated from semblance analysis ('RMS velocity field'). Furthermore, aperture angle from 10° to 60° were tested (see Fig.5.14 and Fig.5.15).
Final migrations were performed with velocity fields reported in Fig.5.11, Fig.5.12 and 25° of aperture.

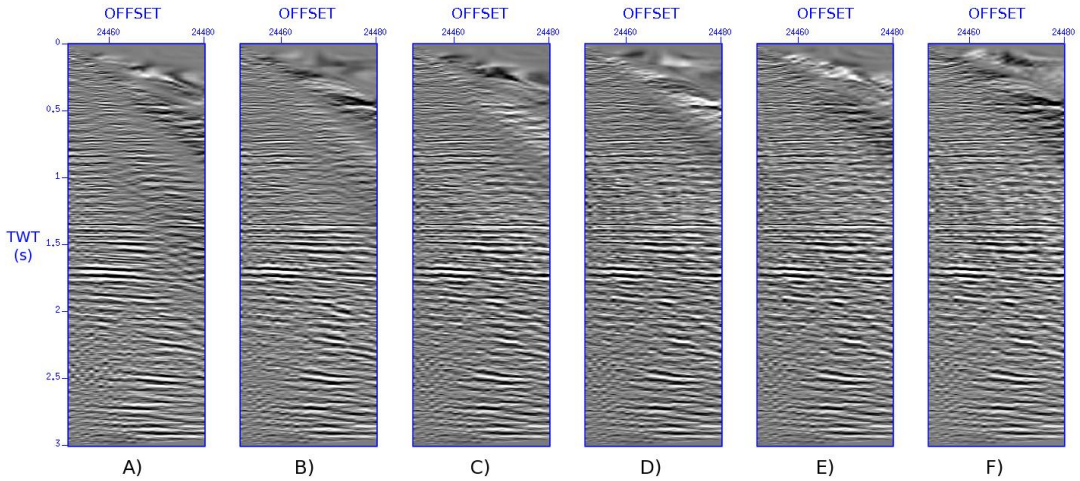

Figure 5.14: SP migrated with 'LOG velocity fields' and aperture angle from A) 10° to F) 60°.

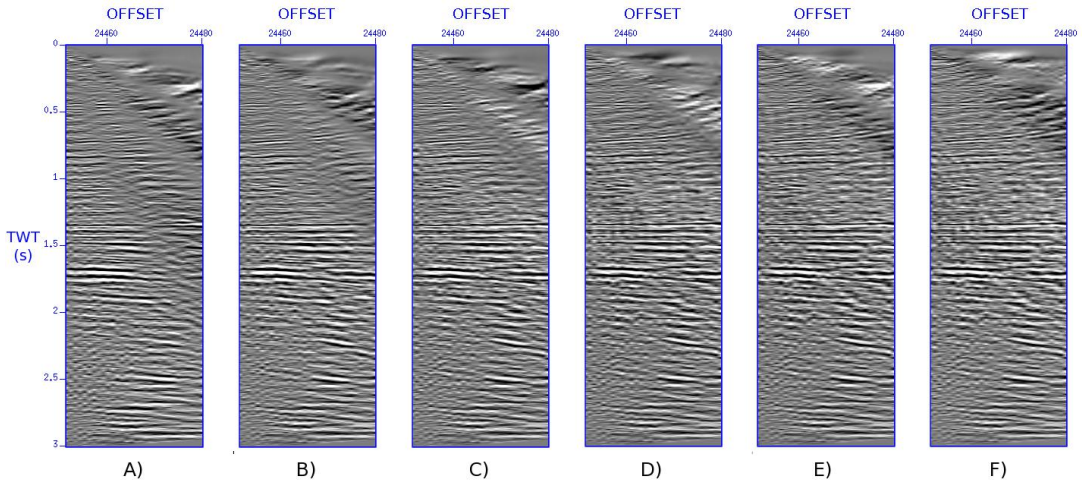

Figure 5.15: SP migrated with 'RMS velocity fields' and aperture angle from A) 10° to F) 60°.

5.1.8 Predictive deconvolution

At this point of the flow, predictive deconvolution was applied in time domain, to remove long-period multiples. In Table 5.3 parameters of pre-stack predictive deconvolution, set on the basis of traces autocorrelation, are reported.

Table 5.3: Pre-stack deconvolution parameters.

	$n\,(ms)$	$\alpha\,(ms)$	$\epsilon\,(\%)$	Time window (ms)
GANDI 09	65	13	0.1	0-2200
GANDI 09	1299	1299	0.1	1700-3000
STENAP 08	35	13	0.1	0-3000

In Fig.5.16 the STENAP 08 shot point 759 is showed after the application of: A) migration; B) TMDDF filter and migration; C) migration and predictive deconvolution; D) TMDDF filter, migration and predictive deconvolution. The net effect of TMDDF filtering is to improve laterally continuity, predictive deconvolution removes multiples and enhances the S/N.

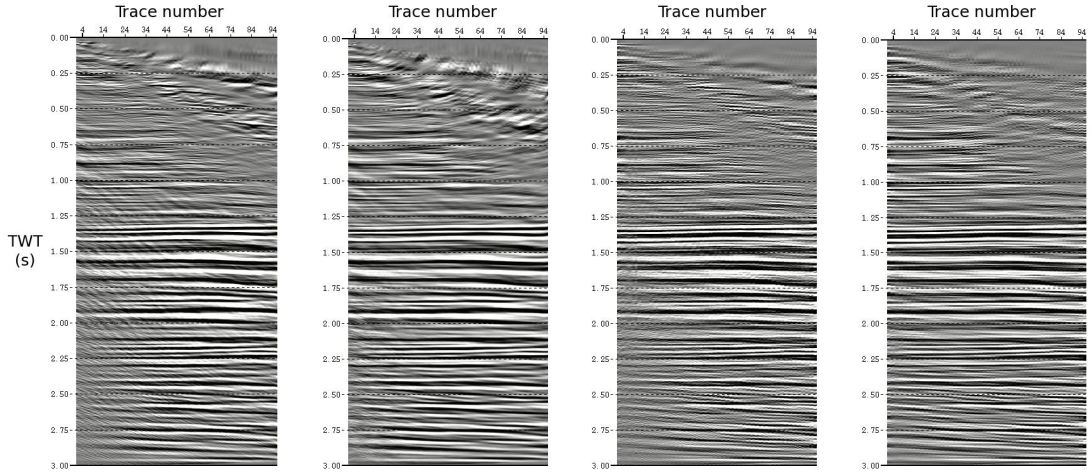

Figure 5.16: STENAP shot point 759. A) After migration; B) After TMDDF + migration; C) After migration + predictive deconvolution; D) After TMDDF + migration + predictive deconvolution.

5.1.9 NMO and stack

Consider a reflection event on a CDP gather. The difference between the two-way time at given offset and the two-way zero-offset time is called *normal moveout* (NMO). Reflection traveltimes must be corrected for NMO prior to summing the traces in the CDP gather along the offset axis (stacking). NMO depends on the velocity above the reflector, the offset, the two-way zero-offset time associated with the reflection event, the dip of the reflector, the source-receiver azimuth with respect to the true-dip direction, and the degree of complexity of the near-surface and the medium above the reflector (Yilmaz, 2001).
NMO flattens reflection hyperbola, see synthetic example in Fig.5.17.

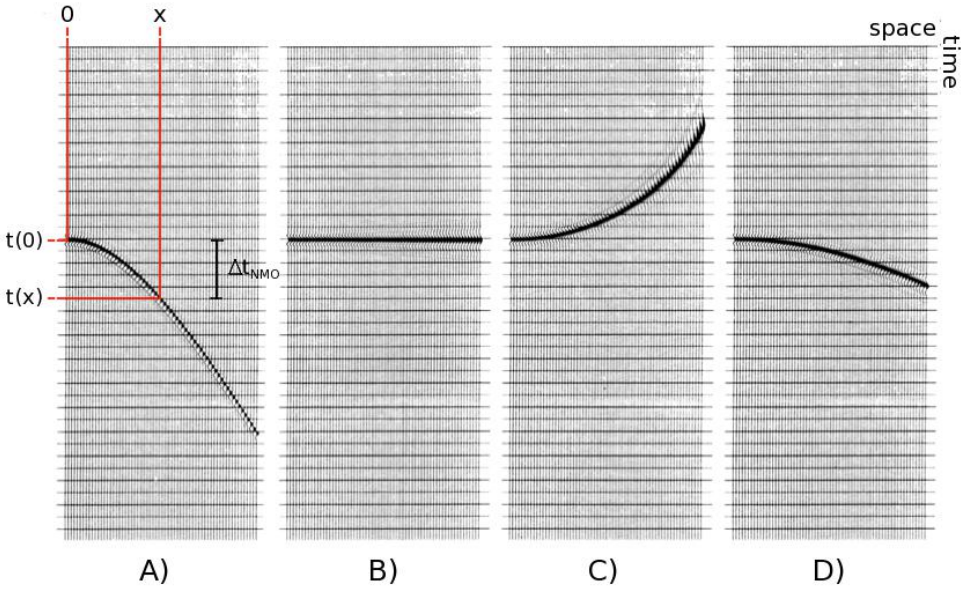

Figure 5.17: Single event. A) Before NMO; B) After NMO with the correct v_{NMO} velocity; C) After NMO, overcorrected; D) After NMO, under-corrected. Modified from Yilmaz (2001).

NMO is described by the equation below:

$$t_x^2 = t_0^2 + \frac{x^2}{v_{NMO}^2} \tag{5.17}$$

where x is source-to-receiver offset, t_0 zero offset TWT, t_x offset x TWT and v_{NMO} the NMO velocity

The NMO correction is given by the difference between t_x and t_0:

$$\Delta t_{NMO} = t_0 \left[\sqrt{1 + \left(\frac{x}{v_{NMO} t_0} \right)^2} - 1 \right] \tag{5.18}$$

It increases with offset and decreases with depth.

Velocity sections reported in Fig.5.11 and Fig.5.12 are used as v_{NMO}.
As a result of NMO correction, a frequency distortion occurred, particularly for shallow events and at large offsets. This is called *NMO stretching*, and it is a frequency distortion in which events are shifted to lower frequencies. It can be quantified by:

$$\frac{\Delta f}{f} = \frac{\Delta t_{NMO}}{t_0} \tag{5.19}$$

This problem can be solved by muting the stretched zones in the gather. A stretch mute was applied to zero any samples whose stretch was greater than 45%. Amplitude traces were then summed, sample by sample, and the first stack sections were obtained.

5.1.10 Time variant band-pass filtering

The frequency content of the source wavelet changes in a time-variant manner as it propagates. In particular, high frequencies are absorbed more rapidly than low frequencies. This is because of the intrinsic attenuation in rocks. In fact, Earth behaves like a low-pass filter, resulting in decreased resolution and S/N with depth in seismic images. This is why is good practice to apply a *time variant frequency filter*, to reflect the reduced bandwidth of the signal. The applied filter is described in Table 5.4.

Table 5.4: Time variant frequency filter.

Time window	0-1500 ms	1500-3000 ms
GANDI 09	10-20 120-240 Hz	5-10 80-160 Hz
STENAP 08	10-20 120-240 Hz	5-10 80-160 Hz

5.1.11 Post-stack predictive deconvolution

Predictive deconvolution was applied also in post-stack domain. In Table 5.5 are reported the parameters of post-stack predictive deconvolution, set again on the basis of traces autocorrelation.

Table 5.5: Post-stack deconvolution parameters.

	$n\,(ms)$	$\alpha\,(ms)$	$\epsilon\,(\%)$	Time window (ms)
GANDI 09	1199	1199	0.1	0-1200
GANDI 09	100	13	0.1	1000-3000
STENAP 08	60	13	0.1	0-1000
STENAP 08	180	13	0.1	800-3000

5.1.12 f-x post-stack deconvolution

Random noise attenuation in seismic data can be implemented in the frequency and time domain using prediction filters (Abma and Claerbout, 1995). The $f-x$ prediction technique was introduced by Canales (1984) and further developed by Gulunay (1986), it is also referred as $f-x$ deconvolution. After having used Fast Fourier Transform (FFT) to transform a specific window of traces into the $f-x$ domain, it applies a linear prediction filter, assuming that the signal can be described by an autoregressive (AR) model. When the data are contaminated by random noise, the signal is considered to be predicted by the AR filter and the noise is the residual (Bekara and Van der Baan, 2009). The conventional $f-x$ domain prediction uses windowing strategies to avoid that the seismic events are not linear. The data are assumed to be piece-wise linear and stationary in time and space. Abma and Claerbout (1995) discussed $f-x$ and $t-x$ approaches to predict linear events and concluded that $f-x$ prediction is equivalent to $t-x$ prediction with a long time length.

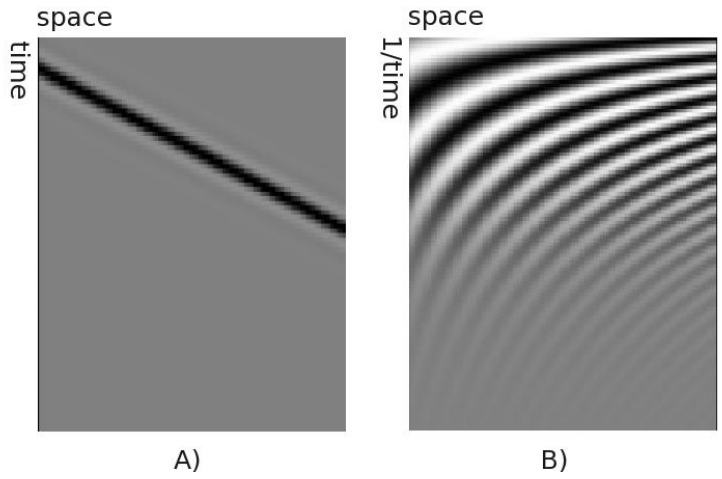

Figure 5.18: A single dip in: A) time domain and B) Fourier domain. Modified from Yilmaz (2001).

The technique can be described with the following procedure:

- A window of traces specified with parameters x_{len} and t_{len} is transformed with FFT (Fast Fourier Transform) and evaluated over a specified frequency range;
- The calculated $f - x$ series are autocorrelated;
- For each series, a prediction filter is designed that attenuates the random part of the complex autocorrelation and enhances the predictable part. The filter is built using a Wiener inversion technique;
- The prediction filter is applied to the $f - x$ series;
- The original $f - x$ series and the filtered $f - x$ series are scaled and summed;
- Inverse FFT is applied to transform back to the $x - t$ domain;
- The procedure is repeated increasing the width and time length of the FFT window.

A unique filter is constructed for each frequency.

Table 5.6: f-x deconvolution parameters.

	x_{len}	$t_{len}\,(ms)$	$filter_{length}$	Frequency range (Hz)
GANDI 09	14	500	4	0-Nyquist
STENAP 08	14	500	4	0-Nyquist

Fig.5.19 shows the result of $f - x$ deconvolution. The overall continuity of reflectors is improved an S/N ratio is slightly better. A small number of traces (x_{len}) was used to avoid creating artifacts.

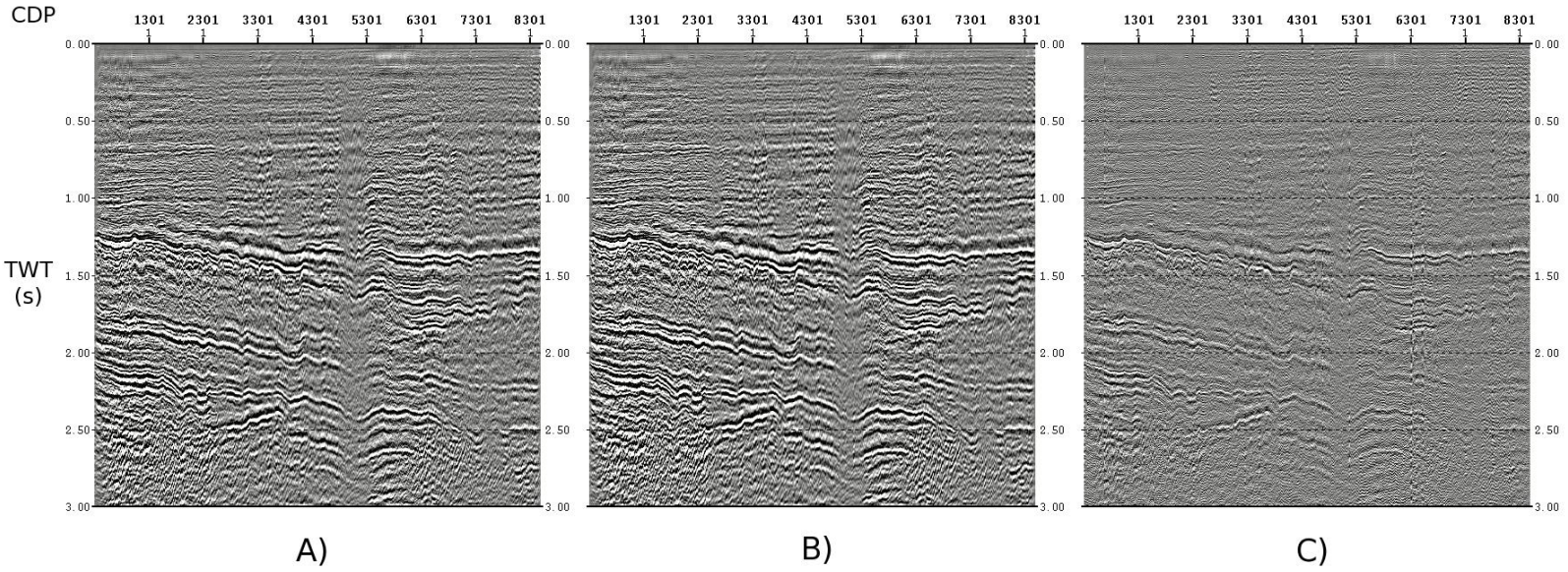

Figure 5.19: STENAP 08 stack section. A) Before f-x deconvolution; B) After f-x deconvolution; C) Difference between them: A) - B).

5.1.13 Final stack sections

In the following figures, final stack sections of both lines are reported, excluding or including the application of the TMDDF filter.

STENAP 08

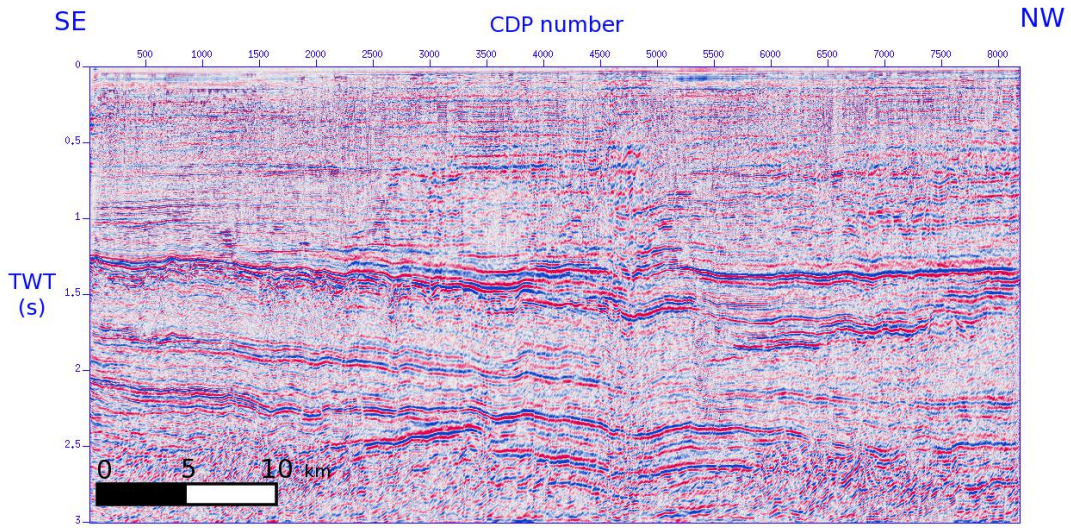

Figure 5.20: STENAP 08 final stack section.

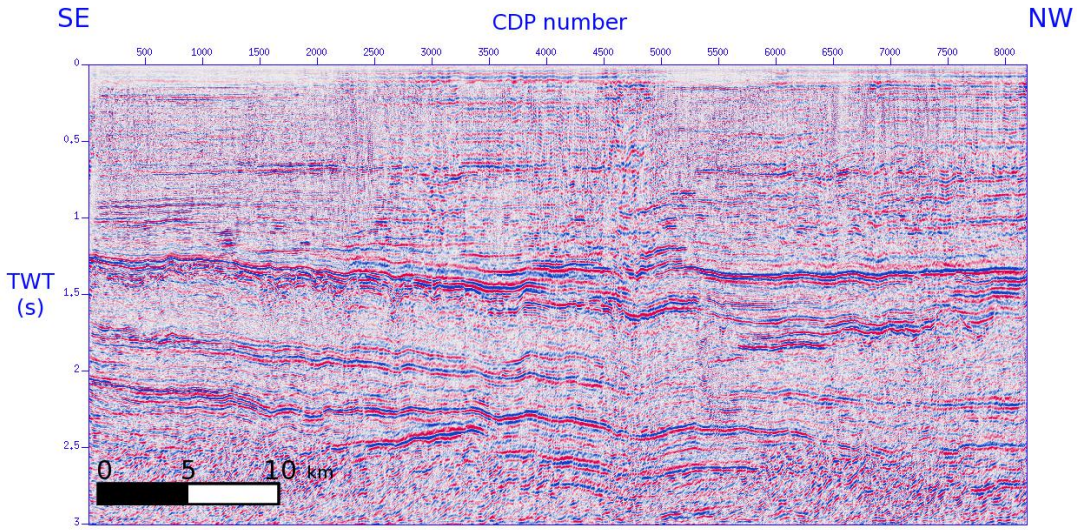

Figure 5.21: STENAP 08 final stack section, with TMDDF.

GANDI 09

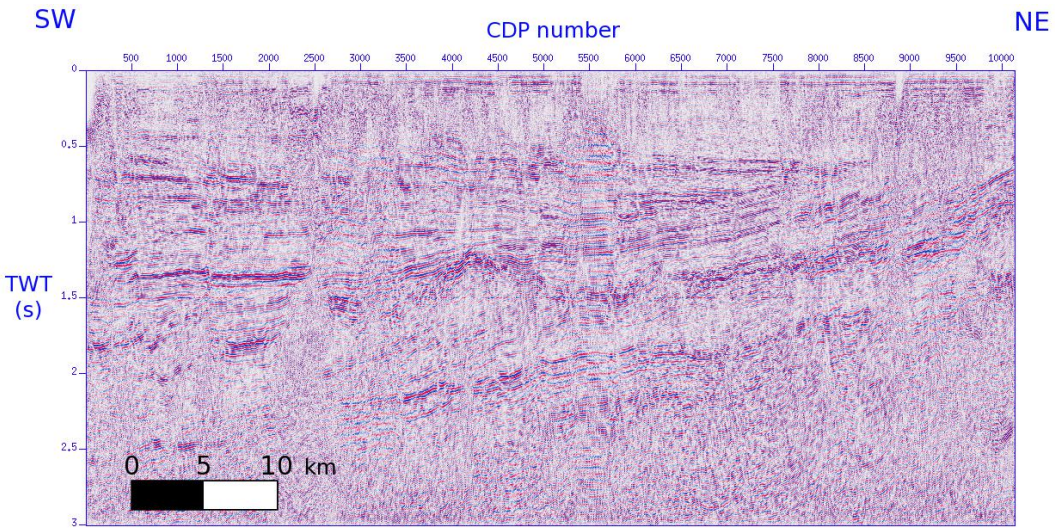

Figure 5.22: GANDI 09 final stack section.

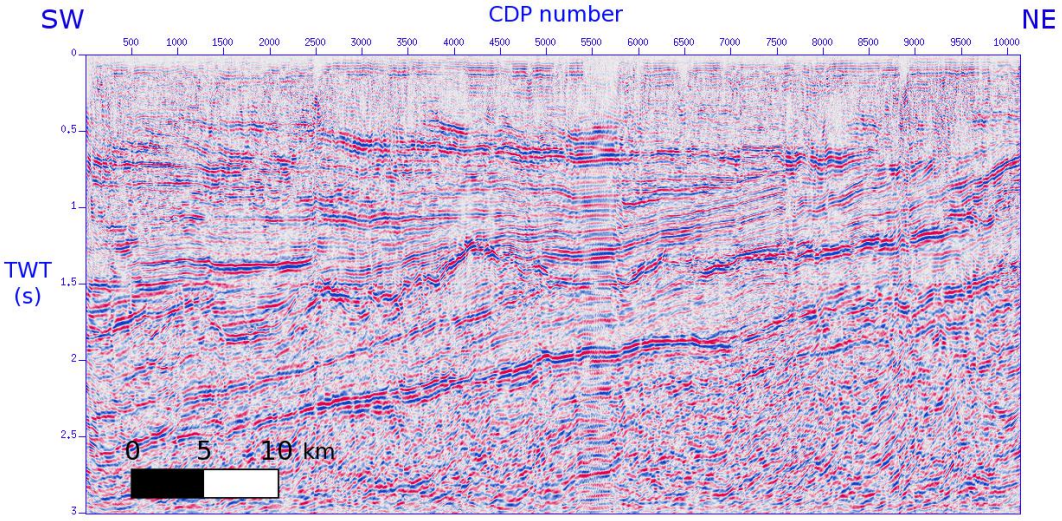

Figure 5.23: GANDI 09 final stack section with TMDDF.

5.2 Amplitude preserving processing sequence

A second processing flow (Fig.5.24) used specific algorithms to improve the S/N and to remove multiples without affecting the relative amplitude information. For this reason, specific processes, such as deconvolution or migration, commonly used and usually very effective to enhance the data quality, were not applied because of their influence on the original amplitude of the signal.
Instead, the focus of the amplitude preserving flow is the *surface-related multiple elimination* (SRME), an adaptive amplitude-preserving algorithm which does not assume a subsurface velocity model.
The resulted processed lines are the ones used for the log-seismic correlation, inversion and gas content quantification. These analysis are strongly amplitude dependent as they are based on the degree of contrasts across the sediment interfaces, on their extent and nature.

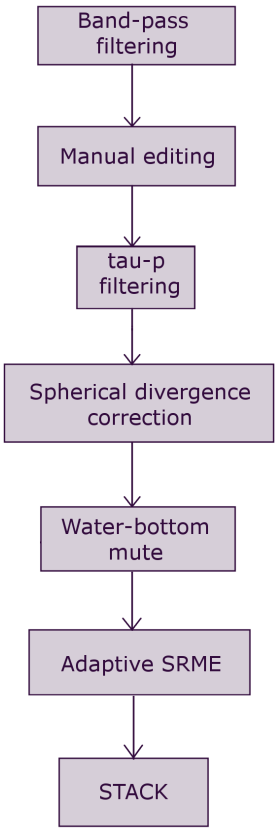

Figure 5.24: Processing flow

5.2.1 Surface-Related Multiple Elimination

Surface-related multiples include all multiples except those generated by totally internal reflections. They are typically the strongest multiple events present in the seismic data and they are classified into different orders depending on how many times they are reflected back from the free surface. In general, a n-th order surface-related multiple gets reflected n times at the free surface.
Methods to remove multiples fall into three broad categories: exploiting the differences in the properties moveout of primary and multiple reflection events in seismic records, wave-equation-based modeling of multiple reflections using an earth model and so-called data-driven methods that predict multiple reflections directly from information contained in seismic records. Surface-related multiple elimination (SRME) (Verschuur et al., 1992) falls in the third category. SRME deals only with multiples whose raypaths include one or more downwgoing reflections from the surface. There are also data-driven methods related to SRME that predict internal multiple reflections (Jakubowicz, 1998) and recent advances in computer hardware have made it feasible to apply advanced versions of 3D SRME to seismic data on a routine basis. In this processing sequence, 2D SRME was applied with excellent results.
SRME is an algorithm that kinematically predicts all surface multiples by a convolutional process applied to seismic field data (first step). Only minimal preprocessing is required. Once predicted, the multiples are removed from the data by adaptive subtraction (second step). Unlike other methods of multiple attenuation, SRME does not rely on assumptions or knowledge about the subsurface, nor does it use event properties to discriminate between multiples and primaries. Instead, SRME requires some knowledge of the acquisition wavelet and a dense spatial distribution of sources and receivers. The seismic data itself is used to predict the multiple field. In fact, according to the theory by Verschuur et al. (1992), the multiple prediction operator can be expanded into a Taylor series. In practice, each CDP gather is expanded into its Taylor series, starting from 0-th order. Each term contains free surface-related multiples starting from a certain order. The zero-order is a frequency-filtered version of the input gathers and contain both primaries and multiples. The first Taylor term contains all first order and higher order multiples but no primary reflections. The algorithm uses the original shot gathers (zero-order Taylor terms) and the first-order Taylor term as multiple model to estimate least-squares matching filters. The predicted multiple traces are convoluted with the matching filters and subtracted from the data traces. Least squares matching

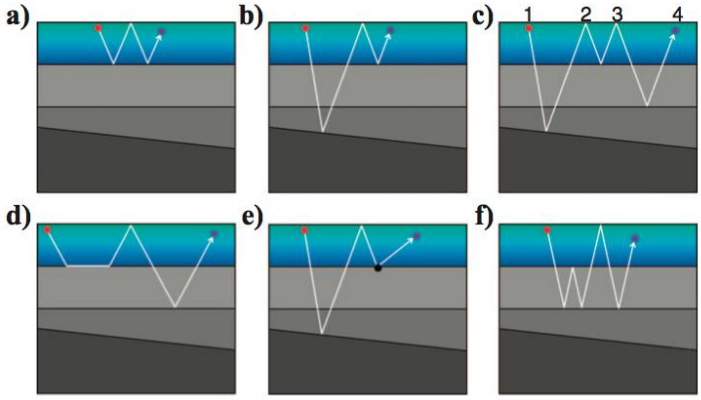

Figure 5.25: A variety of seismic events represented by their raypaths. (a) Water-bottom multiple. (b) Water-bottom peg-leg. (c) Second-order multiple. (d) Refracted multiple. (e) Diffracted multiple. (f) Hybrid multiple. Because each event includes at least one downward reflection at the surface, it is classified as a surface-related multiple. A key characteristic of all surface multiples is that they can be segmented into subevents which can be recorded in a seismic measurement performed at the surface. For example, the second-order multiple (c) consists of three subevents: 1–2, 2–3, and 3–4. Each subevent is measurable by a surface experiment. Given a suitable set of measurements, SRME can predict all types of surface multiples, including those shown here, without knowing any properties of the subsurface. Red dots are the source, purple dots are the receiver, and the black dot is the diffractor. From Dragoset et al., 2010.

filters are designed such that the residual energy between the data traces and the filtered multiple traces is minimized in a specified 2D window. In other words, the filtered multiples will match the recorded multiples as closely as possible, in terms of traveltimes, amplitude and wavelet shapes. This should result in the optimal attenuation of the multiple field.
In the implementation of the SRME algorithm used in this thesis, input data must be pre-stack CDP ordered data. Direct wave, source-side and receiver-side ghosts (spurious reflections of the wavefield at the sea surface due to source and receivers being towed at depth) should be removed from the input gathers before SRME application. Merge and adaptive subtraction were performed in shot gathers domain. Trace selection criteria is based on offset. The algorithm needs to know the maximum offset of the recording geometry and the intertrace (correlation step size).
Matching filters were estimated from a moving 2D window which contain x_{len} traces and t_{len} ms in time. A single matching filter of length $filter_{len}$ was estimated from each 2D window and was applied at the center of the window in the multiple model. The filtered multiple traces were then subtracted from the data traces and the 2D window was moved horizontally of x_{step} and vertically of t_{step}. Too long filters may lead to unexpected attenuation of primaries. In Table 5.7 SRME parameters are reported, Fig.5.26 application of SRME on a single shot point is shown.

Table 5.7: SRME parameters.

	$IL_{max}\,(m)$	$IL_{step}\,(m)$	$filter_{len}\,(ms)$	$window_{xlen}\,(traces)$	$window_{tlen}\,(ms)$
GANDI 09	1525	12.5	80	11	600
STENAP 08	1200	25	80	11	600

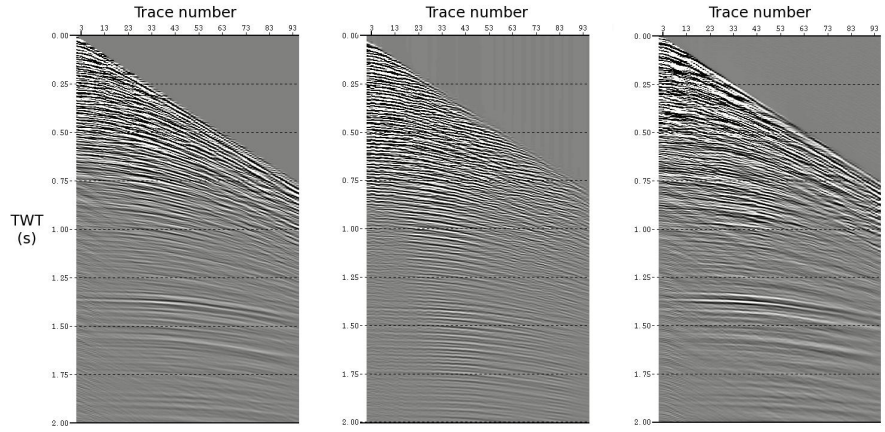

Figure 5.26: STENAP shot point 759. A) Before SRME; B) Extracted multiple field; C) After adaptive subtraction of the multiple field through SRME.

5.2.2 Final stack sections

Final preserving amplitude stack sections are reported in Fig.5.27 and Fig.5.28.

STENAP 08

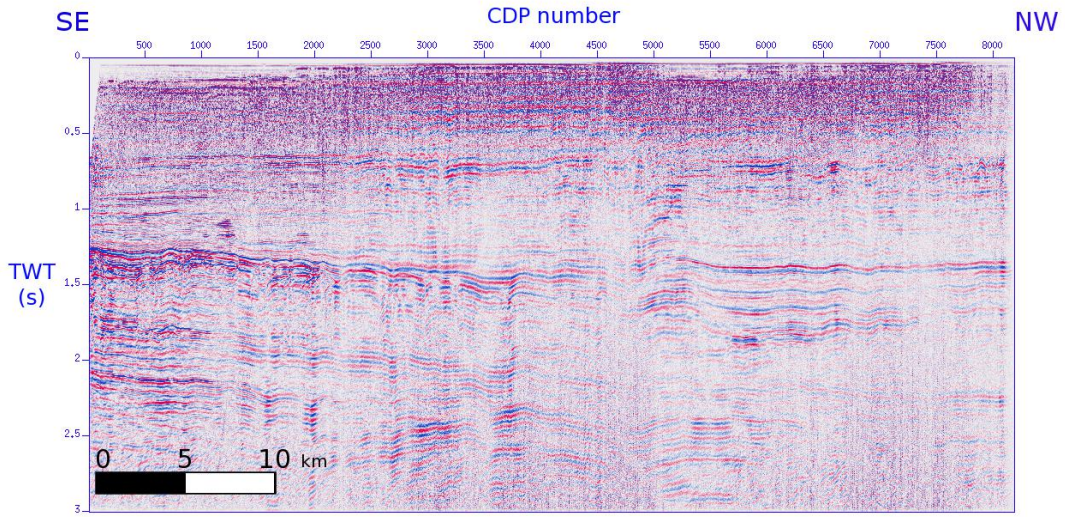

Figure 5.27: STENAP 08 amplitude preserving stack section.

GANDI 09

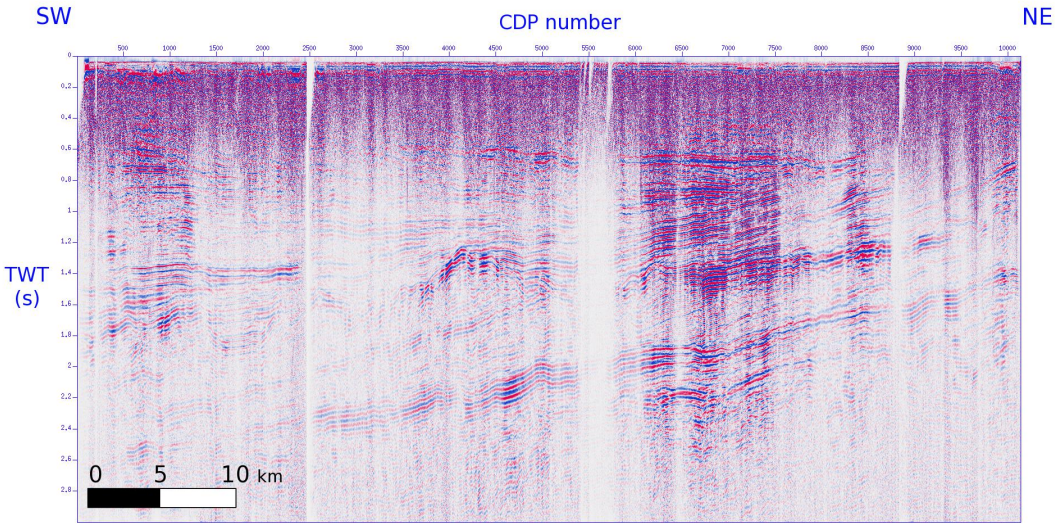

Figure 5.28: GANDI 09 amplitude preserving stack section.

Chapter 6

Log processing

Our purpose was to correlate the log information, which is actually a measure of the petrophysical properties of the rocks with the seismic data to better characterize the subsurface. Log data are available from the so-called "*composite log chart*", so they were digitized to be processed and resampled to be consistent with the frequency of the seismic data. Not every well contained the same logs, so additional work has been done to derive the missing logs. Our approach was to investigated via cross-correlation, fit and χ^2 tests, experimental relationships between pairs of logs, for the same well and among different wells. The basic idea was to seek for a common trend in the log properties which could be representative of the rock formations and then used in the prediction of the missing logs using empirical formulas.
The whole processing, except for the digitalization, was performed writing scripts in python. Acoustic impedance (IP) profiles were reconstructed for each borehole of interest with an iterative procedure of comparison between synthetic and real signals. The procedure was guided by a geological interpretation of the lithostratigraphic column of all the boreholes drilled in the study area, and based on the geological information taken from the technical drilling reports, as explained in sec.6.3. IP at well-location was then used to perform acoustic inversion.

6.1 Digitalization, interpolation and resampling

Log data were made available by the ViDePi project in raster format (see Fig.6.1A)). They were digitized using Kingdom software and corrected for rotary table height. Then, they were interpolated (and smoothed) with linear spline functions.
Spline functions are essentially generalizations of the notion of polygonal lines. They are formed by joining polynomials together at fixed points called knots. The interval extending from lower limit to upper limit over which a curve has to be approximated is divided into $L + 1$ sub-intervals separated by L interior boundaries ζ. Consider the simplest case in which a single breakpoint divides interval into two sub-intervals. The spline function is, within each interval, a polynomial of specified degree (the highest power defining the polynomial) or order (the number of coefficients defining the polynomial, which is one more than its degree). At the interior breakpoint ζ_1, the two polynomials are required to join smoothly. In the most common case, this means that the derivatives match up to the order one less than the degree. Thus, a spline function defined in this way has one extra degree of freedom than a polynomial extending over the entire interval. If the spline is linear, this means that each polynomial is a straight line segment, and therefore of degree one. Straight lines join at the breakpoint with matching derivatives up to degree 0; in short, they simply join and having identical values at the break point.

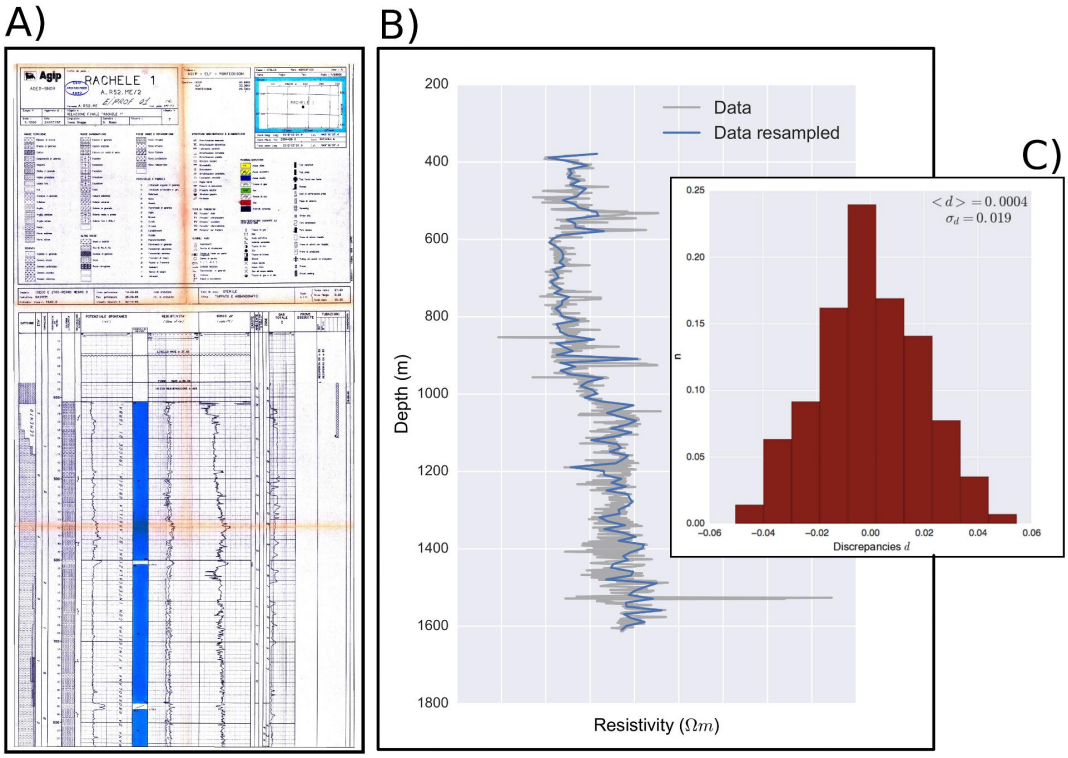

Figure 6.1: A) Rachele well-logs report in raster format; B) Rachele resistivity after spline interpolation and resampling; C) Resampling error distribution.

In the linear case, spline can be simply written as:

$$y = \frac{x_i - x}{x_i - x_{i-1}} y_{i-1} + \frac{x - x_{i-1}}{x_i - x_{i-1}} y_i \tag{6.1}$$

where $y(x_{i-1}) = y_{i-1}$ and $y(x_i) = y_i$.
In interpolating problems, spline interpolation is often preferred to polynomial interpolation because it yields similar results, even when using low degree polynomials, while avoiding Runge's phenomenon for higher degrees[1]. Log data were then resampled each 10 m and an average error was associated to each point of each curve, defined as weighted average of discrepancies between initial and resampled values at each point. Resistivity resampled spline is shown for the case of Rachele well in Fig.6.1B) Discrepancies distribution was found to be approximately gaussian and centered around 0 (see Fig.6.1C)).
Sonic, gamma-ray, self-potential and resistivity logs were analyzed (Fig.6.3, Fig.6.2).

Spontaneous potential log, also called self-potential (SP), measures the natural or spontaneous potential difference existing between the borehole and the surface in the absence of any artificially applied current. It is a very simple electrical well log that requires only an electrode in the borehole and a reference electrode at the surface. It is usually recorded in mV. These spontaneous potentials arise from the different access that different formations provide for charge carriers in the borehole and formation fluids, which lead to a

[1]It is referred to a problem of oscillation at the edges of an interval that occurs when using polynomial interpolation with polynomials of high degree over a set of equispaced interpolation points.

spontaneous current flow, and hence to a spontaneous potential difference.

Resistivity log is an electrical well log that records the resistivity of a formation. The ability of a rock to transmit a current is almost entirely a function of the fluid in the pores and the pore geometry. This is why resistivity logs can be used to infer information about the porosity of a formation, the water saturation and the presence of hydrocarbons. During logging, a current is produced within the formation and the formation's response is recorded. There are two main type of tools: electrode tools, that apply a direct current and measure the resistivity; induction tools, that induces an alternating current and measure the conductivity. Electrode tools generally measure the shallow resistivity, while induction tools generally measure the deep resistivity. Resistivity is usually recorded in Ωm and reported in logarithmic scale.

Gamma-ray log measures that natural radioactivity of rocks. It uses passive devices, made of Geiger counters, solid-state scintillators or spectral devices to detect γ-ray emissions. Emission depends on the radioactive isotope content, that is strongly correlated with the mineralogy. Gamma-ray logs are used to determine lithology and identify shale volumes (presumed to be composed of clay minerals, possibly characterized by high levels of radioactivity. This kind of logging measurements is also used to calibrate cores, especially in the case of spectral devices, that distinguish the various present isotopes. Common scale in γ-ray logs is the API (American Petroleum Institute), calibrated with a special facility built by API at the University of Houston.

Sonic log is an acoustic log which measures the travel time of an elastic wave through the formation. This information is used to derive the velocity of elastic waves through the formation. Its main use is to provide information to support and calibrate seismic data and to derive the porosity of a formation. Sonic log tools measure the time it takes for an elastic wave to travel from a transmitter to a receiver, which are both mounted on the tool. The transmitted pulse is very short and of high amplitude. This travels through the rock in various different forms while undergoing dispersion (spreading of the wave energy in time and space) and attenuation (loss of energy through absorption of energy by the formations). The data is presented as a slowness or the travel time per foot traveled through the formation and is usually measured in $\mu s/ft$. In this work, velocity is calculated from slowness and converted in SI unit m/s

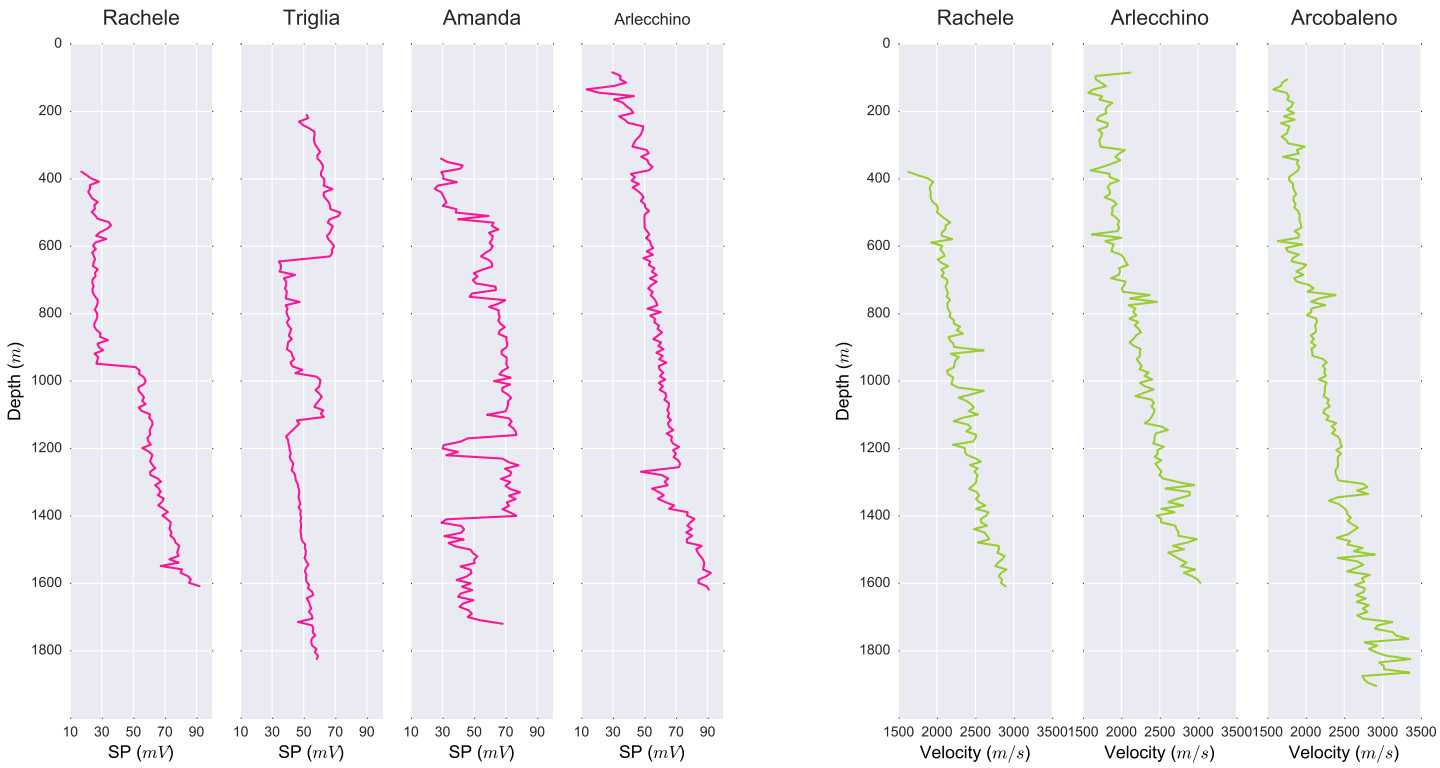

(a) SP logs

(b) Velocity logs

Figure 6.2

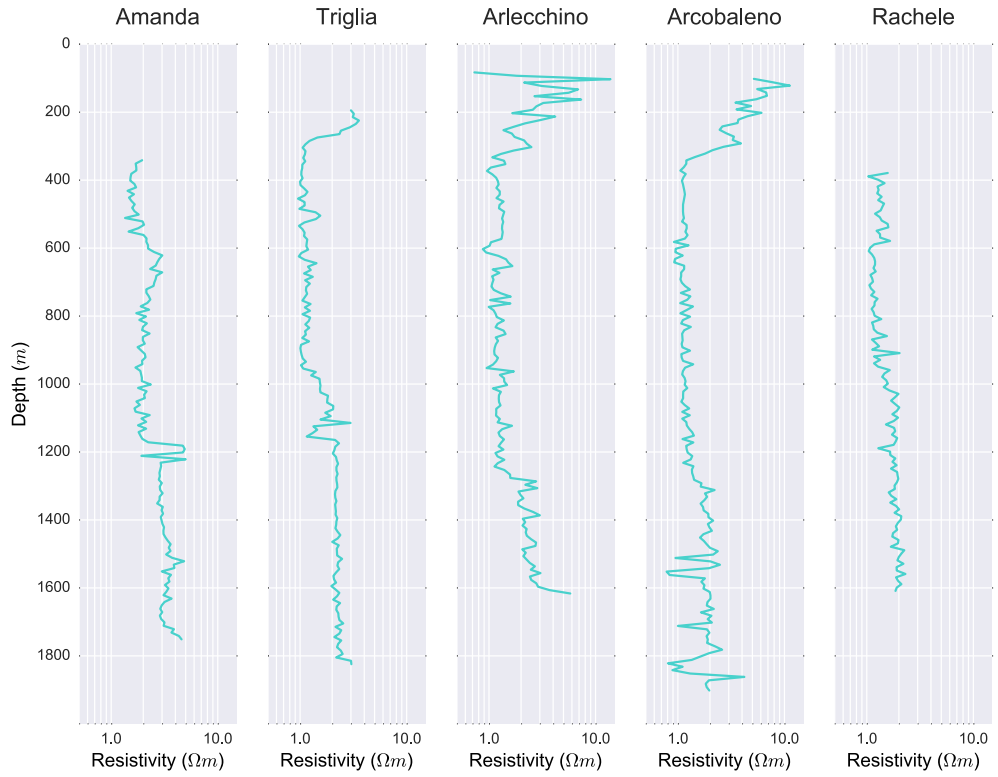

(a) Resistivity logs

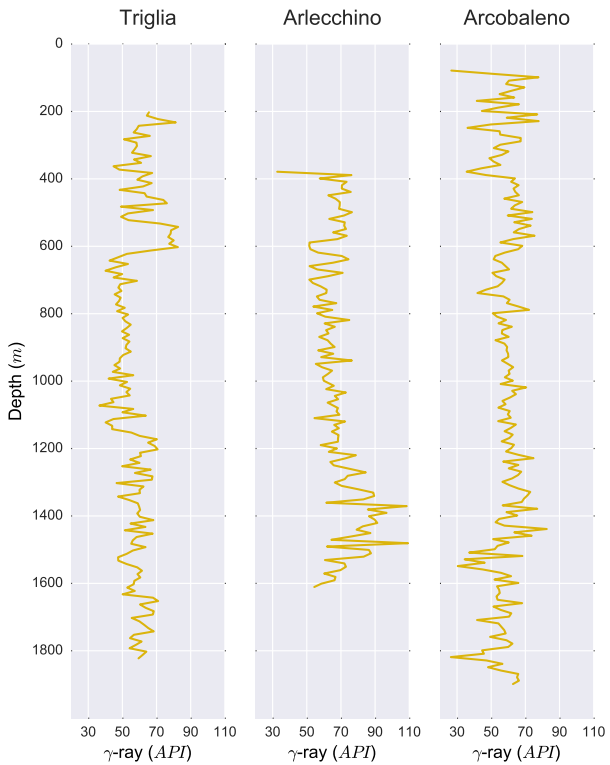

(b) Gamma-ray logs

Figure 6.3

6.2 Editing and cross-plot analysis

After having digitized and resampled them, log curves were edited.
A first outliers removal was performed to filter out all the points with associated relative error greater than 50%. Then, on the basis of known lithological changes and/or evident different behaviors, curves were divided in depth intervals. Every interval was fit to find its trend with the non-linear simplex, Nelder-Mead, algorithm (see details in subsec.6.2.1). Then, a second outliers removal filtered out every point distant more than 2 standard deviation from the fitting curve.
Eventually, a χ^2 test was carried out to assess the goodness of fit. Each pairs of curves were cross-plotted to determine their correlation.
A scheme of the all procedure is reported in Fig.6.4.

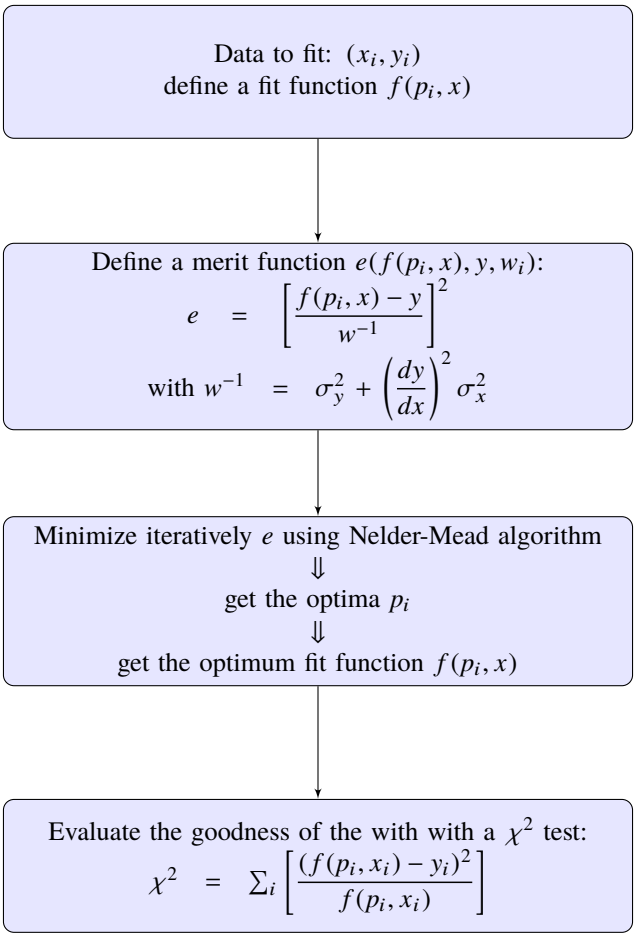

Figure 6.4: Fitting procedure

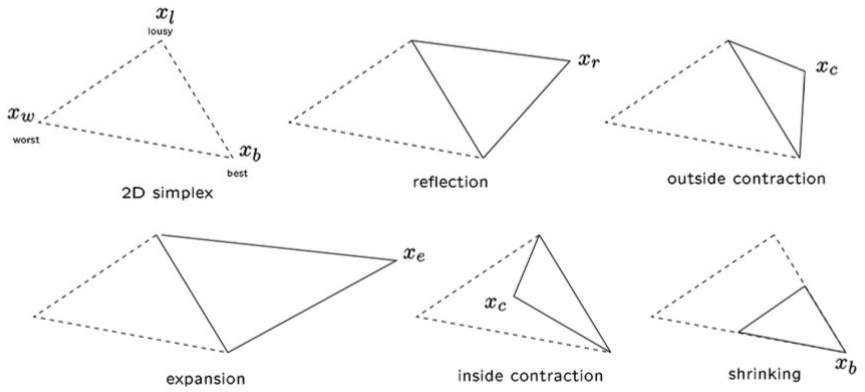

Figure 6.5: Simplex transformation. From Hicken et al. (2000).

6.2.1 Fitting procedure: Non-linear simplex algorithm: the Nelder-Mead method

The Nelder-Mead algorithm (Nelder and Mead, 1965) is one of the best known algorithms for multidimensional unconstrained optimization without derivatives. The method does not require any derivative information, which makes it suitable for problems with non-smooth or discontinuous, but also for multilocal, functions. The algorithm is designed to solve the classical unconstrained optimization problem of minimizing a given non-linear function $f : \mathbb{R}^n \rightarrow \mathbb{R}$. It does not try to calculate approximate gradients, hence it belongs to the general class of direct search methods (see Kolda et al., 2003).
The Nelder-mead method is simplex based. A simplex S in $\mathbb{R}^n$ is defined as the convex hull of $n + 1$ vertices $x_0 \ldots x_n \in R^n$ (see Fig.6.5). A simplex in $\mathbb{R}^2$ is a triangle, a simplex in $\mathbb{R}^3$ is a tetraedron. A simplex-based direct search method begins with a set of $n + 1$ points $x_0 \ldots x_n \in \mathbb{R}^n$ that are considered as the vertices of a working simplex S and the corresponding set of function values at the vertices $f_j \doteq f(x_j)$ fro $j = 0 \ldots n$. The initial working simplex S has to be non-degenerate, i.e. the points $x_0 \ldots x_n$ must not lie in the same hyperplane. The method then performs a sequence of transformation of the working simplex S, aimed at decreasing the objective function values at each of its vertices. These can be: reflection away from the worst vertex (the one with the largest objective function value), shrinkage towards the best vertex (the one with the smallest objective function value), expansion, outside contraction, inside contraction. In this way, the working simplex changes in size and shape. At each step, the transformation is determined by computing one or more test points, together with their objective function values, and by comparison of these function values with those at the vertices. This process is terminated when the working simplex S becomes sufficiently small in some sense, or when the function values f_j are close enough in some sense.
Strengths of the Nelder-Mead algorithm are that it requires no derivatives to be computed and that it does not require the objective function to be smooth. Typically, it requires only one or two function evaluations at each step, while many other direct search methods use n or even more function evaluations. The weakness of this method is that it is not very efficient for problems with more than about 10 design variables.

6.2.2 Cross-plot results

The main issue related to the available logs is that each well does not contain the same type of logs, thus we would find out which of them was most representative of the lithological variation with depth. This is of particular interest in case of missing logs when an empirical relationship has to be applied to an

existing logs to derive the missing one. At the same well we assume that common trends at different depths between cross-plotted logs would confirm that they measure the same lithological variation and they are then representative of the subsurface characteristic. Cross-plots of logs between wells are used to verify possible common behaviors and to confirm the presence of lithological units with the same petrophysical characteristics that can validate the extrapolation of the data from one well to another. Velocity and resistivity were found to have a good correlation in Rachele, Arcobaleno and Arlecchino well (see Fig.6.6 and Fig.6.7 (a)). Where velocity logs were missing, cross-plot analysis was carried out between other types of logs. In particular, a relationship between resistivities of Amanda and Rachele was seek to help in building a velocity pseudo-log for Amanda, located in a key position along the GANDI 09 seismic line. Unfortunately, it was not possible to successfully fit the cross-plot (see Fig.6.7 (b)).

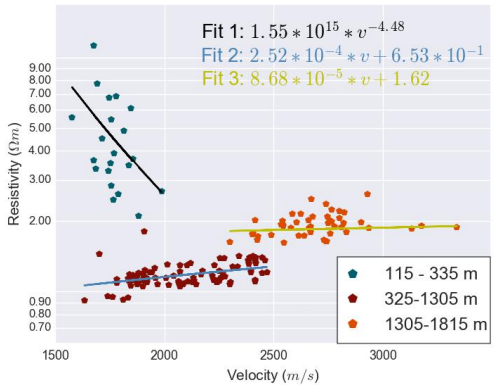

(a) Arcobaleno velocity-resistivity cross-plot

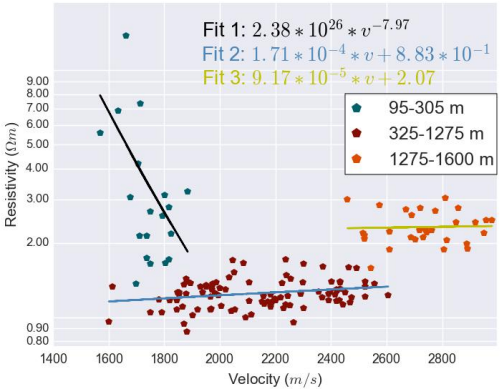

(b) Arlecchino velocity-resistivity cross-plot

Figure 6.6

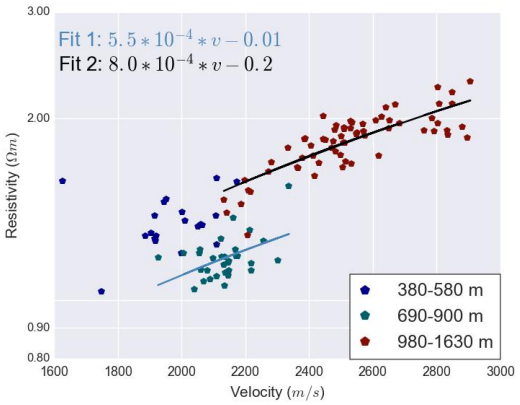

(a) Rachele velocity-resistivity cross-plot

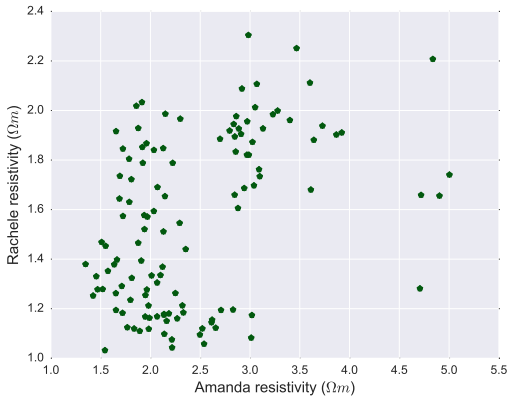

(b) Amanda vs Rachele resistivity cross-plot

Figure 6.7

6.3 IP estimation

To perform acoustic inversion of seismic data (see chap.7), it is necessary to know acoustic impedance logs at well locations. Those were not available in the dataset and estimation of IP pseudo-log at well locations was required.
Acoustic impedance is defined as the product of seismic P-wave velocity and density $IP = v_P \cdot \rho$, the SI unit is the pascal second per cubic metre ($Pa \cdot s/m^3$). Seismic reflection occurs when there is contrast in acoustic impedance across a layer boundary. From the acoustic impedance log, it is possible to calculate the reflection coefficient for each reflecting interface in the subsurface. Amongst the selected boreholes logs, density logs are not available and so neither impedance logs. A complete reconstruction of the density/IP log can be made if lithology is known. In this case, an integrated approach between all the other available log data allowed the estimation of IP pseudo-logs. A lithostratigraphic interpretation of the sedimentary column was carried out analyzing the single trends of every log curves and the correlation amongst them. Information reported in the well report and headers were used to guide the analysis. Resulting lithostratigraphic columns are shown in Fig.6.8. Rough density profiles ρ_0 were then built for each well, assigning average values to each facies and smoothing the results. They were multiplied by the available velocity logs to get preliminary IP_0 curves. IP_0 were used to calculate reflectivity and to generate synthetic seismograms at well locations. Synthetic seismograms are the convolution between seismic wavelet and reflectivity. Wavelets were statistically extracted in the vicinity of each well, from the near offset stack sections (with the same procedure reported in sec.7.1.2. Then, comparing real and synthetic traces at well locations, IP_0 were adjusted iteratively. Arcobaleno final synthetic trace and comparison with the real trace and final IP pseudo-curves are shown in Fig.6.9.

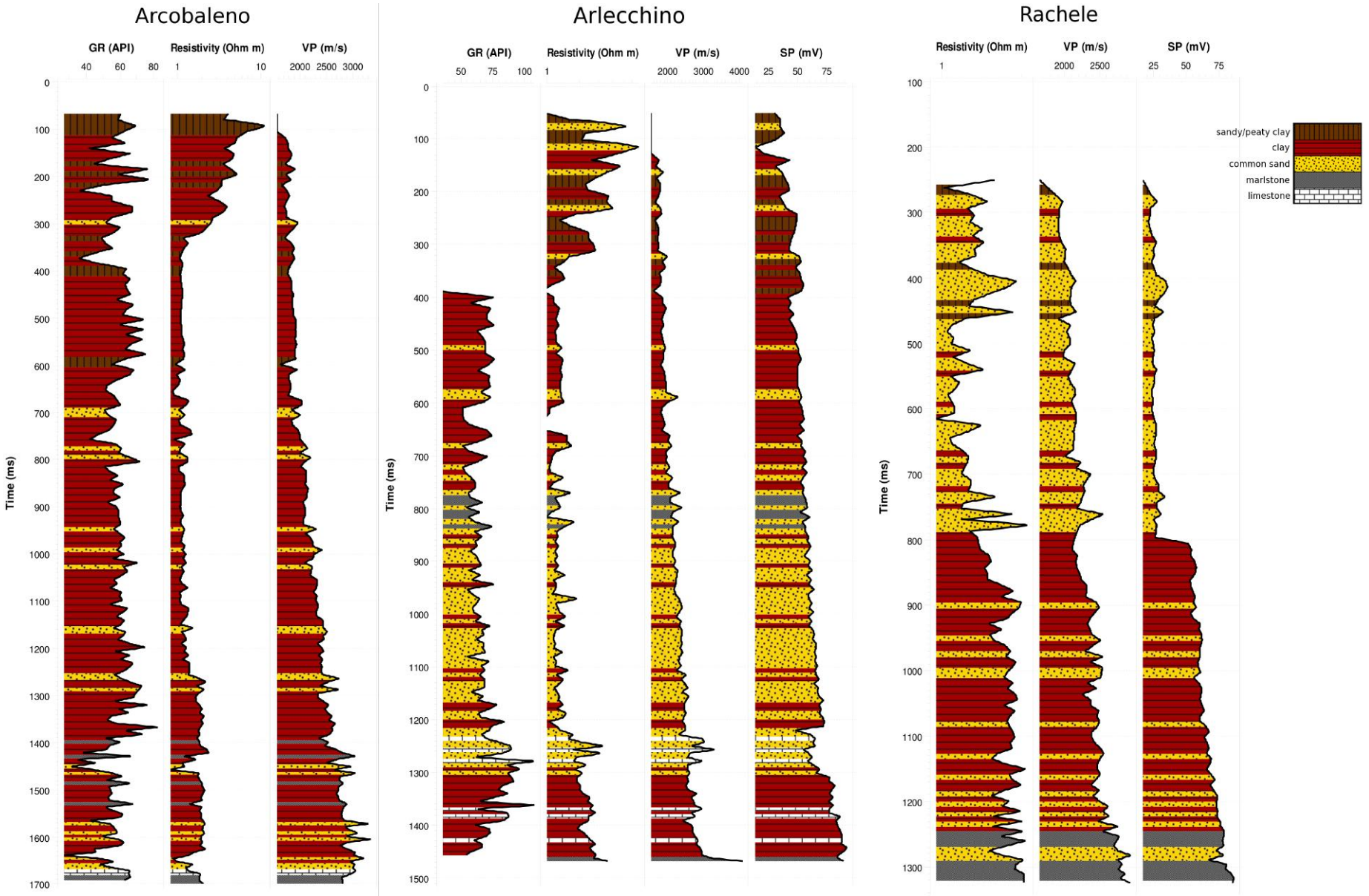

Figure 6.8: Lithostratigraphic columns of the three wells, Arcobaleno, Arlecchino, Rachele. Color scale is reported in the upper right corner.

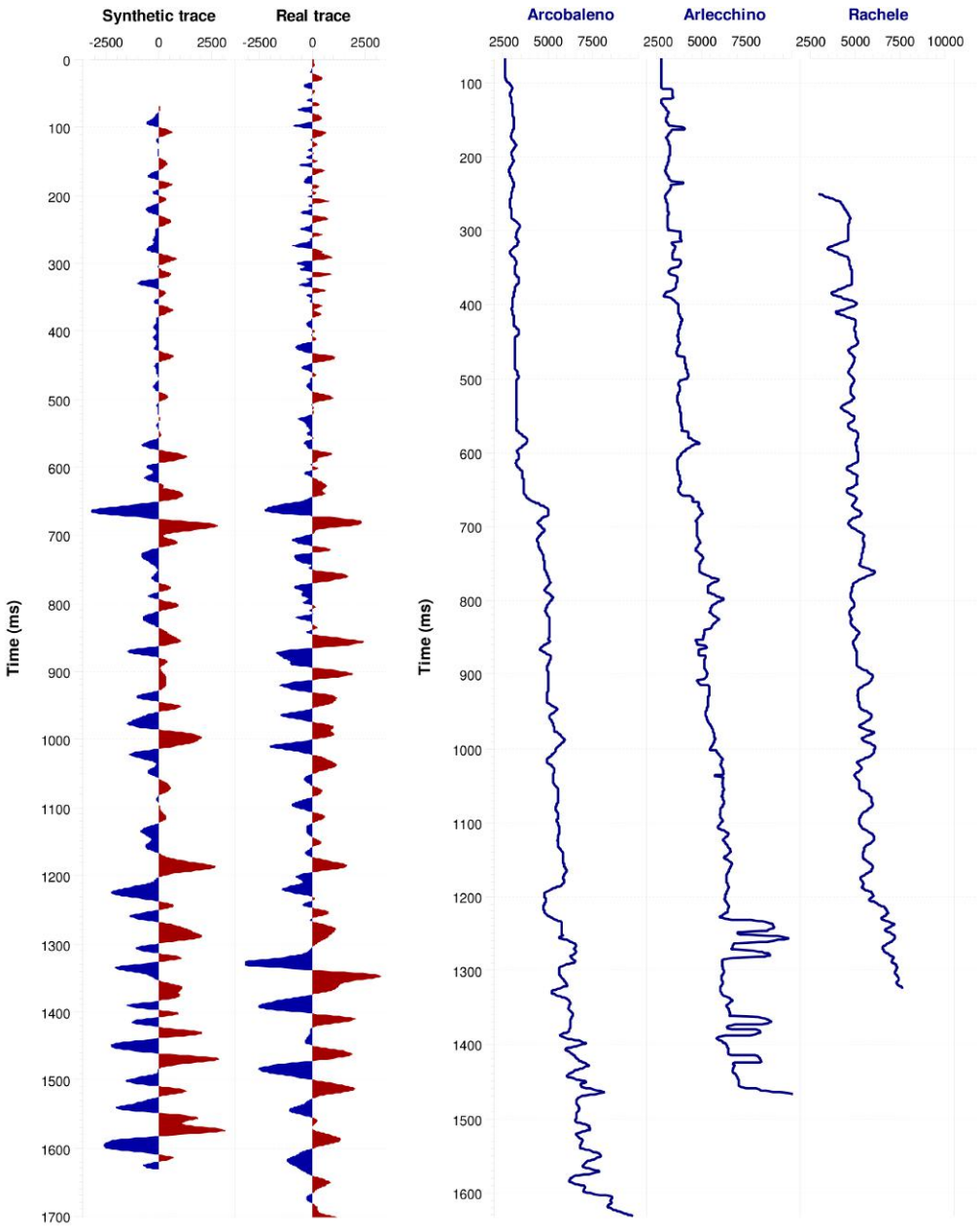

Figure 6.9: Comparison between synthetic and real trace at Arcobaleno well location. On the left, final calculated IP pseudo-logs.

Chapter 7

Stratigraphic inversion

7.1 Theory and methodology

7.1.1 Principles

Stratigraphic inversion combines seismic and log data to produce **impedance sections**.
Impedances are crucial in constraining every kind of reservoir model and they are used in this thesis in two way:

- As input data in the porosity estimation with Effective Medium Modeling (EMT);
- As input data to calculate density in the final gas content quantification (STENAP 08 line).

The performed inversion is based on a **geological 'a priori' model**, which constrains the inversion and reduces the space of solutions (Brac et al., 1988). Furthermore, the coupling between data acquired at different scales (well logs and seismic) gives back a calibrated and wide-bandwidth information.
The whole procedure can be summarized in three steps:

- Well-seismic calibration;
- Creation of an 'a priori' model;
- Inversion.

It is performed using $INTERWELL^{TM}$ software, developed by IFPEN, in post-stack domain, producing P-impedances.

7.1.2 Well-seismic calibration

Well-seismic calibration allows the correlation of seismic data recorded in time-domain and depth-data acquired at high resolution by logging tools. It is aimed to determine the **optimal wavelet** and the **optimal wells-locations** for the considered seismic data. Optimal wavelet and well-positions are the ones minimizing the difference between the synthetic trace calculated at wells and the corresponding seismic ones. The similarity between the two can be quantified with a correlation coefficient and well-positions are adjusted in order to maximize this correlation. A reasonable change of spatial and temporal coordinates is justified by logs and seismic uncertainties. Eventually, assuming the presence of signal dispersion, it is also possible to apply a stretch/squeeze to the logs. However, there were no need to stretch/squeeze log data at this point.

The calibration procedure can be divided in two parts: a multi-coherence analysis, in which a preliminary zero-phase wavelet is defined and the correlation with logs, which estimates the optimal wavelet and well locations.

Multi-Coherence Analysis (MCA)

Multi-Coherence Analysis (MCA) is aimed at:

- Extracting the amplitude spectrum of the wavelet;
- Defining the seismic bandwidth;
- Estimating the seismic S/N.

MCA relies on convolutional model, with the hypothesis of random reflectivity and noise.
Conventionally, a seismic trace is modeled as:

$$x(t) = w(t) * r(t) \tag{7.1}$$

With $x(t)$ the seismic signal, $r(t)$ the reflection coefficient series and $w(t)$ the wavelet. Assuming $r(t)$ white (random reflectivity) and $w(t)$ stationary in time, Fourier transform can be used to analyze the characteristics of the signal. The hypothesis is that two neighboring seismic traces x and y can be modeled as sum of signal and noise. The signal component is the same for both traces:

$$\begin{array}{rcl} x(t) & = & s(t) + n(t) \\ y(t) & = & s(t) + m(t) \end{array} \tag{7.2}$$

$s(t)$ is the signal component we are interested in, whereas $n(t)$ and $m(t)$ are different noise components, independent from $s(t)$ and uncorrelated. All the cross-correlations C involving the noise are null:

$$C_{sn}(\tau) = C_{ns}(\tau) = C_{sm}(\tau) = C_{ms}(\tau) = C_{nm}(\tau) = C_{mn}(\tau) = 0 \tag{7.3}$$

Therefore, the autocorrelation functions can be written as:

$$\begin{array}{rcl} C_{xx}(\tau) & = & C_{ss}(\tau) + C_{sn}(\tau) + C_{ns}(\tau) + C_{nn}(\tau) \\ & = & C_{ss}(\tau) + C_{nn}(\tau) \\ C_{yy}(\tau) & = & C_{ss}(\tau) + C_{sm}(\tau) + C_{ms}(\tau) + C_{mm}(\tau) \\ & = & C_{ss}(\tau) + C_{mm}(\tau) \end{array} \tag{7.4}$$

The cross-correlation functions can be written as:

$$\begin{cases} C_{ss}(\tau) = C_{xy}(\tau) = C_{yx}(\tau) = \dfrac{1}{2}\left[C_{xy}(\tau) + C_{yx}(\tau)\right] \\ C_{nn}(\tau) = C_{xx}(\tau) - C_{ss}(\tau) = C_{xx}(\tau) - \dfrac{1}{2}\left[C_{xy}(\tau) + C_{yx}(\tau)\right] \\ C_{mm}(\tau) = C_{yy}(\tau) - C_{ss}(\tau) = C_{yy}(\tau) - \dfrac{1}{2}\left[C_{xy}(\tau) + C_{yx}(\tau)\right] \end{cases} \tag{7.5}$$

Signal and noise amplitude spectra extraction, and therefore wavelet amplitude spectrum extraction, is based on a **statistical approach**. A large number of traces is taken into account for a more reliable result. C_{signal} is defined as the average of signal auto-correlations of every trace and C_{noise} as the average of noise auto-correlations of every trace. The frequency content of the zero-phase signal (assimilated to the seismic bandwidth) is estimated from the amplitude spectrum of the average signal autocorrelation

function.
The noise to signal ratio is estimated as:

$$SNR_{db} = 10\,log\left(\frac{P_S}{P_n}\right) = 10\,log\left(\frac{C_{signal}(0)}{C_{noise}(0)}\right) \tag{7.6}$$

It's a measure of the uncertainty on the seismic data.
The output of MCA analysis is a **zero-phase wavelet**, with an amplitude spectrum in agreement with the seismic data.

Optimal wavelet estimation

This step is based on the analysis of correlations between synthetic traces and seismic traces in the vicinity of selected wells. For each well, wavelet obtained from MCA is adjusted applying a **time delay**, a **dephasing** and a **normalization coefficient**.
Time delay is calculated for every trace in the vicinity of the selected wells. A preliminary wavelet is convoluted with reflectivity to generate a synthetic trace at well-location. For each trace, delay corresponds to the deviation between maximum of the wavelet auto-correlation and the inter-correlation function envelope between this trace and the synthetic trace. No hypothesis on phase spectrum has to be done at this point. An average delay is applied to every well, defining the origin of convolution between wavelet and reflectivity.
To define the wavelet optimal phase, an ensemble of synthetic traces is created varying the phase from 0° to 360°. For every seismic trace of the ensemble, optimal phase is chosen as the one which maximizes correlation. An average phase is then calculated and applied to every well.
Normalization coefficient is evaluated as the average of the energy ratio between observed and synthetic traces.
The whole procedure is performed interactively, analyzing all the wells at the same time and building a final wavelet consistent with every well and associated at the seismic section of interest.
This procedure/technique allows to obtain a **constant phase wavelet** and its associated *convolution origin* and **time/CDP shifted well logs**.

7.1.3 Model building

After having correctly located well information with the optimal wavelet estimation step (see sec.7.1.2), a geometrical framework is defined and a 'a priori' model is built using a direct stratigraphic modeling procedure. Building such a model helps to constrain inversion and it provides a basic initial structure, low frequency, of inversion parameters.
The model geometry consists in a series of units. The boundaries of these units are defined thanks to the structural seismic interpretation. Then, a **sedimentary depositional mode** is assigned to each unit (parallel to the top, or to the base, or concordant). Finally, correlation surfaces are built with respect to the chosen depositional modes. This ensures the most consistent inversion result with the stratigraphy.
IP logs, filtered and resampled to be consistent with the seismic data, are then extrapolated along these surfaces with an inverse distance weighting[1].
The result is then low-pass filtered, to eliminate all the high frequencies outside the seismic band.

[1]IDW is a type of deterministic method for multivariate interpolation with a known scattered set of points. The assigned values to unknown points are calculated with a weighted average of the values available at the known points. Here weight decreases as distance increases from the interpolated points.

7.1.4 Stratigraphic acoustic inversion

Inversion integrates geological framework, well data and seismic amplitudes to determine an optimal distribution of IP. This methodology is based on a Bayesian formalism: seismic noise and model uncertainties are described by Gaussian probabilities with null expectation value and covariance operator C_D for the space of data and C_M for the space of model (Tonnellot et al., 2010). The objective is to find an **optimal model** which minimizes the **cost function** J, sum of a seismic term J_s and a geological term J_g:

$$J(m) = J_s(m) + J_g(m) \tag{7.7}$$

where m is the actual model.
Optimization is performed iteratively and the 'a priori' model is used as initial model.
The **seismic term**:

$$J_s(m) = \sum_{\theta=1}^{n} \| d_\theta - d_\theta^{obs} \|^2_{C^{-1}_{D_\theta}} = \sum_{\theta=1}^{n} \| d_\theta - d_\theta^{obs} \|^T C^{-1}_{D_\theta} (d_\theta - d_\theta^{obs}) \tag{7.8}$$

is the deviation between the observed seismic data d_θ^{obs} and the synthetic d_θ calculated with the running optimal model. For post-stack inversion, only one seismic section/cube is used, and $n = 1$.
C_D^{-1} is a constant matrix containing the standard deviation of seismic data, meaning that the noise is assumed to be uncorrelated from sample to sample. This assumption is not entirely realistic: as seismic traces are band-limited, the noise will never be an uncorrelated sequence. This value is set to the seismic N/S ratio, evaluated in the MCA (see sec.7.1.2) by spectrum analysis. In practice, it allows tuning the weight of the seismic term.
The **geological term**:

$$J_g = \| m - m^{prior} \|^2_{C_M^{-1}} = (m - m^{prior})^T C_M^{-1} (m - m^{prior}) \tag{7.9}$$

quantifies the difference, at each iteration, between the 'a priori' model m^{prior} and the running optimal model m. The geological term is weighted by the confidence in the 'a priori' model, C_M^{-1}. To quantify this confidence, two parameters have to be defined: the standard deviation of the model IP values (σ_{IP}) and the IP horizontal correlation length λ.

Parameters influence

The N/S ratio, the IP standard deviation σ_{IP} and the IP correlation length λ directly control the inversion cost function J.
They can be interpreted as follows:

- The N/S weights the confidence in the seismic data: the higher is the value, the lower the confidence in the seismic data. If this ratio is high, seismic information is only partially incorporated into the optimal IP distribution, and the optimal model remains close to the initial model: the geology is trusted more than the seismic data. This parameter is expressed as percentage of noise in the data and it can be derived from the MCA;
- The IP standard deviation σ_{IP} weights the confidence in the direct model (geology). The higher the deviation, the less trustworthy is the initial model;
- The IP correlation length λ is linked to the lateral continuity of the impedance distribution. The higher this parameter is, the smoother is the optimal distribution along correlation surfaces.

Several tests have been done to estimate optimal inversion parameters. Two quality tools help to interpret the seismic inversion results. The decreasing of the cost function J and the **residual seismic sections**, difference of the input seismic data and the synthetic seismic data can help in assessing the goodness of the inversion. Residuals must not contain strong coherent events.
It is possible to input additional constraints to the inversion parameters. Minimum and maximum values can be chosen to condition the inversion output in term of IP. It is also possible to compute the inversion using the 'a priori' model only as input model in the algorithm. In such case, results obtained do not depend on the chosen inversion parameters but only on initial IP values of the structures.

7.2 IP final sections

The STENAP 08 and the GANDI 09 seismic lines are inverted using the amplitude preserving processed data. Two different inversions were performed for the STENAP 08 line: a first one for the shallowest part ($0 \div 630\,ms$) and a second one for the deepest part ($500 \div 3000\,ms$). This was required by a strong change both in amplitude and in frequency behavior of the seismic data. Results are then merged, averaging the values at the boundary zone. Furthermore, both STENAP 08 and GANDI 09 were inverted also using the 'a priori' model only as input model (**seismic-driven inversion**), assigning the minimum confidence to the geological interpretation and fully incorporating the seismic information into the optimal IP distribution (including seismic noise). In this way, it is possible to evaluate the residuals (see Fig.7.5 and Fig.7.10) of the inversion calculation, avoiding potential geological misinterpretation.
Inversion parameters and initial IP values are reported in Table 7.1 and Table 7.2. Structures and depositional modes are reported in Fig.7.1, Fig.7.2 and Fig.7.6, Fig.7.7; 'a priori' models are reported in Fig.7.3 and Fig.7.8. Inversion results are reported in Fig.7.4 and Fig.7.9.

Table 7.1: Inversion parameters.

	$\lambda\,(m)$	$\sigma_{IP}\,(g/cm^3 m/s)$	$N/S\,(\%)$	$n\,iterations$
GANDI 09	60	2000	30	30
STENAP 08 shallow	60	2000	50	30
STENAP 08 deep	60	2000	25	30

Table 7.2: Units IP values ($g/cm^3 m/s$).

Unit	1	2	3	4	5	6
GANDI 09	2500	4000	5500	7500	8500	9000
STENAP 08	2500	x	5500	7500	8500	9500

7.2.1 STENAP 08

Fig.7.4 shows how, differently weighting the input model, it is possible to exclude noise without eliminating useful information from the IP results. Indeed, both the general IP trend and the localized anomalies are present in the model-driven version. The residual seismic section (Fig.7.5), calculated using the seismic-driven inversion (Fig.7.4, second panel) shows that only low-frequency and low-amplitude events were not inverted by the algorithm, except for the first part of the line.

In fact, the first 2000 CDPs, characterized by a dense and thin horizontal layering, are not always properly treated. This must be taken into account when such results will be used later in the analysis.

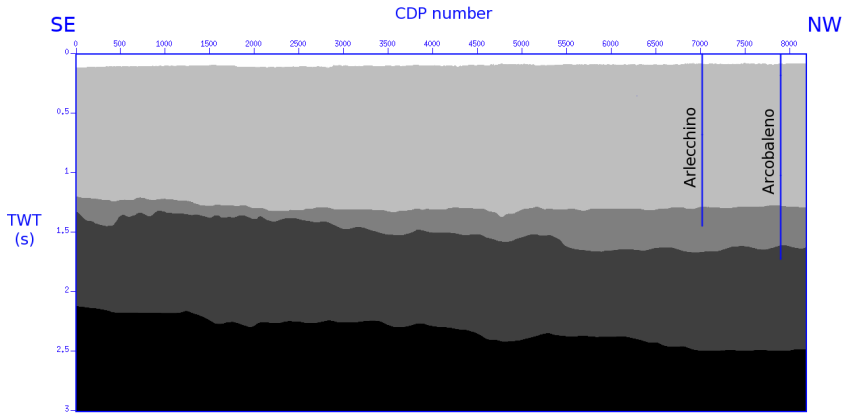

Figure 7.1: STENAP 08 structure. The panel shows the units used to constrain the inversion. To each unit an initial reasonable value is assigned (see Table 7.2). Well locations are shown.

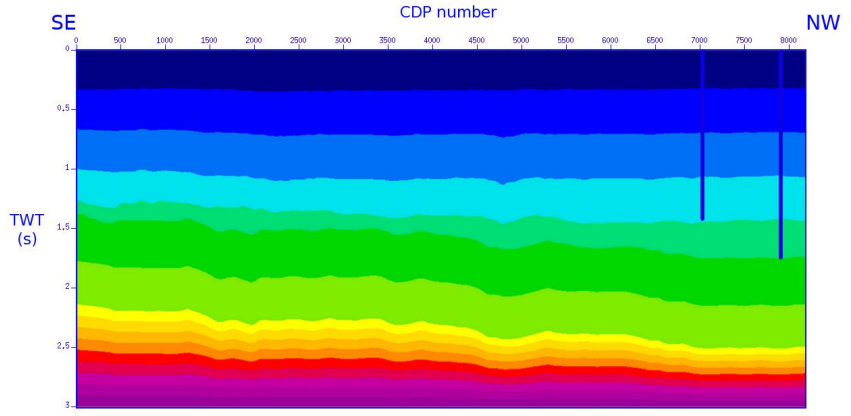

Figure 7.2: STENAP 08 depositional modes modeled for every unit. Well locations are shown.

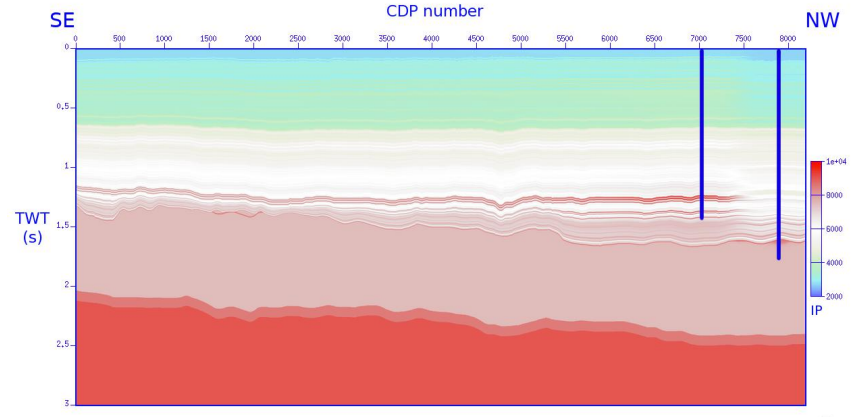

Figure 7.3: STENAP 08 IP 'a priori' geological model. Well locations are shown.

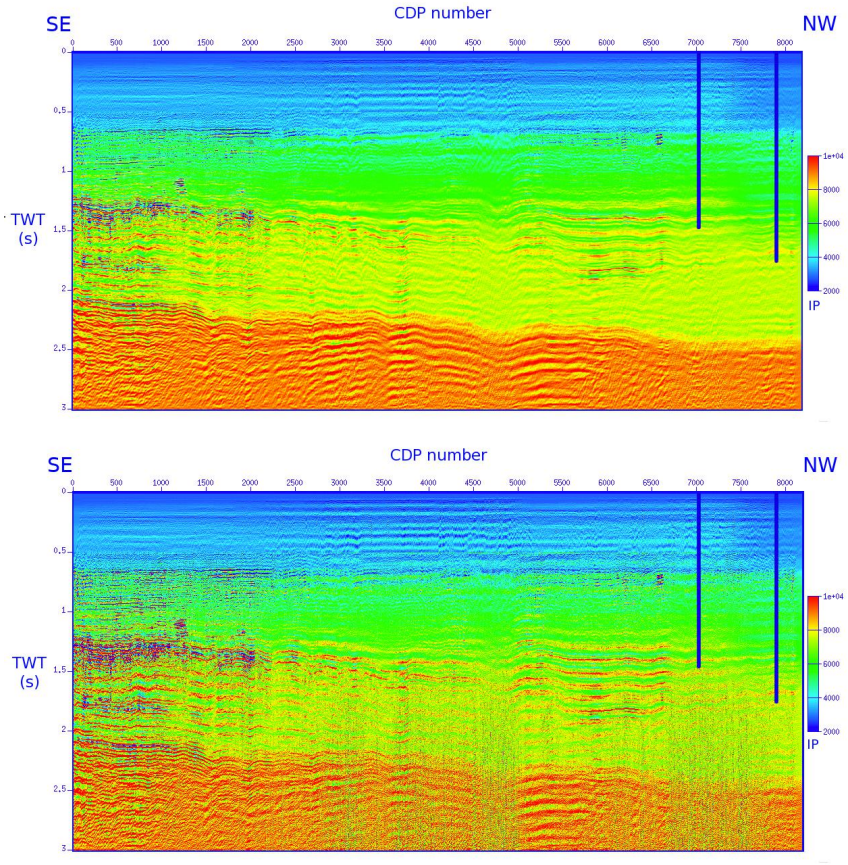

Figure 7.4: STENAP 08 IP inversion results. The first panel refers to the inversion performed with the geological model reported in Fig.7.3 and inversion parameters reported in Table 7.1 (model-driven inversion). The second panel refers to the inversion performed using the 'a priori' model only as input model, independently from the inversion parameters (seismic-driven inversion). Well locations are shown.

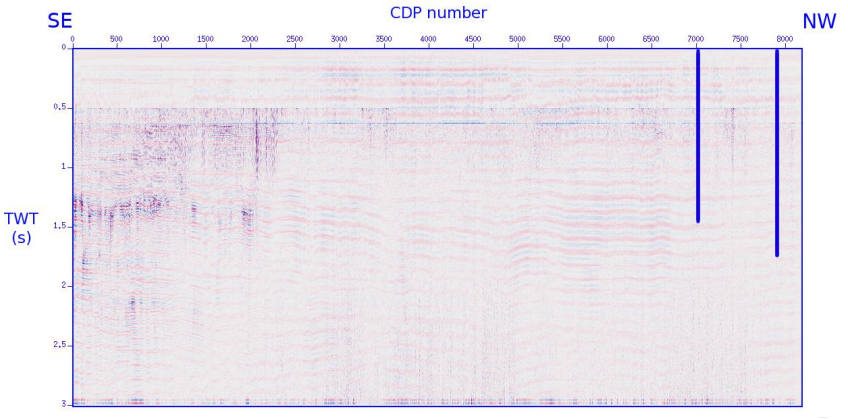

Figure 7.5: STENAP 08 residual seismic section. Well locations are shown.

7.2.2 GANDI 09

GANDI 09 IP sections are reported in Fig.7.9, here presented up to 2.5 *s* TWT. Seismic data are characterized by various amplitude-related critical issues, including poor fold coverage. This affects the inversion, leading to a possible misinterpretation of anomalies. However, the general IP trend, recognizable both in the seismic-driven and in the model-driven inversions, can be considered reliable.

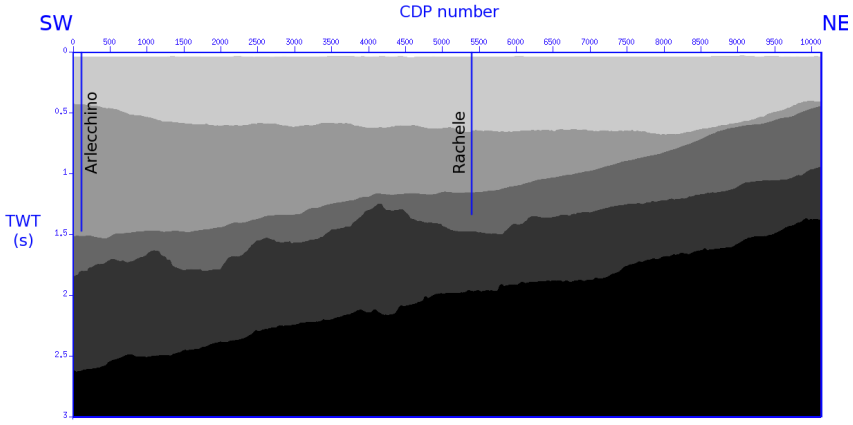

Figure 7.6: GANDI 09 structure. The panel shows the units used to constrain the inversion. To each unit an initial value is assigned. Well locations are shown.

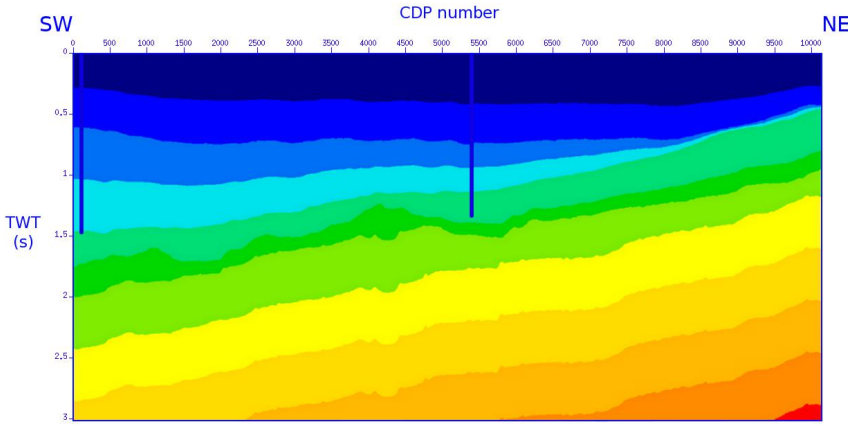

Figure 7.7: GANDI 09 depositional modes modeled for every unit. Well locations are shown.

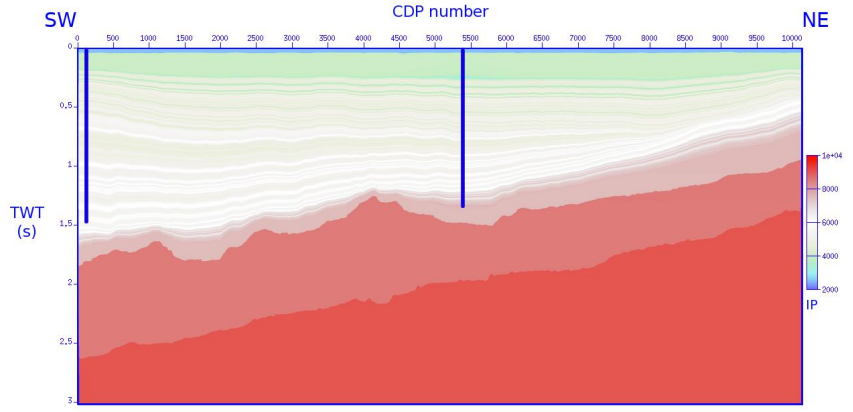

Figure 7.8: GANDI 09 IP 'a priori' geological model. Well locations are shown.

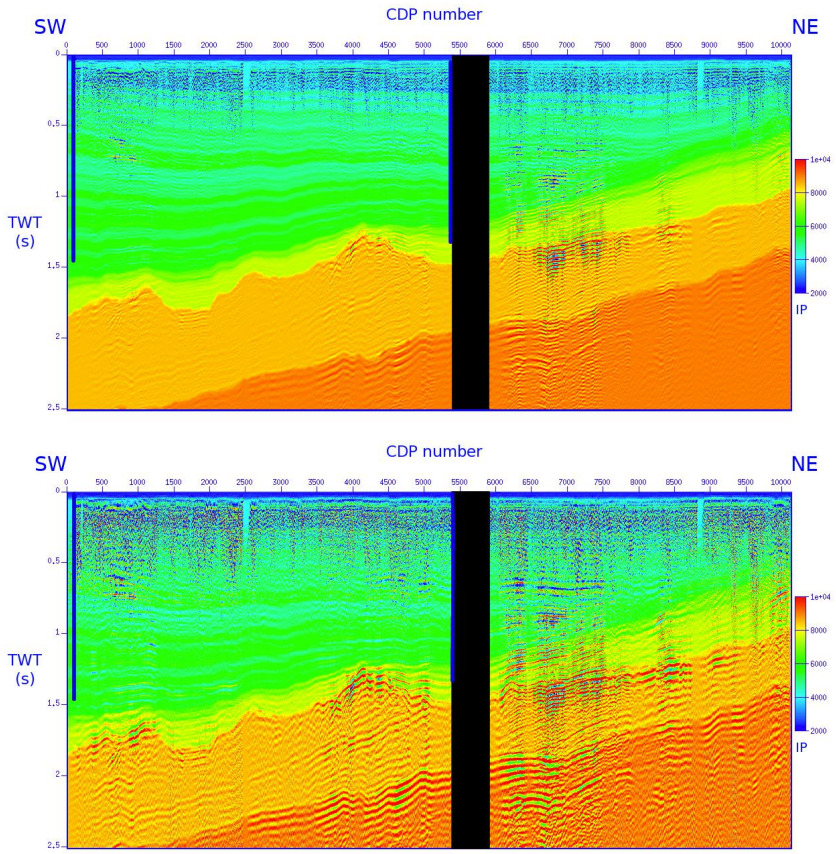

Figure 7.9: GANDI 09 IP inversion results. The first panel refers to the inversion performed with the geological model reported in Fig.7.8 and inversion parameters reported in Table 7.1 (model-driven inversion). The second panel refers to the inversion performed using the 'a priori' model only as input model, independently from the inversion parameters (seismic-driven inversion). Black box indicate area with no coverage. Well locations are shown.

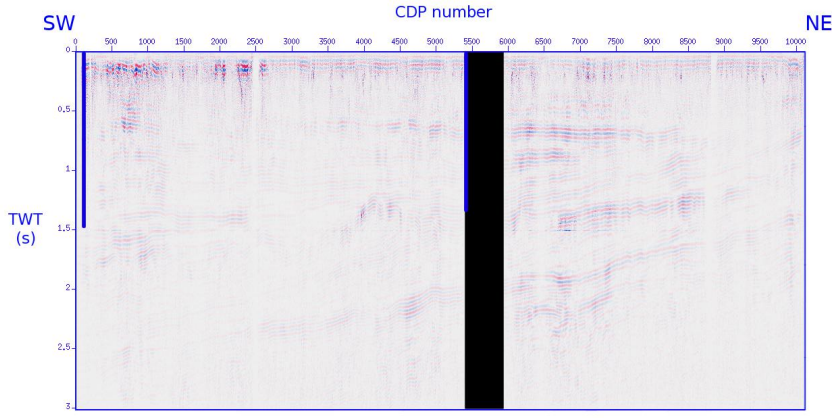

Figure 7.10: GANDI 09 residual seismic section. Black box indicate area with no coverage. Well locations are shown.

Chapter 8

Porosity estimation

8.1 Porosity estimation through effective medium theory (EMT)

The effective medium theory (EMT) relies on a representative elementary volume (REV), i.e. the smallest volume over which a property is considered as a representative value for the whole material (Adelinet et al., 2011). The EM model used in this thesis is an homogenization approach based on Eshelby's inclusion theory (Eshelby, 1957). Eshelby (1957) proposes one ellipsoidal inclusion embedded within an infinite medium and evaluates the disruption in the strain field in the medium due to this inclusion. He showed that for general homogeneous conditions imposed in the far-field, the strain set up inside an isotropic homogeneous ellipsoidal inclusion is uniform.
According to Eshelby's theory, the strain tensor E^i in the inclusion i can be written as:

$$E^i = (I + P : (C^i - C^0))^{-1} : \sigma^{inf} \tag{8.1}$$

where C^i and C^0 are the elastic tensors for the inclusion and the matrix respectively. I is the identity tensor, P is the Hill polarization tensor and σ^{inf} is the stress field far away from the inclusion.

A homogenized Eshelby's model considers a medium composed by a matrix and a given amount of inclusions. Evaluating the elastic properties of this medium is evaluating the macroscopic elasticity at the REV scale. In this case, the self-consistent scheme is used (Budiansky and O'Connell, 1976).
Knowing the homogenized elastic moduli, P-wave and S-wave velocities can be derived at the REV scale using Christoffel's equation:

$$|| \Gamma_{ik} - \rho(v_{model})^2 \delta_{ik} || = 0 \tag{8.2}$$

where Γ_{ik} is the symmetrical Christoffel matrix, δ_{ik} is the Kronecker symbol, ρ is the matrix density and v_{model} is the velocity. Subscript i and k correspond to the three directions of space. This is the **forward problem**. Solutions of Eq.8.2 are P-wave, slow S-wave and fast S-wave velocities. These can be transformed into impedances to be relevant with seismic data.
The **inverse problem** estimates the micro-structural parameters from the known impedances IP (or velocities). This is achieved minimizing an objective function J defined as:

$$J(x) = \left(1 - \frac{IP^2_{model}(x)}{IP^2_{known}}\right)^2 \tag{8.3}$$

IP_{model} and $v_{P_{model}}$ can be calculated using elastic moduli, for example bulk modulus K and shear modulus G in an isotropic case:

$$v_P = \sqrt{\frac{K + 4/3G}{\rho}}, \qquad IP = \rho \cdot v_P \tag{8.4}$$

where ρ is the density of the medium.
J is the misfit between the known squared IP (or velocities) and the corresponding numerical response. Vector x represents the unknown parameters, in this case porosity. If both P-wave and S-wave velocities are available it is possible to infer also another micro-structural parameter, such as the crack density (Adelinet et al., 2011; Adelinet and Le Ravalec, 2015). The minimization process is iterative, J is computed for an initial set of parameters and the gradients are determined using classical techniques (Le Ravalec et al., 2014).

EMT was used in two cases:

1. To estimate the porosity at the wells location using the sonic logs (see subsec.8.1.1);
2. To estimate the porosity along the STENAP 08 and the GANDI 09 lines (see subsec.8.1.2) using impedance sections derived from stratigraphic inversion of the seismic data (see chap.7).

More details about how the model have been used are reported in subsec.8.1.1 and subsec.8.1.2.

It is important to underline that inclusion-based EMT models should be used to estimate high-frequency elastic moduli related to unrelaxed states. To compare these results with seismic-derived data it is necessary to transfer them from high to low frequency domain. Saturated media moduli depend on frequency and they need the application of Biot-Gassmann equations (Adelinet et al., 2011). However, to build a first approximate model, low frequency effects are not taken into account. This is very important to remember for results evaluation, which has to be qualitative.
Further available data on micro-structure of materials involved could allow a more precise analysis, considering the transition between high and low frequency domain.

8.1.1 Porosity estimation at wells location

The facies interpreted using information from the available logs (subsec.6.3) were modeled considering a solid matrix and a porous part. A mineral composition was supposed for the solid matrix and the correspondent elastic moduli (bulk modulus K_s and shear modulus G_s) were calculated, using Eq.8.5. Pores are considered ellipsoidal with a constant aspect ratio by facies (see Fig.8.1).

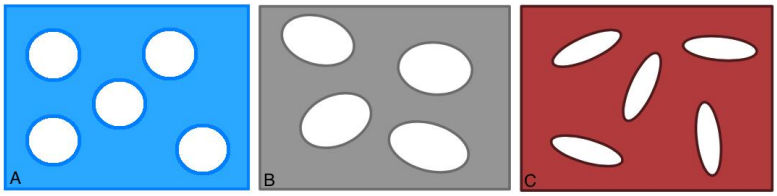

Figure 8.1: Simple model of the isotropically distributed pore inclusions. A) Spherical pores (aspect ratio=1) for facies/unit 3 (sandstone) and facies/unit 5 (limestone); B) Quasi-spherical pores (aspect ratio=0.5) for facies/unit 4 (marlstone); C) Ellipsoidal (aspect ratio=0.1) pores for facies/unit 1 (sandy clay) and facies/unit 2 (clay1).

For every facies and every well, a mixed-fluid totally saturating the pores was assigned. Mixed-fluid was assumed using information about the gas saturation from the well reports at sparse depths. The pore fluid bulk modulus of the mixed-fluid was calculated using Eq.8.6.

The bulk modulus of a solid matrix composed of solid 1 and solid 2 with saturations s_1 and s_2 is:

$$\frac{1}{K_s} = \frac{1}{2}\left(\frac{s_1}{K_1} + \frac{s_2}{K_2}\right) + \frac{1}{2}\left(s_1 \cdot K_1 + s_2 \cdot K_2\right)^{-1} \tag{8.5}$$

and analogously for the solid shear modulus G_s (Tinivella, 1999).
The pore fluid bulk modulus of a mix of salt water sw and a gas g with saturations s_{sw} and s_g is:

$$\frac{1}{K_f} = \frac{s_{sw}}{K_{sw}} + \frac{s_g}{K_g} \tag{8.6}$$

Table 8.1 shows the mineral composition and the elastic moduli assigned to the interpreted facies. Moduli are calculated with Eq.8.5 using mineral values reported in Table 8.2. 'Common sand' values are revised by Vernik and Kachanov (2010). Table 8.2 reports elastic moduli of some key minerals, from literature.

Table 8.1: Mineral composition, bulk modulus (K_s) and shear modulus (G_s) of the solid matrix composing the 5 facies considered.

	Facies 1 (Sandy clay)	Facies 2 (Clay1)	Facies 3 (Common sand)	Facies 4 (Marlstone)	Facies 5 (Limestone)
Mineral composition	70% Clay1 30% Common sand	40% Illite 35% Smectite 25% Kaolinite	Quartz	60% Calcite 40% Clay1	100% Calcite
K_s (GPa)	20.06	15.45	35.6	40.35	75.50
G_s (GPa)	10.55	5.51	33	15.84	39.39

Table 8.2: Bulk modulus (K_s) and shear modulus (G_s) of some key minerals.

	K_s (GPa)	G_s (GPa)	Reference
Illite	27	17	(Greenberg and Castagna, 1992)
Smectite	9	1.5	(Mondol et al., 2008)
Kaolinite	13	3	(Mondol et al., 2008)
Quartz	36	44	(Greenberg and Castagna, 1992)
Feldspar	48	24	(Wang, 2001)
Calcite	75	31	(Greenberg and Castagna, 1992)

Table 8.3 reports the pore fluid bulk modulus K_f of the considered facies. Values are calculated with Eq.8.6 using K_{sw} = 2.3 GPa for salt water and K_{CH4} = 0.024 GPa for CH_4.

Table 8.3: Pore fluid bulk modulus (K_f) of the considered facies.

	Facies 1	Facies 2	Facies 3	Facies 4	Facies 5
Arcobaleno	97% sw 3% CH_4 K_f = 0.6 GPa	96% sw 4% CH_4 K_f = 0.48 GPa	92% sw 2% CH_4 K_f = 0.79 GPa	99% sw 1% CH_4 K_f = 1.18 GPa	99.5% sw 0.5% CH_4 K_f = 1.56 GPa
Arlecchino	91% sw 9% CH_4 K_f = 0.24 GPa	90% sw 10% CH_4 K_f = 0.22 GPa	92% sw 8% CH_4 K_f = 0.27 GPa	99% sw 1% CH_4 K_f = 1.18 GPa	99.5% sw 0.5% CH_4 K_f = 1.56 GPa
Rachele	98% sw 2% CH_4 K_f = 0.79 GPa	97% sw 3% CH_4 K_f = 0.6 GPa	99% sw 1% CH_4 K_f = 1.18 GPa	99.5% sw 0.5% CH_4 K_f = 1.56 GPa	99.5% sw 0.5% CH_4 K_f = 1.56 GPa

From these facies distribution, impedance logs were inverted into porosity. Two different inversions were performed: the first assuming a fully water saturated medium and the second one considering a mixed-fluid. The minimum value reached by the cost function J was used to check the accuracy of the minimization process.

8.1.2 Porosity estimation along STENAP 08 and GANDI 09 seismic lines

EMT was applied using as input the impedance sections inverted from the seismic data (see chap.7).
The horizons recognized in the seismic data during the inversion process were used to discriminate 5 units, considering for each of them the same mineralogical composition used for the 5 facies previously described (see Table 8.4 and Table 8.5). A density value was assigned to each unit, on the basis of the interpreted associated lithology, taking into account the consolidation effect (Table 8.4 and Table 8.5). As in the previous case, two different inversions were performed, the first assuming a fully water saturated medium and the second one considering a mixed fluid (water+methane) assumed for every unit (laterally averaging on some punctual gas saturation values taken from well reports).

Table 8.4: Density values ρ for the five units identified by the horizons picked on the STENAP 08 seismic line.

	Unit 1 (Sandy clay)	Unit 2 (Clay1)	Unit 3 (Common sand)	Unit 4 (Marlstone)	Unit 5 (Limestone)
$\rho\,(kg/cm^3)$	1.8	2	2.5	2.6	2.8
K_f (GPa)	0.42	0.35	0.53	1.18	1.56

Table 8.5: Density values ρ for the five units identified by the horizons picked on the GANDI 09 seismic line.

	Unit 1 (Sandy clay)	Unit 2 (Clay1)	Unit 3 (Common sand)	Unit 4 (Marlstone)	Unit 5 (Limestone)
$\rho\,(kg/cm^3)$	1.8	2	2.5	2.6	2.8
K_f (GPa)	0.24	0.41	0.72	1.37	1.56

8.1.3 Results

Porosity at well location

Fig.8.2 shows porosity curves calculated at wells locations. Both fully water-saturated sediments and mixed fluid-saturated sediments porosities are drawn. The two curves are almost parallel and tend to coincide at deeper depths. Water-saturated porosity values are always higher than mixed fluid values. Such curves were considered a good representation of porosity at wells locations and they were correlated with the seismic data (see chap.9) to perform the final gas quantification.

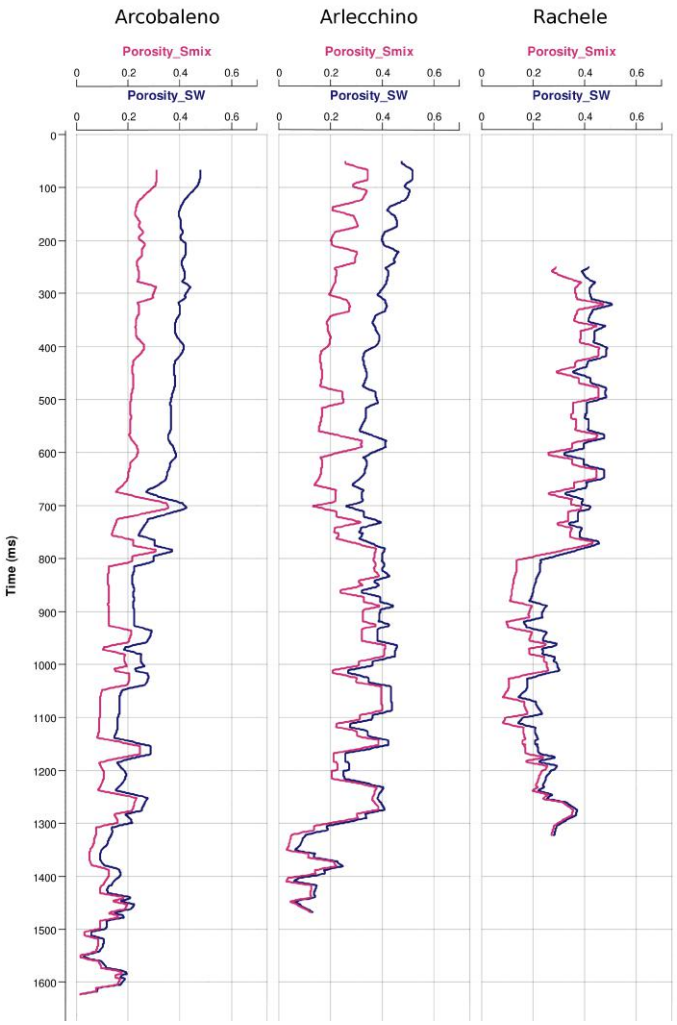

Figure 8.2: Porosity estimated through EMT at wells locations. Porosities of fully water-saturated sediments are reported in blue, porosities of mixed fluid-saturated sediments are reported in magenta.

STENAP 08 and GANDI 09 porosity results

Result of EMT along the two seismic lines, assuming a mixed-fluid fully saturated medium, are reported below (Fig.8.3 and Fig.8.4). They are clearly strongly guided by the facies modeling, and possibly also by IP modeling, even if minimum weight was assigned to the geological model (see chap.7). Porosity shows a peculiar behavior in both lines, with a 800 ms-thick unit characterized by anomalous low porosity values. Furthermore, the two results are not consistent. For all these reasons they were not considered reliable and they were not used later in the analysis. Instead, EMT porosity at wells location (see Fig.8.11) were the ones used in gas quantification.

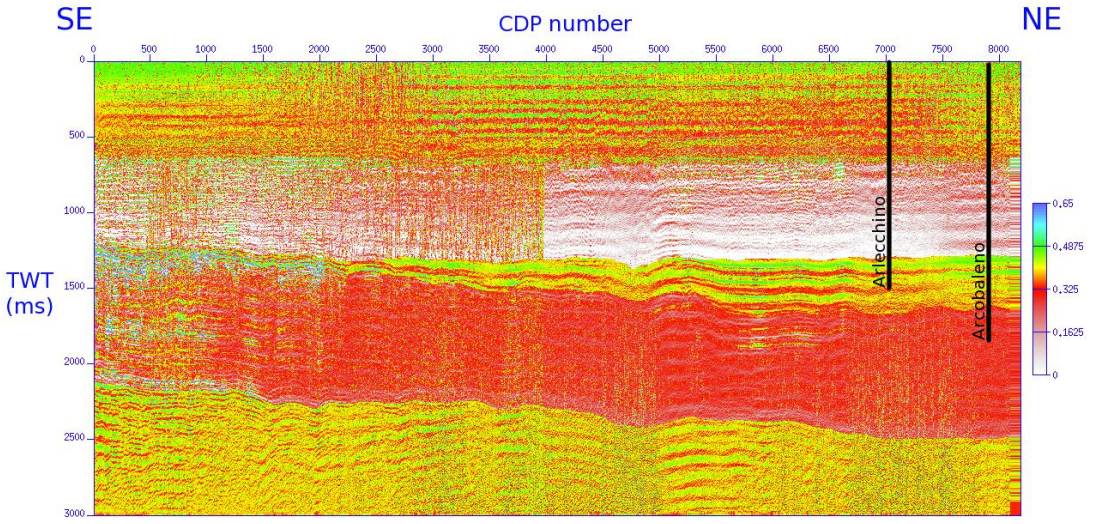

Figure 8.3: EMT STENAP 08 porosity section. Well locations are shown.

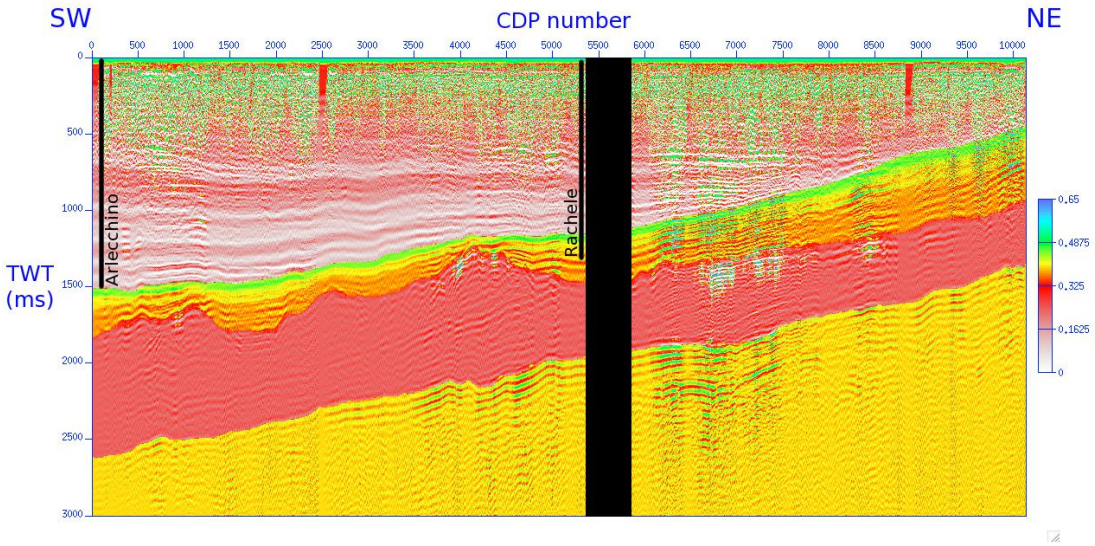

Figure 8.4: EMT STENAP 08 porosity section. Well locations are shown.

8.2 Porosity estimation at well locations with Archie's law

Porosity at wells location was estimated.
In the case of a partially water saturated rock, Archie empirically demonstrated that the resistivity of a rock can be linked to the resistivity of the fluids saturating the rock, knowing the porosity of the formation and the fractional degree of saturation of each fluid present (see Appendix C for details).
This relationship is described by the following equation:

$$R_t = R_w \, \phi^{-m} \, S_w^{-n} \tag{8.7}$$

where:

R_t is the bulk resistivity of a rock partially saturated with an aqueous fluid
R_w is the aqueous fluid resistivity
ϕ is the total porosity of the rock
S_w is the fractional water saturation of the rock
n is the saturation exponent
m is the cementation index

From Eq.8.7 porosity can be written as:

$$\phi = \left(\frac{R_w}{R_t} \, S_w^{-n} \right)^{\frac{1}{m}} \tag{8.8}$$

Assuming m and n constant and errorless and S_w measured with negligible errors, porosity uncertainties can be written as:

$$\frac{\Delta\phi}{\phi} = \left| -\frac{1}{m} \right| \left(\frac{\Delta R_t}{R_t} + \frac{\Delta R_w}{R_w} \right) \tag{8.9}$$

Porosity at wells locations was calculated using Eq.8.8 and the related uncertainties using Eq.8.9.
R_t and ΔR_t are represented by the resampled resistivity logs obtained in chap.6. R_w and ΔR_w, normally measured on extracted fluid samples, are estimated using Rachele borehole, spontaneous-potential (SP) log and all the information available on logs headers concerning drilling muds and extracted fluid-samples, as explained in subsec.8.2.1. m and n values comes from the literature. Sources for input parameters are reported in Table 8.6.

Table 8.6: Sources for input parameters of Eq.8.8 and Eq.8.9.

Parameter	**Source**
R_t, ΔR_t	Resistivity log
R_w, ΔR_w	From SP log, mud resistivity and T
m	2 (from literature)
n	1.9 (from literature)

8.2.1 R_w estimation: spontaneous potential log-method

One of the uses of SP log is the determination of R_w, resistivity of the aqueous fluid saturating the pores. This is one of the quantitative use of SP log and it is very useful when no formation water samples are available to obtain R_w.
There are three methods to estimate R_w using SP log, the most common is called *Quick-Look Method*. It does not require any knowledge of Q_v (clay/shale content)[1] and it doesn't take into account the presence of electrokinetic potentials. For these reasons it is to be used with caution. The other possible procedures are the *Single Chart Method* (same approximations as the *Quick-Look Method*) and the *Smith Method* (the most accurate ones, which considers both electrokinetic potentials and the effect of shaliness of the formation, but does not account for the possible presence of hydrocarbons). The *Quick-Look Method* procedure is applied to Rachele borehole, which crosses a 560 *m*-thick sandy formation between 380 *m* and 940 *m* depth (see Fig.8.5). The average formation temperature is $30°C$. All the information about the drilling mud comes from the log header. Invasion is neglected, with the result of overestimating resistivity in the first hundreds of meters. This can be justified because filtrate resistivity is supposed to be very similar to the ones of the formation. In fact, the drilling mud was water-based, with salinity < 10 g/l $NaCl$. The procedure is described in Rider (1996) and reported in diagram 8.6. Input parameters are reported in Table 8.7.

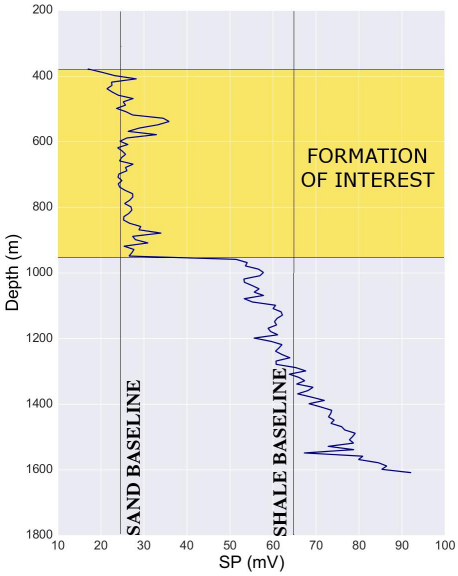

Figure 8.5: Rachele SP log. The sandy formation used to infer Rw is highlighted in yellow. Sand and shale baseline are reported in black.

Table 8.7: Parameters used in the *Quick-Look Method*.

Parameter	**Value**
Formation of interest	Sand, 560m-thick
SP in the center of formation of interest	25 mV
Formation temperature	$30°C$
Mud resistivity, R_m@$55°C$	$0.044\,\Omega m$
Mud Filtrate resistivity, R_{mf}	$R_{mf} = R_m$

[1]The present understanding of the electrical effect of clays in reservoir rocks depends largely upon the concept of cation exchange capacity, Q_v, which is the cation concentration in milliequivalents of exchange sites for sodium ions per cubic centimeter of pore volume. To use this method a value of Q_v is needed from the shale beds above or below the formation of interest, and a value of Q_v for the formation of interest. These values are normally obtained from standard chemical methods carried out in the laboratory upon cores or sidewall cores. Note that in petrophysics the terms clay and shale are used interchangeably.

The whole procedure was carried out to estimate R_w in absence of extracted and analyzed fluid samples. Actually, in some of the boreholes of the study area, drilling companies had extracted and analyzed some fluids. In Amanda borehole, two fluid samples were extracted, both of them at around 6000 m depth, and its salinities measured. This fluid permeates a deep limestone formation and it's not possible to assess which processes it had gone through. The different temperature-pressure conditions and the different dynamics make these samples unreliable to assess the resistivity of the fluid of interest, the ones permeating the first 2000 m of depth. Anyway, the two salinity values reported in Amanda were averaged and corrected for the depth using Fig.8.7. The result is $R_w = 0.218$, in agreement with the value found using the *Quick-Look Method*. The chart used in the R_w estimation are reported in Fig.8.9, Fig.8.10, Fig.8.8, Fig.8.7. The sandy formation used to infer R_w is highlighted in Rachele SP log (see Fig.8.5).
The final estimated porosity curves are reported in Fig.8.11.

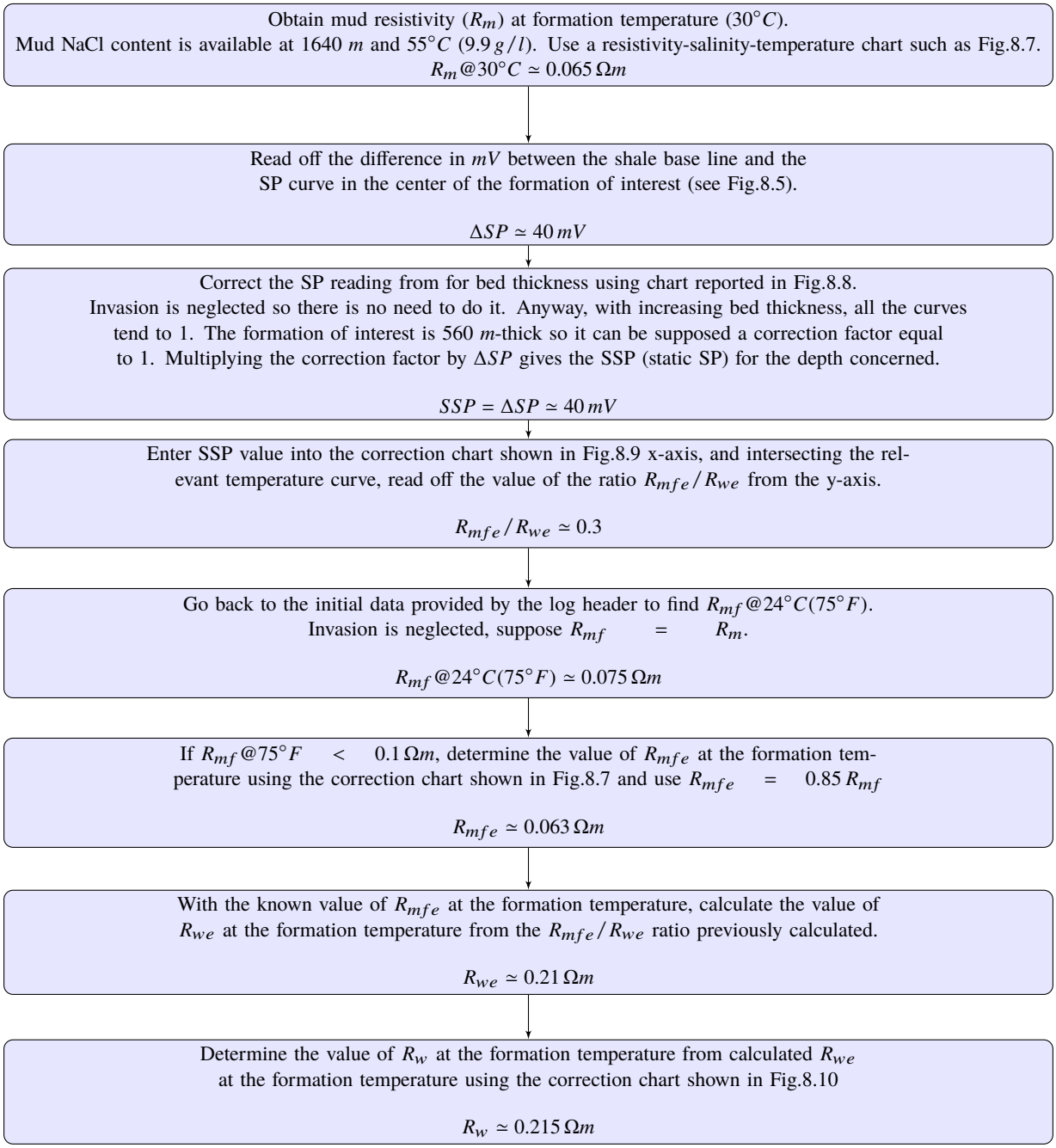

Figure 8.6: Flow diagram for R_w estimation.

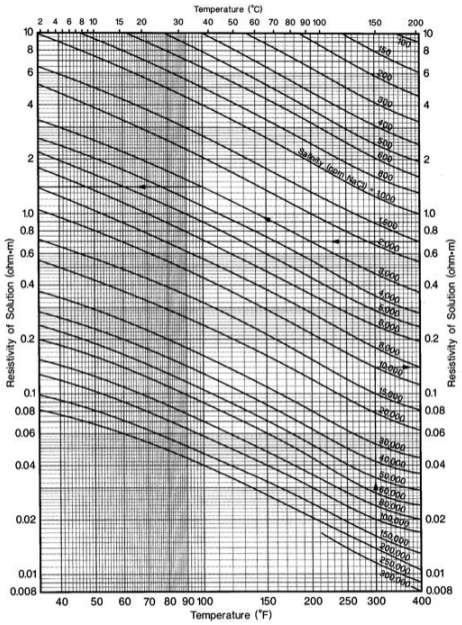

Figure 8.7: Correction chart for fluid resistivity-salinity-temperature. From Schlumberger (1991).

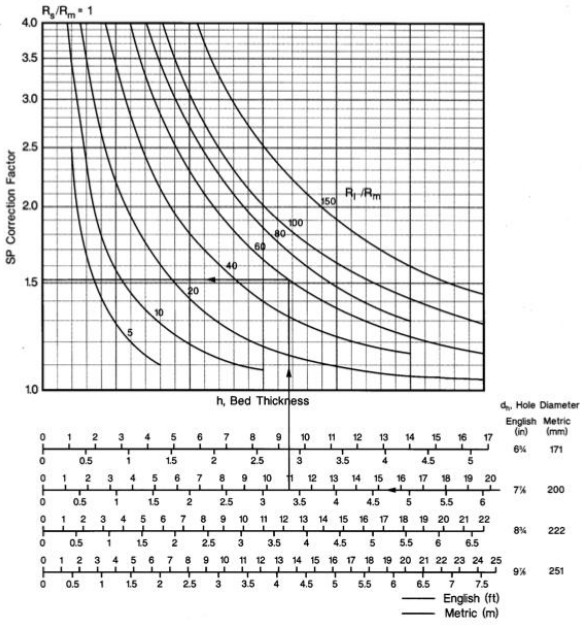

Figure 8.8: Correction chart bed thickness for diameter of invasion equals twice the borehole diameter. For this thesis, it is only important to notice that all the curves tend asymptotically to 1. From Schlumberger (1991).

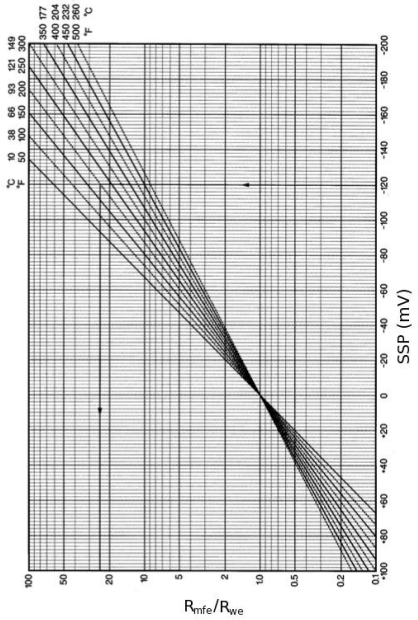

Figure 8.9: Correction chart for the R_{mfe}/R_{we} ratio from SSP for various formation temperatures. SSP represents the ideal spontaneous potential that would be observed opposite a permeable bed if the SP currents were prevented from flowing and any shaliness in the bed were ignored. From Schlumberger (1991).

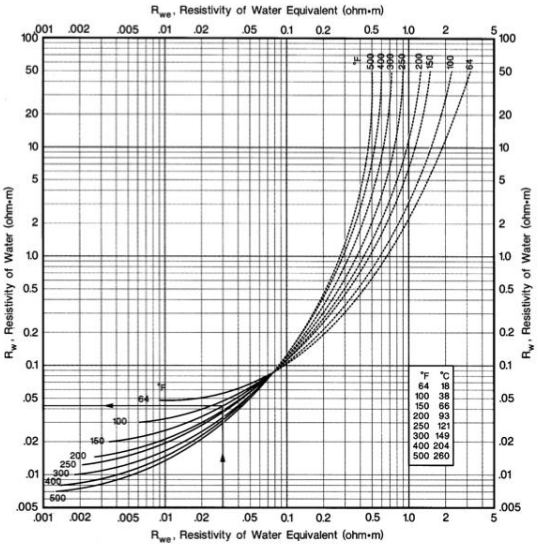

Figure 8.10: Correction chart for the R_w from R_{we} for various formation temperatures. From Schlumberger (1991).

8.2.2 Results

In Fig.8.11 porosities at wells location are shown. It clearly appears that Archie-porosity is strongly guided by the **resistivity response**, which correctly represents the variation of the fluid characteristic with depth (a peculiarity in the study area). Since no direct measurements of water saturation and pore water resistivity are available, Archie porosity itself is not a good indicator of the trend with depth, which should not distinguish among the fluids present within the formation. For this reason EMT porosity at wells locations (Fig.8.2) is considered more reliable and it was used in the following analysis.

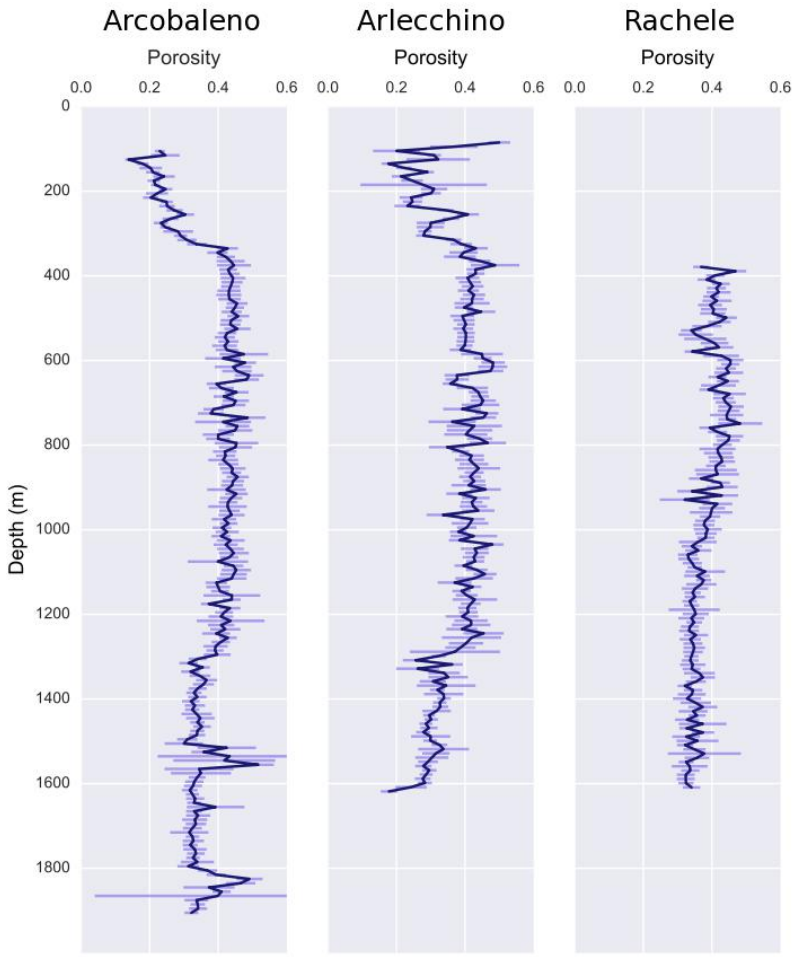

Figure 8.11: Estimated porosity at wells locations, with error-bars propagated from the resistivity uncertainties.

Chapter 9

Multi-attribute analysis

Starting from the well log information, the spatial distribution of petrophysical properties has been imaged along the two seismic profiles, by using seismic and a wide family of seismic-derived attributes as a guide, using CGG $EMERGE^{TM}$ commercial software. Seismic attributes can be defined as all properties contained in seismic, derived after considering the seismic trace as the actual components of a complex seismic trace (Taner et al., 1979). The basic attributes are instantaneous amplitude, instantaneous phase and instantaneous frequency, and many other attributes can be derived from these (Barnes, 1998). The seismic-log correlation is based on a generalized multiple linear regression equation, which is solved by least-square minimization to find the best set of attributes (and weights) which best describe the log data. Seismic is trained to predict the rock parameter of interest at tie locations and then the resulting function is applied to the whole seismic profile, generating a target log predicted section.
P-wave velocity, porosity and resistivity logs available or derived at wells were extrapolated along the analyzed seismic lines, resulting in the related sections. Porosity and resistivity were used to quantify the gas content.

9.1 Theory and methodology

Linear regression is a linear approach to model the relationship between a dependent variable and one or more independent variables (predictors). The case of one single predictor is called simple linear regression, for more than one predictors, the process is called multiple linear regression. Models which depend linearly on their unknown parameters are easier to fit than non-linear models and they are often fitted using the least-squares approach.
Prediction of a single log parameter P from M input attributes can be written as:

$$P = w_0 + w_1 a_1 + ... + w_M a_M \tag{9.1}$$

where a_i is the i-th attribute, w_0 is a constant shift and w_i the i-th weight. w_0 and w_i are the unknown variables.
At each time sample, the target log property can be modeled as a linear combination of several attributes, in matrix form:

$$\mathbf{P} = \mathbf{AW} \tag{9.2}$$

where P is the N-dimensional target property vector, W is the N-dimensional weight vector and A the MxN-dimension attributes matrix:

$$P = \begin{bmatrix} p_1 \\ \vdots \\ p_n \end{bmatrix} \qquad W = \begin{bmatrix} w_1 \\ \vdots \\ w_n \end{bmatrix} \qquad A = \begin{bmatrix} a_{11} & \dots & a_{1m} \\ \vdots & \vdots & \vdots \\ a_{m1} & \dots & a_{nm} \end{bmatrix}$$

This can be solved by least-square minimization to give $\mathbf{W}$:

$$\mathbf{W} = [\mathbf{A^T A}]^{-1} \mathbf{A^T P} \tag{9.3}$$

where w_i are the ones which minimize the total prediction error E:

$$E = \sqrt{\frac{1}{N} \sum_{i,j=1}^{N,M} \left(p_i - w_0 - w_j A_{ij} \right)^2} \tag{9.4}$$

Regression Eq.9.3 is solved step by step: the best single attribute is found by trial and error, calculating the prediction error E. Then, the best pair of attributes is found, keeping fixed the first attribute previously determined. Attributes are added until E is sufficiently small. By increasing the order of polynomial, the value of E decreases, but it can lead to worse result in interpolating and extrapolating beyond the limits of the data.
To determine the validity of attributes, we used the procedure reported in Coren et al. (2001):

- Divide the entire data set into two groups:
  - Training data set, that is the data used to perform the analysis;
  - Validation data set, that is the data used to verify the analysis.
- Determine coefficients by regression, using the training data set;
- Measure the prediction error, using the validation data set.

In this case, only two wells were available for each seismic line. One of them was used as validation dataset and the other as training dataset.
Well logs were manually calibrated to the seismic data, extracting the most reliable wavelet from near-offset fields and applying a stretch to the logs in order to maximize the correlation between the seismic trace and the synthetic P-velocity. Then, 10 sample data trace around well locations were extracted to find a relationship between the seismic attributes at those locations and the measured logs. Eq.9.3 was solved for regression coefficients and prediction error was calculated at the first well. Then, the process was repeated iteratively for all wells to optimize the order of polynomial and the number of attributes to consider. Fig.9.1 shows resistivity log/seismic-attributes correlation for Arlecchino and Arcobaleno well. Fig.9.2 shows the related training and validation error. After the validation, assuming that the derived relationship is valid for the entire seismic section, prediction between wells along the seismic profile was performed.

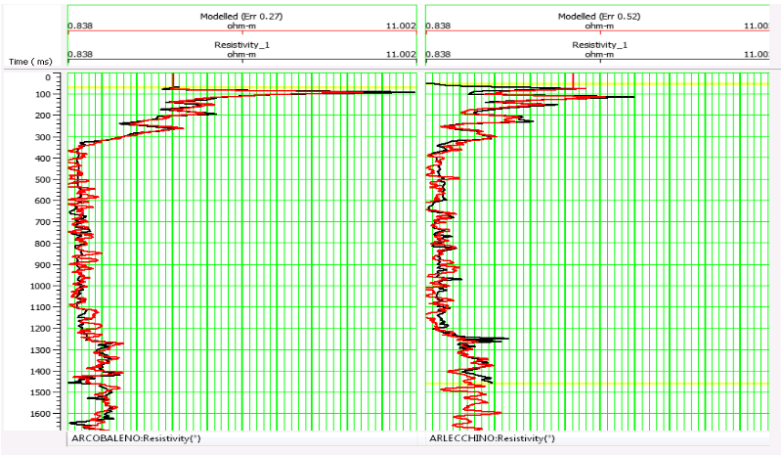

Figure 9.1: Resistivity log and modelled resistivity log for Arlecchino and Arcobaleno wells. These are the relationships used to train the STENAP 08 seismic line.

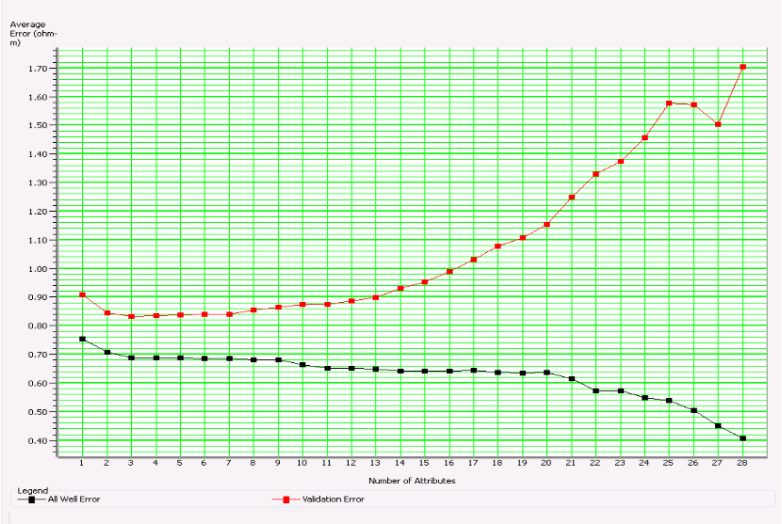

Figure 9.2: Validation (red line) and prediction (black line) errors for multi-attribute list used in Arlecchino and Arcobaleno correlations.

The result of this elaboration is the prediction of P-wave velocity, porosity and resistivity panels. Log data use are the available sonic and resistivity logs and the calculated porosity pseudo-log (estimated through EMT, see sec.8.1). The seismic data used are the amplitude preserving stack for the STENAP 08 line and a migrated stack section for the GANDI 09 line. In fact, it was not possible to successfully correlate logs and the amplitude preserving stack of the GANDI 09 line. This is because of the strong amplitude variations and the diffuse blanking.

9.2 Results

For each seismic section, P-wave velocity, resistivity and the porosity distribution were obtained (Fig.9.3–Fig.9.11). P-wave values represent an overall normal trend of increasing velocity with depth. Even where logs locally identify presence of gas, velocity measurements not show relevant anomalies (see Fig.9.3 and Fig.9.4). For this reason they were excluded from the gas content assessment.

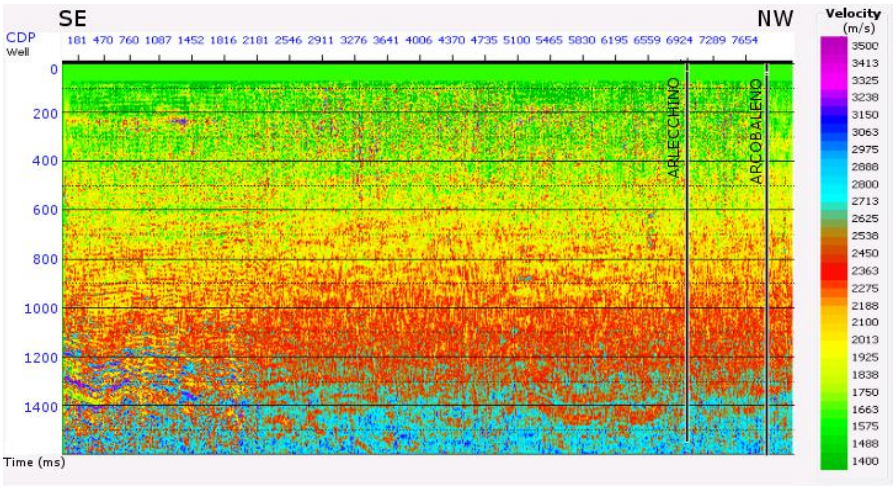

Figure 9.3: STENAP 08 correlated velocity. Arlecchino and Arcobaleno well locations are shown.

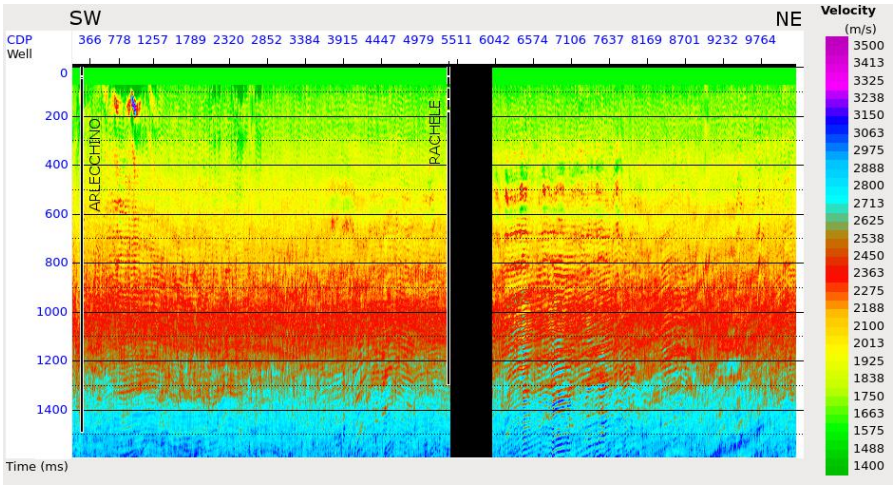

Figure 9.4: GANDI 09 correlated velocity. Arlecchino and Rachele well locations are shown. Black box indicates a zone of no coverage.

However, resistivity sections show strong anomalies in the regions where seismic data present a strong variation in frequency content. These anomalies can be assumed as induced by the presence of gas. For this reason, resistivity was predicted in two ways: excluding or including frequency-related seismic attributes (see Fig.9.6, Fig.9.5 and Fig.9.10, Fig.9.9). The resistivity section estimated without

the frequency-related attributes is thought to be a background resistivity. The resisitivity section estimated including the frequency-related attributes is considered as total resistivity, being representatives of the gas-induced anomalies over the background resistivity field.
Table 9.1 and Table 9.2 report prediction parameters for all the target log of the STENAP 08 and the GANDI 09 lines.
In subsec.9.2.1 and subsec.9.2.2 all the results used for gas quantification are reported. They were all resampled every 10 ms. STENAP 08 and GANDI 09 final stack sections are reported to help the comprehension.

Table 9.1: Prediction parameters (STENAP 08).

Target log	P-wave (m/s)	Porosity	Resistivity (Ωm)	Background resistivity (Ωm)
Number of attributes	24	28	28	24
Operator length	150	150	150	150
Training error	102.08	0.0549	0.4078	0.5674
Validation error	412.48	0.322	1.705	1.379
Correlation	0.9691	0.8902	0.9321	0.8648

Table 9.2: Prediction parameters (GANDI 09).

Target log	P-wave (m/s)	Porosity	Resistivity (Ωm)	Background resistivity (Ωm)
Number of attributes	x	6	28	10
Operator length	x	200	200	200
Training error	x	0.0584	0.21836	0.5004
Validation error	x	0.289	-	3.042
Correlation	x	0.8789	0.9519	0.7097

9.2.1 STENAP 08

STENAP 08 total resistivity panel (Fig.9.6) represents the resistivity pattern along the line, apparently not correlated to the stratigraphy, while the background resistivity (Fig.9.5) obtained leaving out the frequency-derived seismic attributes, is more correlated to the main reflectors and the seismic amplitude distribution, but it does not represent the effective anomaly associated to the presence of gas. In fact, total resistivity panel is characterized by a zone with strong positive anomalies coincident with the high frequency zone in the seismic line in the first 2500 CDPs (see Fig.9.8). In the rest of the section high resistivity values are distributed along vertical paths. Porosity panel (Fig.9.7), calculated predicting the EMT pseudo-log along the line, has been smoothed and represents a normal decreasing porosity trend with depth.

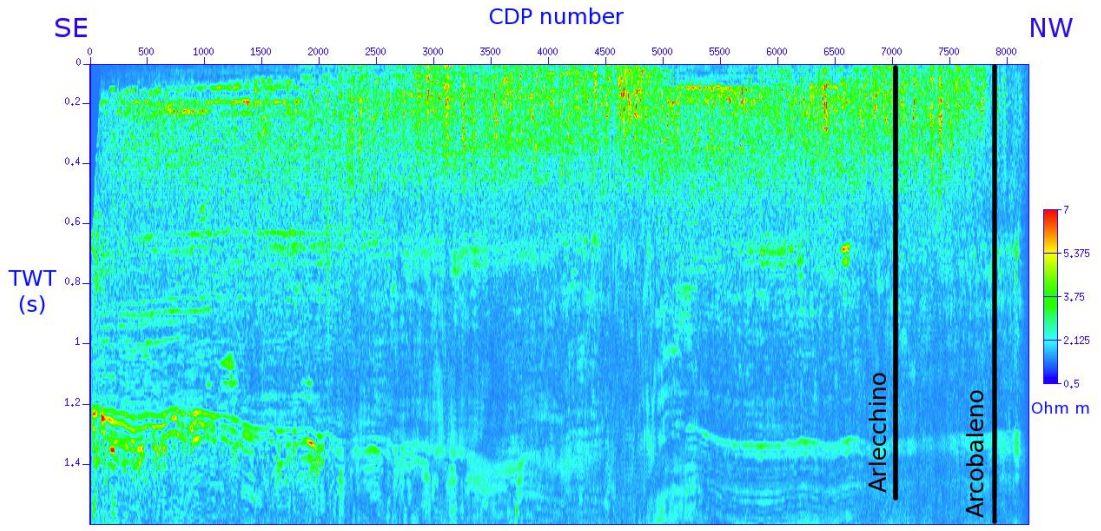

Figure 9.5: STENAP 08 background resistivity. Arlecchino and Arcobaleno well locations are shown.

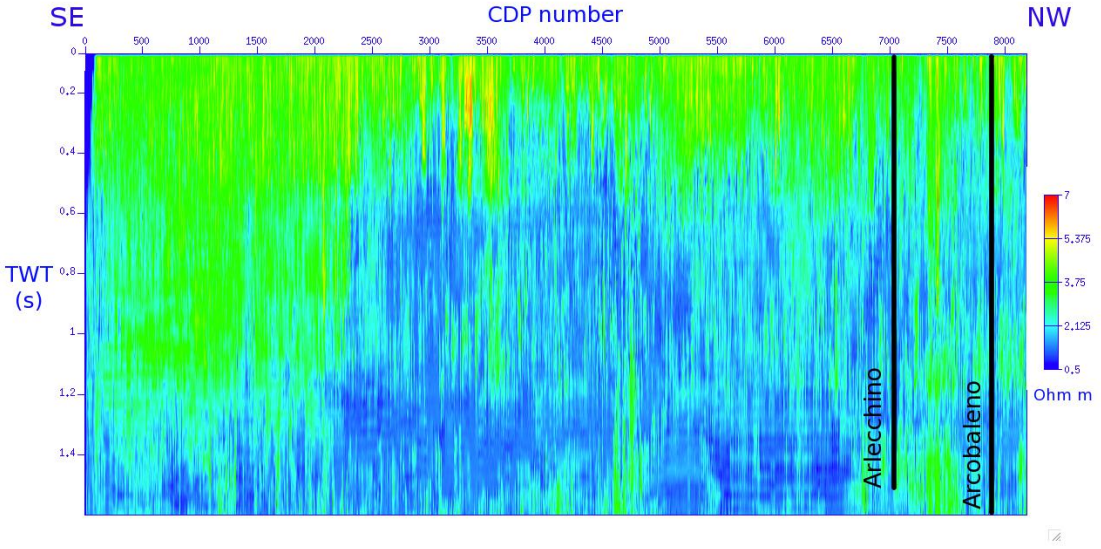

Figure 9.6: STENAP 08 total resistivity. Arlecchino and Arcobaleno well locations are shown.

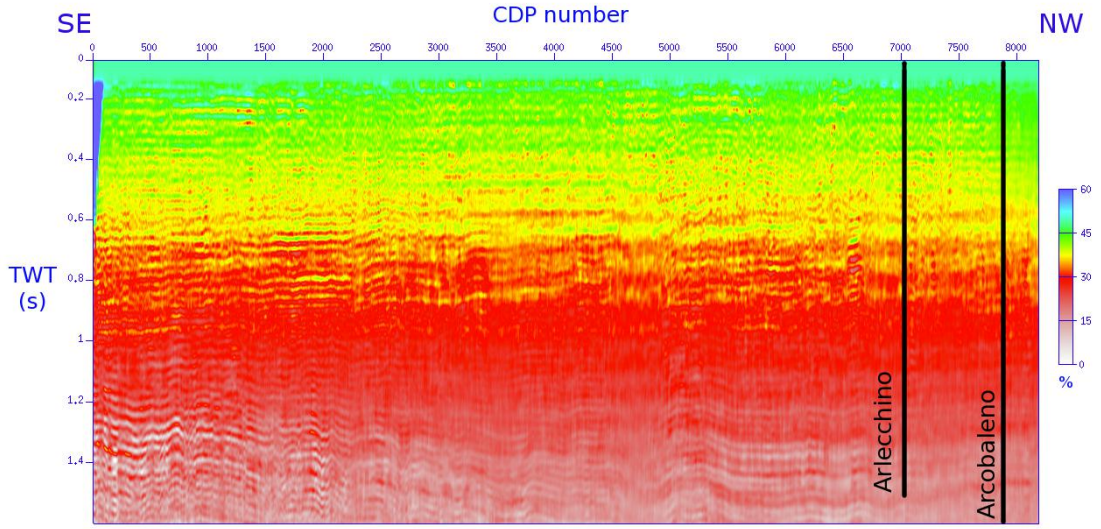

Figure 9.7: STENAP 08 total porosity. Arlecchino and Arcobaleno well locations are shown.

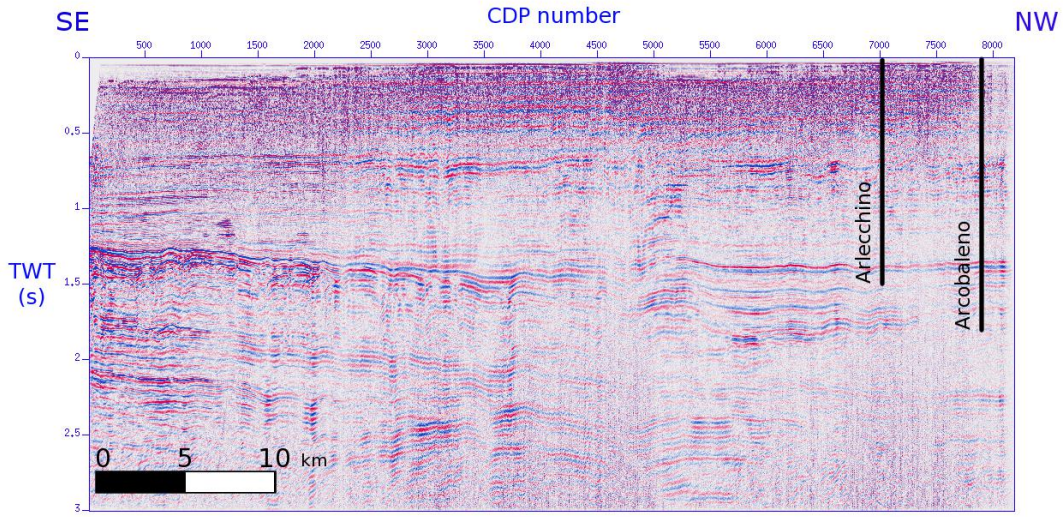

Figure 9.8: STENAP 08 amplitude preserving stack. Arlecchino and Arcobaleno well locations are shown.

9.2.2 GANDI 09

GANDI 09 total resistivity panel (Fig.9.10) represents, as for the STENAP 08, the effective resistivity distribution along the line. In this case, a higher correlation with the stratigraphy is observed, likely due to a difference in the gas behavior in the sedimentary succession. Furthermore, the seismic section does

not show any relevant difference in the frequency content along the line itself (Fig.9.12). In comparison with the background resistivity (Fig.9.10), higher values are distributed along the whole section. As for the STENAP 08, the resistivity anomalies are sensible to the frequency-derived seismic attributes, even if with a minor impact. Porosity panel (Fig.9.11), calculated predicting the EMT pseudo-log along the line, had been smoothed and represents a normal decreasing trend with depth.

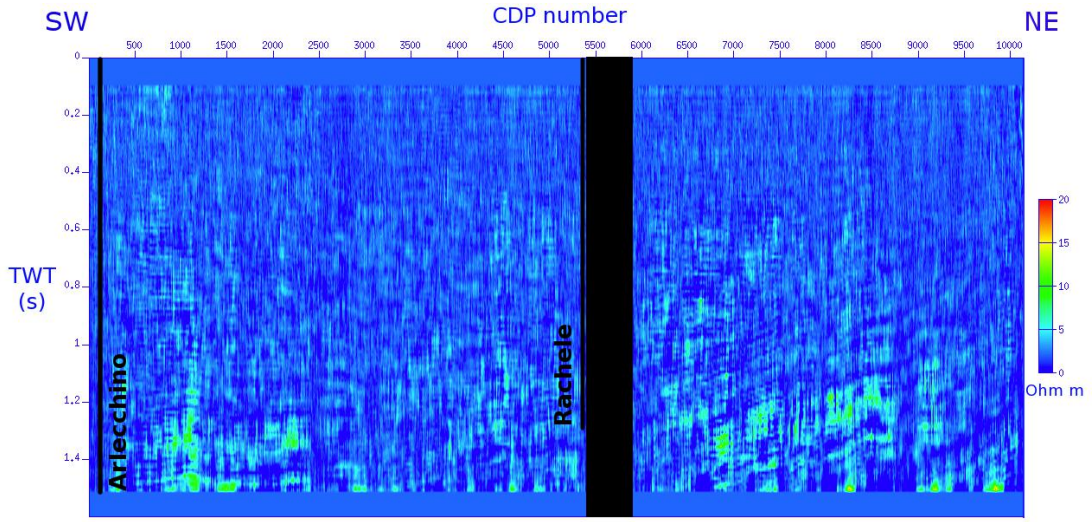

Figure 9.9: GANDI 09 background resistivity. Arlecchino and Rachele well locations are shown. Black box indicates a zone of no coverage .

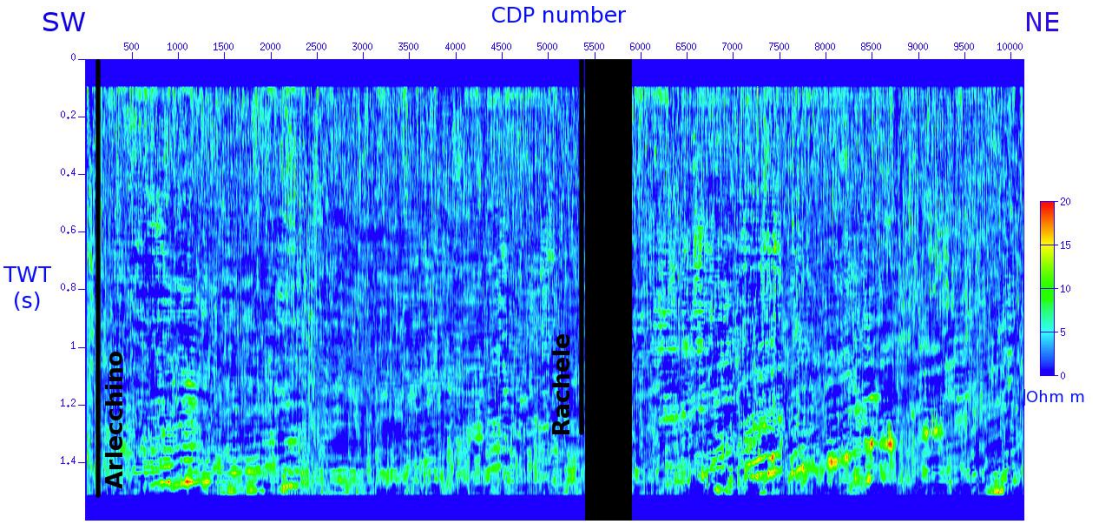

Figure 9.10: GANDI 09 total resistivity. Arlecchino and Rachele well locations are shown. Black box indicates a zone of no coverage.

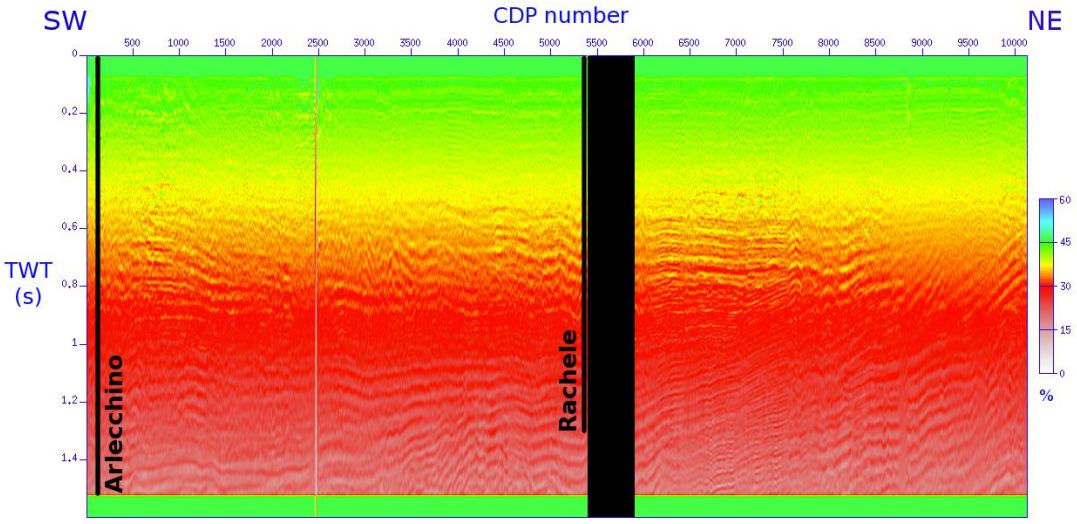

Figure 9.11: GANDI 09 total porosity. Arlecchino and Rachele well locations are shown. Black box indicates a zone of no coverage.

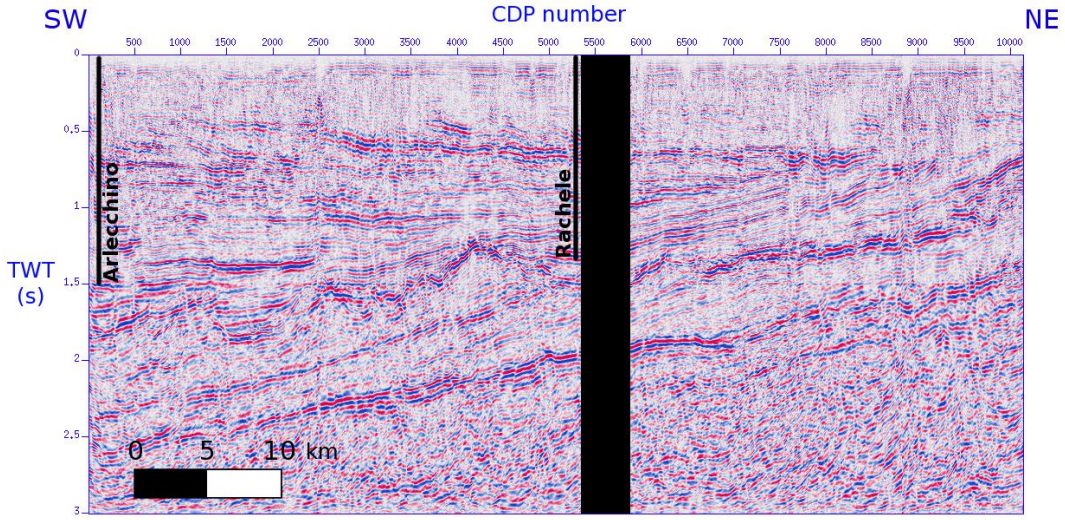

Figure 9.12: GANDI 09 stack. Arlecchino and Rachele well locations are shown. Black box indicates a zone of no coverage.

The 2D sections above described have been used as input parameters for the estimation of gas content for the STENAP 08 and the GANDI 09 lines.

Chapter 10

Gas content quantification

10.1 Archie's second law

Results from log-seismic correlation revealed that P-wave velocities do not detect the presence of gas in the sediments, which instead is proven by different geological/geophysical evidences. Thus, gas saturation was estimated using **Archie's law** and resistivity theory. Gas concentration is obtained multiplying *gas saturation* and *porosity* calculated in chap.9.
As reported in Appendix C, the bulk resistivity of a rock R_t partially saturated with an aqueous fluid is directly proportional to the resistivity of the same rock when fully saturated with the same fluid:

$$R_t = IR_0 \tag{10.1}$$

The constant of proportionality I is called *resistivity index* and describes the effect of partial desaturation of the rock. For the purpose of gas content quantification, I was thought to be the ratio between **partially water-saturated (gas bearing) sediments** (R_t) and **fully water-saturated (gas free) sediments** (R_0).
From Archie's Second Law, resistivity index I can be written also as:

$$I = S_w^{-n} \tag{10.2}$$

where S_w is the *fractional water saturation* of the rock, I is the *resistivity index*, n is the *saturation exponent*.
Knowing I and n is possible to estimate the water saturation S_w.

Therefore, assuming total saturation of the pores, is possible to estimate the gas saturation S_g:

$$S_g = 1 - S_w = 1 - I^{-1/n} \tag{10.3}$$

Eq.10.3 was solved for S_w using resistivity sections reported in chap.9. The resistivity sections estimated without the frequency-related attributes (*background resistivity*) are representative of the case of fully water saturation. Instead, the resistivity sections estimated including the frequency-related attributes (*total resistivity*), being representative of the **gas-induced anomalies** over the background resistivity field, represent the water/gas mix fully saturated sediments.
Eq.10.3 can be re-written as:

$$S_g = 1 - \left(\frac{R_0}{R_t}\right)^{-1/n} = 1 - \left(\frac{R_{back}}{R_{tot}}\right)^{-1/n} \tag{10.4}$$

Gas concentration can be then directly calculated as product of gas saturation and porosity:

$$C_g = S_g \cdot \phi \tag{10.5}$$

10.2 Saturation exponent estimation

An estimate of the saturation exponent n is needed to solve Eq.10.4.
From Eq.10.4, n can be written as:

$$n = \frac{ln\left(\frac{R_{back}}{R_{tot}}\right)}{ln\left(1 - S_g\right)} \tag{10.6}$$

Some values of gas saturation S_g, relative to sparse depth values z_i, are reported in the drilling reports of Arlecchino and Arcobaleno wells, so that they have been used to calibrate n.
Traces of the the STENAP 08 R_{back} and R_{tot} were extracted at well locations and evaluated at z_i. Using Eq.10.6, n was calculated at z_i. Density profiles ρ were extracted ad well locations and evaluated again at z_i. Then, a relationship between $\rho(z_i)$ and $n(z_i)$ were found (see Fig.10.1) and used to provide an estimate of n over the whole STENAP 08 line.

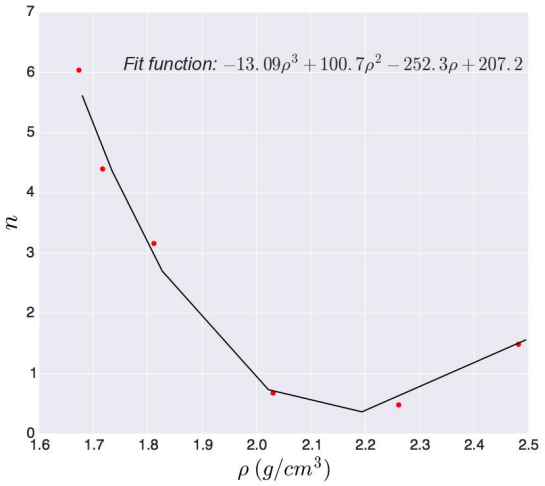

Figure 10.1: Fit of $\rho - n$ crossplot.

The STENAP 08 density section ($\rho = IP/v$), was calculated as ratio between IP section estimated in chap.7 and velocity section estimated in chap.9.
The same procedure was applied to the GANDI 09 line but no satisfying relationship was found between ρ and n. This has probably two reasons: first, local values of S_g are too shallow to be representative of the gas distribution; second, density section was less reliable than in the case of the STENAP 08 line. So, a profile of the STENAP 08 n section was extracted in correspondence of the crossing with the GANDI 09 line. This profile was smoothed and average values of each of the main lithological units, recognizable in both lines, were calculated. Such values were used to reconstruct a realistic n section for the GANDI 09 line.
Resulting n sections are reported in Fig.10.2 and Fig.10.3.

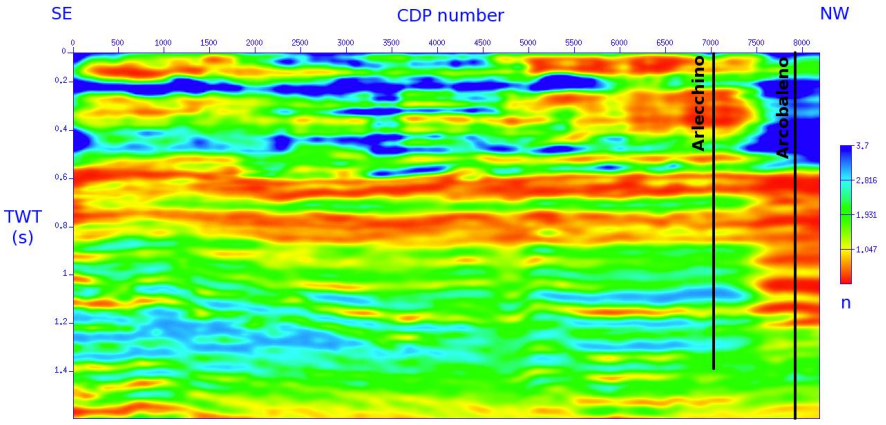

Figure 10.2: STENAP 08 saturation exponent *n* section. Well locations are shown.

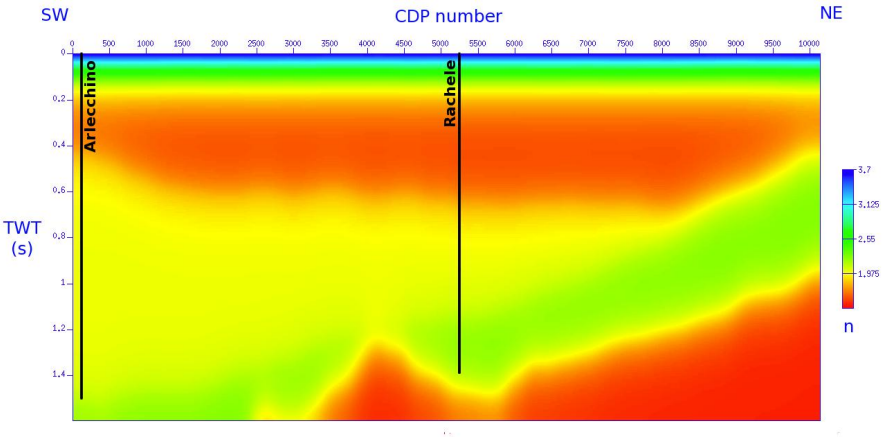

Figure 10.3: GANDI 09 saturation exponent *n* section. Well locations are shown.

10.3 Results

Fig.10.4 and Fig.10.5 show the general distribution of gas concentration obtained from the resistivity anomalies and it should be considered in its relative context. More reliable gas concentration evaluation needs more accurate in situ measurements to constrain the analysis.
Comparing the results obtained for the two selected seismic profiles, a general different distribution of the higher concentrations can be observed.
Along the STENAP 08 (Fig.10.4), high values can be seen in the shallowest (< 0.25 *s* TWT) parts in CDPs 1-2000 and CDPs 5000-6500. The SE part of the line is characterized by high concentration values, distributed horizontally and following the stratigraphy. Relevant concentration values are found also along vertical paths and in the zone where the stack section shows a "pull-down", most likely gas-related, effect.
The GANDI 09 line (Fig.10.5) shows low values of concentration distributed along the entire seismic section and no accumulations at specific depths or stratigraphic layers. Instead, increase in gas concentration

is present along vertical paths (i.e. around CDP 2200, 6500, 7250, 8500).

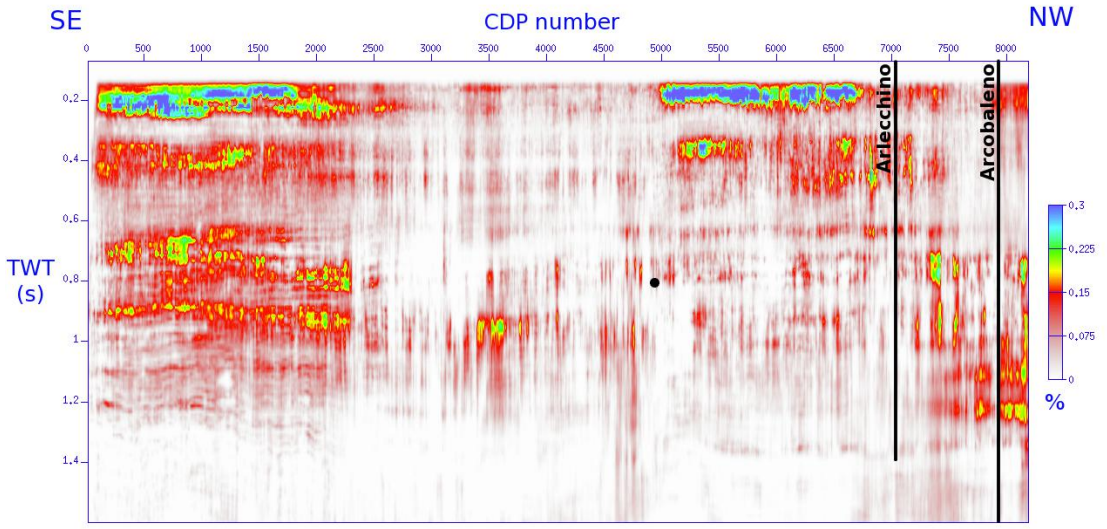

Figure 10.4: STENAP 08 gas concentration. Well locations are shown.

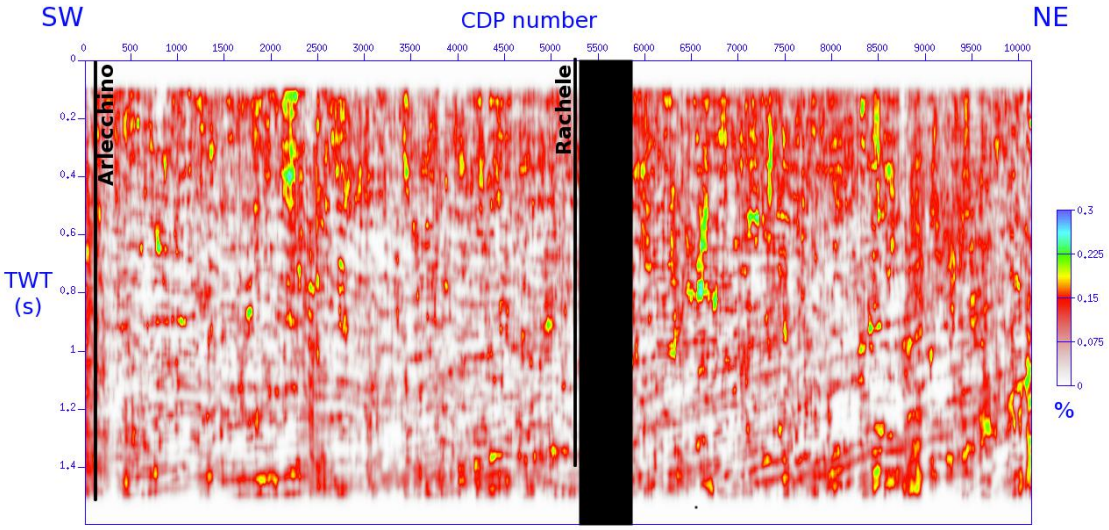

Figure 10.5: GANDI 09 gas concentration. Well locations are shown. Black box indicate a zone of no seismic coverage.

Part III

Discussion

Chapter 11

Seismic interpretation in relation to gas presence

The integrated geophysical approach used in this thesis allows to obtain gas content sections for the two selected seismic profiles. The frequency content of the seismic data was found to be strongly correlated to the presence of gas, with a direct influence on the resistivity response.
In this chapter, the gas-related seismic features recognized throughout the sedimentary succession are analyzed and interpreted in relation to the gas content results. The role of the identified geological structures in the gas distribution and migration is investigated.
Results demonstrated that the gas distribution and migration are strongly consistent with the interpreted seismostratigraphic and tectonic setting of the study area, investigated analyzing the whole seismic dataset by Brancolini et al. (under review)[1].
It is important to underline that in this work the gas content should be considered in terms of relative concentration. In this case study, despite great attention put in error analysis, a proper error propagation along the whole analysis is almost impossible. However, this approach can still be used to recognize specific patterns in the distribution of gas within the sediments, which can help to explain its occurrence and migration.
The two seismic lines are discussed below.

The STENAP 08 line (Fig.11.1) is characterized by a heterogeneous distribution of gas, that is thought to influence its seismic frequency content. Gas content quantification begins at 70 *ms*, corresponding to the starting depth of the log measurements.
Gas ranges between 0-0.3% of total rock volume. This small fraction of gas is general very difficult to determine and in this case, as explained, the absolute value is only indicative of the overall variation in gas content. The highest concentration values are distributed horizontally in the shallower levels (TWT<0.25 *s*) in CDP ranges 0-2000 and CDP 5000-6500. In the SE portion of the line, gas appears to be horizontally distributed following the stratal configuration, in the area characterized by fine turbidites, which likely provide the pore space for gas accumulation in the coarser-grained sand beds (e.g. Malvic, 2016). In the rest of the line, several vertical paths are recognizable.
In order to understand the meaning of such a gas distribution, the main gas-related seismic features, both vertically focused and laterally persistent, have been recognized and analyzed (see Fig.11.2). Seismic data reveal how the main tectonic lineaments are able to act as seal by-pass system for the gas.

[1]Brancolini, G., Civile, D., Donda, F., Tosi, L., Zecchin, M., Volpi, V., Rossi, G., Sandron, D., Ferrante, G.M. and Forlin E. (2018). NEW INSIGHTS ON THE ADRIA PLATE GEODYNAMICS. Under review in *Scientific Reports.*

Along the STENAP 08 seismic line, two main structures were recognized as being part of regional lineaments, imaged in various other seismic lines (Brancolini et al., under review). They are indicated with numbers 1 and 2 in Fig.11.2. Structure 1, beneath the Arlecchino well, can be considered part of the **Schio-Vicenza fault system**; structure 2, between CDP 4500 and CDP 5500, could be produced by the same regional stress field as Schio-Vicenza system but it is not directly associated with it.
The Schio-Vicenza fault system extends for approximately 120 *km* from the foot of the Prealps to the Po Delta with a NW-SE trend. It is rooted in the Upper Cretaceous carbonate units and heavily affects the sediments above the Messinian Unconformity. It appears to be active until at least 20 *ka* (Pola et al., 2014) and it may be regarded as the western boundary of the Northern Adriatic region.
Seismic pull-downs correlating with the main highlighted tectonic systems are recognizable (Fig.11.2: B) and C) panels and Fig.11.3: B) and C) panels).
The STENAP 08 line shows a 700 CDP-wide, 2*s*-long window characterized by pull-downs (Fig.11.2 and Fig.11.3 B)). The amplitude preserving version of the stack section (Fig.11.4) shows how this area is affected by widespread strong blanking. This entire pull-down zone is characterized by a degradation in the stack response and micro-fracturing. This has has been interpreted as a **giant chimney**, rooted below the Messinian Unconformity and guided by the tectonics in focusing the gas migration.
Other smaller-scale pull-downs are present along the line. One is located in the area of the Arlecchino structure previously described as structure 1, at CDP 7500 (Fig.11.2 and Fig.11.3 C)). The other, less clear and much deeper, is at CDP 2700 (Fig.11.2 and Fig.11.3 A)). These two features are characterized by a loss of amplitude (Fig.11.4), which results in a poor coherence after the non-amplitude preserving processing, the first one (CDP 2700) is interpreted as **gas pipe** while the other one (CDP 7500) as a **chimney**.
Fig.11.3 C) reveals a pull-up effect in the Messinian Unconformity that is quite difficult to interpret. It could represent real morphology, the signature of an up-ward migration of sediment or a velocity artefact.
In the STENAP 08 line, the very first reflectors in CDP ranges 0-2000 and 5000-6500, near the seabottom, are characterized by **low amplitude**, as shown in the preserving amplitude stack section (Fig.11.4, zoom in Fig.11.5). However, it is likely that the processing has distorted the signal in these zones, producing an apparent low-frequency effect in the non-amplitude preserving section (Fig.11.2). This is probably due to deconvolution, which often fails in low amplitude zones. Indeed, their occurrence can be explained by the presence of gas, which results laterally-varying distributed along the line, possibly because of a variable permeability. Furthermore, these zones seems affected by fractures that can reach the seabed possibly allowing the fluids to escape. Fig.11.1 shows a remarkable presence of gas just below these low-amplitude zones.
Finally, **bright spots** occur at various depths in the STENAP 08 line and the two most evident are highlighted in Fig.11.2 and Fig.11.4. One is associated with the Arlecchino structure 1 and the other with the clayey-sandy Plio-Quaternary turbidite sequence in the SE part of the line. Here, bright spots are interpreted as local gas accumulation (e.g. Donda et al., 2015). However, the inversion for gas concentration is not reliable in these zones, as petrophysical properties are laterally extrapolated and so small, local anomalies cannot be properly resolved.

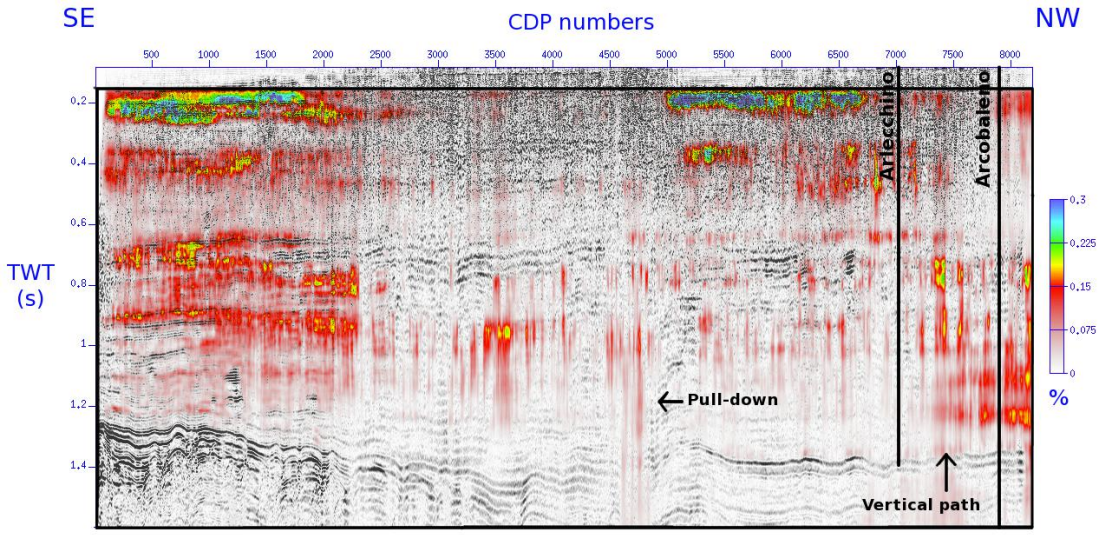

Figure 11.1: STENAP 08 gas concentration superimposed on the stack section. Horizontal layering can be observed in the SE of the line. The strongest vertical path, located between Arlecchino and Arcobaleno wells is highlighted. The wide pull-down recognizable in the seismic data, in the middle of the line, is associated with a vertical distribution of the gas. Well locations are shown.

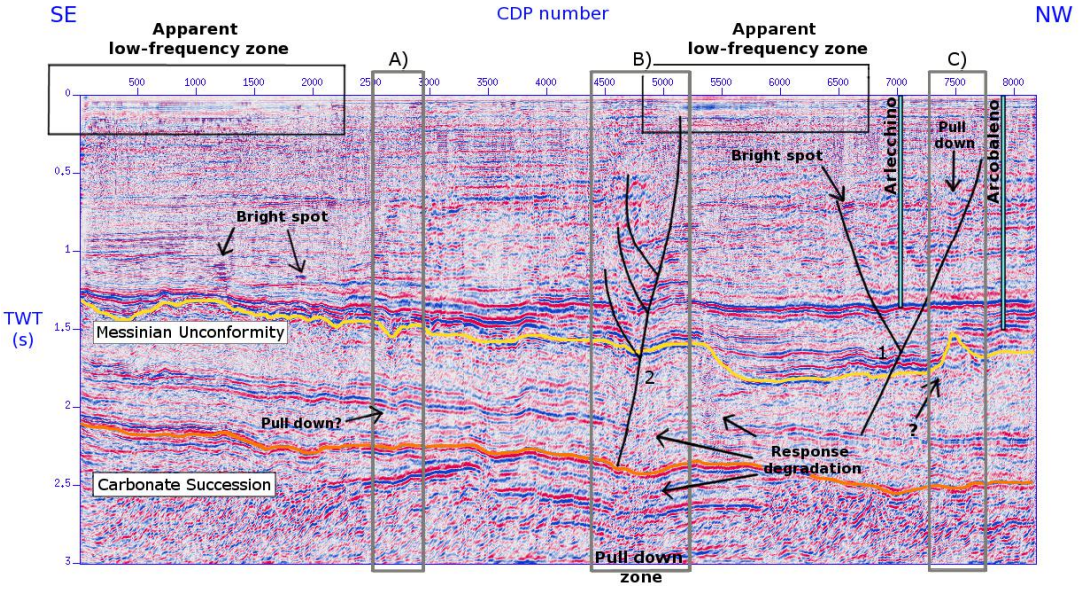

Figure 11.2: STENAP 08 stack section interpretation. Main faults lineament are drawn in black. Gas-related features are indicated. Apparent low-frequency zones are highlighted. Messinian Unconformity is in yellow, top of Carbonate Succession is in orange. Well locations are shown. See Fig.11.3 for explanation of grey box areas A), B), C).

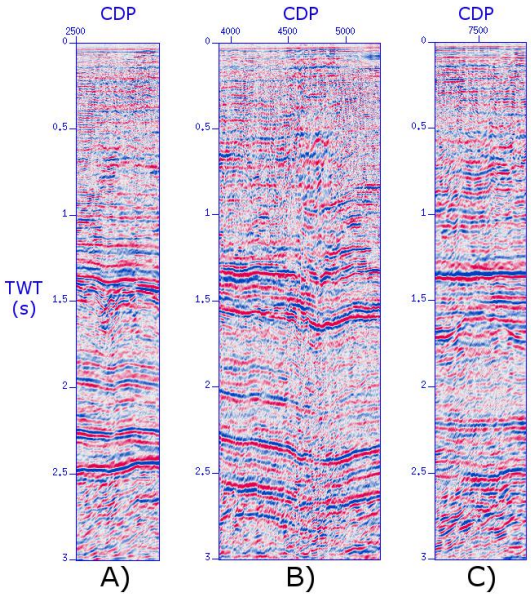

Figure 11.3: Main gas related features recognizable in the STENAP 08 line. A) A pull-down at 2 *s* associated with a lateral discontinuity of the reflectors, possibly indicating a gas pipe; B) Wide pull-down zone in the middle of the line, possibly indicating a giant chimney; C) A possible pull-down at 0.8 *s* associated with a gas pipe. All of the examples show strong variation in dominant frequency, both vertically and laterally, and signal degradation.

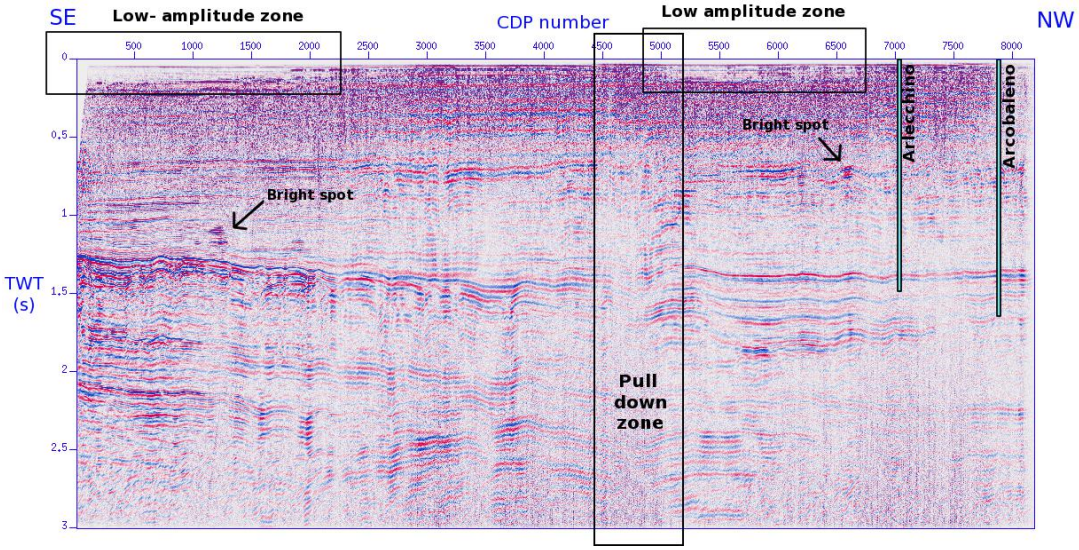

Figure 11.4: STENAP 08 amplitude preserving stack section. Bright spots are indicated. The pull-down zone is inside the black box. Shallow low-amplitude zones are highlighted. Well locations are shown.

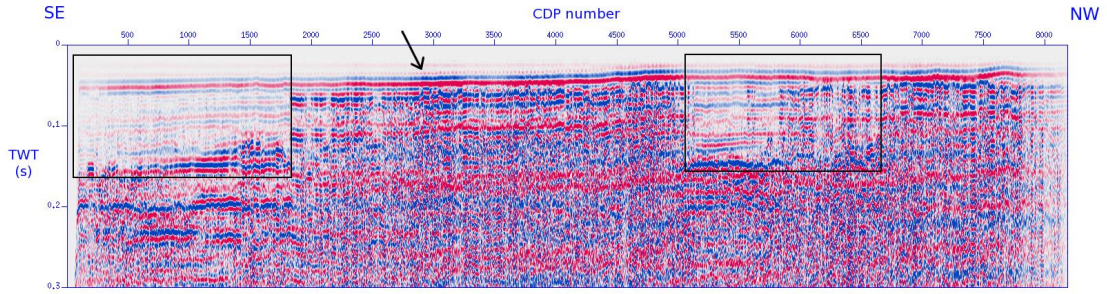

Figure 11.5: STENAP 08 amplitude preserving stack section, zoom on the first 300 ms. Strong lateral amplitude variation could testify the presence of gas in the very shallowest layers. The seabed is indicated by the black arrow.

Gas content along the GANDI 09 line is show in Fig.11.6. Gas content quantification begins at 100 *ms*, corresponding to the starting depth of the log measurements. The GANDI 09 line is affected by zones of poor or no seismic coverage. Furthermore, the amplitude preserving stack section (Fig.11.9) appears to be poorly balanced except for a 1550 CDP-wide zone, between CDP 6000 and CDP 7500, where amplitudes are higher and the stratigraphy is better imaged. For this reason, it was not possible to successfully correlate seismic data with log curves, so the amplitude preserving seismic section was not used. Instead, a migrated and gained version of the line was used for correlation (see chap.9) and gas content assessment (see chap.10).
Gas content ranges between 0% and 0.3% (as in the case of the STENAP 08 line) of the total rock volume, with relatively higher concentration mainly distributed vertically (Fig.11.6).
Several **sub-vertical faults** are recognizable; they belong to the regional-scale tectonic lineaments identified by Brancolini et al. (under review) (Fig.11.7). The fault system recognized in the STENAP 08 line, close to Arlecchino well (Fig.11.2, structure 1), is visible on this line (Fig.11.7, structure 1). Very often, the faults are associated with a **degraded stack response** and the presence of **pipes** (Fig.11.7 and Fig.11.8 C)).
An apparent **pull-up** is observed close to areas of relatively high (vertically distributed) gas concentration (Fig.11.8 B))). It is not clear if it is a processing artefact, the consequence of related adjacent pull-downs or actual geological structure. As the inversion shows relatively high gas concentration in the overburden and there is an associated low frequency anomaly, it could be interpreted as an expression of strong lateral velocity variation in the overburden due to shallow gas accumulation.
No bright spots were recognized in the GANDI 09 stack section (Fig.11.7).
Reflectors in the shallowest tens of *ms*, in the GANDI 09 line, show the same loss in amplitude found along some parts of the STENAP 08 line (see Fig.11.4). In the GANDI 09, however, the shallowest sediments do not show any change in amplitude response along the line (see Fig11.4). This suggests a different type of shallow gas distribution between the two lines.
In the GANDI 09 line, gas is distributed generally along vertical paths, located at different depths. In both seismic lines, faults seem to act as preferential conduits for gas migration. Small shallow faults may allow gas to reach the seabed, however the data does not provide any information for at least the first tens of *ms*.

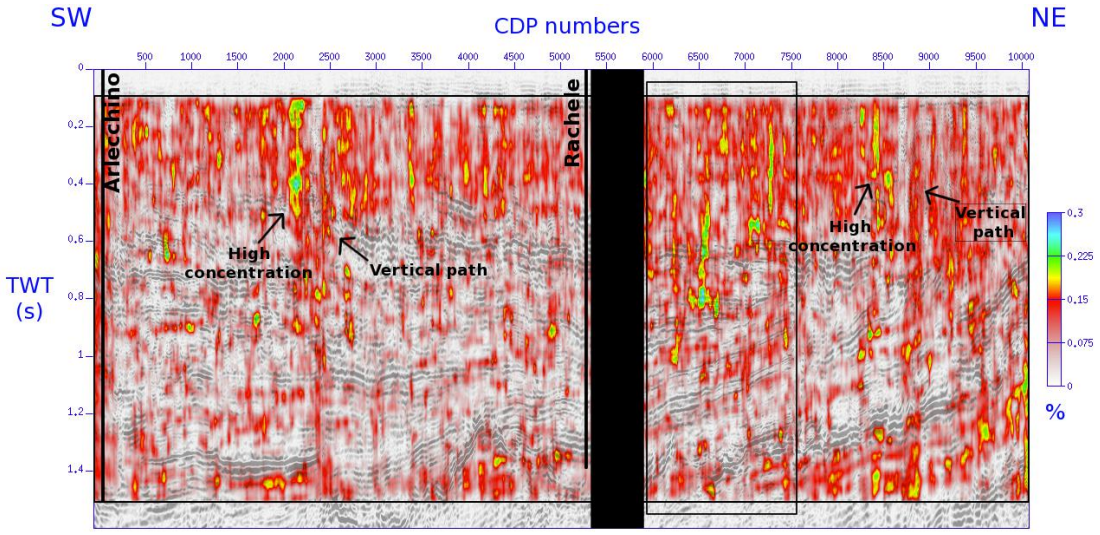

Figure 11.6: GANDI gas concentration superimposed on the stack section. High concentration zones and vertical paths are highlighted. Well locations are reported. Black box indicates an area of no coverage.

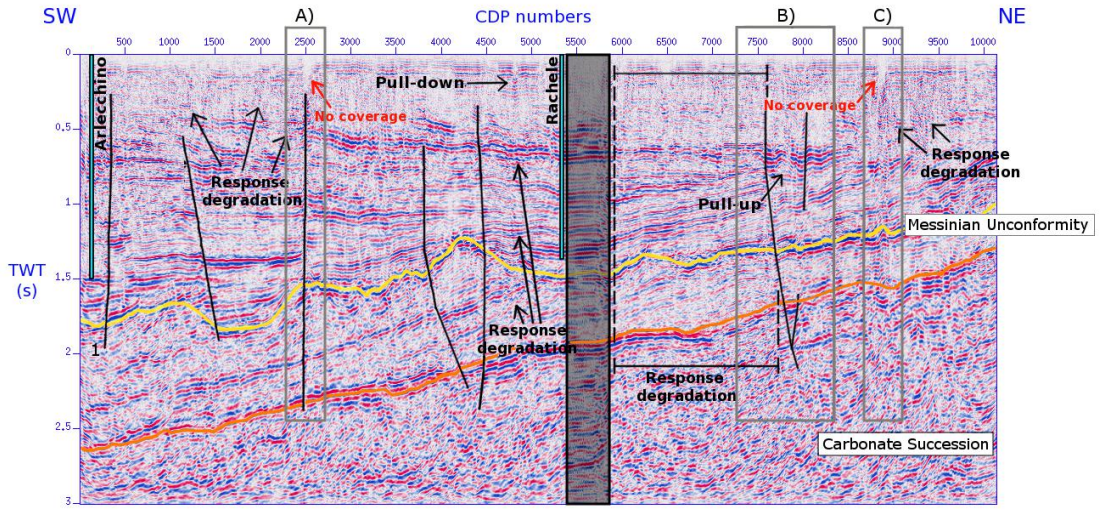

Figure 11.7: GANDI 09 stack section interpretation. Red arrows indicate CDPs of poor coverage, translucent box indicates an area of no coverage. Main fault lineaments are drawn, gas-related features are highlighted. The Messinian Unconformity is in yellow, the top of Carbonate Succession is in orange. Well locations are shown. See Fig.11.8 for an explanation of areas A), B), C).

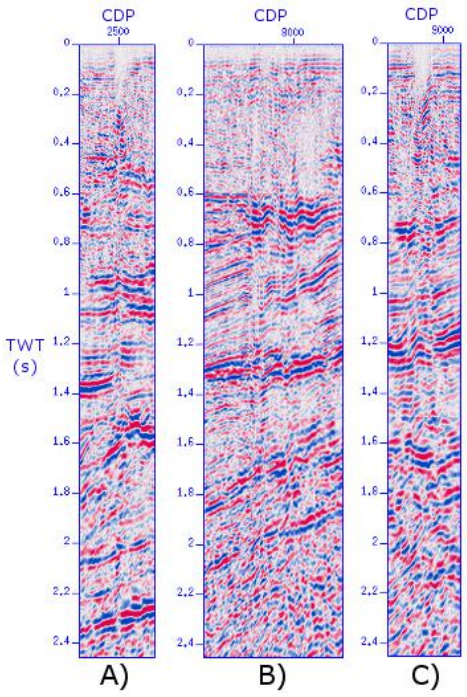

Figure 11.8: Main gas related features recognizable in the GANDI 09 line. A) Possible gas migration path, associated with the presence of a fault; B) An apparent pull-up in the vicinity of a fault system; C) An apparent pull-up in Messinian Unconformity associated with a possible gas chimney.

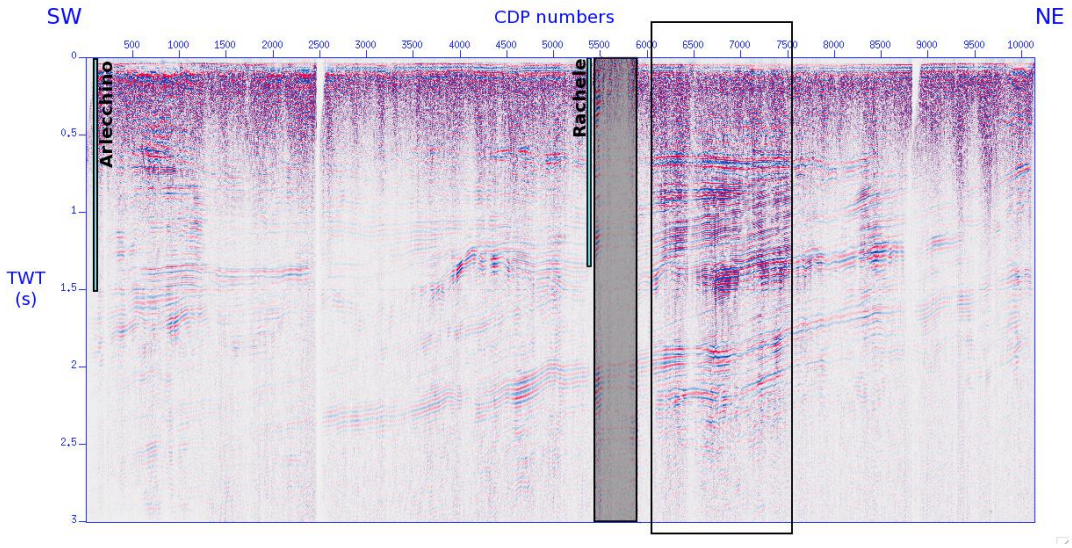

Figure 11.9: GANDI 09 amplitude preserving stack. The only zone characterized by relevant amplitude is highlighted. Well locations are reported. Transparent box indicates an area of no coverage.

Chapter 12

Relevance to the regional gas plumbing system

12.1 Origin of gas and possible play

A number of large and giant-size **biogenic gas** fields and medium to large oil fields have been discovered in the Adriatic foreland (Cazzini et al., 2015; Bertello et al., 2016). Two petroleum systems have been identified: a Plio-Pleistocene biogenic gas system, and an Upper Triassic-Lower Jurassic oil system, this one being **thermogenic gas**-prone.

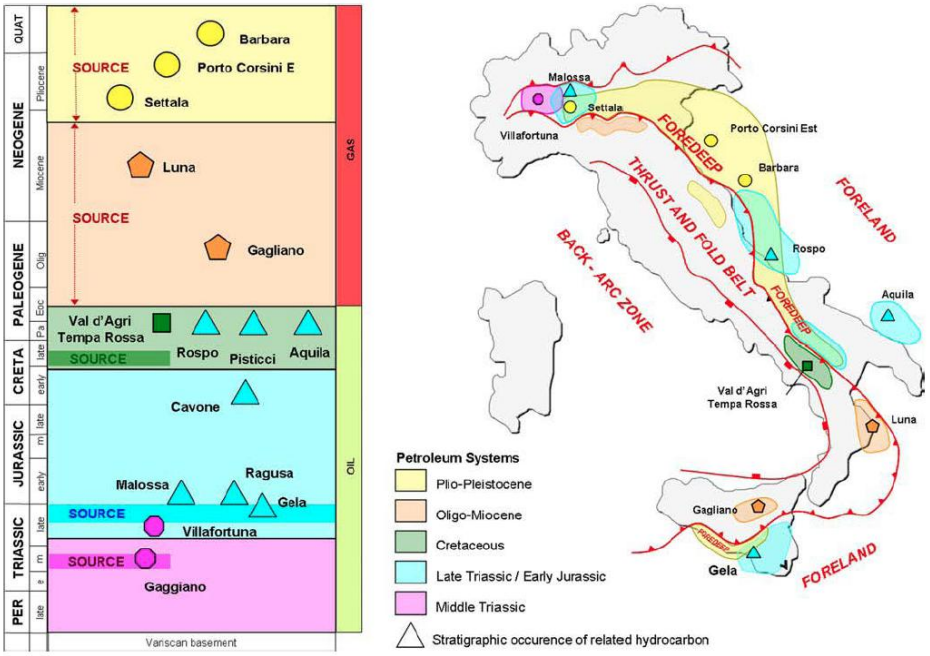

Figure 12.1: Stratigraphic and geographic location of the Italian petroleum systems. From Bertello et al. (2016)

Biogenic gas is at the origin of the largest and most productive fields in Italy but its play is nowadays considered mature and significant additional discoveries are unlikely to be made without a breakthrough in DHI technology (Fantoni, 2017). The Mesozoic oil play is as yet unproven in the Northern Adriatic area, whereas it characterizes the Central and Southern Adriatic where several oil fields (thermogenic gas-prone) are currently under production (Fantoni, 2017). Furthermore, a Cretaceous petroleum system has been presumed in the central and southern part of the Adriatic offshore in Croatian waters (Croatian Hydrocarbon Agency, https://www.azu.hr/en).

In the study area, biogenic gas is known to occur within Pliocene-to-Pleistocene turbiditic sands, commonly characterized by multiple pools within thin sand beds at approximately 1200-1500 mbs (Donda et al., 2015, and references therein). Structural and stratigraphic traps can occur, but they are generally related to gentle anticlines resulting from differential compaction of Pliocene-Pleistocene turbidite sandstones and are sealed up-dip by Pleistocene clays (Casero, 2004). These organic-rich clays, interbedded in the turbidite successions, are thought to be both source-rock and the effective vertical seal of the system (Casero and Bigi, 2013; Bertello et al., 2010). Such organic matter (very low TOC), is of terrestrial origin, with kerogen of type III which generates biogenic gas associated to a very low geothermal gradient (Croatian Hydrocarbon Agency, https://www.azu.hr/en). The gas generation is then hypothesized to start right after the deposition (Bertello et al., 2010).

In essence, the open literature reports that all the gas in the study area has been generated in situ by bacterial activity on the immature organic-rich clays interbedded with thin reservoir sands (Casero and Bigi, 2013, see Fig.12.1). Source rock, reservoir and seal coincide and primary and secondary gas migrations are considered to be negligible[1]. Tertiary migration (occurring when hydrocarbons move from one trap to another or to a seep) and seeping/expulsion from the sediments has been investigated by Donda et al. (2015).

Gas distribution resulted from the two seismic lines analyzed in this thesis, however, supports the hypothesis of a **secondary deeper gas source of pre-Pliocene origin**. This does not contradict what is reported in the literature, in which Plio-Pleistocene sands are identified as the main gas source/reservoir. These two gases would locally reach the shallowest depths and possibly mix with the gas generated by the peat layers known in the area, both at a depth of ca. 350 m and immediately under the seabed (Donda et al., 2019, in press). Very high log resistivity values found in the first 350 m in the analyzed boreholes would support the hypothesis of this very shallow peat-generated gas.

Considering the presence of known abandoned gas fields in the area (see Fig.12.2), interactions of the hypothesized pre-Pliocene gas with the exploited hydrocarbon reservoirs cannot be discounted. Such systems could have been partially sourced by the deeper ascending gas and they could contribute to seeps (leakage from reservoirs).

A possible source for the pre-Pliocene gas can be hypothesized in organic-rich layers in the Carbonate succession, possibly in the Cretaceous "**Calcare di Soccher**" formation, which have been found to be intercalated by thin shale and bituminous black marls (as reported in Amanda bis well, see Fig.12.4 for stratigraphy).

This gas system is supposed to be biogenic-prone and the conditions leading to the formation of microbial gas are well established. Methanogen microbes require organic matter and anoxic sulfate-free conditions, at temperature at about 60° (see Fig.12.3), which corresponds, in the study area, to a maximum depth of about 2000-2500 m.

Reservoir for this gas would be the same **Cretaceous carbonates**. A very low-permeability formation, such as the "**Marne di Gallare**" Eocene-Miocene formation could act as a seal for this reservoir.

[1]Primary migration is the process by which hydrocarbons are expelled from the source rock into an adjacent permeable carrier bed. Secondary migration is the movement of hydrocarbons along a "carrier bed" from the source area to the trap.

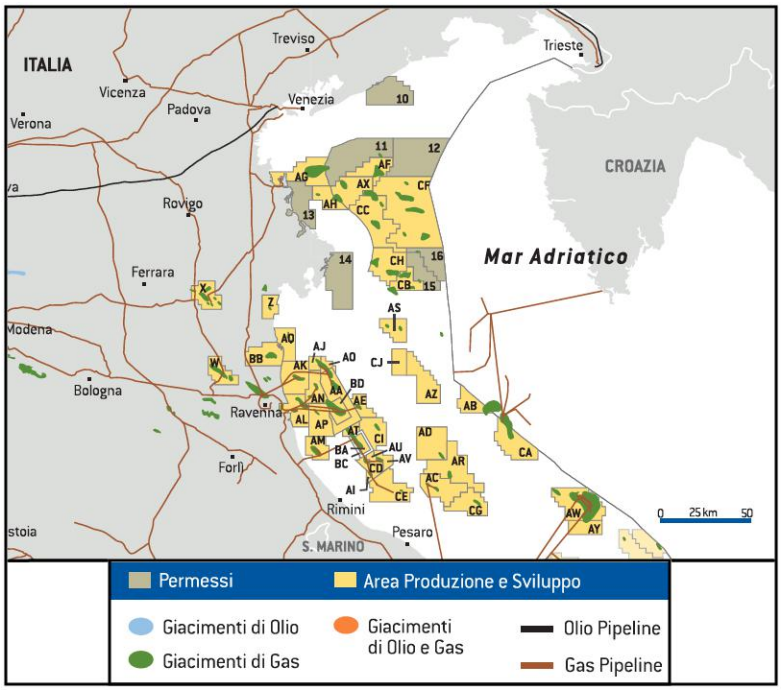

Figure 12.2: Hydrocarbon production fields in the Northern Adriatic. From ENI (2013)

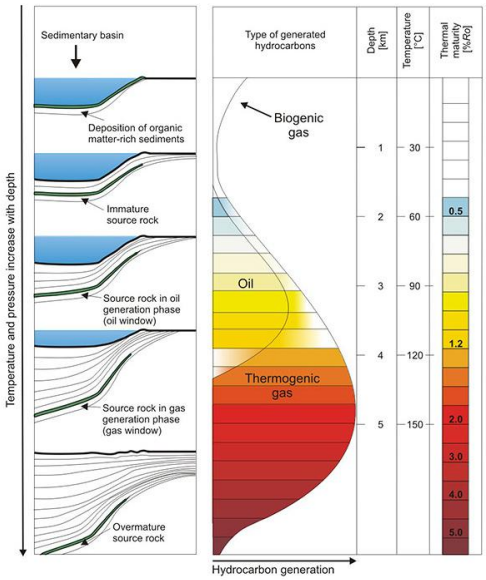

Figure 12.3: Biogenic VS thermogenic gas generation. From https://infolupki.pgi.gov.pl/en/gas/thermal-maturity-organic-matter-and-gas-exploration.

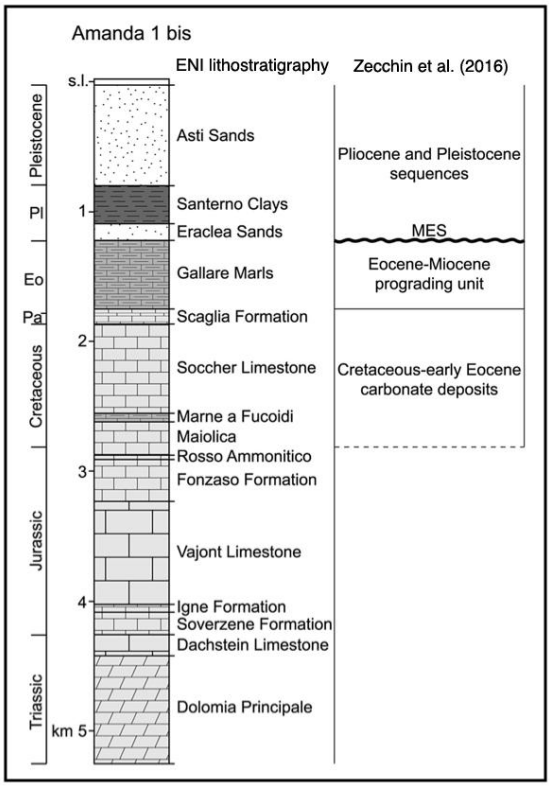

Figure 12.4: Schematic stratigraphy of Amanda 1 bis well. MES - Messinian Erosion Surface. From Zecchin et al. (2017).

Furthermore, in the Northern Apennines, in a total different geological context with respect to the study area but still in its vicinity, the upper Cenomanian pelagic sediments are characterized by a 1.5-m-thick organic-rich stratigraphic horizon called the Bonarelli Level, which represents the second major oceanic anoxic event in the Cretaceous. The Bonarelli Level is depleted in carbonates and consists essentially of biogenic quartz, phyllosilicates, and organic matter, with values of TOC reaching 18% (Mort et al., 2007). The Bonarelli level is recognizable also in the onshore Belluno basin (see Sedico 1 well, www.videpi.com). In spite of their high TOC, the reduced thickness of the outcrop does not support the idea of including this level within the effective Italian petroleum source rocks (Craig et al., 2018).
Considering the presence and the regional character of the Bonarelli level, one should not exclude the existence of similar bituminous levels in the study area.

12.2 Gas migration

Regarding the possible presence of a secondary deep gas play sourced in a pre-Pliocene formation, primary and secondary migrations, from the source rock to the trap, are very difficult to constrain from the dataset considered in this thesis. Seismic data is in fact not able to resolve the Carbonate Succession and the analyzed geophysical logs ends before reaching the Messinian Unconformity. The supported hypothesis is that gas migrates through fractures in the Carbonates until it is trapped by the "Marne di Gallare". Instead,

several pieces of evidence of tertiary migration (leaking from reservoir) are found in the resulting seismic and gas concentration sections.
In both seismic lines, the major recognized fault systems possibly act as a preferential path for gas migration. They are rooted below the Messinian Unconformity and they can represent local fluid escapes for gas trapped in the "Marne di Gallare" formation. Furthermore this formation, very likely characterized by low porosity and permeability, locally shows the presence of thin levels of sandstone (Nicolich et al., 2004). These levels have the potential to enhance the permeability of the formation and guide the gas migration until the Messinian Unconformity.
In the seismic data, along the entire sedimentary column from the surface to the Miocene, the recognized faults appear to be linked with chimneys and pipes, often in presence of a degradation in the seismic response. Pull-down effects corroborate the hypothesis of focused vertical fluid flow.
However, vertical migration features and chaotic/disrupted horizons in the seismic data, together with relatively higher gas concentration values along vertical paths, are not always found to be correlated with the main tectonic lineaments of the area. This suggests that hydrofracturing of sediments could be another important factor at the origin of gas conduit formation. The fracture network could have been generated at some point of the basin history when condition of overpressure occurred. Considering the high sedimentation rates known in the area due to increasing climatic variability in Plio-Pleistocene times, overpressure conditions could have been due to rapid burial relative to pore-fluid drainage (see chap.2).
Another relevant factor to explain migration preferential paths in Miocenic and/or older successions is the opening of conduits during abrupt changes in the vertical stress field due to big sea level fluctuations. This is the case of Messinian Salinity crisis, which have been reported worldwide as triggering mechanism of fluid expulsion (Iadanza et al., 2015). In the northern Adriatic Sea, ca. 800 m of the Messinian sea-level drop was estimated by several authors (Ghielmi et al., 2013; Mancin et al., 2016; Amadori et al., 2018), suggesting a relevant change in the vertical stress field during the crisis.

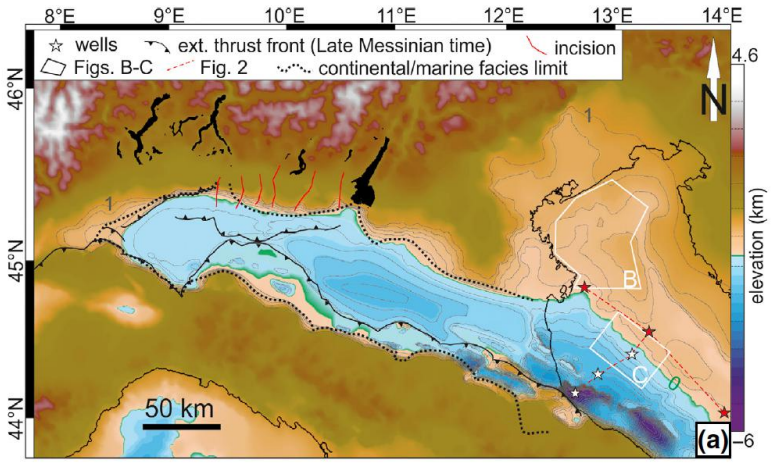

Figure 12.5: Restored late Messinian landscape, with 200 m contouring applying, from a model accounting for a 850 m sea-level drop. The dotted black line shows the continental vs marine shelf-to-basin facies boundary. From Amadori et al. (2018)

The study area experienced sub-aerial exposure, erosion and possibly opening of conduits and fluid expulsion. In post-Messinian, open-marine conditions have been controlled by both the erosional surface and the thrusting activity of the Southern Alps and Northern Apennines; the shelf depth reached a minimum value of less than 50 m (Mancin et al., 2016).

In summary:

- Pre-existing main fault systems seems to act as preferential migration paths for the gas, as already reported in Donda et al. (2015). This is not obvious, as demonstrated in several cases worldwide, where faults act as seals.
- Paleobathymetric variations, subsidence/uplift trends, reflecting the change in the tectonic control of the basin and the balance between subsidence and sediment supply, are thought to have been crucial in the opening of gas migration conduits.

Fig.12.6 and Fig.12.7 show the chronostratigraphic frame of the Cenozoic subsurface succession and the geological reconstruction along two seismic profiles crossing the study area (Mancin et al., 2016).

Along the two analyzed lines, only part of the deeper gas (both the Plio-Pleistocene and the hypothesized Cretaceous ones) would reach the surface. The uppermost (i.e. 50 m) stratigraphic succession, not investigated by the gas concentration assessment, is dominated by fine-grained sediments (according to data from the Venezia 1 and Triglia Mare 1 boreholes, www.videpi.com) and indicates that it could have acted as a seal for upward-migrating gases.
However, as reported in Donda et al. (2015), local leakage from the seabed is observed (see sec.3.3). Geochemical analyses performed at three leakage areas (see sec.3.1) revealed that seeping gases are microbial, and ^{14}C isotopes indicate that they mostly originate from the degradation of organic material with an apparent age of ca. $32,000 - 34,000$ yrs BP (Donda et al., 2019, in press). These ages are consistent with the Denekamp Interstadial, during which the climatic conditions would have favored the deposition of peat layers (Canali et al., 2007). This would result in the formation of shallow microbial methane within laterally persistent, Late Pleistocene peat layers, which are widely distributed throughout the northern Adriatic Sea (Donda et al., 2015) and would not have any relationship with the deep gas. Anyway, gas estimate for these shallow layers has not been investigated since no reliable constraints are available for such a shallow depth.

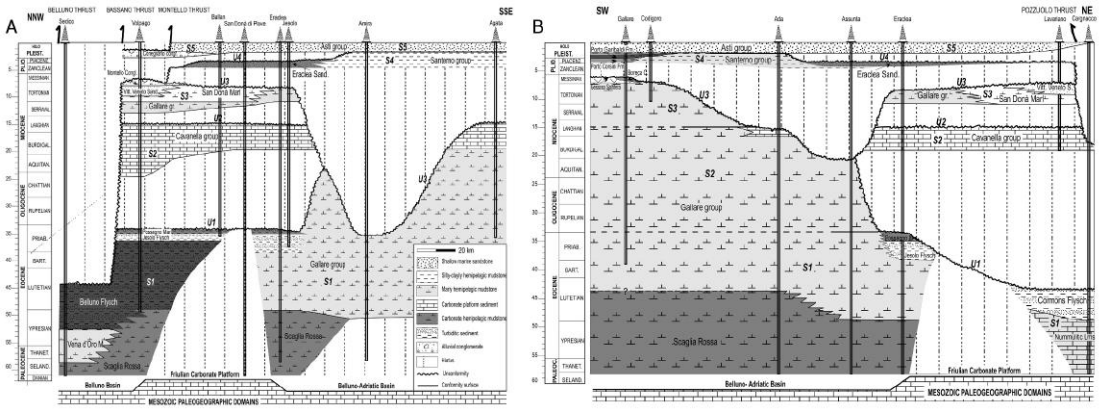

Figure 12.6: Chronostratigraphic frame of the Cenozoic subsurface succession of the Friulian-Venetian area. A) South-alpine transect AA'; B) Dinaric/Apennine transect BB'. From Mancin et al. (2016).

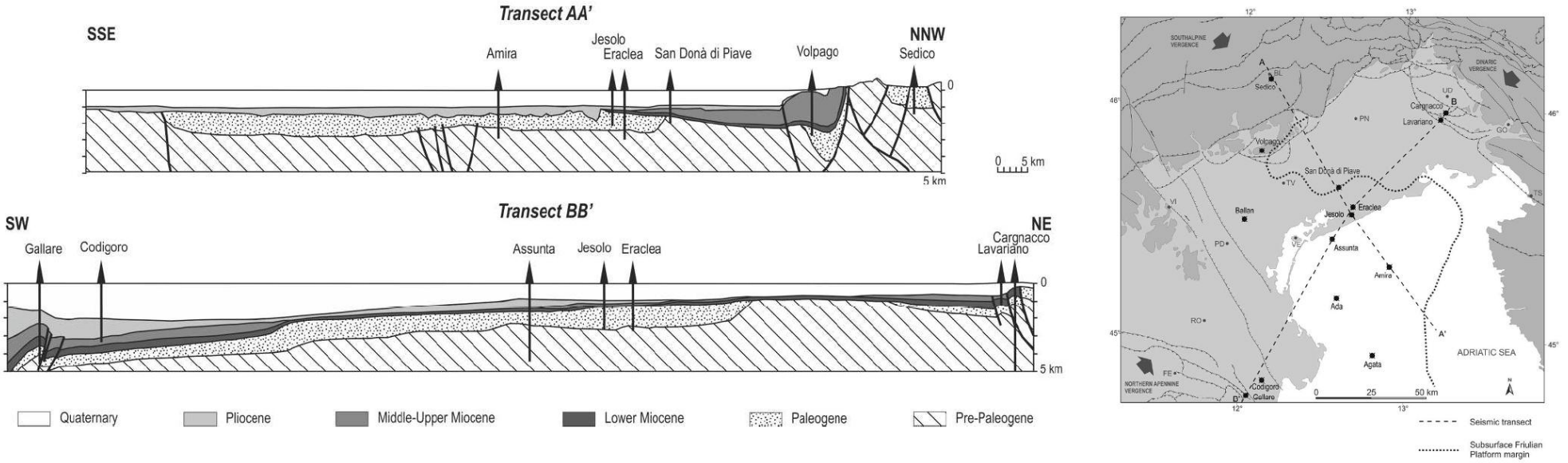

Figure 12.7: Geological sections reconstructed from two seismic sections that cross the study area. They are oriented, respectively, orthogonal to the South-alpine (AA') and Dinaric/Apennine (BB') directions of tectonic transport (grey arrows). From Mancin et al. (2016).

12.3 Gas distribution in relation with gas fields

Apart from vertical migration, the obtained concentration results suggest that gas is able to accumulate within horizontal layering.
The STENAP 08 line, in particular, shows relatively high gas concentration in the horizontal turbiditic layering in the SE part of the line and from CDP 5000 to CDP 6500, especially in the shallower 450 ms. This pattern is interrupted by wide zones of relatively relevant amount of gas vertically distributed. Two of these zones are able to affect the whole sedimentary column (Fig.11.1):

- The first one (CDP 4500) is evident from 400 ms to the end. It is characterized by a strong pull-down effect in the seismic.
- The second one (CDP 7500) seems to reach shallower depths (70 ms) and it exhibits a moderate pull-down effect in the reflectors, together with noise.

Both of them are interpreted as gas chimneys, the first one being rooted below the Messinian Unconformity. Gas fields location map in the study area (Fig.12.8) shows that these two features could be associated to two abandoned biogenic-prone Plio-Pleistocene gas fields. However, at least one of these chimneys appear to be clearly rooted at deeper levels, in the Carbonate Succession, in agreement with the hypothesis of a second, deep, gas system in the area. This gas, possibly mixed with gas from Plio-Pleistocene source/reservoir, migrates along the zones of tectonic weakness and/or permeable paths and accumulate laterally in the turbiditic sequence. Furthermore, the alternation of sandy and clay layers in the shallower 400 ms could contain other-sourced biogenic gas pools that can contribute to the final concentration values.

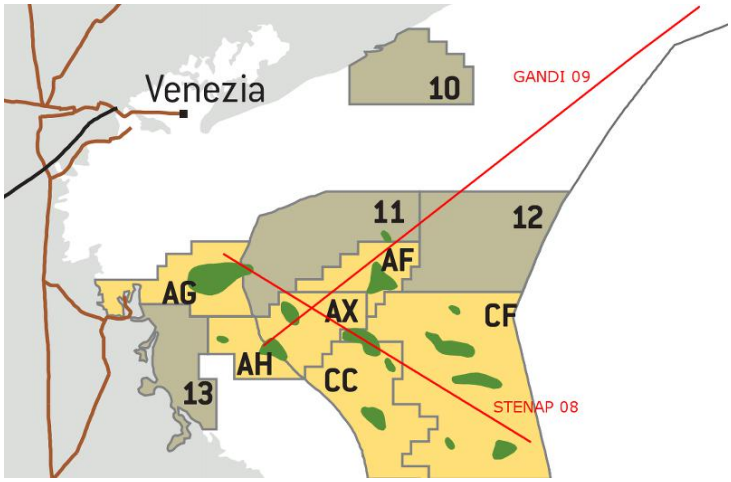

Figure 12.8: Gas production fields in study area. From ENI (2013)

The GANDI 09 line meet two gas fields, one at its very SW part and the other around CDPs 4000-5000. At these locations the seismic data show signal degradation and faulting, correlated to vertical distribution. Some of the tectonic lineaments seems to be rooted in the Carbonate Succession. The GANDI 09 reveals a completely different gas distribution pattern in respect to the STENAP 08. Gas appear widely vertically distributed, without the horizontal accumulations recognized in the STENAP 08 and with lower maximum concentration values. However, the hypothesis of a deep source for the gas is corroborated by the analysis performed on both lines.

Chapter 13

Outlook

In this thesis a complex methodology was applied to obtain the information required to quantify the gas content along the two chosen seismic lines. All the useful data available in the study area were carefully analyzed and used to proceed step by step in the gas quantification. Several missing parameters and petrophysical quantities were estimated and/or extrapolated in the best confident way.
However, a proper characterization of gas presence on the considered spatial scale would require more data to constrain the analysis. In particular:

- 3D seismic data would allow to better image the gas-related features and their extent.
- More well-log data and a denser borehole distribution would definitely help in calibrating the seismic data and the related inversions. Especially, **density logs** could improve the reliability of impedance and porosity calculation. Furthermore, all the boreholes in the area were drilled in the '70s and the composite log were made available in raster format and very often in poor quality. More recently acquired logging measurements would avoid the digitization process with all the related uncertainties and possible misinterpretations.
- The availability of cores samples from the seabed would provide a clearer image of the gas system in the shallower strata. This could be used to extend the analysis from the starting depths of the logs (70-100 ms) to the seabed. In particular, the peat as shallow gas source could be clarified.
  Analysis on cores extracted during the borehole drilling would guide the estimation of density and porosity and give a clue about permeability. Unfortunately, in the selected boreholes, no cores were extracted, neither from the bottom of the borehole nor from the walls. Only a few pore fluid samples were extracted, their salinity measured and resistivity calculated. This information have been used in this analysis. However, the overall conductivity of a rock depends also on the clay content, so that conductivity measurements on cores, together with their description and characterization, could help in the evaluation of the resistivity behavior along the seismic lines.

Apart from the missing constraints, the main issue of this analysis comes from the fact that it was not possible to build a velocity field that could properly represent the shallower layers. The minimum offset in the seismic is not suitable for the water column thickness in the area and refractions heavily affect the main shallow reflections. Having little or no information about the shallower depths made the velocity field poorly reliable at all TWT and not able to detect anomalies possibly related to gas.
So, despite the fact that velocity is traditionally used in detecting gas presence, resistivity anomalies were used in this thesis. However, other methods such as **refraction seismic inversion** or Scholte waves analysis could help in estimating a good velocity field and making this study more trustworthy. **Scholte waves** are acoustic waves propagating at a fluid–solid interface and decaying exponentially. They are dispersive and

characterized by low-velocity and low-frequency (ca 2-20 Hz). Their large amplitudes are able to mask deep reflections. Because they decay rapidly with increasing distance to the liquid/solid interface, sources and receivers must be close to the seabed. Hence, Scholte waves can be recorded by OBC and, in very shallow water, by towed streamers (Boiero et al., 2013). This type of waves have been recorded in some parts of the two analyzed seismic lines, where the right combination of impedance contrast and water thickness occurs. They could be used to invert for near seafloor shear wave velocity structure, particularly problematic for the case study.

Considering that gas is able to influence the resistivity of formations, the procedure built in this thesis could be applied to other case studies where the velocity field is not able to detect gas anomalies.
In any case, it is of crucial importance to be able to assess the gas distribution within sediments in shallow water environments and to recognize seeping of gas. In fact, the potential transfer of gas from sediment to the water column and then into the atmosphere could be significant. Therefore, understanding the mechanisms of gas seepage is important from a climatological point of view. Moreover, fluid leakage can represent a problem for infrastructures stability and could help in the understanding of sediment remobilization.
Deep and cold biogenic gas is becoming more and more important for the hydrocarbon industry, demonstrating an unexpected exploitability. The largest gas discovery ever made in the Mediterranean Sea (Bertello et al., 2016) is in fact the Zohr play in Egyptian waters, a biogenic gas prone system discovered in 2015. A good understanding of both biogenic gas systems and their migration paths and leakages is therefore crucial nowadays.

Conclusions

A multidisciplinary geophysical approach has been used for the first time to estimate the gas distribution and concentration in the Northern Adriatic sea subsoil. In particular, a complex procedure was required to quantify the gas content along the STENAP 08 and the GANDI 09 seismic lines, as described below.

Seismic processing produced stack sections of the two chosen seismic lines. A first version, migrated, was aimed at imaging the subsurface and to help geological interpretation (Fig.5.20 and Fig.5.23). A second processing sequence was devoted to preserving amplitudes, the crucial information for the quantification of gas (Fig.5.27 and Fig.5.28).

In the **borehole log analysis** empirical relationships between each pair of logs were investigated. In particular, velocity-resistivity cross-plots showed a good correlation, demonstrating a strong relationship between the two quantities for the considered data (Fig.6.7). Such a relationship is important, as velocity is the one of the main parameters conventionally used to recognize and quantify the gas presence.

Acoustic impedance (IP) was estimated at well locations, with an iterative procedure of comparison between real and synthetic traces, guided by a lithological interpretation of the boreholes. IP logs were used to constrain the acoustic inversion of the seismic data, guided by a geological 'a priori' model. This resulted in IP calibrated sections for the STENAP 08 and the GANDI 09 lines (Fig.7.4 and Fig.7.9). The STENAP 08 IP section was used in the estimation of the saturation exponent n, an essential parameter for the gas content quantification (Fig.10.2).

Porosity was estimated at well locations in two ways: using the Effective Medium Theory (Fig.8.2) and using Archie's Law (Fig.8.11). Archie-derived porosities were not considered reliable for the analysis, while EMT porosities were correlated with a multi-attribute analysis (Fig.9.7 and Fig.9.11) and used in the final gas quantification.

Seismic-well logs multi-attribute correlation was performed to predict P-wave velocity, resistivity and porosity along the two seismic lines. The estimated P-wave velocity (Fig.9.3 and Fig.9.4), traditionally used in assessing gas presence, didn't detect any relevant anomaly. Actually, the main issue encountered in the whole analysis came from the fact that it was not possible to build a velocity field that could properly represent the shallower layers. The minimum offset in the seismic is not suitable for the water column thickness in the area and refractions heavily affect the main shallow reflections. Having little or no information about the shallower depths made the velocity field poorly reliable at all TWT and not able to detect anomalies possibly related to gas.
However, resistivity sections (Figs.9.5-9.10) showed strong anomalies in the regions where seismic data present a strong variation in frequency content. These anomalies have been assumed to be induced by the presence of gas, and resistivity sections as representative of the gas-induced anomalies over a background resistivity field. Taking advantage of Archie's law, they were used, together with porosity, to quantify the gas content along the two seismic lines (Fig.10.4 and Fig.10.5).

Gas content results range between 0% and 0.3% of the whole rock volume, in both seismic lines. In

the STENAP 08, an heterogeneous gas distribution can be observed. Highest concentrations are found corresponding to the sub-horizontal strata located at the initial portion of the seismic lines, between 70 *ms* and 1200 *ms* and along vertical paths (Fig.11.1). In the GANDI 09, the highest gas concentrations are found along vertical paths (Fig.11.6).

Gas content results were integrated with a geological interpretation of the two seismic lines, in the broader context of the whole study area. Several gas-related features were identified in the seismic data (Fig.11.2 and Fig.11.7), using the amplitude preserved stack sections as a reference for the amplitude information (Fig.11.4 and Fig.11.9). Both vertical and laterally extensive fluid flow were recognized and interpreted in relation to seal by-pass systems. This analysis better constrains the gas occurrence and distribution within the sedimentary succession and helps in clarify the role of tectonics.
According to the previous qualitative analyses (Donda et al., 2015), gas appears to be widely distributed within the Plio-Quaternary succession. Both the stratigraphic and the structural setting strongly influence the gas occurrence. Gas appears to permeate the sub-horizontal Plio-Pleistocene turbiditic layers, but is also concentrated along sub-vertical paths, deeply rooted. The latter are represented by pipes and chimneys observed in the seismic, which originate at various levels of the sedimentary succession. some of them at pre-Pliocene depths. Locally they appear to be associated with faults, which would then represent preferential paths for gas upward migration.
Along the two seismic profiles, results suggest that a secondary gas source could be hypothesized in a pre-Messinian formation, possibly in the Cretaceous Succession. Gas then migrates upward and possibly mix with the Plio-Pleistocene accumulations.
The gas is not always able to reach the shallowest sediments, possibly because of the occurrence of clay seals, as shown by the lithological logs. Unfortunately, the shallowest sediments were not included in the gas quantification. Concentration values were not obtained for the first 70 *ms* (STENAP 08) and 100 *ms* (GANDI 09), which corresponds to starting depth of the resistivity log measurements.
However, local leakage from the seabed has been observed, sampled and analyzed (see sec.3.4). This have been addressed to very shallow (depth<350m) laterally persistent Late-Pleistocene peat layers (Donda et al., 2019, in press).

Geophysical characterization is a fundamental tool in investigating fluid bearing sediments. The approach used in this thesis was to correlate seismic and log data to image and provide an estimate of the gas distribution within the sedimentary succession. Amplitude preserving processing of the seismic data and a quantitative analysis of log data were found to be essential.
Results demonstrate that a multidisciplinary approach is required to interpret the seismic response, which is generally the starting point in the subsurface investigation. Log data provide information on the characteristic of the sediments and record the variations of the fluids present, thus a geological and geophysical data integration was performed. The analysis of the results were conducted considering the constraints coming from the different datasets.
Additional measurements (such as cores or fluid samples) could help in constraining the quantification. More well-log data and a denser borehole distribution would provide a more precise quantification. Availability of 3D seismic data would be invaluable to better image the various gas related features. To assess the overall gas content within sediments in the study area, such a procedure should be applied to the other lines available in the seismic dataset. Nevertheless, the combined analysis on the two chosen perpendicular lines, that cross the entire study area, provides a first attempt at large-scale quantitative assessment of gas content in the Northern Adriatic.

Appendices

Appendix A

Deconvolution

This appendix gives a mathematical background to deconvolution. It starts from the definition of convolutional model, arriving to the construction of the prediction error filter. The seismic processing performed in this thesis makes extensive use of this procedure, at various levels of the flow.
Deconvolution is a signal processing procedure that has important applications in various scientific fields such as radar signal and astronomical image processing, in order to improve the sharpness of images.
In seismic exploration deconvolution is an important step of seismic processing, applied to improve **temporal resolution** of traces, allowing better top and bottom identification of thinner layers and thus better definition of subsurface geology.
Deconvolution is also used to attenuate multiple reflections that occur when the seismic energy is reflected more than once at each interface. In this case, it is called *predictive deconvolution* and the multiple reflections are considered as noise to be eliminated.

A.1 Convolutional Model and Inverse Filter

In the linear stationary system theory, the seismic trace can be represented as the result of the wavelet convolution with the impulse response of the medium, also called reflectivity function:

$$s(t) = w(t) * e(t) \tag{A.1}$$

$s(t)$= seismic trace (output)

$w(t)$= wavelet (input)

$e(t)$= reflectivity function

Note that the random noise component is neglected.
Deconvolution is used for:

- Compute the earth's reflectivity $e(t)$ given the seismic trace $s(t)$ and the source wavelet $w(t)$;
  - If the source wavelet is known, the deconvolution becomes deterministic;
  - If the source wavelet is not known, the deconvolution becomes statistical.

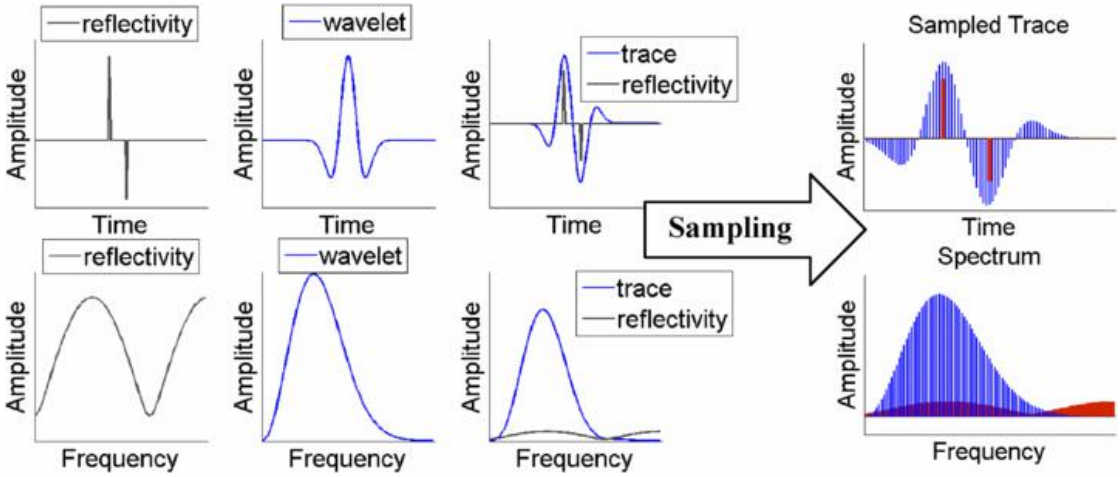

Figure A.1: Convolutional Model. From Guo and Wang (2012)

- Compute the source wavelet $w(t)$ given the seismic trace $s(t)$ and the earth's reflectivity $e(t)$ (this is used if a seismic trace is recorded near a borehole).

To know the medium, the inverse filter $f(t)$ should be found such that:

$$f(t) * w(t) = \delta(t) \tag{A.2}$$

$$\Downarrow$$

$$f(t) * s(t) = f(t) * w(t) * e(t) = e(t) \tag{A.3}$$

So that the effect of the source is eliminated, leaving only the effect of the Earth.

In the frequency domain Eq.A.2 becomes:

$$W(f)F(f) = 1 \tag{A.4}$$

$$F(f) = \frac{1}{W(f)} = \frac{1}{\mid W(f) \mid} exp[-i\Phi_w(f)] \tag{A.5}$$

so that:

$$\Re[F(f)] = \frac{1}{\mid W(f) \mid} \tag{A.6}$$

$$\Phi_f(f) = -\Phi_w(f) \tag{A.7}$$

Therefore, the amplitude spectrum of the inverse filter is the reciprocal of that of the source wavelet whereas its phase spectrum is the negative of that of the wavelet.
Taking the Inverse Fourier Transform of $F(f)$, the desired inverse filter $f(t)$ is found, but its energy has to be limited and the limits should be justified from a physical point of view:

- If $w(t)$ is causal $\Rightarrow$ $f(t)$ will be causal (it will have a lower limit);
- If $f(t)$ is stable (with finite energy, realizable), i.e. $\Sigma_n \mid f(t) \mid < \infty$
  $\Rightarrow$ can be truncated.

Causal and realizable filters are by definition also minimum phase filters and for having a minimum phase filter a *minimum phase wavelet* is required. To be precise, a *minimum delay wavelet* is required, i.e. a minimum phase and front loaded wavelet.
So, using an exact inverse filter requires a special kind of wavelet.
We can also use the Z transform in Eq.A.4, which results in:

$$F(Z) = \frac{1}{W(Z)} \tag{A.8}$$

$F(Z)$ is an infinite polynomial of Z that is convergent (again) only if $w(t)$ is a minimum phase wavelet.
For practical reasons (realizable filter), the infinite polynomial $F(Z)$ has to be truncated to n terms (i.e., $F_n(Z)$).
Truncation generates less error if:

- $w(t)$ is a minimum phase wavelet;
- more terms of $F_n(Z)$ are included.

The truncated filter $f_n(t)$ is calculated by taking the inverse Z-transform of $F_n(Z)$.
Because of truncation, convolution of the truncated filter $f_n(t)$ with the wavelet will *not* give the desired output $d(t) = \delta(t) = (1, 0, 0...0)$.
The actual output $y(t)$ is given by:

$$y(t) = f_n(t) * w(t) \tag{A.9}$$

Apparently, $y(t) \neq d(t)$ and there will be a truncation error E defined as:

$$E = \Sigma_i (d_i - y_i)^2 \tag{A.10}$$

where d_i and y_i are the i-th samples of the desired and actual outputs, respectively.

Deconvolution is based on the application of a Wiener filter $f(t)$ which is designed so that the least-squares error E between the actual and desired outputs is minimum.

$$E = \Sigma_i (d_i - (f(t) * w(t))_i)^2 \tag{A.11}$$

This is a typical least squares problem, and the minimum error is obtained by setting the partial derivatives of E to zero:

$$\frac{\partial E}{\partial f_j} = 0, \qquad j = 0...(n-1) \tag{A.12}$$

$$\Downarrow$$

$$\Sigma_{i=0}^{n-1} r_{j-i} f_i = g_j \tag{A.13}$$

where g_j is the j-th term of the crosscorrelation between $d(t)$ and $w(t)$ and r_j is the j-th term of the autocorrelation of $w(t)$:

$$g_j = \Sigma_i d_i w_{i-j} = (d(t) \star w(t))_j \tag{A.14}$$

$$r_j = \Sigma_i w_i w_{i-j} = (w(t) \star w(t))_j \tag{A.15}$$

and the minimum error is:

$$E_{min} = \Sigma_i \delta_i^2 - \Sigma_j f_j g_j \tag{A.16}$$

If $g(t)$ and $r(t)$ are known, equations A.13 can be solved uniquely to find the filter $f(t)$. Equations A.13 are known as the normal equations. The associated autocorrelation matrix of R_{ij} is called Toeplitz matrix and it can be inverted efficiently using the Levinson recursion procedure.
The simplest application of the normal equations A.13 is the design of an inverse optimum filter such that the desired output is a zero-lag spike. This kind of deconvolution, called *spiking deconvolution*, could be seen as special case of the more general *predictive deconvolution*. The goal of predictive deconvolution is to generalize the normal equations to remove multiple contamination.
To perform deterministic deconvolution, autocorrelation of the wavelet $r_w(t)$ and crosscorrelation between the desired output and the wavelet $g(t)$ need to be known. Unfortunately, in most cases, the source wavelet is not known. However, it is possible to derive a relationship between the trace autocorrelation $r_s(t)$ and the wavelet autocorrelation $r_w(t)$. In fact, because of the (supposed to be) random nature of $e(t)$, its autocorrelation $r_e(t)$ is generally zero anywhere except at $t = 0$:

$$r_{e0} = \Sigma_i e_i^2 \tag{A.17}$$

Therefore:

$$r_e(t) = r_{e0}\delta(t) \tag{A.18}$$

Using convolution and correlation properties:

$$\begin{aligned} r_s(t) &= s(t) \star s(t) \\ &= s(t) * s(-t) \\ &= \big[w(t) * e(t)\big] * \big[w(-t) * e(-t)\big] \\ &= \big[w(t) * w(-t)\big] * \big[e(t) * e(-t)\big] \\ &= r_w(t) * r_e(t) \\ &= r_{e0}\delta(t) * r_w(t) \\ &= r_{e0} r_w(t) \end{aligned}$$

$$r_s(t) = C\, r_w(t) \tag{A.19}$$

i.e. the autocorrelation of the seismic trace is a scaled version of the autocorrelation of the source wavelet.
Note that if the earth response $e(t)$ can safely be approximated as a white random series of impulses, the amplitude spectrum of $e(t)$ will be constant. Using the convolutional model:

$$s(t) = w(t) * e(t) \tag{A.20}$$

$$\mid S(f) \mid = \mid W(f) \mid \mid E(f) \mid = E_0 \mid W(f) \mid \tag{A.21}$$

Which means that the amplitude spectrum of the seismic trace is a scaled version of the amplitude spectrum of the source wavelet. So, provided the randomness and whiteness about $e(t)$, $\mid S(f) \mid$ and $r_s(t)$ can be used instead of $\mid W(f) \mid$ and $r_w(t)$ in the filter design, missing just a scaling factor.
The other function that need to be known is the cross-correlation between $d(t)$ and $w(t)$: $g(t)$. This, again,

requires the wavelet to be known. One way to walk around this problem is to replace the crosscorrelation $g(t)$ with the autocorrelation of the source wavelet $r(t)$. This can be done requiring the desired output $d(t)$ to be a time-advanced version of the input. Basically normal equations are solved for the filter $f(t) = p(t)$ that can transform the input signal to the same signal but only advanced a certain number of samples (let's say α samples or lag).

Given $x(t)$ as input, since

$$d(t) = x(t + \alpha) \tag{A.22}$$

$$\Downarrow$$

$$g(t) = d(t) \star x(t) = x(t + \alpha) \star x(t) = r(t + \alpha) \tag{A.23}$$

Therefore $g_0 = r_\alpha$, $g_1 = r_{\alpha+1}$, ..., $g_{n-1} = r_{\alpha+n-1}$.

$$\begin{bmatrix} r_0 & r_1 & r_2 & \dots & r_{n-1} \\ r_1 & r_0 & r_1 & \dots & r_{n-2} \\ \vdots & \vdots & \vdots & \vdots & \\ r_{n-1} & r_{n-2} & r_{n-3} & \dots & r_0 \end{bmatrix} \begin{bmatrix} p_0 \\ p_1 \\ \vdots \\ p_{n-1} \end{bmatrix} = \begin{bmatrix} r_\alpha \\ r_{\alpha+1} \\ \vdots \\ r_{\alpha+n-1} \end{bmatrix} \tag{A.24}$$

When $p(t)$ is convolved with the input $x(t)$, it will give an actual output $y(t)$ that is the best least squares fit to the desired output $d(t) = x(t + \alpha)$.
In the case of seismic trace deconvolution, $x(t)$ is the seismic trace $s(t)$, which includes a predictable part (e.g., multiples) and a non-predictable (random) part consisting of primaries:

$$s(t) = m(t) + e(t) \tag{A.25}$$

Therefore, $y(t)$ will only contain an estimate $\widehat{m}(t + \alpha)$ of the shifted predictable part $m(t + \alpha)$ of the desired output $d(t) = s(t + \alpha) = m(t + \alpha) + e(t + \alpha)$, where $e(t + \alpha)$ represents the random part of $s(t + \alpha)$ generated by shifting the earth response $e(t)$.
Therefore, $e(t + \alpha)$ can be found as:

$$e(t + \alpha) = d(t) - y(t) = s(t + \alpha) - p(t) * s(t) \tag{A.26}$$

Eq.A.26 can be manipulated to yield the earth response $e(t)$:

$$e(t) = s(t) * \left[\delta(t) - p(t - \alpha)\right] = s(t) * a(t) \tag{A.27}$$

where $a(t) = \delta(t) - p(t - \alpha)$.

Eq.A.27 states that the earth response $e(t)$ can be retrieved by convolving the filter $a(t)$ with the seismic trace $s(t)$.
The filter $a(t)$ is called the *prediction error filter* and is given by:

$$a(t) = (1, \underbrace{0, 0, ..., 0}, \overbrace{-p_0, -p_1, ..., -p_{n-1}}). \tag{A.28}$$

with $(\alpha - 1)$ 0 and n filter coefficients.
For $\alpha = 1$, $a(t) = (1, -p_0, -p_1, ..., -p_{n-1})$ and the normal equations can be manipulated to have the same structure as equations of spiking deconvolution) except for a scaling factor k:

$$\begin{bmatrix} r_0 & r_1 & r_2 & \dots & r_{n-1} \\ r_1 & r_0 & r_1 & \dots & r_{n-2} \\ \vdots & \vdots & \vdots & \vdots & \\ r_{n-1} & r_{n-2} & r_{n-3} & \dots & r_0 \end{bmatrix} \begin{bmatrix} 1 \\ -p_0 \\ \vdots \\ -p_{n-1} \end{bmatrix} = \begin{bmatrix} k \\ 0 \\ \vdots \\ 0 \end{bmatrix} \tag{A.29}$$

Hence, the spiking prediction error filter $a(t) = (1, -p_0, -p_1, ..., -p_{n-1})$ is the inverse filter of the source wavelet of our input seismic trace s(t) except for a scaling factor.
To perform spiking deconvolution $a(t)$ must be convolved with the trace $s(t)$ to get the earth response $e(t)$.
Prediction error filters with prediction lags of $\alpha \gg$ sample interval are used for multiple suppression.

Appendix B

Migration

In this appendix one of the main concept behind migration algorithms is revised and the main migration strategies are commented. Migration was one of the most time-consuming step of the processing flow applied in this thesis. However, its cost is rewarded by a great improvement in the quality of the data.

B.1 Exploding reflectors method

Migration needs zero-offset section (recorded by moving a single source and a single receiver along the line with no separation between them). Recorded energy follows a raypath that is normal incidence to reflecting interfaces. However, such a geometry is not realizable in practice (not only for multi-channel acquisition, as stacked data are not exactly the same of zero-offset ones, but also for single-channel data), but an alternative geometry can be considered, that will produce the same seismic section.
The model described by this alternative geometry is referred to as the *exploding reflectors model*. It represents reflecting interfaces as a set of punctual sources exploding in unison at $t = 0$ (Fig.B.1).

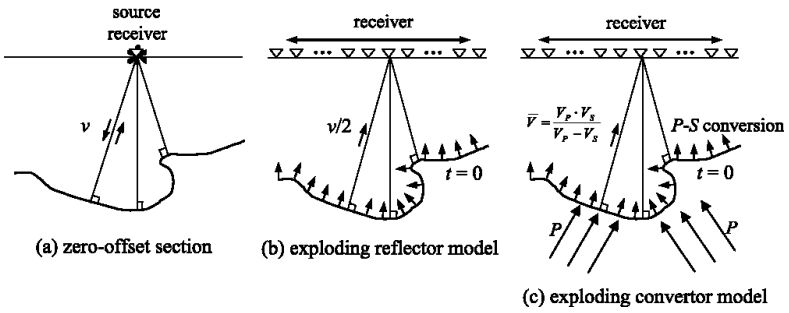

Figure B.1: Exploding reflectors model. From Chen and Wen (2005).

Waves generated on the reflecting interface travel upward and are recorded at surface. Multiple reflections are excluded and every source is supposed to have the amount of energy related to the reflecting coefficient at that point. Thus, recorded data can be thought as the result of an explosion on the interested reflecting interface and the seismic section that results is largely equivalent to the zero-offset ones, but recorded as one-way travel time.
If $u(x, z, t)$ is the displacement field and $t = 0$, is the explosion time, then $u(x, z, 0)$ represents the

reflector's geometry. The recorded field at t is $u(x, 0, t)$.
Let's consider a medium with constant velocity v on which a punctual source (x_0, z_0), a **diffractor**, explodes at $t = 0$. The displacement field will be formed by spherical wavefronts (here, circular), propagating with velocity v:

$$u(x, z, t) = \delta((x - x_0)^2 + (z - z_0)^2 - (vt)^2) \tag{B.1}$$

at the surface, $z = 0$:

$$u(x, z, t) = \delta((x - x_0)^2 + z_0^2 - (vt)^2) \tag{B.2}$$

The resulting seismic section is nothing but a diffraction hyperbola with apex in $(x = x_0, t = z_o/v)$ (see Fig.B.2).

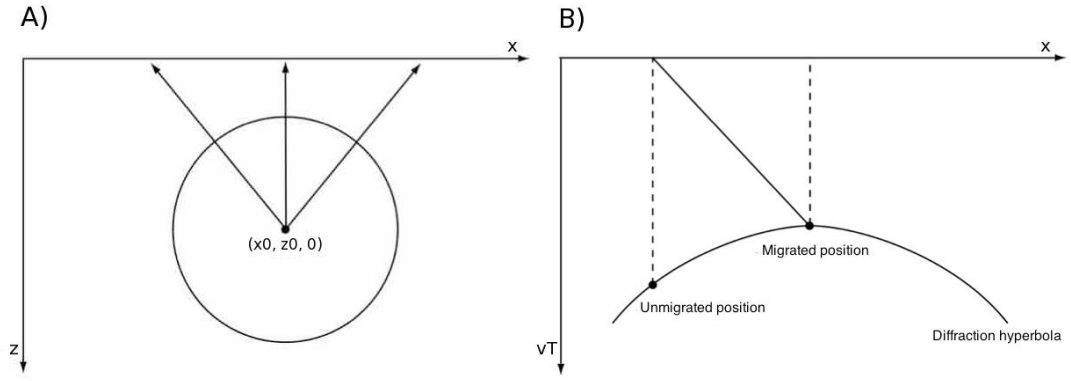

Figure B.2: A) Diffractor; B) Diffraction hyperbola. Modified from Yilmaz (2001)

This diffraction hyperbola does NOT represent a real geological structure and, as for dipping reflectors, the only point visualized well in the section is the one on the vertical of x_0.
Huygens' principle stated that every reflecting interface can be thought as a set of punctual sources and the related reflection as the sum of those sources wavefronts, i.e. as superposition of diffraction hyperbola. Diffraction hyperbola amplitude is maximum in the apex decaying to the sides as the cosine's angle. To correct these diffraction hyperbola we have to bring back energy to the diffraction point. An interface with dip θ will produce the same reflections of a a set of diffraction points very close to each other.
Such an interface will create an apparent dipping layer in the section, with angle $\theta' < \theta$. The same angle could arise from constructive interference of diffraction hyperbola generated by the mentioned set of diffractors.
Making the two related arrival times the same (r=real, a=apparent), the relation between θ and θ' is obtained:

$$vT_r = vT_a \Rightarrow \ sin(\theta) = tg(\theta') \tag{B.3}$$

Eq.B.3 is called *fundamental equation of migration*.

Basically, the apparent interface doesn't pass through the apex of each hyperbola, but it's shifted respect to the real interface and it looks less sloping (see Fig.B.3).

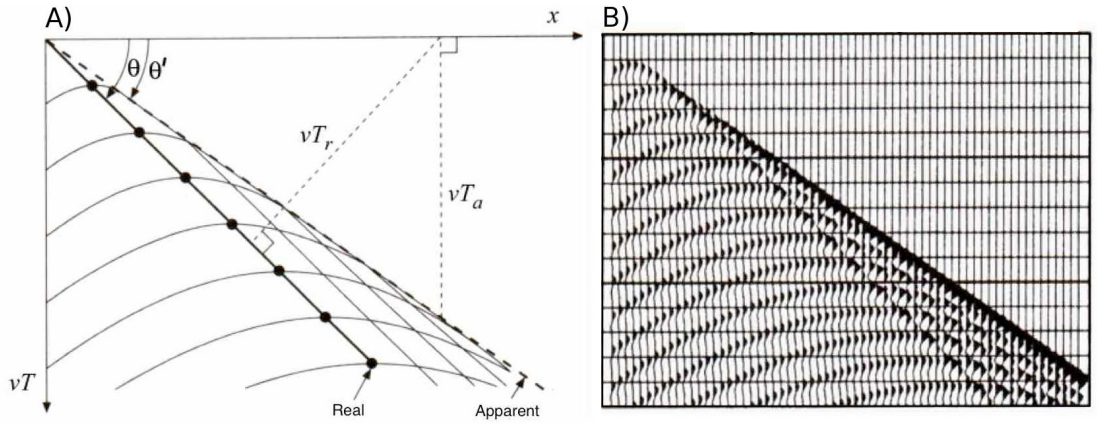

Figure B.3: Real vs Apparent dipping reflector. A) Theoretical plot; B) Synthetic example. Modified from Yilmaz (2001).

Generally speaking, even very simple geological structures could appear deformed in a not migrated section.

B.1.1 Exploding reflectors limits

Exploding reflectors method is simple and powerful but it has some limits. First, it can be applied only in zero-offset section, second, even with zero-offset section, it could give wrong results. It fails in:

1. Treating lateral velocity variation.
   If there is a lateral variationin the velocity field, exploding reflectors geometry is not equivalent to the zero-offset ones and the model misses some rays actually present in the unmigrated section;

2. Treating multiples.
   Considering a flat seabed with travel time $2t_1$, multiples will be predicted at $4t_1$, $6t_1$, $8t_1$ etc. In our model the first multiple will travel from reflector to the surface, then from back to the reflector and in the end back to the surface for a total time of $3t_1$. Following multiples will arrive at $5t_1$, $7t_1$ etc. However, migration algorithms don't model the multiple field (or surface waves or noise in general), the whole energy is treated as primary energy;

3. Treating polarity of waves bouncing off both sides of an interface.

Appendix C

Resistivity Theory: Archie's laws

This appendix treats some delicate issues related to Archie's theroy, which is widely used in this thesis. The main concepts of the theory are explained and approximations/corrections of the related equations are investigated. The whole appendix is based on Glover (2009).

C.1 Basic definitions

Resistance r is a property of the material which describes how much the material resists the passage of a current I for a given applied potential difference ΔV:

$$r = \frac{\Delta V}{I} \tag{C.1}$$

Resistance per unit length and area is called resistivity R and can be expressed as:

$$R = \frac{\Delta V}{I}\frac{A}{L} \tag{C.2}$$

where:

R = resistance of the sample (Ωm)
ΔV = potential difference across the sample (V)
I = current flowing through the sample (A)
A = cross-sectional area of the sample (m^2)
L = length of the sample (m)
Note that conductivity is the reciprocal of resistivity R.

C.2 Resistivity of rocks

Generally speaking, drilled and reservoir rocks contain the following constituents:

- Matrix material;
- Formation waters (mostly saline);
- Oil/Gas;

- Water-based mud filtrates;
- Oil-based mud filtrates.

They all have a high electrical resistivity except formation waters and water-based mud filtrates, which are good electrical conductors and have low electrical resistivity [1].
Therefore, resistivity of the drilled/reservoir rocks depends mainly upon the water or water-based mud filtrate occupying their pore space.

C.2.1 Drilling fluid invasion

Invasion is a process whereby drilling mud fluid is forced into the rock due to differential pressure. The liquid component of the drilling fluid (known as the mud filtrate) continues to invade the porous and permeable formation until the solids present in the mud, commonly bentonite, clog enough pores to form a mud cake capable of preventing further invasion.
The mud filtrate displaces some or all of the moveable fluids in the formation, leaving an invaded zone. The invasion process is complex, it depends mainly on formation and mudcake permeability, filtrate and formation fluid densities and saturations and differential pressure.
Invasion has significant implications for well logging. Well logs depth of investigation is very small (a few centimeters) and it is possible that the drilling fluid has invaded beyond this depth, affecting the readings. This is particularly true in the case of resistivity logs, the crucial ones for Archie's porosity estimation. Normally, a number of corrections are made to account for this effect, during the acquisition, processing and interpretation. It is very important to choose the appropriate resistivity tool for the expected environmental conditions. For example, induction tools are best suited for low-resistivity formations, drilled with fresh mud. This is the case of all the resistivity logs used in this section. Laterolog tools, instead, are most accurate in medium to high resistivity formations.
With either laterolog or induction deep-resistivity measurements, it is essential to record at least three resistivity-log curves with different depths of investigation. This is because the correction is based on a invasion model (such as step profile or transition zone model) which considers always at least three parameters. With less than three measurements it is not possible to model and correct for the invasion.

Uninvaded Zones

For uninvaded formations, the measured bulk resistivity of the rock depends only upon the amount of the aqueous formation fluids present in the rock, and the resistivity of those aqueous fluids. Since the amount of formation fluids depends both on porosity ϕ and water saturation S_w, resistivity of the formation R_t depends upon porosity, water saturation, and the resistivity of the formation water R_w. This resistivity is called the *true resistivity* of the formation. It is the resistivity of the formation in the uninvaded zone, where the rock contains some saturation of oil S_o, gas S_g, and water S_w, and where $S_o + S_g + S_w = 1$. Typical values of R_t range from 0.2 to 2000 Ωm.

C.2.2 Temperature and pressure

Resistivity of formation fluids and water-based drilling muds varies little with pressure but greatly with temperature. The increase is approximately 4% per degree centigrade and it causes the resistivities measured with downhole tools to increase steadily down the borehole. To avoid this added complication, all downhole resistivity measurements are corrected to read the resistivity they would read if the entire borehole was at some constant temperature ($24°C/75°F$) is often used). This is normally done by the wireline logging company using a chart or an equation that represents the chart. Correction is based

[1] Except when the matrix material has a relevant clay content, which is conductive

upon Hilchie's equation for the variation of the resistivity of aqueous fluids with temperature. Hilchie's equation relates the resistivity of an $NaCl$ solution at one temperature to that at another.
In the case of invaded formations, variations of drilling mud, mudcake and mud filtrate resistivity with temperature is also to be taken into account.

C.3 Formation Factor

Archie observed that the bulk resistivity of a rock R_0 fully saturated with an aqueous fluid of resistivity R_w is directly proportional to the resistivity of the fluid itself:

$$R_0 = F\, R_w \tag{C.3}$$

The constant of proportionality F is called *Formation Factor* and describes the effect of the presence of the rock matrix. It can be immediately seen that $F = 1$ for a rock with 100% porosity (100% fluid, no matrix). In real rocks F takes values usually between 20 and 500.
Formation factor can be seen as a factor that describes the extent to which electrically insulating mineral grains dilute the conducting fluid, making the bulk material more resistive than the fluid alone. The formation factor includes both the effect of the variable porosity and the effect of the tortuous pathways that the current is forced to take through the conducting fluid due to the presence of the insulating rock grains. Therefore, the F factor is related to the porosity of the rock and the connectivity of the pore spaces. Archie experimentally noticed that the folowing rule is commonly true:

$$F = \phi^{-m} \tag{C.4}$$

Eq.C.4 is called **Archie's First Law** and m is the cementation index.

Note that sometimes a constant a is placed before the porosity term, and so $F = a$ when $\phi = 1$. However, there is no physical justification for this term. It arises from applying a best fit engineering equation to F versus porosity data and should be avoided. Parameter a is called tortuosity.
Combining the two previous equation we get:

$$R_0 = R_w\, \phi^{-m} \tag{C.5}$$

The cementation factor m has a theoretical value of 1 for uniform pores penetrating the rock directly from one side of the sample to the other (direct tubes of pore space), and it is 0 for a rock with 100% porosity (no grains to get in the way of the fluid flow). No other values of m are able to be defined in a purely theoretical way, because of the complexity of the way that pore spaces are arranged. In real rocks the cementation index usually varies between 1.0 and 3.0. Values between 1.4 and 2.0 are found in sandstones, with the higher values found in more consolidated sandstones, where the current flow paths are more tortuous. Both the formation factor and the cementation exponent can be measured on core plugs in the laboratory. It should be mentioned that there are a range of equations used in the oil industry to calculate F but Archie's equation is the most flexible and reliable. All the others are infact simply specific cases of Archie's, experimentally successful, working very well for a given type of rock.

C.4 Partial Water Saturation

The bulk resistivity of a rock R_t partially saturated with an aqueous fluid of resistivity R_w is directly proportional to the resistivity of the rock when fully saturated with the same fluid:

$$R_t = IR_0 \tag{C.6}$$

The constant of proportionality I is called *resistivity index* and describes the effect of partial desaturation of the rock. If the rock is fully saturated $I = 1$, if it is full of dry air, $I \rightarrow \infty$.
Archie noticed that the following relationship exists empirically for sandstones

$$I = S_w^{-n} \tag{C.7}$$

Eq.C.7 is called **Archie's Second Law**.
S_w is the fractional water saturation of the rock, I is the resistivity index, n is the saturation exponent.

The saturation exponent normally has a range of values from 1.8 to 2.0, however much lower and much higher values have been found. The value of the saturation exponent can be obtained from laboratory experiments on core samples.

Eq.C.4 and Eq.C.7 can be combined into one controlling equation:

$$R_t = R_w \, \phi^{-m} \, S_w^{-n} \tag{C.8}$$

Eq.C.8 is the ones used in section 8.2.

Bibliography

Abma, R. and Claerbout, J. (1995). Lateral prediction for noise attenuation by t-x and F-X techniques. *Geophysics*, 60.

Adelinet, M., Fortin, J., and Gueguen, Y. (2011). Dispersion of elastic moduli in a porous-cracked rock: Theoretical predictions for squirt flow. *Tectonophysics*, 503(1-2).

Adelinet, M. and Le Ravalec, M. (2015). Effective medium modeling: How to efficiently infer porosity from seismic data? *Interpretation*, 3(4).

Amadori, C., Garcia-Castellanos, D., Toscani, G., Sternai, P., Fantoni, R., Ghielmi, M., and Di Giulio, A. (2018). Restored topography of the Po Plain-Northern Adriatic region during the Messinian base-level drop—Implications for the physiography and compartmentalization of the palaeo-Mediterranean basin. *Basin Research*, 30(6).

Andresen, K. (2012). Fluid flow features in hydrocarbon plumbing systems: What do they tell us about the basin evolution? *Marine Geology*, s 332–334.

Aplin, A., Fleet, A., and Macquaker, J. (1999). Mud and Mudstone: Physical and Flui-flow Properties. *Geological Society, London*, Special Pubblications 158(1).

Bacon, M., Simm, R., and Redshaw, T. (2003). *3-D Seismic Interpretation*. Cambridge, United Kingdom.

Baltzer, A., Tessier, B., Nouzé, H., Bates, R., Moore, C., and Menier, D. (2005). Seistec seismic profiles: A tool to differentiate gas signatures. *Mar. Geophys. Res.*, 216(26).

Barnes, A. (1998). The complex seismic trace made simple. *The leading Edge*, 17(4).

Battaglia, M., Murray, M., Serpelloni, E., and Burgmann, R. (2004). The Adriatic region: An independent microplate within the Africa-Eurasia collision zone. *Geophys. Res. Lett.*, 31(9).

Bekara, M. and Van der Baan, M. (2009). Random and coherent noise attenuation by empirical mode decomposition. *Geophysics*, 74(2).

Berkhout, A. (1980). *Seismic Migration*. Elsevier, first edition.

Bernard, B., Books, J., and Sackett, W. (1976). Natural gas seepage in the Gulf of Mexico. *Earth Planet. Sci. Lett.*, 31.

Berndt, C. (2005). Focused fluid flow in passive continental margins. *Philosophical Transactions of the Royal Society A: Mathematical, Physical and Engineering Sciences*, 363(1837).

Bertello, F., Fantoni, R., and Franciosi, R. (2008). Overview on Italy's petroleum systems and related oil and gas occurrences. *70th EAGE Conference & Exhibition, Rome, Italy*, Extended Abstract & Exhibitor's Catalogue.

Bertello, F., Fantoni, R., Franciosi, R., Gatti, V., Ghilemi, M., and Pugliese, A. (2010). From thrust-and-fold belt to foreland: hydrocarbon occurrences in Italy. *Petroleum geology Conference series*, 7.

Bertello, F., Harby, H., and Brandolese, S. (2016). Egypt: Zohr, an Outstanding Gas Discovery in a New Deep-Water Hydrocarbon Play. . *MOC 2016*.

Bertoni, C., Kirkham, C., Cartwright, J., Hodgson, N., and Rodriguez, K. (2017). Seismic indicators of focused fluid flow and cross-evaporitic seepage in the Eastern Mediterranean . *Marine and Petroleum Geology*, 88.

Bjørlykke, K. (1993). Quartz Cementation in Sedimentary Basins. *AAPG Bulletin*, 77.

Boetius, A., Ravenschlag, K., and Schubert, C. (2000). A marine microbial consortium apparently mediating anaerobic oxidation of methane. *Nature*, 407(6804).

Boiero, D., Wiarda, E., and Vermeer, P. (2013). Surface- and guided-wave inversion for near-surface modeling in land and shallow marine seismic data. *The Leading Edge*, 32(6).

Brac, J., Déquirez, P., Hervé, F., Jacques, C., Lailly, P., Richard, V., and Tran Van Nieuh, D. (1988). Inversion with a priori information: An approach to integrated stratigraphic inversion. *58th SEG Annual Meeting, Anaheim, USA*, Expanded Abstract.

Brambati, A., Ciabatti, M., Fanzutti, G., Marabini, F., and Marocco, R. (1983). A new sedimentological textural map of the northern and central Adriatic Sea. *Boll. Oceanogr. Teor. Appl.*, 1(4).

Budiansky, B. and O'Connell, R. (1976). Elastic moduli of a cracked solid. *Int. J. Solids Structures*, 12(2).

Bünz, S., Mienert, J., and Berndt, C. (2003). Geological controls on the Storegga gas-hydrate system of the mid-Norwegian continental margin. *Earth and Planetary Science Letters*, 209(3).

Calderoni, G., Curzi, P., Paganelli, A., and Sartori, E. (1998). Stratigraphic paleoenvironmental preliminary results of Late Quaternary gassy sediments in Venice Lagoon. *Paper presented at 5th International Conference on Gas in Marine Sediments, Bologna, Italy*.

Canali, G., Capraro, L., Donnici, S., Rizzetto, F., Serandrei-Barbero, R., and Tosi, L. (2007). Vegetational and environmental changes in the eastern Venetian coastal plain (Northern Italy) over the past 80,000 years. *Palaeogeogr. Palaeocl.*, 253.

Carminati, E., Doglioni, C., and Scrocca, D. (2003). Apennines subduction-related subsidence of Venice (Italy). *Geophys. Res. Lett.*, 30(13).

Cartwright, J. and Huuse, M. (2005). 3D seismic technology: the geological 'Hubble'. *Basin Research*, 17.

Cartwright, J., Huuse, M., and Aplin, A. (2007). Seal bypass systems. *AAPG Bulletin*, 91.

Cartwright, J., James, D., and Bolton, A. (2003). The genesis of polygonal fault systems: a review. *Geological Society, London, Special Publications*, 216(1).

Cartwright, J. and Santamarina, C. (2015). Seismic characteristics of fluid escape pipes in sedimentary basins: Implications for pipe genesis. *Marine and Petroleum Geology*, 65.

Casero, P. (2004). Structural Setting of Petroleum Exploration Plays in Italy. *Special Volume of the Italian Geological Society for the IGC 32 Florence-2004*.

Casero, P. and Bigi, S. (2013). Structural setting of the Adriatic basin and the main related petroleum exploration plays. *Marine and Petroleum Geology*, 42.

Cathles, L., Su, Z., and Chen, D. (2010). The physics of gas chimney and pockmark formation, with implications for assessment of seafloor hazards and gas sequestration. *Marine and petroleum Geology*, 27.

Cazzini, F., Dal Zotto, O., Fantoni, R., Ghilemi, M., Ronchi, P., and Scotti, P. (2015). Oil and gas in the Adriatic foreland, Italy. *Journal of Petroleum Geology*, 38(3).

Chen, D., Wu, S., Dong, D., Mi, L., Fu, S., and Shi, H. (2013). Focused fluid flow in the Baiyun Sag, northern South China Sea: Implications for the source of gas in hydrate reservoirs. *Chinese Journal of Oceanology and Limnology*, 31.

Chen, L. and Wen, L. (2005). A wave equation migration method for receiver function imaging: 1. Theory. *Conference Proceedings*.

Chopra, S. and Marfurt, K. (2007). *Seismic Attributes for Prospect Identification and Reservoir Characterizatio*. SEG, first edition.

Claerbout, J. (1985). *Imaging the earth's interior*. Blackwell Scientific Publications.

Cohen, J. and Stockwell, J. (2008). *CWP/SU: Seismic Un*x Release No.4.0: an open source software package for seismic research and processing*. Center for Wave Phenomena, Colorado School of Mines.

Coren, F., Volpi, V., and Tinivella, U. (2001). Gas hydrate physical properties imaging by multi-attribute analysis—Blake Ridge BSR case history. *Marine Geology*, 178(1-4).

Correggiari, A., Roveri, M., and Trincardi, F. (1996). Late Pleistocene and Holocene evolution on the North Adriatic Sea. *Ital. J. of Quat. Sc.*, 9.

Craig, J., Gerali, F., and MacAulauy, R. (2018). *History of the European Oil and Gas Industry*. Geological Society of London.

Cuffaro, M., Riguzzi, F., Scrocca, D., Antonioli, F., Carminati, E., Livani, M., and Doglioni, C. (2010). On the geodynamics of the northern Adriatic plate. *Rend. Fis. Acc. Lincei*, 21(1).

Curzi, P., Danovaro, R., and Bruni, R. (1998). Gas, bacterial biomass and OM composition in marine and continental sediment layers from the Venice Lagoon. *Paper presented at 5th International Conference on Gas in Marine Sediments, Bologna, Italy*.

Curzi, P., Fabiano, M., and Fava, G. (1997). Gas and organic matter in last glacial and holocenic sediments of Venice lagoon. *Chem. Ecol.*, 14.

Degobbis, D., Precali, R., Ivancic, I., Smodlaka, N., Fuks, D., and Kveder, S. (2000). Long-term changes in the northern Adriatic ecosystem related to anthropogenic eutrophication. *Int. J. Environ. Pollut.*, 13(1).

Devoti, R., Riguzzi, F., Cuffaro, M., and Doglioni, C. (2008). New GPS constraints on the kinematics of the Apennines subduction. *Earth Planet. Sci. Lett.*, 273(1-2).

Di Stefano, R., Kissling, E., Chiarabba, C., Amato, A., and Giardini, D. (2009). Shallow subduction beneath Italy: Three-dimensional images of the Adriatic–European–Tyrrhenian lithosphere system based on high-quality P wave arrival times. *J. Geophys. Res.*, 114(B5).

Donda, F., Brancolini, G., Tosi, L., Kovavevic, V., Baradello, L., Gacic, M., and Rizzetto, F. (2008). The ebb-tidal delta of the Venice Lagoon, Italy. *The Holocene*, 18.

Donda, F., Civile, D., Forlin, E., Volpi, V., Zecchin, M., Merson, B., and De Santis, L. (2013). The northernmost Adriatic Sea: A potential location for CO2 geological storage? *Marine and Petroleum Geology*, 42.

Donda, F., Forlin, E., Gordini, E., Panieri, G., Buenz, S., Volpi, V., Civile, D., and De Santis, S. (2015). Deep-sourced gas seepage and methane-derived carbonates in the Northern Adriatic Sea. *Basin research*, 27.

Donda, F., Tinivella, U., Gordini, E., Panieri, G., Volpi, V., Civile, D., Forlin, E., Facchin, L., Burca, M., Cova, A., and Ferrante, G. (2019). The origin of gas seeps in the Northern Adriatic Sea. *Italian Journal of Geoscience*.

England, W., Mackenzie, A., Mann, D., and Quigley, T. (1987). The movement and entrapment of petroleum fluids in the subsurface. *Journal of the Geological Society*, 144(2).

ENI (2013). Fact Book 2013.

Eshelby, J. (1957). The determination of the elastic field of an ellipsoidal inclusion, and the related problems. *Proc. R. Soc.*

Fannin, N. (1980). The use of regional geological surveys in the North Sea and adjacent areas in the recognition of offshore hazards. *in Ardus, D.A. (ed.), Offshore Site Investigation. Graham and Trotman, London*.

Fantoni, R. (2017). Mesozoic petroleum system of the adriatic foreland. *Journal of Mediterranean Earth Sciences*, 9.

Fantoni, R. and Franciosi, R. (2010). Tectono-sedimentary setting of the Po Plain and Adriatic Foreland. *Rendiconti Lincei-scienze Fisiche E Naturali*, 21.

Foschi, M. and Cartwright, J. (2016). South Malvinas/Falkland Basin: Hydrocarbon migration and petroleum system. *Marine and Petroleum Geology*, 77.

Ghielmi, M., Minervini, M., Nini, C., Rogledi, S., and Rossi, M. (2013). Late Miocene-Middle Pleistocene sequences in the Po Plain - Northern Adriatic Sea (Italy): The stratigraphic record of modification phases affecting a complex foreland basin. *Marine and Petroleum Geology*, 42.

Ghielmi, M., Minervini, M., Nini, C., Rossi, M., and Vignolo, A. (2010). Sedimentary and tectonic evolution in the eastern Po Plain and northern Adriatic Sea area from Messinian to Middle Pleistocene (Italy). *Rend. Fis. Acc. Lincei*, 21(1).

Glover, P. (2009). *Petrophysics MSc course notes*.

Gordini, E. (2009). *Integrazione di metodologie geofisiche, geomorfologiche, sedimentologiche e geochimiche, per la definizione della genesi e dell'eta' degli affioramenti rocciosi presenti sul fondale marino dell'Adriatico settentrionale*. PhD thesis, Universita' di Trieste.

Gordini, E., Falace, A., Kaleb, S., Donda, F., Marocco, R., and Tunis, G. (2012). *Methane-Related Carbonate Cementation of Marine Sediments and Related Macroalgal Coralligenous Assemblages in the Northern Adriatic Sea in Seafloor Geomorphology as Benthic Habitat-GeoHAB Atlas of Seafloor Geomorphic Features and Benthic Habitats*. Elsevier, first edition.

Greenberg, M. and Castagna, J. (1992). Shear-wave velocity estimation in porous rocks: theoretical formulation, preliminary verification and application. *Geophysical Prospecting*, 40(2).

Gulunay, N. (1986). FXDECON and complex wiener prediction filter. *SEG Technical Program Expanded Abstract*.

Guo, R. and Wang, S. (2012). A spectral method for reflectivity estimation. *Journal of Geophysics and Engineering*, 9(6).

Heggland, R. (2005). Using gas chimneys in seal integrity analysis: A discussion based on case histories. *AAPG Hedberg Series*, 2.

Hicken, J., Alonso, J., and Farhat, C. (2000). *Introduction to Multidisciplinary Design Optimization: Lecture Notes*.

Hosseinyar, G., Moussavi-Harami, R., and Behbahani, R. (2014). Shallow gas accumulations and seepage in the sediments of the Northeast Persian Gulf. *Acta Geophysica*, 62.

Huuse, M., Jackson, C., Van Rensbergen, P., Davies, R. J., Flemings, P. B., and Dixon, R. J. (2010). Subsurface sediment remobilization and fluid flow in sedimentary basins: an overview. *Basin Research*, 22(4).

Iadanza, A., Sampalmieri, G., and Cipollari, P. (2015). Deep-seated hydrocarbons in the seep "Brecciated Limestones" of the Maiella area (Adriatic foreland basin): Evaporitic sealing and oil re-mobilization effects linked to the drawdown of the Messinian Salinity Crisis. *Marine and Petroleum Geology*, 66.

Jakubowicz, H. (1998). Wave equation prediction and removal of interbed multiples. *SEG Technical Program Expanded Abstract*.

Joksimović, A., Djurović, M., Semenov, A., Zonn, I., and Kostianoy (2016). *The Boka Kotorska Bay Environment*. Springer.

Jonk, R. (2010). Sand-rich injectites in the context of short-lived and long-lived fluid flow. *Basin Research*, 22(4).

Judd, A. and Hovland, M. (1992). The evidence of shallow gas in marine sediments. *Continental Shelf Research*, 12(10).

Judd, A. and Hovland, M. (2007). Seabed fluid flow – impact on geology, biology and the marine environment. *Impact on Geology, Biology, and the Marine Environment*.

Le Ravalec, M., Doligez, B., and Lerat, O. (2014). *Integrated reservoir characterization and modeling*. IFPEN.

Lipizer, M., Partescano, E., Rabitti, A., Giorgetti, A., and Crise, A. (2014). Qualified temperature, salinity and dissolved oxygen climatologies in a changing Adriatic Sea. *Ocean Science*, 10.

Long, D. (1992). Devensian late-glacial gas escape in the central North Sea. *Continental Shelf Research*, 12.

Løseth, H., Gading, M., Duffaut, K., and Springer, M. (2011). Can hydrocarbon source rocks be identified on seismic data? *Geology*, 39(12).

Løseth, H., Gading, M., and Wensaas, L. (2009). Hydrocarbon leakage interpreted on seismic data. *Marine and Petroleum Geology*, 26.

Maestrelli, D., Iacopini, D., Jihad, A., Bond, C., and Bonini, M. (2017). Seismic and structural characterization of fluid escape pipes using 3D and partial stack seismic from the Loyal Field (Scotland, UK): A multiphase and repeated intrusive mechanism. *Marine and Petroleum Geology*, 88.

Malvic, T. (2016). Regional turbidites and turbiditic environments developed during Neogene and Quaternary in Croatia. *Materials and Geoenvironment*, 63.

Mancin, N., Barbieri, C., Di Giulio, A., Fantoni, R., Marchesini, A., Toscani, G., and Zanferrari, A. (2016). The Friulian-Venetian Basin II: paleogeographic evolution and subsidence analysis from micropaleontological constraints. *Italian Journal of Geosciences*, 135.

Mantovani, E., Babbucci, D., Viti, M., Albarello, D., Mugnaioli, E., Cenni, N., and Casula, G. (2006). Post-Late Miocene Kinematics of the Adria Microplate: Inferences from Geological, Geophysical and Geodetic data. *In: Pinter, N., Grenerczy, G., Weber, J., Stein, S. and Medak, D., Eds., The Adria Microplate: GPS Geodesy, Tectonics and Hazard*, 61(NATO Science Series IV-Earth and Environmental Sciences).

Mazzini, A., Svensen, H., Planke, S., Forsberg, C., and Tjelta, T. (2016). Pockmarks and methanogenic carbonates above the giant Troll gas field in the Norwegian North Sea. *Marine Geology*, 373.

Mele, G. (2001). The Adriatic lithosphere is a promontory of the Africa Plate; Evidence of a continuous mantle lid in the Ionian Sea from efficient Sn propagation. *Geophys. Res. Lett.*, 28(3).

Mondol, N., Jahren, J., Bjorlykke, K., and Brevik, I. (2008). Elastic properties of clay minerals. *The Leading Edge*, 27(6).

Mort, H., Jacquat, O., Adatte, T., Steinmann, P., Føllmi, K., Matera, V., and Stüben, D. (2007). The Cenomanian/Turonian anoxic event at the Bonarelli Level in Italy and Spain: enhanced productivity and/or better preservation? *Cretaceous Research*, 28(4).

Moss, J. L. and Cartwright, J. (2010). 3D seismic expression of km-scale fluid escape pipes from offshore Namibia. *Basin Research*, 22(4).

Nicolich, R., Della Vedova, B., Giustiniani, M., and Fantoni, R. (2004). Carta del sottosuolo della Pianura Friulana. *Regione FVG e Univ. Trieste*.

Nocquet, J. and Calais, E. (2003). Crustal velocity field of western Europe from permanent GPS array solutions. *Geophys. J. Int.*, 154(1).

Nocquet, J. M., Calais, E., Altamini, Z., Sillard, P., and Boucher, C. (2001). Intraplate deformation in western Europe deduced from an analysis of the International Terrestrial Reference Frame 1997 (ITRF97) velocity field. *J. Geophys. Res.*, 106(B6).

Nunn, J. (1996). Buoyancy-driven propagation of isolated fluid-filled fractures: Implications for fluid transport in Gulf of Mexico geopressured sediments. *Journal of Geophysical Research*, 101.

Oldow, J., Ferranti, L., Lewis, D., Campbell, J., D'Argenio, B., Catalano, R., Pappone, G., Carmignani, L., Conti, P., and Aiken, C. (2002). Active fragmentation of Adria, the north Africa promontory, central Mediterranean orogen. *Geology*, 30(9).

Osborne, M. and Swarbrick, R. (1997). Mechanisms for generating overpressure in sedimentary basins: A reevaluation. *Aapg Bulletin - AAPG BULL*, 81.

Plaza-Faverola, A., Bünz, S., and Mienert, J. (2011). Repeated fluid expulsion through sub-seabed chimneys offshore Norway in response to glacial cycles. *Earth and Planetary Science Letters*, 305.

Plaza-Faverola, A. and Keiding, M. (2019). Correlation between tectonic stress regimes and methane seepage on the western Svalbard margin. *Solid Earth*, 10.

Pola, M., Ricciato, A., Fantoni, R., Fabbri, P., and Zampieri, D. (2014). Architecture of the western margin of the North Adriatic foreland: The Schio-Vicenza fault system. *Italian Journal of Geosciences*, 133.

Rider, M. (1996). *The Geological Interpretation of Well Logs*. Caithness, Whittles Publishing, second edition.

Schlumberger (1991). *Log Interpretation Charts*. Schlumberger limited, New York.

Schrag, D. P., Higgins, J. A., Macdonald, F. A., and Johnston, D. T. (2013). Authigenic Carbonate and the History of the Global Carbon Cycle. *Science*, 339(6119).

Schroot, B. and Schuttenhelm, R. (2003). Expressions of shallow gas in the Netherlands North Sea. *Neth. J. Geosci.*, 82(1).

Taner, M., Koehler, F., and Sheriff, R. (1979). Complex seismic trace analysis. *Geophysics*, 55(6).

Tinivella, U. (1999). A method for estimating gas hydrate and free gas concentrations in marine sediments. *Bollettino di Geofisica Teorica e Applicata*, 40(1).

Tonnellot, T., Bernard, M., and Clochard, V. (2010). Method of Joint inversion of Seismic Data Represented on Different Time Scales. *Patent US2010004870 AA*.

Tosi, L., Zecchin, M., Franchi, F., Bergamasco, A., Da Lio, C., Baradello, L., Mazzoli, C., Montagna, P., Taviani, M., Tagliapietra, D., Carol, E., Franceschini, G., Giovanardi, O., and Donnici, S. (2017). Paleochannel and beach-bar palimpsest topography as initial substrate for coralligenous buildups offshore Venice, Italy. *Scientific Reports*, 7(1321).

Vadakkepuliyambatta, S., Buenz, S., Mienert, J., and Chand, S. (2013). Distribution of subsurface fluid-flow systems in the SW Barents Sea. *Marine and Petroleum Geology*, 43.

Van Rensbergen, P., Hillis, R., Maltman, J., and Morley, C. (2003). Subsurface sediment mobilization: introduction Geological Society, London, Special Publications. *Geological Society, London, Special Publications*, 216.

Van Straaten, L. (1970). Holocene and late-Pleistocene sedimentation in the Adriatic Sea. *Geol. Runds.*, 60(1).

Vernik, L. and Kachanov, M. (2010). Modeling elastic properties of siliciclastic rocks. *Geophysics*, 75(6).

Verschuur, D., Berkhout, A., and Wapenaar, C. (1992). Adaptive surface-related multiple subtraction. *Geophysics*, 57.

Virs, R. (2015). *A comparative seismic study of gas chimney structures from active and dormant seepage sites offshore mid-Norway and west-Svalbard*. PhD thesis, UIT-The Arctic University of Norway.

Wang, Z. (2001). Fundamentals of seismic rock physics. *Geophysics*, 66(2).

Whiticar, M. (1999). Carbon and hydrogen isotope systematics of bacterial formation and oxidation of methane. *Chemical Geology*, 161.

Wilkens, R. and Richardson, M. (1998). The influence of gas bubbles on sediment acoustic properties: in situ, laboratory, and theoretical results from Eckernforde Bay, Baltic sea. *Continental Shelf Research*, 18.

Yardley, S. and Swarbrick, G. (2000). Lateral transfer: A source of additional overpressure? *Marine and Petroleum Geology - MAR PETROL GEOL*, 17.

Yilmaz, O. (2001). *Seismic Data Analysis*. SEG, second edition.

Zecchin, M., Donda, F., and Forlin, E. (2017). Genesis of the Northern Adriatic Sea (Northern Italy) since early Pliocene. *Marine and Petroleum Geology*, 79.

Zecchin, M., Tosi, L., and Caffau, M. (2011). Relationship between peat bed formation and climate changes during the last glacial in the Venice area. *Sediment Geol*, 238.